

*GDSA Repository
Systems Analysis
Investigations in FY2020*

Spent Fuel and Waste Disposition

*Prepared for
US Department of Energy
Spent Fuel and Waste Science and
Technology
Tara LaForce, Kyung W. Chang, Frank
V. Perry, Thomas S. Lowry, Eduardo
Basurto, Richard Jayne, Dusty Brooks,
Spencer Jordan, Emily Stein, Rosie
Leone, Michael Nole*

September 30, 2020

M2SF-20SN010304052

SAND2020-12028 R

DISCLAIMER

This information was prepared as an account of work sponsored by an agency of the U.S. Government. Neither the U.S. Government nor any agency thereof, nor any of their employees, makes any warranty, expressed or implied, or assumes any legal liability or responsibility for the accuracy, completeness, or usefulness, of any information, apparatus, product, or process disclosed, or represents that its use would not infringe privately owned rights. References herein to any specific commercial product, process, or service by trade name, trade mark, manufacturer, or otherwise, does not necessarily constitute or imply its endorsement, recommendation, or favoring by the U.S. Government or any agency thereof. The views and opinions of authors expressed herein do not necessarily state or reflect those of the U.S. Government or any agency thereof.

DISCLAIMER

This is a technical report that does not take into account contractual limitations or obligations under the Standard Contract for Disposal of Spent Nuclear Fuel and/or High-Level Radioactive Waste (Standard Contract) (10 CFR Part 961). For example, under the provisions of the Standard Contract, spent nuclear fuel in multi-assembly canisters is not an acceptable waste form, absent a mutually agreed to contract amendment.

To the extent discussions or recommendations in this report conflict with the provisions of the Standard Contract, the Standard Contract governs the obligations of the parties, and this report in no manner supersedes, overrides, or amends the Standard Contract.

This report reflects technical work which could support future decision making by DOE. No inferences should be drawn from this report regarding future actions by DOE, which are limited both by the terms of the Standard Contract and Congressional appropriations for the Department to fulfill its obligations under the Nuclear Waste Policy Act including licensing and construction of a spent nuclear fuel repository.

Sandia National Laboratories is a multi-mission laboratory managed and operated by National Technology & Engineering Solutions of Sandia, LLC., a wholly owned subsidiary of Honeywell International, Inc., for the U.S. Department of Energy's National Nuclear Security Administration under contract DE-NA0003525.



APPENDIX E
NFCSC DOCUMENT COVER SHEET¹

Name/Title of Deliverable/Milestone/Revision No. GDSA Repository Systems Analysis Investigations in FY2020 / M2SF-20SN010304052
Work Package Title and Number GDSA - Repository Systems Analysis – SNL / SF-20SN01030405
Work Package WBS Number. 1.08.01.03.04

Responsible Work Package Manager Tara LaForce (Name/Signature)
Date Submitted 9/30/2020

Quality Rigor Level for Deliverable/Milestone ²	<input type="checkbox"/> QRL-1	<input type="checkbox"/> QRL-2	<input checked="" type="checkbox"/> QRL-3	<input type="checkbox"/> QRL-4
	<input type="checkbox"/> Nuclear Data			Lab QA Program ³

This deliverable was prepared in accordance with Sandia National Laboratories
(Participant/National Laboratory Name)

QA program which meets the requirements of
 DOE Order 414.1 NQA-1 Other

This Deliverable was subjected to:

<input checked="" type="checkbox"/> Technical Review	<input type="checkbox"/> Peer Review
Technical Review (TR)	Peer Review (PR)
Review Documentation Provided	Review Documentation Provided
<input type="checkbox"/> Signed TR Report or,	<input type="checkbox"/> Signed PR Report or,
<input type="checkbox"/> Signed TR Concurrence Sheet or,	<input type="checkbox"/> Signed PR Concurrence Sheet
or,	
<input type="checkbox"/> Signature of TR Reviewer(s) below	<input type="checkbox"/> Signature of PR Reviewer(s)
below	

Name and Signature of Reviewers

Paul Mariner

NOTE 1: Appendix E should be filled out and submitted with the deliverable. Or, if the PICS:NE system permits, completely enter all applicable information in the PICS:NE Deliverable Form. The requirement is to ensure that all applicable information is entered either in the PICS:NE system or by using the NFCSC Document Cover Sheet.

- In some cases there may be a milestone where an item is being fabricated, maintenance is being performed on a facility, or a document is being issued through a formal document control process where it specifically calls out a formal review of the document. In these cases, documentation (e.g., inspection report, maintenance request, work planning package documentation or the documented review of the issued document through the document control process) of the completion of the activity, along with the Document Cover Sheet, is sufficient to demonstrate achieving the milestone.

NOTE 2: If QRL 1, 2, or 3 is not assigned, then the QRL 4 box must be checked, and the work is understood to be performed using laboratory QA requirements. This includes any deliverable developed in conformance with the respective National Laboratory / Participant, DOE or NNSA-approved QA Program.

NOTE 3: If the lab has an NQA-1 program and the work to be conducted requires an NQA-1 program, then the QRL-1 box must be checked in the work Package and on the Appendix E cover sheet and the work must be performed in accordance with the Lab's NQA-1 program. The QRL-4 box should not be checked.

SUMMARY

The Spent Fuel and Waste Science and Technology (SFWST) Campaign of the U.S. Department of Energy Office of Nuclear Energy, Office of Spent Fuel and Waste Disposition (SFWD), has been conducting research and development on generic deep geologic disposal systems (i.e., geologic repositories). This report describes specific activities in the Fiscal Year (FY) 2020 associated with the Geologic Disposal Safety Assessment (GDSA) Repository Systems Analysis (RSA) work package within the SFWST Campaign. The overall objective of the GDSA RSA work package is to develop generic deep geologic repository concepts and system performance assessment (PA) models in several host-rock environments, and to simulate and analyze these generic repository concepts and models using the GDSA Framework toolkit, and other tools as needed.

A summary of the specific objectives in FY2020 is to:

- Develop the technical bases for representing generic repository reference case concepts in GDSA Framework simulations for deep geologic disposal in any of four possible host-rock environments: argillite, crystalline, bedded salt, and unsaturated zone formations.
- Ensure that generic repository concepts include potential disposal of large, high-decay-heat waste packages.
- Incorporate relevant near field and far field processes as well as geologic/material properties and stratigraphic information developed in conjunction with geologic framework models (GFMs).
- Perform GDSA Framework performance assessment (PA) simulations and, in collaboration with the GDSA Uncertainty and Sensitivity Analysis Methods work package, associated uncertainty and sensitivity analyses for generic repository reference case concepts containing high-decay-heat waste packages.
- Include, as needed, detailed coupled processes in the EBS (e.g., waste form and waste package degradation, engineered barrier system (EBS) flow and transport, disturbed rock zone (DRZ) evolution) and natural system (e.g., near-field and far-field flow and transport, multi-phase flow).
- Reference case development, simulation, and analysis, as appropriate, for international collaborations, including for example, DECOVALEX, the Integration Group for the Safety Case (IGSC) sensitivity analysis task group, and the long-standing US-German collaboration on PA methodology applied to generic repositories in salt.

Section 1 of this report is a brief introduction. Section 2 summarizes a separate report that discusses development of disposal concepts for a generic high-temperature repository in shale (Stein et al., 2020a); ductile and brittle shale host rocks are considered. A new geological conceptual model of the brittle shale endmember is presented in subsection 3.2. The development of a DRZ evolution model for shale in the presence of bentonite buffer swelling is presented in subsection 3.1. Section 5 discusses progress to date on the international Development of COupled models and their VALidation against Experiments (DECOVALEX) 2023 Task F performance assessment comparison, which is being led by the GDSA team. Finally, Section 6 documents investigations into PFLOTRAN simulations on alternative mesh types and meshing tools as a step towards improving capability and improving stratigraphic modelling.

This report fulfills the FY2020 GDSA Repository Systems Analysis work package (SF-20SN01030405) Level 2 milestone entitled *GDSA Repository Systems Analysis FY20 Update* (M2SF-20SN010304052).

ACKNOWLEDGEMENTS

This work was supported by the US Department of Energy (DOE) Office of Nuclear Energy, through the Office of Spent Fuel and Waste Science and Technology (SFWST), within the Office of Spent Fuel and Waste Disposition (DOE NE-8).

Thanks go to our DOE customer for their support of this work. Thank you to David Sevougian (retired) for leading the Repository Systems Analysis team for the past few years and the start of this year; we would not have been able to do this work without his leadership and support. Thank you to Terry Miller and Phil Stauffer at Los Alamos National Laboratory for ongoing technical support for LaGrit, and to LianGe Zheng and Jonny Rutqvist of Lawrence Berkeley National Laboratory for input to the shale geomechanical analysis. Thanks to Lindsay McCabe, our OAA for assistance with formatting and referencing this report. Finally, thanks to our technical reviewer, Paul Mariner, for comments and suggestions that improved the report.

This report incorporates principal contributions from the following coauthors:

Eduardo Basurto (Section 6.2)

Dusty Brooks (Section 4)

Kyung Chang (Section 3.1)

Tara LaForce (Section 1, Sections 6.1, 6.3, and 6.4)

Rosie Leone (Section 5.2.8)

Thomas Lowry (Section 4)

Richard Jayne (Section 5.3)

Spencer Jordan (Section 6.3.3.2 two-domain heating benchmark)

Michael Nole (Section 3.1.2.1)

Frank Perry (Section 3.2)

Emily Stein (Section 2 and Sections 5.1 and 5.2)

This page is intentionally left blank.

CONTENTS

SUMMARY	iv
ACKNOWLEDGEMENTS	v
ACRONYMS	xix
1. INTRODUCTION	1
2. DISPOSAL CONCEPTS FOR A HIGH-TEMPERATURE SHALE (ARGILLITE) REPOSITORY	5
2.1 Geologic Setting	5
2.2 Natural Barrier System	5
2.3 Repository Design and Construction	5
2.4 Disturbed Rock Zone	6
2.5 Engineered Barrier System	6
2.6 High-Temperature Effects	7
3. SHALE REFERENCE CASE STUDIES	9
3.1 Buffer and DRZ Evolution	9
3.1.1 Evolution of Permeability and Porosity	9
3.1.1.1 Effective Swelling Stress	9
3.1.1.2 Stress-dependent Permeability and Porosity Functions	10
3.1.2 Model Setting	10
3.1.2.1 PFLOTRAN Implementation	10
3.1.2.2 Model Domain	10
3.1.2.3 Parameters	11
3.1.3 Results and Discussion	13
3.1.3.1 Effect of Permeability Evolution	13
3.1.3.2 Effect of Porosity Evolution	17
3.1.4 Future Work	18
3.2 Conceptual Model for Brittle Shales	19
3.2.1 Summary of Shale Conceptual Model from Argillite Concepts Workshop	19
3.2.2 Fracture Systems and Fracture Permeability	19
3.2.2.1 Overview of Fracture Systems	19
3.2.2.2 Fracture Sealing and Permeability	20
3.2.3 Generalized Stratigraphic and Hydrologic Framework for Paleozoic Shales	21
3.2.3.1 Stratigraphy and Major Aquifers	21
3.2.3.2 Hydrologic Properties of Aquifers and Confining Units	28
3.2.4 The Regional Groundwater System of the Illinois Basin	29
3.2.5 Summary of Brittle Shale Properties	31

4.	GDSA SALT REFERENCE CASE	33
4.1	Engineered Barriers.....	33
4.1.1	Engineered Barrier Characteristics	34
4.1.2	Inventory	34
4.1.3	Waste Form.....	36
4.1.4	Waste Package	36
4.1.5	Crushed Salt Backfill	37
4.1.6	Salt Seals.....	37
4.2	Geosphere / Natural Barriers.....	37
4.2.1	Natural Barrier Characteristics.....	38
4.2.2	Halite Host Rock	40
4.2.2.1	Chemical Environment	40
4.2.2.2	Solubility.....	41
4.2.3	Disturbed Rock Zone (DRZ).....	42
4.2.4	Anhydrite	42
4.2.5	Fractured Dolomite Aquifer.....	43
4.2.6	Solubility and Sorption of Radionuclides	43
4.3	Biosphere.....	44
4.4	Post-Closure Performance Assessment Model	44
4.4.1	Conceptual Model.....	44
4.4.2	Numerical Implementation	45
4.4.2.1	Model Domain and Discretization	46
4.4.2.2	Initial Conditions	47
4.4.2.3	Boundary Conditions	47
4.4.2.4	Waste Package Heat Sources	47
4.4.2.5	Waste Package Breach and Radionuclide Source Team.....	48
4.4.2.6	Material Properties.....	48
4.5	Deterministic PA Simulation	49
4.5.1	Temperature	50
4.5.2	Waste Package Breach	53
4.5.3	Radionuclide Transport.....	54
4.6	Probabilistic Assessment.....	64
4.6.1	Anhydrite East of the Repository.....	64
4.6.2	Dolomite East of the Repository	68
4.6.3	Dolomite End.....	73
4.6.4	DRZ_16_25 & DRZ_41_25.....	77
4.6.5	Shaft3 Mid.....	84
4.6.6	Sensitivity.....	88
5.	DECOVALEX CRYSTALLINE AND SALT REFERENCE CASES	94
5.1	Introduction	94
5.2	Crystalline Reference Case	94
5.2.1	Geologic Setting and Repository Design.....	94
5.2.2	Waste Form and Inventory.....	95
5.2.3	Waste Canister	95
5.2.4	Buffer (in Deposition Holes).....	95

5.2.5	Backfill (in Tunnels)	96
5.2.6	Fractured Host Rock	96
5.2.7	Evolutionary Scenarios	97
5.2.8	Benchmark problems	97
5.3	DECOVALEX Salt Reference Case	99
5.3.1	Generic Geologic Setting	99
5.3.1.1	United States	99
5.3.1.2	Germany.....	100
5.3.2	Waste Inventory, Waste Form, Waste Package, and Emplacement Concept	103
5.3.3	Backfill.....	105
5.3.4	Process-Events	105
6.	PRELIMINARY INVESTIGATION INTO ALTERNATIVE MESHES	108
6.1	Motivation for alternate meshing	108
6.1.1	Polyhedral meshes.....	108
6.1.2	Voronoi meshes.....	108
6.2	ANSYS-Fluent simulations.....	108
6.2.1	Setting up models.....	109
6.2.1.1	Geometry.....	109
6.2.1.2	ANSYS Fluent Meshing	110
6.2.2	PFLOTRAN Simulations	113
6.3	VoroCrust Simulations.....	119
6.3.1	VoroCrust development overview	119
6.3.2	Workflow to make meshes suitable for PFLOTRAN simulation	119
6.3.3	Analytical benchmark models.....	120
6.3.3.1	VoroCrust Meshes	120
6.3.3.2	PFLOTRAN Simulations.....	123
6.3.4	Large-scale simulations.....	126
6.3.4.1	Wyoming Uplift tracer example	126
6.3.4.2	Unfractured shale GFM	128
6.3.5	VoroCrust simulation results and future work.....	133
6.4	Comparison of ANSYS-Fluent and VoroCrust meshes.....	134
7.	REFERENCES	136
Appendix A	Argillite Concepts Meeting Agenda	A-1
Appendix B	DECOVALEX Crystalline Questionnaire.....	A-4
Appendix C	VoroCrust Output Conversion.....	A-12

LIST OF FIGURES

Figure 1-1. Information flow and the role of performance assessment for RD&D prioritization during a single stage of repository development. (Taken from Sevougian et al., 2019b).....	3
Figure 3-1. Model domain and grid. Four sections are modeled: waste package (red), buffer (blue), disturbed rock zone (yellow), and shale host rock (grey).	11
Figure 3-2. Evolution of liquid saturation (solid line) within the buffer and corresponding changes in swelling stress (dashed line) acting on the DRZ for three permeability functions: (1) Power law function (blue), (2) Modified cubic function (green), and (3) Two-part Hooke’s law model (magenta). Black line shows the reference case with a constant DRZ permeability and is very similar to TPHM result.	14
Figure 3-3. Evolution of physical quantities at the DRZ cell nearest the buffer for three cases with different stress-dependent permeability functions: (a) gas pressure, (b) gas saturation, (c) liquid pressure, (d) liquid saturation and swelling stress, (e) temperature, and (f) permeability.	15
Figure 3-4. DRZ permeability evolution using TPHM with variation in the fraction of soft-part. The host rock permeability ($1 \times 10^{-20} \text{ m}^2$) is indicated by a black line.....	16
Figure 3-5. (a) Evolution of the DRZ porosity from the simulation integrating permeability functions and log-linear relationship between permeability and porosity. (b) Evolution of the DRZ permeability.....	17
Figure 3-6. Schematic depiction of fracture frequency and quartz content in shale layers of the Antrim/Ellsworth shales in the Michigan Basin.....	20
Figure 3-7. Location map and generalized cross-section of the Illinois Basin from Panno et al. (2013).....	23
Figure 3-8. Reference stratigraphic column associated with the New Albany Shale in the southern Illinois Basin.....	24
Figure 3-9. N-S geologic cross-section of the Illinois Basin showing Cl concentrations and isocontours. Low Cl concentrations are present in the northern part of the basin and follow permeable units such as the St. Peter Sandstone, indicating freshwater recharge. The southern part of the basin is characterized by high concentrations of Cl at shallow depth, indicating upward flow of saline waters. The dilute downward plume at the IL-KY border is the location of the Ohio River.....	31
Figure 4-1. Distribution and depth to top of salt formations in major sedimentary basins of the U.S. Salt formations are labeled by name or by common reference and listed in stratigraphic order where more than one salt formation is present in a basin. [Figure from Perry et al. (2014).].....	39
Figure 4-2. Generic stratigraphic column for salt reference case. The repository horizon, including the DRZ and backfill, is centered between two thin beds of anhydrite at $z = 600 \text{ m}$	40
Figure 4-3. Relationship between the Log_{10} permeability distribution of Mariner et al. (2015) and Sevougian et al. (2016) and the porosity distribution of Fox (2008). In the model, permeability (k) is given in m^2 as a function of porosity.....	43

Figure 4-4. Repository layout at 600 m elevation showing the drifts numbered left to right, longhall, shorthalls, access halls, and shafts. Drifts 1 to 31 contain 24-PWRs while drifts 32-51 contain 37-PWRs. The model assumes a mirrored image along the closed southern boundary. 46

Figure 4-5. Salt Reference PA model grid showing the repository and shafts in relation to the dolomite aquifer and anhydrite layers. 47

Figure 4-6. Plot of heat generation over time for the PWR-24 and PWR-37 canisters. 48

Figure 4-7. Repository view of the observation points in the model. For the waste packages, observation points were placed along the center-line in waste package #25 in drifts 1, 16, 31, 32, 41, and 51. In addition, waste package observation points were placed at the ends of drifts 16 and 41, which are in the center of the block of 24-PWRs and block of 37-PWRs, respectively. Observation points were also placed at the bottom, mid-elevation, and top of each shaft. For the anhydrite layers and the dolomite aquifer (An1_Repo, An2_Repo, and Dolomite_Repo), observation points were placed 185 m down gradient of drift 51 *at the appropriate elevation for each layer* (they appear as the same point in the figure). The same was done for each layer at the east end of the model, 5000 m down gradient of the repository (not shown)..... 50

Figure 4-8. Average waste package temperature across the 200 PA simulations versus time for the waste package observation points shown in Figure 4-7 and Figure 4-9..... 51

Figure 4-9. Plan view of temperatures in the repository after 20 years (left) and 300 years (right) for the deterministic run. The position of the waste packages corresponding to those in Figure 4-8 are indicated on the 20-year plot..... 52

Figure 4-10. Average temperature across the 200 PA simulations versus time in the backfill (left) and the DRZ (right) immediately downgradient from the waste package observation points. [See Figure 4-7 for the observation point locations.] 52

Figure 4-11. Average temperature across the 200 PA simulations versus time in the upper (An1) and lower (An2) anhydrite layers and the dolomite aquifer for points 185 m (left) and 5 km (right) down gradient of the repository..... 53

Figure 4-12. Cumulative distribution plots of breach time for the 24-PWRs (left) and 37-PWRs (right) 200 PA simulations. The red line is the average of the 200 simulations and the blue line is the results of the single deterministic run using the average parameter values. 54

Figure 4-13. ²³⁷Np concentration iso-volume at a limit of 1.0×10^{-12} M after 1,000,000 years for the deterministic simulation. The pathway up the shafts is clearly evident as is the transport along the dolomite aquifer from Shaft 3. Note the scale difference from Figure 4-14. The "gold band" is the elevation of the dolomite aquifer. 56

Figure 4-14. ¹²⁹I concentration iso-volume at a limit of 1.0×10^{-10} M after 1,000,000 years for the deterministic simulation. The pathway up the shafts is clearly evident, as is the transport along the dolomite aquifer from Shafts 2 and 3 although the column of high concentration solute has diffused out as compared to ²³⁷Np. Note the scale difference from Figure 4-13. The "gold band" is the elevation of the dolomite aquifer. 57

Figure 4-15. Concentration of ²³⁷Np (left) and ¹²⁹I (right) at the bottom, mid-point, and top of each shaft for the deterministic simulation. 57

Figure 4-16. ²³⁷Np concentrations in a horizontal slice through the center of the dolomite aquifer after 10,000, 100,000, and 1,000,000 years for the deterministic simulation. Units are log₁₀ molar concentration values. 58

Figure 4-17. ¹²⁹I concentrations in a horizontal slice through the center of the dolomite aquifer after 10,000, 100,000, and 1,000,000 years for the deterministic simulation. Units are log₁₀ molar concentration values. 59

Figure 4-18. ²³⁷Np concentrations in a horizontal slice through the center of the upper anhydrite layer after 10,000, 100,000, and 1,000,000 years for the deterministic simulation. Units are log₁₀ molar concentration values. Maximum concentrations are slightly higher than the plotted limit. 60

Figure 4-19. ¹²⁹I concentrations in a horizontal slice through the center of the upper anhydrite layer after 10,000, 100,000, and 1,000,000 years for the deterministic simulation. Units are log₁₀ molar concentration values. 61

Figure 4-20. ²³⁷Np concentrations on a vertical slice through shafts 2 (left) and 3 (right) at 10,000, 100,000, and 1,000,000 years for the deterministic simulation. 62

Figure 4-21. ¹²⁹I concentrations on a vertical slice through shafts 2 (left) and 3 (right) at 10,000, 100,000, and 1,000,000 years for the deterministic simulation. 63

Figure 4-22. Plots of ¹²⁹I molar concentrations at the An1_Repo observation point colored by peak concentration (upper left), anhydrite permeability (upper right), DRZ permeability (middle left), dolomite porosity (middle right), backfill permeability (lower left), and mean degradation rate (lower right). 65

Figure 4-23. Scatter plot of the maximum (peak) ¹²⁹I molar concentration at the An1_Repo observation point versus values of the sampled variables. 66

Figure 4-24. Plots of ²³⁷Np molar concentrations at the An1_Repo observation point colored by peak concentration (upper left), anhydrite permeability (upper right), DRZ permeability (middle left), dolomite porosity (middle right), backfill permeability (lower left), and mean degradation rate (lower right). 67

Figure 4-25. Scatter plot of the maximum (peak) ²³⁷Np molar concentration at the An1_Repo observation point versus values of the sampled variables. 68

Figure 4-26. Plots of ¹²⁹I molar concentrations at the Dolomite_Repo observation point colored by peak concentration (upper left), anhydrite permeability (upper right), DRZ permeability (middle left), dolomite porosity (middle right), ShaftFill permeability (lower left), and mean degradation rate (lower right). 69

Figure 4-27. Scatter plot of the maximum (peak) ¹²⁹I molar concentration at the Dolomite_Repo observation point versus values of the sampled variables. 70

Figure 4-28. Planview comparison of Run #71 and Run #92, which have the highest and lowest ¹²⁹I concentration at the Dolomite_Repo observation point (marked by red dot) respectively after 1,000,000 years. The blue dot indicates the location of the Dolomite_End observation point. The actual maximums are slightly higher than the plotted maximum. 71

Figure 4-29. Plots of ²³⁷Np molar concentrations at the Dolomite_Repo observation point colored by peak concentration (upper left), anhydrite permeability (upper right), DRZ permeability (middle left), dolomite porosity (middle right), ShaftFill permeability (lower left), and mean degradation rate (lower right). 72

Figure 4-30. Scatter plot of the maximum ^{237}Np molar concentration at the Dolomite_Repo observation point versus values of the sampled variables.	73
Figure 4-31. Plots of ^{129}I molar concentrations at the Dolomite_End observation point colorized by peak concentration (upper left), anhydrite permeability (upper right), DRZ permeability (middle left), dolomite porosity (middle right), ShaftFill permeability (lower left), and mean degradation rate (lower right).....	74
Figure 4-32. Scatter plot of the maximum ^{129}I molar concentration at the Dolomite_End observation point versus values of the sampled variables.	75
Figure 4-33. Plots of ^{237}Np molar concentrations at the Dolomite_End observation point colorized by peak concentration (upper left), anhydrite permeability (upper right), DRZ permeability (middle left), dolomite porosity (middle right), ShaftFill permeability (lower left), and mean degradation rate (lower right).....	76
Figure 4-34. Scatter plot of the maximum (peak) ^{237}Np molar concentration at the Dolomite_End observation point versus values of the sampled variables.	77
Figure 4-35. Plots of ^{129}I molar concentrations at the DRZ_16_25 observation point colorized by peak concentration (upper left), anhydrite permeability (upper right), DRZ permeability (middle left), backfill permeability (middle right), ShaftFill permeability (lower left) and mean degradation rate (lower right).....	78
Figure 4-36. Scatter plot of the maximum ^{129}I molar concentration at the DRZ_16_25 observation point versus values of the sampled variables.....	79
Figure 4-37. Plots of ^{129}I molar concentrations at the DRZ_41_25 observation point colorized by peak concentration (upper left), anhydrite permeability (upper right), DRZ permeability (middle left), backfill permeability (middle right), ShaftFill permeability (lower left) and mean degradation rate (lower right).....	80
Figure 4-38. Scatter plot of the maximum (peak) ^{129}I molar concentration at the DRZ_41_25 observation point versus values of the sampled variables.	81
Figure 4-39. Plots of ^{237}Np molar concentrations at the DRZ_16_25 observation point colorized by peak concentration (upper left), anhydrite permeability (upper right), DRZ permeability (middle left), backfill permeability (middle right), ShaftFill permeability (lower left) and mean degradation rate (lower right).....	82
Figure 4-40. Plots of ^{237}Np molar concentrations at the DRZ_41_25 observation point colorized by peak concentration (upper left), anhydrite permeability (upper right), DRZ permeability (middle left), backfill permeability (middle right), ShaftFill permeability (lower left) and mean degradation rate (lower right).....	83
Figure 4-41. Plots of ^{129}I molar concentrations at the Shaft3_Mid observation point colorized by peak concentration (upper left), anhydrite permeability (upper right), DRZ permeability (middle left), dolomite porosity (middle right), ShaftFill permeability (lower left) and mean degradation rate (lower right).	85
Figure 4-42. Scatter plot of the maximum (peak) ^{129}I molar concentration at the Shaft3_Mid observation point versus values of the sampled variables.	86
Figure 4-43. Plots of ^{237}Np molar concentrations at the Shaft3_Mid observation point colorized by peak concentration (upper left), anhydrite permeability (upper right), DRZ permeability (middle left), dolomite porosity (middle right), ShaftFill permeability (lower left) and mean degradation rate (lower right).....	87

Figure 4-44. Scatter plot of the maximum (peak) ²³⁷Np molar concentration at the Shaft3_Mid observation point versus values of the sampled variables. 88

Figure 4-45. Sensitivity (left column) and correlation coefficients for the An1_Repo, Dolomite_Repo, and Dolomite_End observation points for Log₁₀ of peak ¹²⁹I concentration..... 90

Figure 4-46. Sensitivity (left column) and correlation coefficients for the An1_Repo, Dolomite_Repo, and Dolomite_End observation points for Log₁₀ of peak ²³⁷Np concentration..... 91

Figure 4-47. Sensitivity (left column) and correlation coefficients for the DRZ_16_25, DRZ_41_25, and Shaft3_Mid observation points for Log₁₀ of peak ¹²⁹I concentration..... 92

Figure 4-48. Sensitivity (left column) and correlation coefficients for the Shaft3_Mid observation points for Log₁₀ of peak ²³⁷Np concentration..... 93

Figure 5-1. Left: Analytical pressure solution for 2D steady state flow. Right: Analytical pressure solution for 3D steady state flow at z = 0.45 m 98

Figure 5-2. Analytical solution at 20,000 sec for 1D transient transport for a conservative, decaying, and adsorbing tracer. 99

Figure 5-3. Generic stratigraphic column used for U.S. salt reference case (from Sevougian et al., 2016). The potential storage formation is between the very two thin anhydrite layers in the center of the figure. 100

Figure 5-4. Geologic reference profile for the "flat-bedded" salt formation scenario (from Bollingfehr et al., 2018). The potential storage formation is the light blue z2NA formation..... 101

Figure 5-5. Geologic reference profile for the "salt pillow" scenario (from Bollingfehr et al., 2018). The potential storage formation is the light blue z2NA formation. 102

Figure 5-6. Simplified NW-SE geological cross-section of the Gorleben salt dome (from Bollingfehr et al., 2017). The potential storage formation is the light blue z2HS formation in the center of the dome..... 102

Figure 6-1. Isometric view of 2D rectangular model with 100x100 x1m domain in ANSYS Fluent. 109

Figure 6-2. Isometric view of the nearfield one quarter waste package model in a 25x10x150m domain in CUBIT. 110

Figure 6-3. Top view of meshes generated on the 2D rectangular model with 100x100x1m domain in ANSYS Fluent. Left: Ansys1 mesh with 10,000 hexahedral elements. Right: Ansys2 mesh with 640,000 hexahedral elements. 111

Figure 6-4. Isometric perspective projection of Ansys3 (23,083 polyhedral elements) generated on the 2D rectangular model with 100x100x1m domain in ANSYS Fluent. 112

Figure 6-5. Isometric view of submap mesh scheme (37,440 cells) of the one quarter waste package model with a 25 x 10 x 150m domain generated on ANSYS Fluent. 112

Figure 6-6. Left: ParaView visualization of left corner view of Ansys1 (10K hex mesh) generated on the 2D rectangular model with 100x100x1m domain showing tracer concentration. Right: ParaView visualization of top view of Ansys2 (640K hex mesh) generated on the 2D rectangular model with 100x100x 1m domain showing tracer concentration. 113

Figure 6-7. Pressure on the plane $z=0.5$ for the Richards Equation test problem on a $100 \times 100 \times 1$ m domain with $380 \times 380 \times 3$ structured mesh. Left: Initial pressure condition. Right: Pressure at $t=0.1$ days. 114

Figure 6-8. Pressure as a function of time in days at four monitoring points for the Richards Equation test problem on mesh Ansys1. Top: Monitoring point a (24.5, 24.5, 0.5). Second: Monitoring point b (49.5, 49.5, 0.5). Third: Monitoring point c (49.5, 74.5, 0.5) Bottom: Monitoring point d (74.5, 74.5, 0.5)..... 115

Figure 6-9. Simulation results for the nearfield one quarter waste package model showing the Total tracer (M), Liquid Pressure (Pa) and Temperature (C) on three columns, each representing a different time. Column 1 represents time at 100 years, column 2 at 1,000 years and column 3 at 10,000 years..... 117

Figure 6-10. Total Tracer as a function of time in years for the full million-year simulation at four monitoring points for the nearfield one quarter waste package problem. Monitoring point wp is in the waste package. Monitoring point buffer is in the buffer adjacent to the waste package. Monitoring point drz is in the DRZ near the waste package. Monitoring point shale is in the shale near the disturbed rock zone. 117

Figure 6-11. Liquid pressure as a function of time in years for the first 50 years of the simulation at four monitoring points for the nearfield one quarter waste package problem. Monitoring point wp is in the waste package. Monitoring point buffer is in the buffer adjacent to the waste package. Monitoring point drz is in the DRZ near the waste package. Monitoring point shale is in the shale near the disturbed rock zone. 118

Figure 6-12. Temperature as a function of time in years for the first 10,000 years of the simulation at four monitoring points for the nearfield one quarter waste package problem. Monitoring point wp is in the waste package. Monitoring point buffer is in the buffer adjacent to the waste package. Monitoring point drz is in the DRZ near the waste package. Monitoring point shale is in the shale near the disturbed rock zone. 118

Figure 6-13. Example surface mesh for the two-domain heating benchmark problem. Material 1 is red and exists from $r=(0,50)$ and Material 2 is yellow and exists from $(50,100)$ 123

Figure 6-14. Pressure as a function of time in days at the four monitoring points for the Richards Equation test problem on mesh Voro3. Top: Monitoring point a (50,50,0.5). Second: Monitoring point c (75,50,0.5). Third: Monitoring point b (50,25,0.5) Bottom: Monitoring point d (25,25,0.5). 125

Figure 6-15. PFLOTRAN 1D-radial structured and VoroCrust mesh temperature results compared to analytical solution at radii of 25 and 62.5 (Note: Structured mesh results are the same for each set of figures for their respective radii since only one simulation was ran for each)..... 126

Figure 6-16. Left: VoroCrust surface mesh of the Wyoming uplift. Right: Material IDs of the Wyoming uplift in the simulation model..... 128

Figure 6-17. Left: Pressure during tracer injection into the Wyoming uplift. Right: Tracer concentration..... 128

Figure 6-18. GFM model of the Pierre Shale from the northeast at 10x vertical resolution (taken from Sevougian et al., April 2019). 130

Figure 6-19. 2.0×1.75 km sector of the shale GFM model simplified to 6 representative rock volumes. Colors are the same as in Figure 6-18 above. Left: Formation volumes. Right: Surface mesh generated in VoroCrust. 131

Figure 6-20. Close up of the VoroCrust mesh around the Niobrara Formation, the thinnest layer in the simulation model..... 131

Figure 6-21. Tracer concentrations 100,000 years after release. Left: ideal tracer. Middle: decaying tracer. Right: adsorbing tracer. North is in the direction of increasing y to the right..... 132

Figure 6-22. Tracer concentrations as a function of time at four monitoring points in the shale GFM sector model. Top Left: In the K-shale at the tracer source. Top Right: In the K-shale at the model boundary immediately downstream of the tracer source. Bottom Left: In the Niobrara aquifer at the model boundary immediately downstream of the tracer source. Bottom Right: In the Inyan Kara aquifer at the model boundary immediately downstream of the tracer source. Notice that the x-scale is logarithmic and adsorbing tracer concentration is so low ($\sim 1 \times 10^{-20}$) it has been cut off all of the subplots except for the one in the repository. 133

LIST OF TABLES

Table 3-1. Material properties for the DRZ evolution base case. (Sevougian et al., 2019b).....	12
Table 3-2. Parameter values for different permeability functions for the DRZ evolution base case.....	12
Table 3-3. Reference stratigraphy and hydrologic properties of brittle shale environment in the Illinois Basin	25
Table 3-4. Summary of properties of the brittle and ductile Shales	32
Table 4-1. Dimensions and counts for the salt repository layout.....	34
Table 4-2. 24-PWR 40-GWd/MTHM, 50-year OoR SNF inventory of selected radionuclides for the salt reference case.	35
Table 4-3. 37-PWR 60-GWd/MTU, 100-year OoR SNF inventory of selected radionuclides for the salt reference case	36
Table 4-4. Representative brine compositions for the salt reference case (Sevougian et al., 2012).....	41
Table 4-5. Element solubility calculated at T = 25°C in concentrated brine (Wang and Lee, 2010 as cited in Clayton et al., 2011).	42
Table 4-6. Kds and Solubility for the materials included in the salt reference case model.....	44
Table 4-7. Conceptual representation of key components in the salt reference PA model.	45
Table 4-8. Listing of the uncertain variables and their probabilistic distributions used in the LHS PA simulations.....	45
Table 4-9. Material properties for constant parameters.	49
Table 5-1. Disposal concepts considered by Prij et al. (1989).....	103
Table 5-2. The waste inventories, waste form, maximum allowable temperatures within the repository, waste package type, and emplacement concept proposed by previously published safety cases for each country.....	104
Table 5-3. Generalized summary of process and events for each country. This is a simplified summary that lumps many processes and events into categories, for more detail see published reference cases.	106
Table 6-1. Properties for the ANSYS Fluent mesh of the 100x100x1m domain. Monitoring points and results for simulations of the 2D domain benchmark against Richards equation analytical solution are also shown. All simulation times are for parallel simulations using 8 nodes on a Linux Workstation with two cores of 8 nodes each.	111
Table 6-2. Simulation summary for ANSYS Fluent generated mesh on nearfield one quarter waste package model. The simulation time is for a parallel simulation using 16 nodes on a Linux Workstation with two cores of 8 nodes each.....	116
Table 6-3. Properties for the VoroCrust and PFLOTTRAN meshes of the 100x100x1m domain. Monitoring points and results for simulations of the 2D domain benchmark against Richards equation analytical solution are also shown. All simulation times are for parallel simulations using 12 nodes on a Linux Workstation with two cores of 12 nodes each.	120

Table 6-4. Properties of the VoroCrust and PFLOTRAN meshes for the two-domain radial simulation. Monitoring points and results for simulations benchmarked against the two-domain heating analytical solution are also shown. 123

Table 6-5. Permeability and porosity of each layer in the Wyoming uplift tracer example. 127

ACRONYMS

DECOVALEX	Development of COupled models and their VALidation against Experiments
DOE	U.S. Department of Energy
DRZ	disturbed rock zone
EBS	engineered barrier system
FY2020	Fiscal Year 2020
GDSA	Geologic Disposal Safety Assessment
GFM	geologic framework model
HLW	high-level radioactive waste
IGSC	Integration Group for the Safety Case
LANL	Los Alamos National Laboratory
m	meter
mm	millimeter
MPa	megapascal
MTHM	metric tons heavy metal
NE	Office of Nuclear Energy
OoR	out of reactor
PA	performance assessment
PFLOTRAN	massively parallel reactive flow and transport model for describing subsurface processes (pflotran.org)
PWR	pressurized water reactor
R&D	research and development
RSA	Repository Systems Analysis
SFWD	Spent Fuel and Waste Disposition
SFWST	Spent Fuel and Waste Science and Technology
SKB	Swedish Nuclear Fuel and Waste Management Company
SNF	spent nuclear fuel
SNL	Sandia National Laboratories
TH	thermal-hydrological
THM	thermal-hydrologic-mechanical
WP	waste package
yr	year

This page is intentionally left blank.

GDSA REPOSITORY SYSTEMS ANALYSIS INVESTIGATIONS IN FY2020

1. INTRODUCTION

The Spent Fuel and Waste Science and Technology (SFWST) Campaign of the U.S. Department of Energy (DOE) Office of Nuclear Energy, Office of Spent Fuel and Waste Disposition (SFWD), is conducting research and development (R&D) on geologic disposal of spent nuclear fuel (SNF) and high-level radioactive waste (HLW). Two of the highest priorities for SFWST disposal R&D are design concept development and disposal system performance assessment (PA) modeling (DOE 2012, Table 6). Generic design (or reference-case) concepts being considered for SNF and HLW disposal since 2010 include mined repository concepts in bedded salt, argillite (shale), and crystalline rock. An additional option began two years ago is a potential mined repository in unsaturated alluvium. The PA R&D since 2012 has mostly focused on disposal of commercial spent nuclear fuel (CSNF) inventory packaged in smaller waste packages, such as 4-PWR and/or 12-PWR waste packages. However, a greater emphasis is given the last two years to simulating disposal of higher decay-heat waste packages containing 21, 24, or 37 pressurized water reactor (PWR) assemblies.

This report describes accomplishments for the Fiscal Year (FY) 2020 in the development of generic repository reference cases and PA modeling and analysis. Prior development and accomplishments are summarized at a high-level in Mariner et al. (2019), with much more detail provided in Mariner et al. (2018), Mariner et al. (2017), Mariner et al. (2016), Mariner et al. (2015), Sevougian et al. (2016), Sevougian et al. (2014), Sevougian et al. (2013), Sevougian et al. (2012), Freeze et al. (2013), Vaughn et al. (2013), Sevougian et al. (2019a) and Sevougian et al. (2019b).

Sassani et al (2020) details a 5-year research R&D plan that “provides a strategic guide to the work within the DR R&D technical areas, focusing on the highest priority technical thrusts” for the SFWST Campaign. The plan discusses the need to focus on four areas (Sassani et al., 2020):

- Capabilities Development and Demonstration
- International Collaboration and Underground Research Laboratories
- Engineered Barrier System Representations
- Evaluation of Potential Direct Disposal of large, high-energy waste packages

The objective of the GDSA Repository Systems Analysis work package is to develop generic deep geologic repository concepts and system Performance Assessment (PA) models in line with the current 5-year plan (Sassani et al., 2020) for several host-rock environments, and to simulate and analyze these generic repository concepts and models using the GDSA Framework toolkit (Mariner et al., 2019), and other tools as needed.

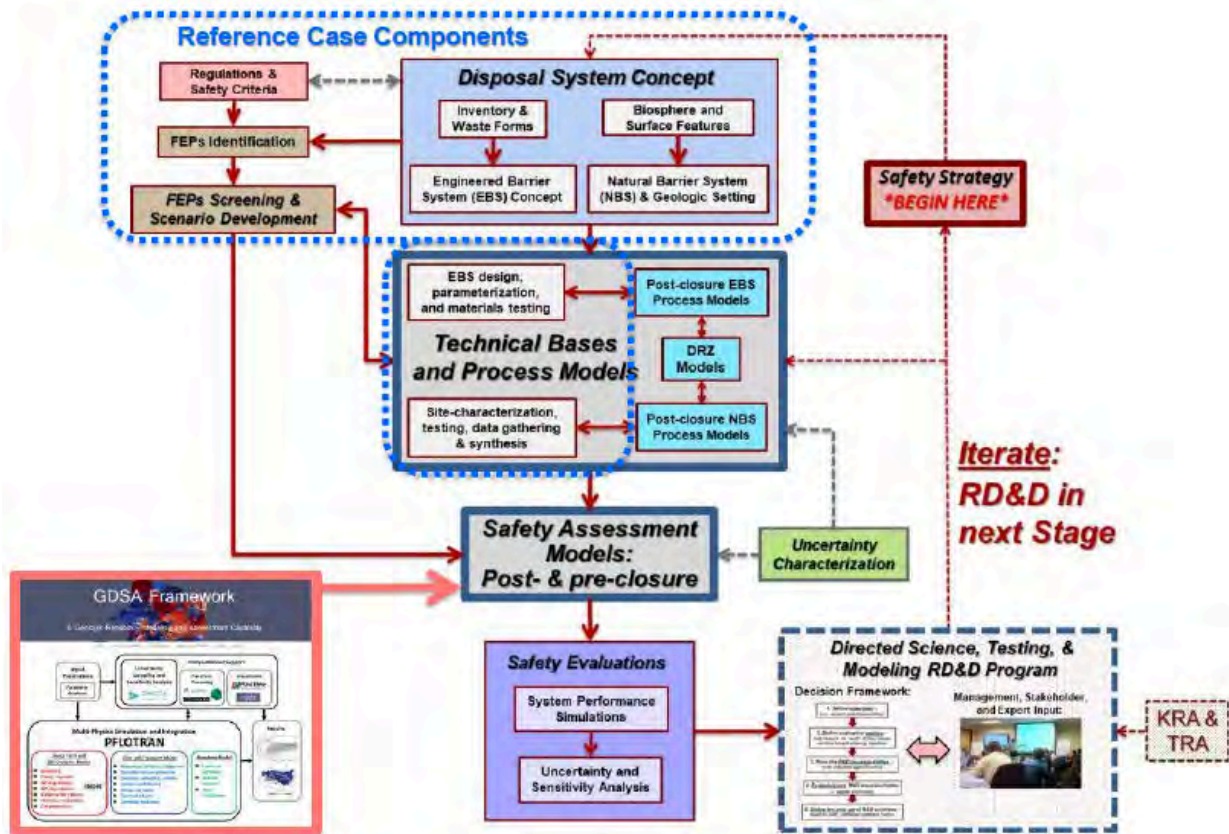
The work accomplished in FY20 applies to the goals of capabilities development and demonstration, international collaboration, engineered barrier systems, and evaluation of disposal of large, high-energy waste packages. The specific goals for FY20 are:

- In Feb 25-26, 2020 a meeting with representatives from several laboratories was held to initiate development of high-temperature disposal concepts for a generic repository in shale; ductile and brittle shale endmembers were discussed. The results of this meeting were written as a report by Stein et al. (2020a), which is summarized in Section 2. The details of the geological conceptual model of the brittle shale endmember are in Section 3.2.

- A study was conducted on the impact of buffer swelling on the disturbed rock zone (DRZ) in a shale reservoir. This study involves PFLOTRAN implementation of a reduced order model for porosity and permeability evolution in the DRZ in response to increased stress from the swelling buffer. The results of this study are in Section 3.1.
- A PA simulation study has been undertaken for a generic bedded-salt reference case. This reference case builds on the reference case for a defense waste repository (Sevougian et al. 2016, Section 4) to model the disposal of 24- and 37-PWR waste packages. Simulation and uncertainty analysis on 200 realizations have been conducted. The results of this study are in Section 4.
- The GDSA team is leading Task F of the DECOVALEX 2023 project on behalf of the US DOE's SFWST Campaign. This project has 9 international partners for the crystalline case and 3 for the salt case. Both cases will involve collaborative development of reference case scenarios for post-closure performance assessment (PA) for deep geologic repositories. An overview of the progress to date is in Section 5.
- Alternative meshing tools have been studied in a step towards improving GDSA capability and to further the goal of having all open-source software in the GDSA Framework workflow. Polyhedral and Voronoi meshes were created for use in PFLOTRAN and a series of simulations have been run using each type of mesh. This work is presented in Section 6.

Figure 1-1 shows the information flow and role of performance assessment in R&D prioritization (Sevougian et al., 2019b). A more detailed discussion of safety case and reference case methodology is included in Section 2 of Sevougian et al. (2019b). This report presents progress on several of the workflow components listed. The new high-temperature shale conceptual model (Sections 2 and 3.2) represents the initial 'Disposal System Concept' for a new generic repository case. The salt reference case (Section 4) in this report includes all of the 'Reference Case Components' inside the blue dashed outline as well as uncertainty and sensitivity analysis for a generic bedded-salt repository. The DRZ evolution work in Section 3.1 is the first step in PFLOTRAN implementation of post-closure EBS and DRZ evolution models in a shale repository. Finally, the alternative meshing in Section 6 contributes to capability development towards improved modelling and open source software in the GDSA Framework.

Figure 1-1. Information flow and the role of performance assessment for RD&D prioritization during a single stage of repository development. (Taken from Sevoungian et al., 2019b)



This page is intentionally left blank.

2. DISPOSAL CONCEPTS FOR A HIGH-TEMPERATURE SHALE (ARGILLITE) REPOSITORY

Disposal of large, heat-generating waste packages containing the equivalent of 21 PWR assemblies or more is among the disposal concepts under investigation for a future repository for SNF in the United States. Without a long (>200 y) surface storage period, disposal of 21-PWR or larger waste packages (especially if they contain high-burnup fuel) would result in in-drift and near-field temperatures considerably higher than considered in previous generic reference cases that assume either 4-PWR or 12-PWR waste packages (Jove Colon et al., 2014; Mariner et al., 2015; 2017). Sevougian et al. (2019c) identified high-temperature process understanding as a R&D area for the SFWST Campaign.

A two-day workshop in February 2020 brought together campaign scientists with expertise in geology, geochemistry, geomechanics, engineered barriers, waste forms, and corrosion processes to begin integrated development of a high-temperature reference case for disposal of spent nuclear fuel in a mined repository in a shale host rock. The agenda is attached in Appendix A. As a result of the workshop, concepts and processes forming the basis for a high-temperature shale repository reference case are described in a report published by Sandia National Laboratories (Stein et al., 2020a). A brief summary is presented here.

2.1 Geologic Setting

Two shale endmembers, ductile and brittle, are considered. These are further described and placed in the context of US sedimentary basins in Sevougian et al (2019b) and Section 3.2 of this report, respectively. Whether a shale is ductile or brittle is determined by its original depositional environment and resulting clay content, as well as the maximum depth of burial experienced and resulting degree of induration. The two endmembers differ in mechanical behavior, porewater chemistry, and thermal and hydrologic properties.

2.2 Natural Barrier System

The ductile shale endmember is characterized by a high clay mineral content, low mechanical strength, low thermal conductivity, and very low permeability within intact blocks of rock (over a scale of several hundred meters). The brittle shale endmember is characterized by a higher proportion of strong grains such as quartz, higher mechanical strength, somewhat higher thermal conductivity, and potentially higher bulk permeability due to the presence of interconnected fractures. The ductile shale endmember has experienced shallower burial depths than the brittle endmember, is less indurated, and has relatively dilute porewater, while the brittle shale endmember has experienced deeper burial depths, is more indurated, and has saline porewater.

2.3 Repository Design and Construction

Repository depths between 300 m and 900 m have been proposed for shale host rock (Shurr, 1977); a nominal depth of 500 m is assumed, with the repository situated in a flat-lying stratigraphy and built on a single level.

The repository would be constructed in stages, with access drifts intended to remain open for the operational lifetime of the repository (approximately 100 years) and disposal drifts intended to remain open for less than about 3 years. Immediate support during or after excavation is necessary in shales (whether ductile or more brittle) to control rock deformation and rockfall hazards. The reference concept assumes a minimal support system consisting of rock bolts, which retain welded wire cloth, covered by a

layer of low pH shotcrete (10 – 30 cm thick). Ground support in temporary openings would be limited to shorter rock bolts and thinner shotcrete, while permanent openings may require multiple applications of shotcrete and steel sets (or other heavy lining) to stabilize against large deformations.

The reference concept assumes axial, in-drift emplacement of waste packages containing 21 PWR assemblies or 44 boiling water reactor (BWR) assemblies. Waste packages would be surrounded with crushed rock or bentonite backfill upon emplacement to provide shielding during the operational phase and to prevent rock fall.

Large waste packages pose a challenge for thermal management in a shale repository. Repository temperature limits may be based on various temperature constraints designed to ensure material integrity of the fuel cladding, waste package materials, a clay-based buffer, and/or the host rock itself. Waste package and drift spacings are selected to be reasonably large (20 m and 70 m, respectively), and waste packages are assumed to be loaded and aged (through surface storage) such that the power output at the time of emplacement is less than about 4 kW/waste package. Such a strategy would meet potential temperature limits of 250 °C at the waste package surface and 100 °C at the drift wall or a short distance into the wall rock. The strategy would (depending on the engineered thermal properties of the backfill) create a zone of “sacrificial” backfill surrounding each waste package in which maintenance of favorable mechanical, chemical, and hydrological properties of the backfill/buffer could not be assumed without site-specific study.

2.4 Disturbed Rock Zone

The mechanical properties of shale, whether more ductile or brittle, will impact the coupled thermal-hydrological-mechanical evolution of the host rock, including the potential for mechanical damage and associated changes in transport properties. In the host rock immediately adjacent to drift walls, both excavation-induced fracturing and thermal spalling are expected. A ductile shale is expected to experience creep (visco-plastic) deformation around excavations and to self-seal fractures on relatively short time scales, while a brittle shale may sustain durable damage. In a high-temperature repository, thermally-induced mechanical damage to the host rock may extend beyond the immediate environment of the drift wall if thermal pressurization of porewater is sufficient to cause hydraulic fracturing or activation of pre-existing natural fractures in the host rock. The potential for near field hydraulic fracturing would depend on coupled feedback between permeability, thermal conductivity, and mechanical strength of the host rock.

2.5 Engineered Barrier System

Two options are proposed for in-drift emplacement of waste packages: 1) waste packages are emplaced on the floor of the drift; 2) waste packages are emplaced on a plinth of compacted bentonite. The first is operationally simpler, and may be suitable in a self-sealing, low-permeability host rock. The second presents additional engineering and design challenges, and may be desirable if flow in connected fractures cannot be ruled out.

Several backfill/buffer emplacement concepts are proposed for further study for a high-temperature shale repository: 1) crushed rock backfill is emplaced in the “sacrificial” zone around each waste package and compacted bentonite buffer is emplaced in the disposal drifts between waste packages; and 2) compacted bentonite buffer is emplaced throughout the disposal drifts. In the second case, the high heat load of the waste packages may be managed by a) enhancing the thermal conductivity of the buffer with additives such as quartz sand, graphite, graphene, or copper wire mesh; or b) determining for a given set of conditions (including clay mineralogy and porewater chemistry) that a higher temperature limit is acceptable in the bentonite buffer.

Steel corrosion, cement degradation, and host rock/bentonite interactions have the potential to have wide ranging effects on the physical and chemical properties of the bentonite buffer where it contacts other materials (e.g., Caporuscio et al., 2019). Changes to physical properties may include dissolution/recrystallization of montmorillonite, loss of bentonite swelling capacity (due to cementation or recrystallization to non-swelling phases), and development of porosity due to the formation denser mineral phases (e.g., zeolites). Such changes will depend on bulk system chemistry and temperature.

Reference waste packages are comprised of a stainless steel canister that may serve multiple purposes including transportation, aging, and disposal; canister internals supporting the fuel assemblies and providing criticality control; and a disposal overpack. Carbon steel, stainless steel, and copper are possible overpack materials that have been studied in a variety of repository programs (e.g., Andra, 2005; SKB, 2010). In the reducing porewater environment of a shale repository, carbon steel would experience general corrosion via reaction with water; copper would experience general corrosion if reduced sulfur species are present; and stainless steel is likely to form a passive, stable oxide film on the surface that slows general corrosion and leads to localized (less predictable) pitting or crevice corrosion. Corrosion rates and stability of passivation films depend on environmental factors, including concentrations of chemical species, temperature, pH, and radiation flux.

The waste form is spent uranium oxide (UO₂) fuel, a polycrystalline ceramic material stable to high temperatures and likely slow to degrade in the anoxic disposal environment (Shoesmith, 2007). In spent oxide fuels, the radionuclide inventory is usually considered to consist of two parts: (1) a part that resides in the fuel rod gap and grain-boundary region and (2) a part that is embedded in the fuel matrix and released only upon degradation of the fuel matrix.

Nominal and bounding initial radionuclide inventories and waste package power outputs as functions of time are constructed using assembly and fuel characteristics from the Unified Database (Clarity et al., 2017; Banerjee et al., 2016).

2.6 High-Temperature Effects

High temperatures in the near field of a shale repository may drive hydrological, mechanical, and chemical changes. The high-temperature concepts report (Stein et al, 2020a) identifies several ways in which temperature may influence the evolution of the repository and radionuclide transport, including 1) development of thermal overpressures and possible hydrofracturing in the near field; 2) acceleration of drift closure processes such as an accelerated rate of creep or thermal spalling; 3) depending on the geochemical environment, enhanced chemical alteration of the bentonite buffer resulting in alteration of swelling capacity or other bentonite properties; 4) faster corrosion rates; and 5) temperature-dependent diffusion, radionuclide solubilities, and sorption. Further evaluation of these and other temperature-dependent coupled processes will enable preliminary material choices and contribute to development of a reference case for a high-temperature repository in shale.

This page is intentionally left blank.

3. SHALE REFERENCE CASE STUDIES

This section summarizes research on two separate studies for disposal in shale. The first subsection is a study of DRZ permeability and porosity evolution as a result of buffer swelling in a soft shale. A single-waste package simulation model is used to study the DRZ evolution in detail. The second subsection outlines the development of a brittle shale geological conceptual model.

3.1 Buffer and DRZ Evolution

An ongoing integration effort between repository-scale PA simulations in PFLOTRAN and TOUGH-FLAC coupled thermo-hydro-mechanical (THM) modeling capabilities developed by Lawrence Berkeley National Laboratory has led to the development of a suite of reduced-order models to approximate near-field geomechanical effects in PA simulations. These integrated efforts focus on the geomechanical evolution of the natural barrier system adjacent to the engineered barrier, referred to as the disturbed rock zone (DRZ), by mapping thermal, hydrological, and mechanical parameters modeled in the THM simulator (e.g., TOUGH-FLAC) into the PFLOTRAN thermo-hydrological (TH) coupled model.

Geomechanical effects are often localized to the near-tunnel environment and occur relatively early in the post-closure period. Modeling geomechanical behavior at PA-scale can therefore benefit from reduced order modeling to avoid having to fully couple rigorous geomechanics at a multi-kilometer scale and over hundreds of thousands of years.

3.1.1 Evolution of Permeability and Porosity

Buffer swelling is one of the most critical geomechanical phenomena observed in the near-field, which may perturb hydrological/mechanical properties of the DRZ over time. A buffer material with high swelling capacity and low hydraulic conductivity will minimize groundwater flow and advective transport in the disposal tunnel, and bentonite is a widely favored buffer material.

Temporal perturbations in swelling stress caused by saturation changes can contribute to the changes in formation properties. During re-saturation, a swelling buffer exerts stress on the surrounding DRZ, which can in turn work to compress fractures in the DRZ. As fractures represent high-permeability pathways through the medium, closing them can result in reduction of the DRZ permeability. Therefore, as imbibition and condensation drive an increase in liquid saturation over time in the buffer, permeability of the surrounding DRZ will correspondingly decrease over time.

In this study the effective stress acting on the DRZ is approximated by the temporal changes of physical quantities within the buffer, and corresponding evolution of the DRZ permeability and porosity is implemented to mimic geomechanical behavior of the DRZ.

3.1.1.1 Effective Swelling Stress

Swelling of bentonite enhances the sealing capacity of the buffer, such that high swelling stress will enhance the buffer sealing capacity at the tunnel wall interface, which is favorable to prevent the seepage of fluids and accompanying transport of radionuclides. When buffer swelling occurs, it exerts stress on the tunnel. The swelling stress can be assumed to act homogeneously in the radial direction:

$$S_{rr} = \sigma_{swelling} \quad (3.1)$$

where, S_{rr} is the radial component of stress and $\sigma_{swelling}$ is the swelling stress exerted by the buffer on the side walls of the drift in N/m^2 . An initially unsaturated bentonite buffer will re-saturate over time by fluid imbibition from the host rock. The increase in swelling stress can be described as a linear function of the change in average liquid saturation within the buffer (Rutqvist et al., 2011):

$$\Delta\sigma_{swelling} = 3K\Delta S_l\beta_{sw} \quad (3.2)$$

where K is the bulk modulus (N/m^2), ΔS_l is the change of liquid saturation from the initial state, and β_{sw} is a dimensionless moisture swelling coefficient, approximately 0.238 for a bentonite buffer material (Rutqvist et al., 2011).

Note that the closure or opening of the pre-existing fractures will be controlled mainly by the normal component of swelling stress acting across the fractures. Then, the effective stress change acting on DRZ can be defined as follows:

$$\Delta\sigma_{eff} = \Delta\sigma_{swelling} \quad (3.3)$$

3.1.1.2 Stress-dependent Permeability and Porosity Functions

Shales are typically characterized as low-permeability (less than $1 \times 10^{-15} m^2$) and low-porosity (less than 0.20) rock. For example see Table 3-3 of Section 3.2 of this report or Section 5.1 of Sevougian et al. (2019b) Permeability, the ability of fluid flow through pore spaces, and porosity, the volume of void space, are the key material properties to determine the efficiency of heat transfer, fluid flow and solute transport in the shaly formation. Previous laboratory observations suggested that the shale permeability and porosity will evolve with deformation that can develop or close preferential pathways (e.g., Chen et al., 2015, Zhang et al., 2016). In this study, we implement three stress-dependent permeability functions: (1) a power-law function (Chen et al., 2015; Shi & Durucan, 2016), (2) a modified cubic-law function (Kwon et al., 2001), and (3) a Two-part Hookes' law model (Liu et al., 2009); as well as log-linear relationship relating porosity to permeability changes (Neuzil, 2019) in the DRZ.

3.1.2 Model Setting

3.1.2.1 PFLOTRAN Implementation

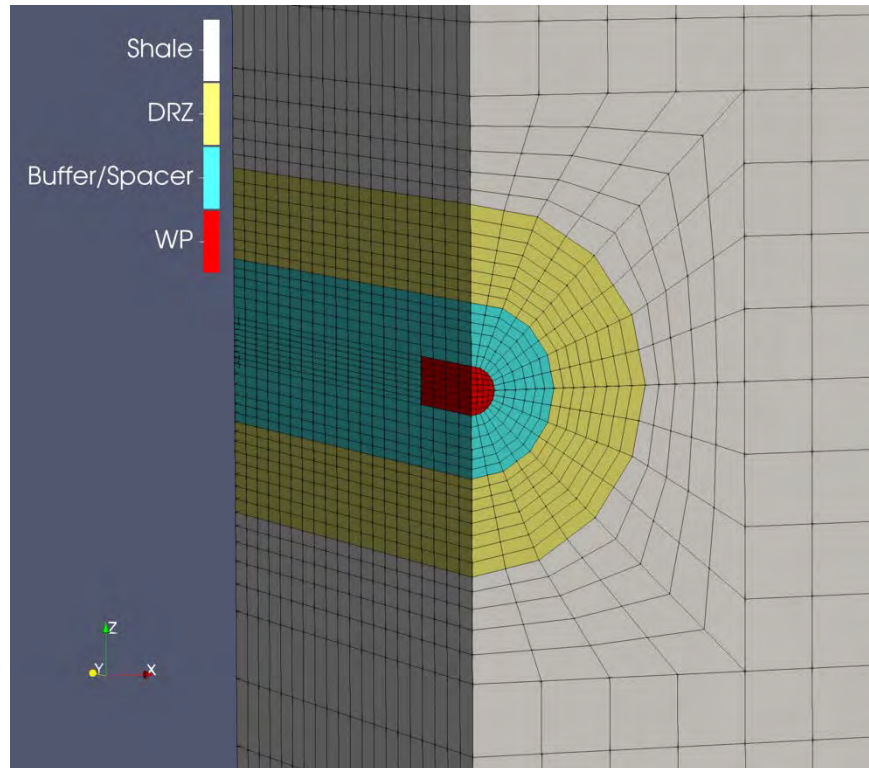
PFLOTRAN has been updated to compute buffer swelling stress as a function of its re-saturation behavior post-closure. The change in liquid saturation in the buffer is mapped to a swelling stress, and that swelling stress is then used to update the permeability of the DRZ by assuming a mechanical connection between the buffer and the DRZ. As liquid saturation in the buffer increases, compressive stress on the DRZ increases, and permeability decreases because fractures in the DRZ close. The effect of compressive stress on permeability reduction via fracture closure can now be modeled with one of three functions: an exponential function, a cubic law function, and a Two-Part Hooke's Law model function. While fracture compression primarily alters the permeability of the medium, it also changes porosity. Currently, porosity can be modeled as a function of permeability changes through a log-linear relationship. These functional forms are outlined in detail in Mariner et al. (2020).

3.1.2.2 Model Domain

The near-field model was run for a 24-PWR waste package within a shale host rock in PFLOTRAN GENERAL mode, which solves two-phase (liquid-gas) miscible flow coupled to energy for unsaturated conditions in waste package, buffer, and DRZ; solute transport is excluded in this study.

The model domain represents a quarter of a waste package in the shale repository system. By invoking closed symmetry conditions at all side boundaries this represents a waste package that is located in the center of an infinite, symmetrical repository system. Three concentric sections of waste package, buffer, and DRZ at 0.42 m, 1.5 m, 3.17 m in radius, respectively, are modeled in the 15 m (width) x 12.5 m (length) x 75 m (height) domain (Figure 3-1). The center of the waste package is located in the middle of z-axis.

Figure 3-1. Model domain and grid. Four sections are modeled: waste package (red), buffer (blue), disturbed rock zone (yellow), and shale host rock (grey).



3.1.2.3 Parameters

The material properties of the base case in which permeability and porosity of all formations are constant over time are given in Table 3-1. These parameters are the same as used in Section 5.2 of Sevougian et al. (2019b). The buffer are filled with compacted bentonite. The DRZ is defined as the portion of the host rock adjacent to the engineered buffer system that experiences elevated permeability due to mining-induced perturbations in stress state. Initial pressure and temperature throughout the model domain are calculated by applying hydrostatic and geothermal gradients (10 kPa/m and 0.025°C/m, respectively) in the vertical direction assuming temperature of 18°C and atmospheric pressure at the surface (462.5 m above the top of the model domain). For the unsaturated condition, initial liquid saturation (S_{li}) is set to 0.65 for waste package/buffer and 0.9 for DRZ, whereas the shale host rock is fully saturated with liquid. The simulation runs 10^6 years.

For each permeability function, we use parameter values outlined in Table 3-2. In this study, we obtain the initial permeability (k_0) for each permeability function by assuming that the buffer re-saturation will

lead to a fully saturated condition ($S_l = 1.0$, such that $\Delta S_l = 0.35$), and subsequently, as buffer swelling stress reaches a maximum the DRZ permeability will approach that of the host rock.

Table 3-1. Material properties for the DRZ evolution base case. (Sevougian et al., 2019b)

	Buffer	DRZ	Shale
Porosity [-]	0.35	0.2	0.2
Permeability [m ²]	1×10^{-20}	1×10^{-20}	1×10^{-20}
Density [kg/m ³]	2700	2700	2700
Heat capacity [J/(kg K)]	830	830	830
Thermal conductivity (dry) W/(K M)	0.6	0.6	0.6
Thermal conductivity (wet) W/(K M)	1.5	1.2	1.2
Initial gas saturation (S_{gi})	0.35	0.1	0.0
Liquid residual saturation (S_{rl})	0.1	0.1	0.1
Gas residual saturation (S_{rg})	0.1	0.1	0.1
Saturation function	Van Genuchten function*		
alpha [Pa ⁻¹]	6.25×10^{-8}	6.67×10^{-7}	6.67×10^{-7}
m [-]	0.375	0.333	0.333

Table 3-2. Parameter values for different permeability functions for the DRZ evolution base case

Power-law function (PL) (Bustin et al., 2008)		
C_{exp} [1/MPa]	0.18	Compressibility
k_0 [m ²]	1.49×10^{-19}	Initial permeability (calculated)
Modified cubic function (Cubic) (Kwon et al., 2001)		
P1 [MPa]	19.3	Effective modulus of asperities for shale
m	0.159	Material constant
k_0 [m ²]	1.38×10^{-18}	Initial permeability (calculated)
Two-Part Hooke's model (TPHM) (Zheng et al., 2016)		
β	1	Stress-sensitive coefficient
C_e [1/MPa]	0.18	Hard-part compressibility
ϕ_e	0.2	Hard-part porosity
α [m ²]	1×10^{-16}	Soft-part initial permeability
m	3.0	Material constant
γ_t	0.005, 0.01, 0.025, 0.05, 0.075	Volume fraction of soft-part
K_t [MPa]	8.0	Effective modulus of soft-part
k_{0e} [m ²]	1.1969×10^{-20}	Hard-part initial permeability (calculated)

3.1.3 Results and Discussion

3.1.3.1 Effect of Permeability Evolution

The swelling stress acting on the DRZ is calculated using changes of average liquid saturation within the buffer as explained in Section 3.1.1.1. Buffer swelling stress and liquid saturation in the buffer is a linear map; over time, divergence in swelling stresses and liquid saturations is indicative of the different effects of swelling stress on the DRZ permeability in each model, but eventually swelling stresses converge when the buffer is entirely saturated with water (Figure 3-2)

Figure 3-2).

The temporal evolution of pressure, temperature and saturation of the gas and liquid phases are obtained at the DRZ cell nearest the waste package for three permeability-function cases; blue is for the power-law function (PL), green is for the cubic-law function (Cubic), and magenta is for the Two-part Hooke's model function (TPHM) (Figure 3-3). At early time, as the DRZ becomes heated, higher permeability causes faster pressurization and imbibition within the DRZ (faster increases in gas pressure and saturation for PL and Cubic; Figure 3-3a and b). At later time the TPHM gives the highest gas pressure and saturation (Figure 3-3a and b), and the greatest total amount of dry-out, similar to the constant permeability benchmark. TPHM also has the slowest re-saturation.

Both PL and Cubic functions give one and two orders of magnitude larger initial permeability than the TPHM, which results in faster re-saturation of the buffer and greater compressive stress on the DRZ in these models (Figure 3-3 d). All three permeability relationships predict the DRZ permeability to converge to the initial permeability of the shale host rock (Figure 3-3f). Note that the initial permeability values are different for each function because they were derived by assuming that the DRZ permeability will converge to the host rock permeability at maximum swelling stress. Figure 3-3f shows that PL and Cubic functions result in relatively larger reduction of the DRZ permeability than TPHM at given saturation changes within the buffer, such that both functions may overestimate the buffer-swelling impact on the DRZ.

The TPHM function is sensitive to the volume fraction of the soft material in a shale (γ_s). Our sensitivity tests show that an order of magnitude more soft material can cause six times larger reduction in the DRZ permeability over time (Figure 3-4), such that earlier re-saturation of DRZ is expected if there is more soft material present. Note that the TPHM function does not consider reciprocal changes in hard- and soft-parts, which means that hard-part fraction remains constant even when there are changes in soft-part fraction. This limitation can cause overestimation of the permeability reduction.

Figure 3-2. Evolution of liquid saturation (solid line) within the buffer and corresponding changes in swelling stress (dashed line) acting on the DRZ for three permeability functions: (1) Power law function (blue), (2) Modified cubic function (green), and (3) Two-part Hooke's law model (magenta). Black line shows the reference case with a constant DRZ permeability and is very similar to TPHM result.

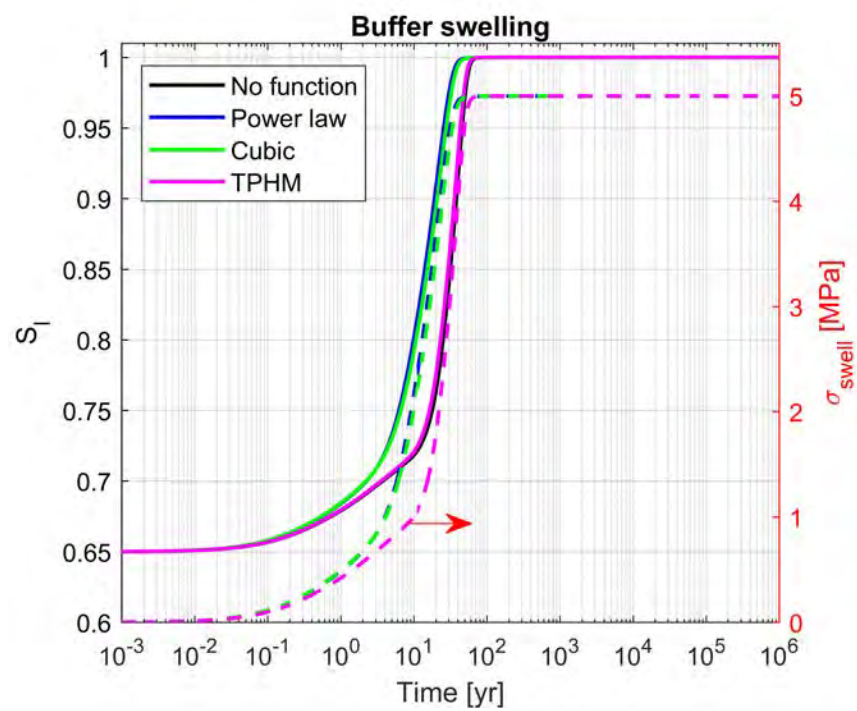


Figure 3-3. Evolution of physical quantities at the DRZ cell nearest the buffer for three cases with different stress-dependent permeability functions: (a) gas pressure, (b) gas saturation, (c) liquid pressure, (d) liquid saturation and swelling stress, (e) temperature, and (f) permeability.

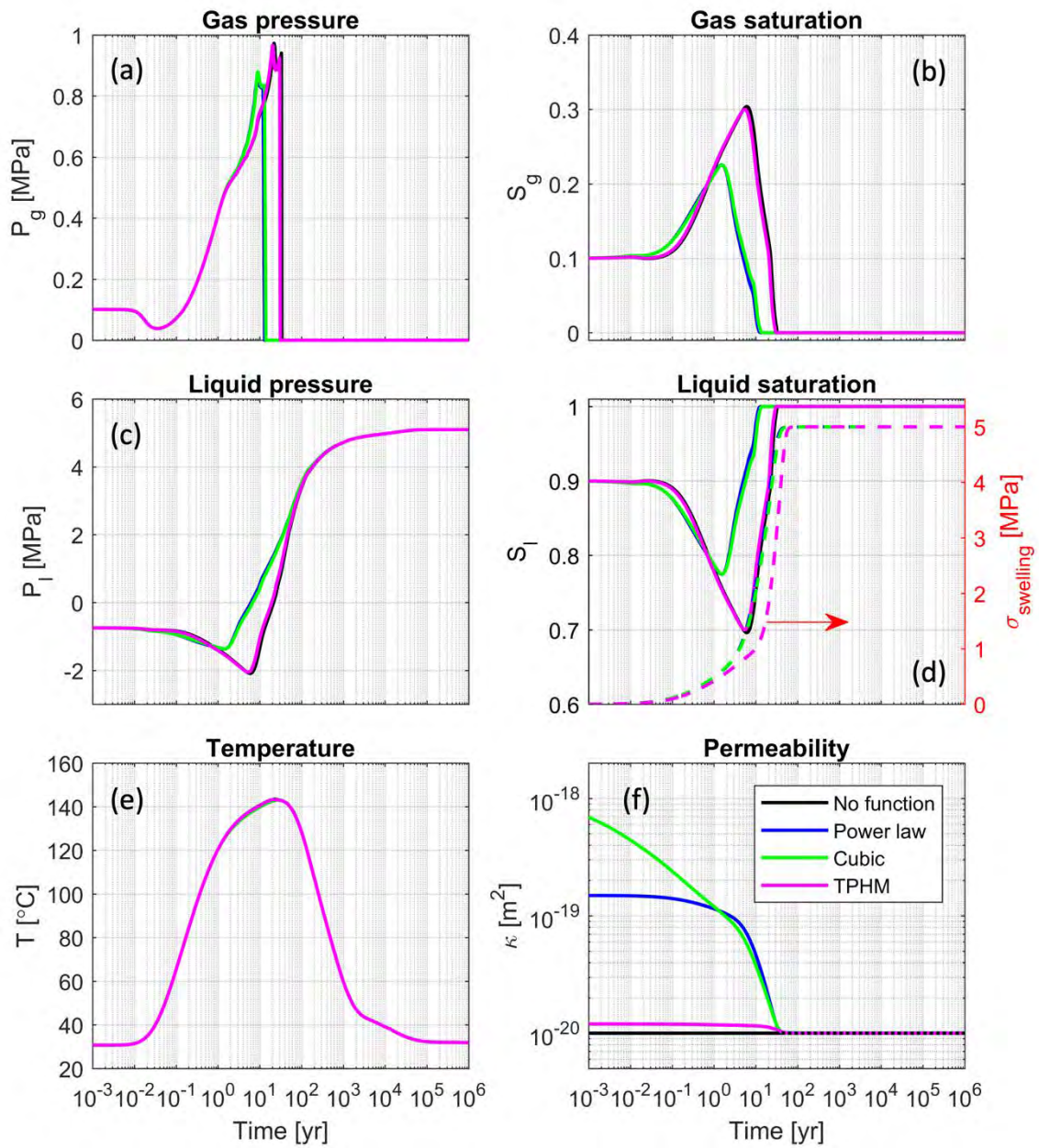
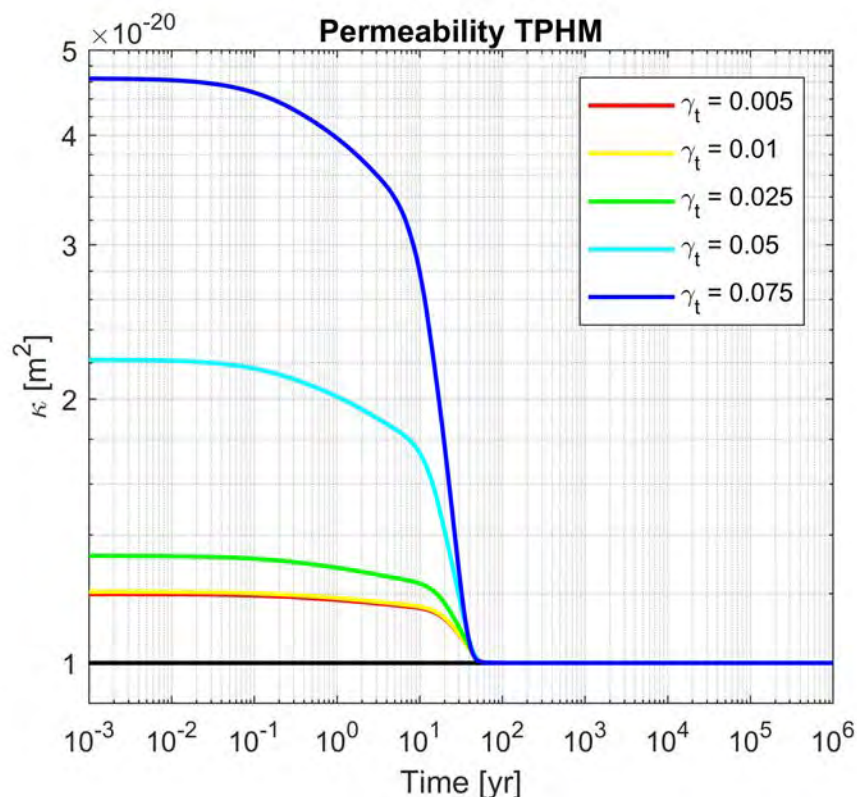


Figure 3-4. DRZ permeability evolution using TPHM with variation in the fraction of soft-part. The host rock permeability ($1 \times 10^{-20} m^2$) is indicated by a black line.

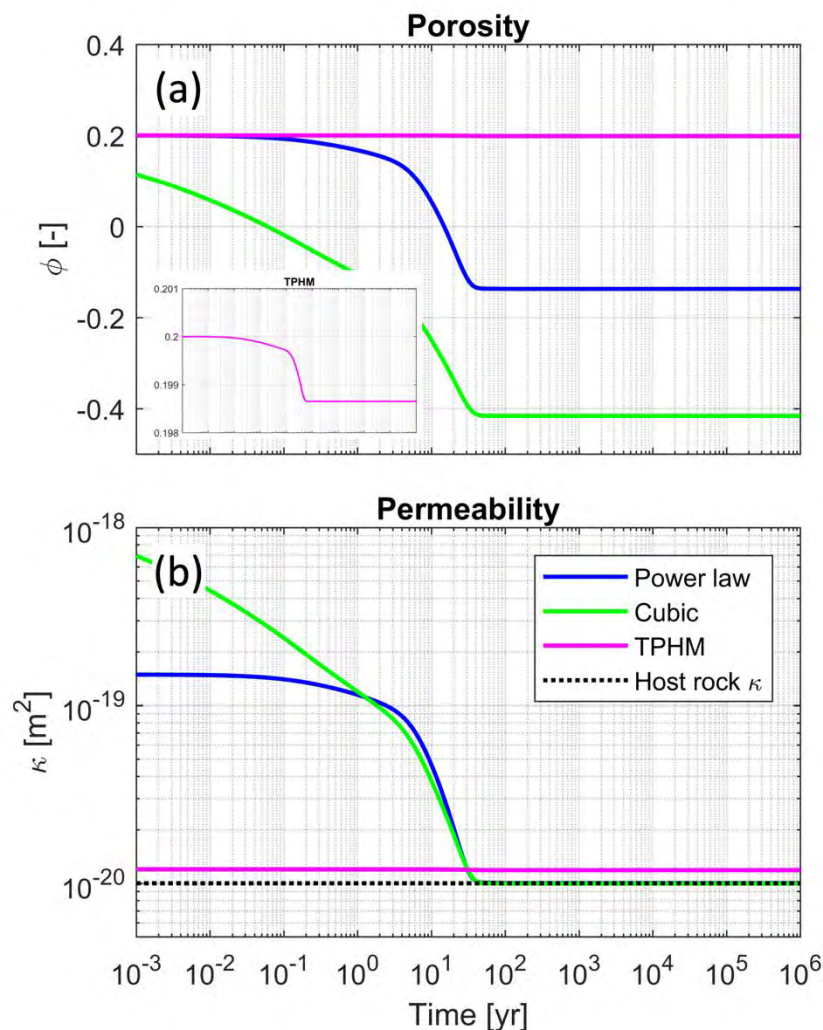


3.1.3.2 Effect of Porosity Evolution

By implementing the log-linear relationship between permeability and porosity of shales into PFLOTRAN, we model porosity evolution in the DRZ over time. Both PL and Cubic permeability functions reduce DRZ permeability dramatically, which results in negative values of porosity with re-saturation. This result implies that the general log-linear trend from laboratory tests may not explain dynamic changes in permeability and porosity driven by compaction after disturbance by subsurface human activities.

The dynamics can be considered by integrating a stress-dependent porosity function based on the TPHM concept (Zheng et al., 2016) into the next PFLOTRAN near-field model, so that the hard part experiences small deformation whereas the soft part (including micro-cracks/fractures) undergoes relatively large deformation.

Figure 3-5. (a) Evolution of the DRZ porosity from the simulation integrating permeability functions and log-linear relationship between permeability and porosity. (b) Evolution of the DRZ permeability.



3.1.4 Future Work

In the short-term, other stress-dependent porosity functions will be tested to generate a reasonable evolution of the DRZ porosity for a given scenario for nuclear waste disposal. The buffer re-saturation and corresponding stress on the surrounding DRZ depends heavily on the waste package thermal loading, and thus, temperature-dependent properties such as thermal conductivity for the buffer and DRZ will be integrated into PFLOTRAN simulations. Furthermore, comparative studies with other software (e.g., TOUGH-FLAC) will be performed to validate the PFLOTRAN model with evolution of DRZ permeability, porosity, and temperature-dependent properties. Then, the solute transport will be included to see how near-field perturbations in DRZ permeability and porosity affect radionuclide transport. The fully coupled THC (Thermo-hydro-chemical) PFLOTRAN model with mechanical impacts of heat and pressure buildup on near-field characteristics will continue with the goal of integrating this near-field process modeling into field-scale PA simulations.

3.2 Conceptual Model for Brittle Shales

3.2.1 Summary of Shale Conceptual Model from Argillite Concepts Workshop

The Argillite Concepts workshop was held February 25-26, 2020 at Sandia National Laboratories and involved participants from multiple national laboratories. The purpose of the workshop was to develop shared concepts for a high-temperature repository in shale (argillite) that would provide a common framework for modeling and experiments. For the shale host rock, we expanded the previous concept of a weak and sealing (ductile) shale (based on the Pierre Shale of the northern Great Plains) to include a stronger and more fractured (brittle) shale that is common in other regions of the US.

The two types of shale can be considered as two endmembers that represent the range of properties likely to be found within shale formations of the US:

1. Ductile: Modeled after the Cretaceous Pierre Shale of Northern Great Plains
 - High clay content, low quartz content
 - Low compressive strength, less indurated
 - Fracture sealing behavior, matrix flow
2. Brittle: Modeled after Paleozoic Shales of the Eastern Interior Basins (e.g., New Albany and Antrim shales of the Illinois and Michigan Basins)
 - Moderate clay content, moderate quartz content
 - Higher compressive strength, more indurated
 - Fracture systems dominate permeability and flow

Stein et al. (2020a, Section 3) summarizes the properties of brittle and ductile shales as initially developed at the workshop and within the framework of the natural barrier system. In this report we focus on a conceptual model for brittle shales based on the features and characteristics of the geologic and hydrologic environment represented by Paleozoic shales in the eastern US. We develop a reference stratigraphy for brittle shale based on the Paleozoic shales and other sedimentary rocks present in the Illinois Basin.

3.2.2 Fracture Systems and Fracture Permeability

3.2.2.1 Overview of Fracture Systems

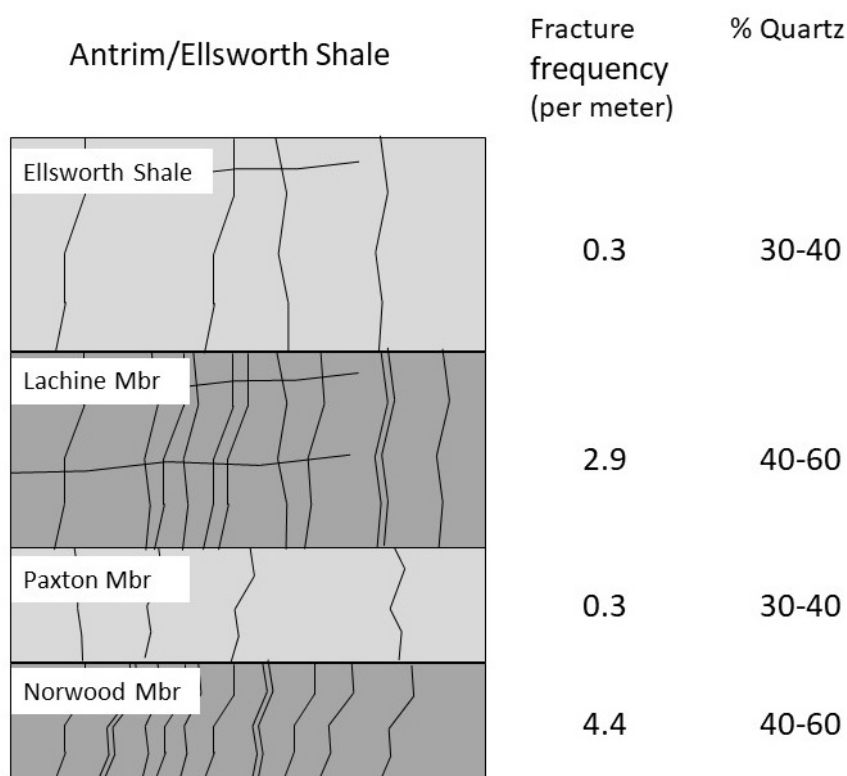
Bourg (2015) showed a correlation between the clay content of shale and unconfined compressive strength and developed a conceptual model wherein the mineral microstructure of shale controls the mechanical properties of the rock. The model depends on the proportion of quartz (+feldspar), a strong mineral and clay (a weak mineral). At higher quartz content, the mineral microstructure consists of a more rigid load-bearing matrix of quartz and feldspar (strong minerals) in grain to grain contact. At higher clay content, the load-bearing matrix becomes less rigid and weaker. Bourg (2015) showed that, above a clay content of approximately 34%, shales show a sharp decrease in compressive strength and a transition to ductile deformation and sealing behavior over brittle deformation. This transition is accompanied by a decrease in permeability and an increase in porosity. The Pierre Shale, a ductile shale, has a clay and quartz content of ~75 and 20%, respectively. Paleozoic shales are characterized by a lower clay content and higher quartz content of ~45% and 50%, respectively, and behave as a more brittle rock with higher compressive strength (Stein et al., 2020a).

An important feature of the conceptual model for brittle shale presented in Stein et al. (2020a) is that shales are layered systems where different members of a shale formation have different mineralogy, mechanical properties and fracture characteristics. An example of this is seen in the Antrim Shale of the Michigan Basin (correlative with the New Albany Shale of the Illinois Basin), which has three members

with different mineralogy and fracture frequency (Ryder, 1996). The Antrim and Ellsworth Shales form an alternating system of gray and black shales with the black shales having significantly higher fracture frequency (Ryder, 1996; Figure 3-6). The gray shales with lower fracture frequency also have lower quartz content, at 30-40%, while the black shales have higher quartz content of 40-60% (Ryder, 1996). Ryder (1996; and references therein) suggest that the black shales with higher quartz content are more brittle and therefore more fractured than the more ductile gray shales (Figure 3-6). This conclusion is consistent with the conclusions of Bourg (2015) that more quartz rich, clay poor shales are more brittle and mechanically stronger than shale with higher clay content.

The presence of fracture layering in at least some Paleozoic shales presents the possibility that less fractured shale horizons could be targeted for repository siting. A similar strategy has been employed in the Swedish high-level waste disposal program where the crystalline rock repository is sited within a volume of sparsely fractured granite bounded by a more fractured deformation zones (Stephens, 2010).

Figure 3-6. Schematic depiction of fracture frequency and quartz content in shale layers of the Antrim/Ellsworth shales in the Michigan Basin



3.2.2.2 Fracture Sealing and Permeability

Fracture sealing in shales refers to the capacity of transmissive fractures to become closed and non-transmissive over time. Bock et al. (2002) identified three main mechanisms that lead to fracture sealing over time:

1. Mechanical closure of fractures – lithostatic stress acting normal to the fracture; ductile creep of fracture walls

2. Swelling of clays along fracture walls
3. Precipitation of minerals on fracture walls (mineral fracture fillings)

These mechanisms and examples are discussed in more detail in Stein et al. (2020a).

Fractured Paleozoic shales that have poorly interconnected or closed fractures have permeabilities that are low and similar to that of less fractured ductile shales (Gale et al., 2014). Permeability of the New Albany Shale in the southern Illinois Basin determined from borehole core samples in a depth interval of 570-580 meters average $9 \times 10^{-20} \text{ m}^2$ with a range of 2×10^{-19} to $8 \times 10^{-21} \text{ m}^2$ (Nuttall, 2013). These values reflect a lack of fracture flow. Eaton et al. (2000) report that unfractured matrix of the Maquoketa Shale in the northern Illinois Basin has permeability ranging from 1×10^{-19} to $2 \times 10^{-21} \text{ m}^2$, while the highly fractured upper half of the formation has permeability ranging from 3×10^{-12} to $3 \times 10^{-17} \text{ m}^2$. The upper part of the formation at this location is dominated by fractured carbonate lithologies, however, and the permeabilities are not representative of the shale lithologies in the formation. The determinations of permeability in the New Albany and Maquoketa Shales are consistent and indicate that permeability of these brittle shales can be extremely low (range of 10^{-19} to 10^{-21} m^2) where the shale is not significantly fractured.

From a synthesis of data from numerous wells in the Illinois Basin region, Gupta (1997) conceptualized a regional flow model that included hydraulic conductivity values for many of the hydrostratigraphic units of the Illinois Basin region. For both the New Albany Shale and Maquoketa Shale present in basins, the hydraulic conductivity values equate to a horizontal permeability of $1.5 \times 10^{-18} \text{ m}^2$ and a lower vertical permeability of $3 \times 10^{-20} \text{ m}^2$, resulting in a K_h/K_v of 50. Gupta (1997) allowed that vertical and horizontal permeabilities of the shales in the Cincinnati Arch region that separates the Illinois Basin from the Appalachian Basin are 1-2 orders of magnitude higher because of a higher frequency of faulting and fracturing in the arch region. This would likely also apply to more fractured shale rock volumes within the Illinois Basin.

Data for permeability of fractured shale is more limited and harder to evaluate on the scale of a repository system because of the fracture heterogeneity present in fractured shale and uncertainty in fracture characteristics at depth (Gale et al., 2014). As discussed in Stein et al. (2020a), understanding of the permeability of fractured shale comes primarily from laboratory experiments, field measurements of fracture properties and conclusions reached from modeling of regional groundwater flow systems (Bredehoeft et al., 1983; Richards et al., 1994; Bernier et al., 2007; Zhang and Rothfuchs, 2008). These studies are consistent in their determinations that the permeability of fractured shales is typically 3-4 orders of magnitude higher than that of intact shale, on the order of 10^{-15} to 10^{-16} m^2 .

3.2.3 Generalized Stratigraphic and Hydrologic Framework for Paleozoic Shales

Paleozoic shale formations of the Illinois, Michigan and Appalachian Basins of the Eastern Interior region are characteristically more brittle and fractured than the Mesozoic Pierre Shale. These shale formations are regionally extensive and have been previously considered as potential repository host rocks (Droste and Vitaliano, 1976; Lomenick et al., 1983; Gonzales and Johnson, 1985). Here we focus on the stratigraphic framework of the Illinois Basin, which contains the New Albany and Maquoketa shales, and consider it representative of the natural barrier system for a brittle-shale reference case.

3.2.3.1 Stratigraphy and Major Aquifers

The Illinois Basin formed as a structural depression in the early Paleozoic and is filled with Cambrian through Pennsylvanian shallow marine to near-shore sediments (Figure 3-7). Typical depth to the

Precambrian basement in most of the central part of the basin is ~4000 meters with a maximum depth of 9000 meters in the southern part of the basin within the Rough Creek graben (Panno et al., 2017). Major confining units in the basin are the New Albany and Maquoketa shales, which lie at typical repository depths near the basin margins (Figure 3-7). Unlike the Michigan and Appalachian Basins, the Illinois Basin does not contain evaporite deposits.

A representative stratigraphic column for the southern Illinois Basin was obtained from borehole data and an east-west structural cross-section prepared by Noger and Drahovzal (2005). Drill hole Shell Oil Co. No. 1 Davis is at the western edge of the cross-section and penetrates 2700 meters of Paleozoic shales, carbonates (limestones and dolomites) and sandstones. We utilize the upper 1500 meters of the stratigraphy at this location to create a reference stratigraphic column for the brittle-shale reference case (Figure 3-8). This interval includes carbonates, shales and sandstones of Mississippian through Ordovician age that are typical of the Illinois Basin. Carbonate rocks make up approximately 80% of the stratigraphic column and constitute the major regional aquifers of the region.

Not included in the cross-section of Nogar and Drahovzal (2005) are surficial deposits. Based on the geology of the region, we include Quaternary gravel and sand deposits with a thickness of 30 meters as the surficial unit, which is typical for this region of the US (Casey, 1996). The New Albany Shale at the drill hole location is approximately 140 meters thick and lies within the depth interval of 320-460 meters (Figure 3-8). This thickness is close to the maximum thickness encountered in the Illinois Basin.

The aquifer system of the Illinois Basin consists of four major aquifers, the surficial aquifer composed of unconsolidated sands and gravels, the Mississippian carbonate aquifer consisting of carbonates, the Silurian-Devonian aquifer consisting of carbonates and the Cambrian-Ordovician aquifer consisting of carbonates and sandstones (Figure 3-8; Table 3-3). Groundwater salinity in these aquifers (except for the freshwater surficial aquifer) generally increases with depth and down-dip into the central parts of the basin. The four aquifer systems are described below.

Figure 3-7. Location map and generalized cross-section of the Illinois Basin from Panno et al. (2013).

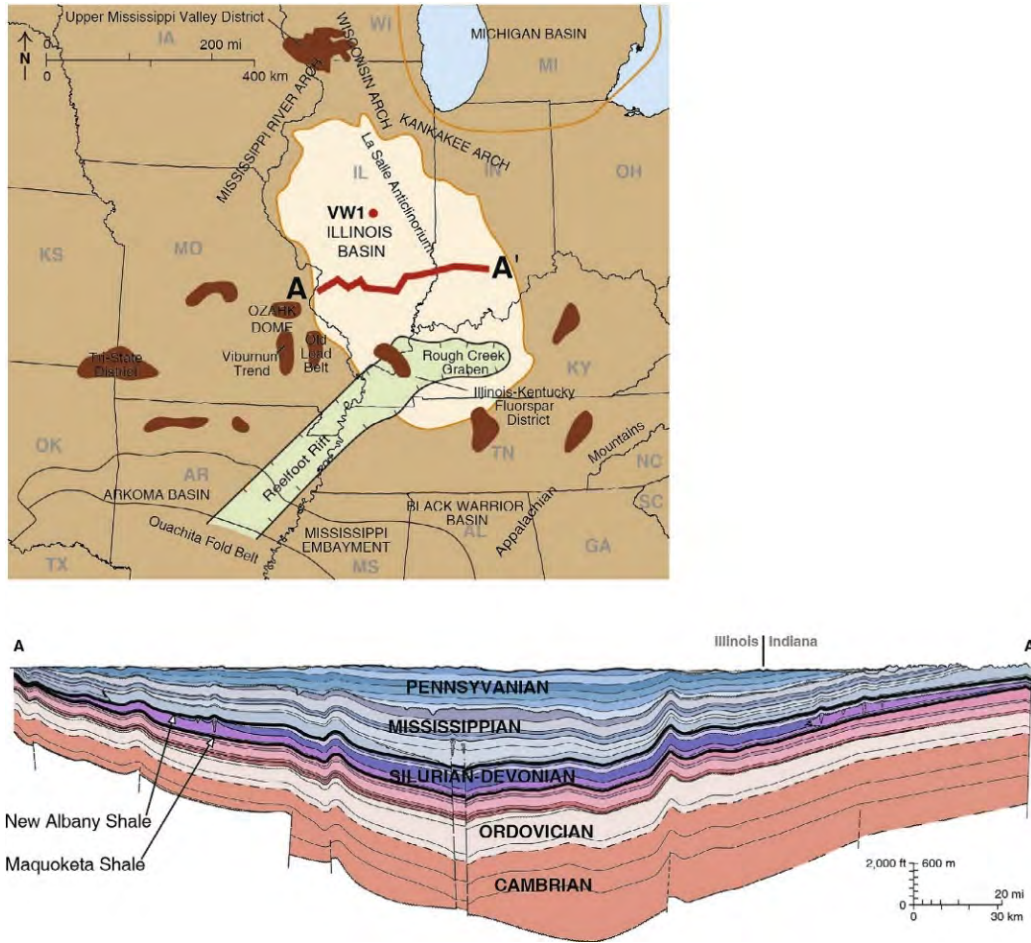


Figure 3-8. Reference stratigraphic column associated with the New Albany Shale in the southern Illinois Basin

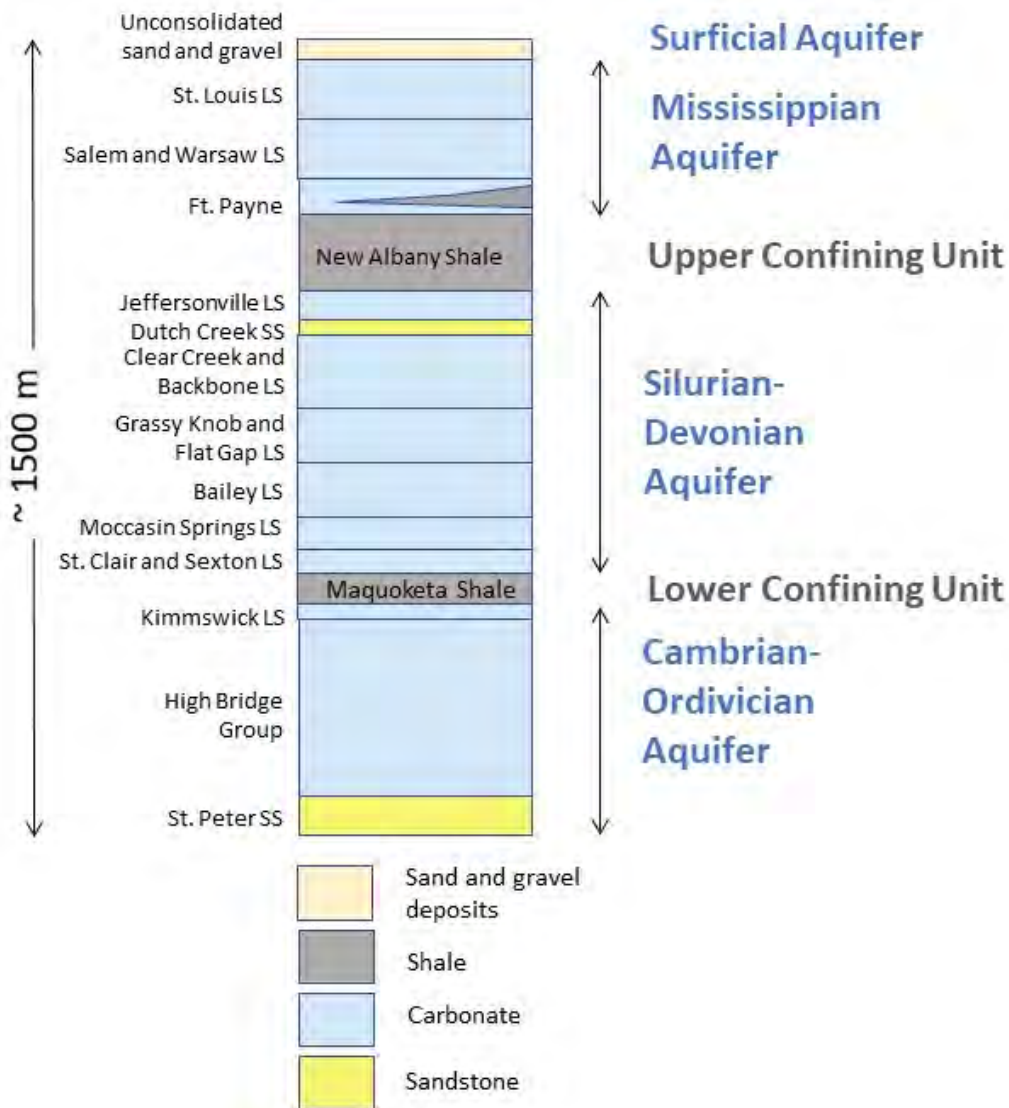


Table 3-3. Reference stratigraphy and hydrologic properties of brittle shale environment in the Illinois Basin

Geologic Age	Stratigraphy	Lithology	Thickness (m)	Hydrologic Unit	K_h (m^2)	Porosity %
Quaternary	Surficial Deposits	Clay, silt, sand and gravel	30	Surficial Aquifer	10^{-13} to 10^{-14}	30
Mississippian	St. Louis Limestone	Limestone	120	Mississippian Carbonate Aquifer	10^{-14}	15
	Salem and Warsaw Limestones	Limestone	110		10^{-14}	15
	Ft. Payne Fm.	Siltstone, shale, limestone,	80		10^{-15}	
	New Albany Shale	Shale	140	Confining Layer	10^{-15} to 10^{-16}	5-10
Devonian	Jeffersonville LS	Limestone	60	Silurian-Devonian Carbonate Aquifer	10^{-14}	10
	Dutch Creek Sandstone	Sandstone	20		10^{-12}	15
	Clear Creek and Backbone Limestones	Limestone	140		10^{-14}	10
	Grassy Knob and Flat Gap Limestone	Limestone	120		10^{-14}	10
	Bailey Limestone	Limestone	110		10^{-14}	10
Silurian	Moccasin Springs Fm.	Alternating Limestone and Shale	60	Silurian-Devonian Carbonate Aquifer	10^{-14}	10
	St. Clair and Sexton LS	Limestone	40		10^{-14}	10
	Maquoketa Shale	Shale, limestone	75		Confining Layer	10^{-15} to 10^{-16}
Ordovician	Kimmswick LS	Limestone	25	Cambrian-Ordovician Aquifer	10^{-14}	5-10
	High Bridge Group	Limestone, shale	330		10^{-14}	5-10
	St. Peter SS	Sandstone	90		10^{-12}	5-10

Surficial Aquifer

Surficial deposits of the Illinois Basin are primarily glacial tills except for the southernmost parts of the basin. Other surficial deposits are alluvial deposits that are mainly derived from erosion of glacial tills. Both deposits are primarily sands and gravels with locally abundant clays. These sand and gravel deposits are productive freshwater aquifers and normally contain the water table that is near the ground surface.

Mississippian Carbonate Aquifer

Rocks of the Mississippian carbonate aquifer underlie the surficial aquifer and are primarily thick-bedded limestones in the lower half of the aquifer. Sandstones are also present in the upper half of the aquifer where not removed by erosion. The Mississippian aquifers contain freshwater in the northwestern Illinois Basin but become saline at greater depths and down dip in the central and southern parts of the basin. Groundwater movement through the Mississippian aquifers is primarily through openings such as bedding planes, fractures and dissolution channels (Lloyd and Lyke, 1995).

The reference stratigraphic column includes the following formations that comprise the Mississippian Carbonate Aquifer:

St. Louis Limestone – Fine-grained limestone and dolomite interbedded with shale and evaporites (gypsum and anhydrite) carbonate deposited in quiet-water shallow marine environment (Noger and Drahovzal, 2005).

Salem and Warsaw Limestones – Fossil-fragmental limestones deposited under moderately high-energy near shore environment (Noger and Drahovzal, 2005).

Fort Payne Formation – Dolomitic siltstone with interbedded shale and limestone (Noger and Drahovzal, 2005). It is considered a semi-confining unit with permeability higher than shale formations. Stratigraphically equivalent rocks (Borden Formation or Group) in the eastern Illinois Basin, along with the New Albany Shale (discussed below), were evaluated as potential repository host rocks by Droste and Vitaliano, 1976).

New Albany Shale Confining Unit

The New Albany Shale includes both black organic rich shale and gray organic poor shale (Noger and Drahovzal, 2005). Organic-rich and fractured reservoirs within the New Albany Shale are the major source of hydrocarbons in the Illinois Basin (Noger and Drahovzal, 2005). The New Albany Shale was evaluated as a potential repository host rock by Droste and Vitaliano (1976) and Gonzales and Johnson (1985).

Lineback (1970) divided the New Albany Shale into five lithologic members. In ascending order these are the 1) Blocher Member, a black carbon-rich dolomitic pyrite-bearing shale, 2) the Selmier member, a gray dolomitic mudstone, 3) the Morgan Trail Member, a black pyrite-bearing shale, 4) the Camp Run Member, an interbedded black and green-gray mudstone and shale, and 5) the Clegg Creek Member, a massive black silty and pyrite-bearing dolomitic shale. Analyzed organic content in the Blocher Member is 10-20 percent (Lineback, 1970).

Silurian-Devonian Carbonate Aquifer

Rocks of the Silurian-Devonian carbonate aquifer are primarily limestones and dolomites with thinner intervals of sandstone and shale (Lloyd and Lyke, 1995; Noger and Drahovzal, 2005). The aquifer contains freshwater where the aquifer is present at shallow depth (<200 m) and becomes more saline at deeper depths (Lloyd and Lyke, 1995). As in other carbonate aquifers, groundwater moves primarily through bedding planes, fractures and dissolution openings. The Silurian-Devonian Carbonate Aquifer lies between New Albany Shale (upper confining unit) and the Maquoketa Shale (lower confining unit) and has a total thickness of approximately 500 meters.

The reference stratigraphic column includes the following formations that comprise the Silurian-Devonian Carbonate Aquifer:

Jeffersonville Limestone – Coarse-grained fossiliferous limestone that is partly dolomitic (Noger and Drahovzal, 2005).

Dutch Creek Sandstone – Composed of fine to coarse-grained well-rounded, carbonate-cemented quartz grains (Noger and Drahovzal, 2005).

Clear Creek and Backbone Limestone – fine-grained fossiliferous limestone with interbeds of chert (Noger and Drahovzal, 2005).

Grassy Knob and Flat Gap Limestone – Medium to coarse-grained non-fossiliferous limestone and dolomite with interbedded chert (Noger and Drahovzal, 2005).

Bailey Limestone – Silty and argillaceous fine-grained limestone (Noger and Drahovzal, 2005).

Moccasin Springs Formation – Argillaceous limestone, siltstone, and silty shale (Noger and Drahovzal, 2005).

St. Clair and Sexton Limestone – fine-grained limestone (Noger and Drahovzal, 2005).

Maquoketa Shale Confining Unit

The Maquoketa Shale is a black organic shale with siltstone and minor interbeds of limestone (Noger and Drahovzal, 2005). The highest organic content is in the lower horizons. Kolata and Graese (1983) divide the Maquoketa Shale Group into four formations distinguished by lithology. In ascending order, these are the Scales, Fort Atkinson, Brainard and Neda Formations. The Fort Atkinson Formation is dominantly composed of carbonate rocks (limestone and dolomite) with interbeds of shale and siltstone while the other three formations are dominantly composed of shale (Kolata and Grease, 1983).

Like the New Albany Shale, the Maquoketa Shale has been evaluated as a potential repository host rock in parts of the basin where it occurs at an appropriate depth (Droste and Drahovzal, 1976; Gonzales and Johnson, 1985).

The Cambrian-Ordovician Aquifer System

Rocks of the Cambrian-Ordovician Aquifer System are primarily carbonates and sandstones (Young, 1992). The Cambrian-Ordovician aquifer system is confined by the overlying Maquoketa Shale and highly saline in the deeper parts of the basin. Dense saline waters impede down-gradient freshwater flow into these parts of the aquifer (Young, 1992; Panno et al., 2017). The reference stratigraphic column includes the following formations.

Kimmswick Limestone – Medium to coarse-grained fossiliferous limestone (Noger and Drahovzal, 2005).

High Bridge Group – Primarily limestone, argillaceous limestone and dolomite with minor interbeds of shale deposited in carbonate tidal flats (Noger and Drahovzal, 2005).

St. Peter Sandstone – Fine to medium-grained, pure quartz sandstone with well-rounded grains (Noger and Drahovzal, 2005).

3.2.3.2 Hydrologic Properties of Aquifers and Confining Units

Permeability and porosity estimates are not available for each formation in the reference stratigraphic column. The permeability and porosity of the formations are therefore generalized based on the available data for each rock type in the region of the Illinois Basin.

Permeability

Surficial Deposits

The major surficial deposit of the Illinois Basin are glacial drift and till comprised of unconsolidated clay, sand and gravel (Young, 1992). Hydraulic conductivity measurements of three types of glacial deposits to the east of the Illinois Basin in the upper Midwest show horizontal permeability ranging from 10^{-13} to 10^{-14} with K_h/K_v of ~ 2 (Strobel, 1993). Melvin et al. (1992) report porosities of $\sim 30\%$ for glacial deposits in southern New England.

Shale Confining Units

Reported shale permeabilities in the region of the Illinois Basin and Michigan Basin range from 10^{-11} to 10^{-21} m^2 depending on whether it is measured or estimated for a fractured or unfractured domain. Estimates at the highest end of the permeability range are from the Norwood Member of the Antrim Shale in the Michigan Basin and represent highly fractured and gas producing shale (Figure 3-6). Shale with these characteristics would be avoided for purposes of repository siting in favor of less fractured and less permeable shale. Based on experimental and field studies discussed in Section 3.2.2.2, we consider a permeability of 10^{-15} to 10^{-16} m^2 to be representative of typical fractured shale (Table 3-4).

Carbonate Rocks (Limestone and Dolomite)

Belcher et al. (2002) compiled a large number of hydraulic conductivity measurements of hydrostratigraphic units of the Death Valley regional groundwater flow system. The Paleozoic carbonates in the Death Valley system form a regional aquifer and would not be expected to have hydrologic properties that are greatly different from other Paleozoic carbonate rocks in the US. Large variations in the hydraulic conductivity of the carbonate rocks are primarily influenced by the presence or absence of secondary fractures and dissolution features, as is the case for carbonate rocks in the region of the Illinois Basin (Casey, 1996; Belcher et al., 2002).

Belcher et al. (2002) divided the carbonate rocks into two groups, those with extensive fracturing and those without. The range of hydraulic conductivities (converted here to permeability) of the two groups overlap, with unfractured carbonates having permeability ranging from $\sim 10^{-11}$ to 10^{-16} m^2 and fractured carbonates having permeability of $\sim 10^{-9}$ to 10^{-14} m^2 .

Based on regional hydrologic measurements, Gupta (1997) assigned hydraulic conductivities (converted here to permeability) to the major carbonate aquifers in the region of the Illinois Basin. Carbonate rocks of the Silurian-Devonian carbonate aquifer have a horizontal permeability of $3 \times 10^{-14} \text{ m}^2$ and a vertical permeability of $3 \times 10^{-16} \text{ m}^2$. Carbonate rocks of the deeper Cambrian-Ordovician aquifer have a horizontal permeability of 2×10^{-14} and vertical permeability of $2 \times 10^{-15} \text{ m}^2$. Given that there is a large variation of permeabilities in carbonates (Belcher et al., 2002), we base the permeability of carbonates in the Illinois Basin on the regional analysis by Gupta (1997) and assign a horizontal permeability of 10^{-14} m^2 for the carbonates of the reference stratigraphic column (Table 3-4). We assume a vertical permeability that is two order of magnitude lower (Gupta, 2017).

Sandstone

Young (1992) reports hydraulic conductivity values for the St. Peter Sandstone that are typically in the range of 10^{-11} to 10^{-12} m^2 . Gupta (1997), based on the regional groundwater flow model calibration, assigned several sandstones present in the regional stratigraphy a horizontal permeability of 10^{-13} m^2 , with a K_h/K_v equal to 2. For the reference stratigraphy, we assign a value of 10^{-12} m^2 for both the St. Peter and Dutch Creek sandstones (Table 3-4).

Porosity

Paleozoic shales with 40-45% clay content are expected to have porosity of 5-10% based on the relationship between clay content and porosity documented by Bourg (2015). Mastalerz et al. (2013) reports porosity of ~5% for two samples of the New Albany Shale at a depth of 700-800 meters.

Person (2012) reported core porosity versus depth data for carbonate and sandstone aquifers of the Illinois Basin. Both sandstone and carbonate samples have a range of porosity from < 5-25% and show a moderate decrease in porosity with depth. Person (1992) modeled the relationship between porosity and effective stress calibrated to core data. The model predicts a porosity of ~15% for the carbonates above the New Albany Shale, 20% for carbonates between the New Albany and Maquoketa shales and 5-10% for the deepest shales (Table 3-1). The model predicts a porosity of ~10% for the deep St. Peter Sandstone and ~15% for the shallower Dutch Creek Sandstone (Table 3-4).

3.2.4 The Regional Groundwater System of the Illinois Basin

The Illinois Basin is an intracratonic structural basin developed on Precambrian crystalline crust that is filled with Paleozoic marine sediments. The major lithologies of the marine sediments are limestones and dolomites (carbonates), sandstones and shales. The Illinois, Michigan and Appalachian Basins are separated by a series of Precambrian basement highs or arches. Groundwater generally flows downdip from the crests of the arches into the basin interiors (Gupta, 1997).

Recharge to bedrock aquifers is mainly along the western and northern margins of the basin where permeable limestones and sandstones are closest to the surface and shale confining units are thin or absent, thereby allowing flow to stratigraphically lower formations (Panno et al., 2017). Freshwater recharge in the northern part of the basin creates more dilute groundwater in this region while more saline waters are present in the central and southern parts of the basin where the groundwater is more isolated from freshwater recharge (Siegel, 1989; Panno et al., 2017). Panno et al. (2017) demonstrated these general flow conditions by mapping chloride (Cl) concentrations within the basin (Figure 3-9). The pattern of Cl concentrations in the basin indicate that salinity is controlled by the presence of bedrock

exposures, presence of confining units and fresh-water recharge at the northwestern basin margins with salinity increasing towards the southern margin (Figure 3-9).

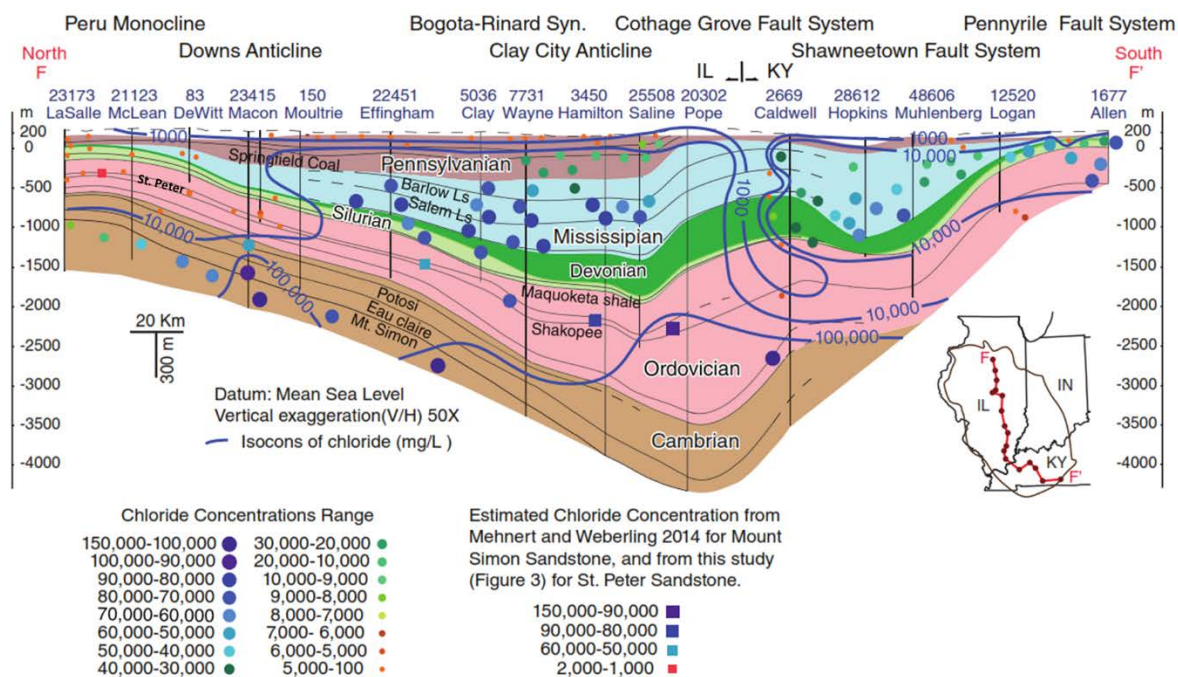
Primary flow directions within the basin are to the south and southeast as indicated by the potentiometric surfaces of carbonate bedrock aquifers (Siegel, 1989). Based on the regional potentiometric surface in the northwest Illinois Basin, the hydraulic gradient within the deep Cambrian-Ordovician carbonate aquifer is approximately 0.0002 (Siegel, 1989), while the gradient in the shallower Silurian-Devonian aquifer is approximately 0.0004 (Young, 1992), consistent with more sluggish flow in the deeper aquifers.

Groundwater discharges downgradient at the southern margin of the basin as evidenced by discharge features that include saline seeps and springs (Panno et al., 2017). Saline groundwaters also discharge in areas of enhanced fracturing and permeability and upward hydraulic gradients as evidenced by thermal anomalies driven by upward advection of saline groundwater (Cartwright, 1970; Panno et al., 2017). Several lines of evidence, including modeling of variable fluid density, 3-D mapping of groundwater salinity (as chloride concentrations) and analysis of thermal anomalies indicate the significance of vertical flow (both upward and downward) through leaky shale confining units (Cartwright, 1970; Gupta, 1997; Panno et al., 2017). This indicates fracture flow through the shale confining units and formation-scale permeability that is higher than that of unfractured shale.

Cl data indicate that structural features within the basin also play a role in groundwater flow. The LaSalle Anticline is a zone of enhanced fracturing and faulting that bisects the central portion of Illinois basin from north to south. Cl concentrations beneath the anticline are diluted beneath the feature indicating enhanced recharge and downward movement of freshwater through fractures (Panno et al., 2017). In addition, thermal anomalies indicate that upward flow occurs at some locations along the LaSalle Anticline (Cartwright, 1970).

In a general sense, locations at the northern and western margins of the Illinois Basin are expected to have downward movement of relatively dilute waters focused within permeable layers while locations in the more southern parts of the basin experience upward flow of more saline waters (Cartwright, 1970; Panno et al., 2017).

Figure 3-9. N-S geologic cross-section of the Illinois Basin showing Cl concentrations and isocontours. Low Cl concentrations are present in the northern part of the basin and follow permeable units such as the St. Peter Sandstone, indicating freshwater recharge. The southern part of the basin is characterized by high concentrations of Cl at shallow depth, indicating upward flow of saline waters. The dilute downward plume at the IL-KY border is the location of the Ohio River.



3.2.5 Summary of Brittle Shale Properties

Consideration of both brittle and ductile shale broadens the range of shale host-rock properties considered as part of a shale reference case. The range in properties exhibited by the two types of shale is conceptualized as two endmembers that bracket the primary types of shale commonly found in the US. The properties of the two shale endmembers are summarized in Table 3-4 and discussed in more detail in Stein et al. (2020a).

The mechanical and hydrologic properties of brittle and ductile shales differ in several important ways that are related to clay content and degree of induration and fracturing (Bourg, 2015; Neuzil, 2019). Separate from the effects of fractures, the lower clay content and higher quartz content of brittle shales leads to higher compressive strength, higher permeability and lower porosity compared to ductile shales (Table 3-4). Lower porosity and higher quartz content of brittle shales also results in higher thermal conductivity compared to ductile shale (Table 3-4).

Interconnected fractures in brittle shale increase permeability by several orders of magnitude, similar to the increases in permeability measured in the EDZ of European URLs (Stein et al., 2020a). Fracture stratigraphy has been documented in brittle shales where layers with different mineralogy and mechanical properties have different fracture frequencies. The presence of fracture stratigraphy in shale formations could play a role in developing strategies for repository siting.

Table 3-4. Summary of properties of the brittle and ductile Shales

Property	Ductile Shale (e.g., Pierre Shale)	Brittle Shale (e.g., New Albany Shale)
Typical thickness	400-600 m	75-150 m
Clay content	65-80%	35-50%
Quartz content	~20%	~ 50%
Compressive strength	5-10 MPa (range of 0.5-18 MPa)	30-160 MPa
Fracture Characteristics	Largely unknown. Widely spaced vertical fracture zones proposed at regional scale.	Dominated by vertical fractures at low to high frequency. Vertical variations in mechanical properties of rock influences fracture stratigraphy.
Thermal Conductivity	0.7-1.2 W/m/K	1.0-2.1 W/m/K
Porosity	~20% (range of 10-30%)	5-10%
Permeability (m ²)	~10 ⁻²⁰ to 10 ⁻²¹ ; 3-4 orders of magnitude higher proposed at regional scale due to widely spaced fracture zones.	~10 ⁻¹⁹ for intact shale based on clay content; ~10 ⁻¹⁵ to 10 ⁻¹⁶ for typical fractured shale.
Salinity (Cl ⁻ concentration)	200-4000 mg/L	10,000-160,000 mg/L

4. GDSA SALT REFERENCE CASE

This report section details the simulations of a full-scale PA using the repository design for high-thermal-output 24- and 37-PWR waste packages. The past bedded salt reference case (Sevougian et al., 2016) for deep geologic disposal of defense-related HLW and SNF was developed from (1) the reference case for a commercial SNF/HLW repository in bedded salt, described in Sevougian et al. (2012) and Vaughn et al. (2013), (2) the repository design proposed in Carter et al. (2012) for a defense-only repository, and (3) elements of the engineered and natural barriers described in previous performance assessments of CSNF disposal in bedded salt (Mariner et al., 2015; Sevougian et al., 2014; Sevougian et al., 2013; Freeze et al., 2013a, Clayton et al., 2011), the characterization of which drew heavily upon parameter values developed for the Waste Isolation Pilot Plant (WIPP) performance assessments.

This update relies on the same history but changes the repository design to accept high-thermal-output 24- and 37-PWR waste packages (Adeniyi et al., 2020), in a 50/50 split by weight of heavy metal for each canister size. A deterministic simulation using the mean or mode values of the sampled parameters is conducted for comparison and visualization purposes.

The conceptual model includes a mined repository 600 m below the surface in a thick bedded salt host rock in a geologically stable sedimentary basin (Figure 4-1). Characteristics of the bedded salt host rock that contribute to or impact post-closure safety include (Freeze et al., 2013b):

- The ability of salt to creep, which is expected to heal fractures, reconsolidate crushed salt backfill, and encapsulate waste, contributing to waste containment.
- The geologic stability of deep salt beds, which have been isolated from surface processes for hundreds of millions of years and can be expected to isolate the repository for the duration of the regulatory period.
- The low permeability and porosity of the host rock, which limits exposure of waste to water, thereby limiting and delaying radionuclide releases.
- The reducing chemical environment, which limits radionuclide solubility, limiting and delaying radionuclide releases.
- The potential presence of anhydrite interbeds, which are more brittle and of higher permeability than halite, providing potential pathways for radionuclide release.

The remainder of this section includes a description of the engineered (Section 4.1) and natural (Section 4.2) barriers followed by the description of the full scale, probabilistic post-closure performance assessment (PA) (Section 4.5).

4.1 Engineered Barriers

Specific post-closure basis information related to the engineered barriers includes:

- Characteristics of the repository (Section 4.1.1)
- Inventory characterization (Section 4.1.2)
- Waste form characterization (Section 4.1.3)
- Waste package characterization (Section 4.1.4)
- Characteristics of the buffer, drifts, and access halls (Sections 4.1.5 and 4.1.6)

4.1.1 Engineered Barrier Characteristics

The salt reference PA assumes a mined repository located 600 m below land surface, accessed by vertical shafts, and containing 32,000 metric tons heavy metal (MTHM) of commercial SNF in 24-PWRs and another 35,000 MTHM in 37-PWRs. This inventory is accommodated with 3065 24-PWR waste packages and 1988 37-PWR waste packages in 102, 1525-m long emplacement drifts (62 drifts contain 24-PWRs and 40 contain 37-PWRs). Each drift, regardless of package type, contains 50 waste packages emplaced lengthwise and spaced 30 m center-to-center. A 25-m long backfill ‘seal’ is placed at either end of each emplacement drift. Drifts are 5.0 m per side spaced 30 m center-to-center resulting in a total emplacement footprint of approximately 4.88 km² (5.24 km² including area for shafts and access halls). The drift and package spacing results in ~11 W/m² peak heat production, after aging (see below). After rounding the number of canisters up to 3100 24-PWRs and 2000 37-PWRs to provide an even distribution across the repository, the actual inventory is 32,364 MTHM in 24-PWRs and 32,190 MTHM in 37-PWRs, for a repository total of 64,554 MTHM.

The PA simulations use a half-symmetry, reflected model domain consisting of thirty-one 24-PWR drifts and twenty 37-PWR drifts (Figure 4-4 and Figure 4-5), meaning that 50% (32,277 MTHM) of the 64,554 MTHM inventory is included in the PA simulations. The specifications for the repository design are listed in Table 4-1.

Table 4-1. Dimensions and counts for the salt repository layout.

Parameters	Reference Case Repository Design
Waste Package (WP)	
WP length (m) [24-PWRs and 37-PWRs]	5.00
WP outer diameter (m) [24-PWRs and 37-PWR]	1.67 / side
WP center-to-center (m) [24-PWRs and 37-PWRs]	30.0
Inventory per 24-PWR WP (MTHM)	11.28 ^c
Inventory per 37-PWR WP (MTHM)	17.39 ^c
Number of 24-PWR WPs	1550 / 3100 ^b
Number of 37-PWR WPs	1000 / 2000 ^b
Emplacement Drift	
Drift diameter (m)	5.0 (on a side)
Drift center-to-center spacing (m)	30
Number of WPs per drift	50
Drift seal length (m)	25
Drift length, including seals (m)	1525
Repository	
Repository Depth (m)	600
Number of drifts	51 / 102 ^b
Number of shafts	3 / 6 ^b
Shaft access size (m)	5 x 5
Emplacement footprint (km ²)	2.44 / 4.88 ^b

^a Hardin and Kalinina (2016, Section 3)

^b half-symmetry domain / with reflection

^c Hardin et al. (2013, Table 4-2)

4.1.2 Inventory

For simplicity, PA simulations assume that the inventory consists entirely of PWR SNF assemblies, each single assembly containing 0.435 MTHM (Sevougian et al., 2013). The 24-PWRs assume a 40 GWd/MTHM burn-up rate with an initial enrichment of 3.72 wt% ²³⁵U and 50 years out of reactor (OoR) storage prior to emplacement. The 37-PWRs assume 60 GWd/MTHM burn-up rate with an initial enrichment of 4.73 wt% ²³⁵U and 100 years OoR. Radionuclide inventories and decay heat versus time curves are calculated from inventories in Carter et al. (2013). Because the average burn-up of SNF under

the “no replacement scenario” is predicted to be only 54 GWd/MTHM (Carter et al., 2013), the assumption of 60 GWd/MTHM results in a conservatively high heat load. Radionuclide inventory in each type of package is shown Table 4-2 and Table 4-3.

Table 4-2. 24-PWR 40-GWd/MTHM, 50-year OoR SNF inventory of selected radionuclides for the salt reference case.

Isotope	Inventory (g/MTHM) ¹	Inventory (g/g waste) ²	Atomic weight (g/mol) ³	Approximate Decay Constant (1/s) ⁴
²⁴¹ Am	1.35E+03	9.36E-04	241.06	5.08E-11
²⁴³ Am	1.38E+02	9.61E-05	243.06	2.98E-12
²³⁸ Pu	1.79E+02	1.24E-04	238.05	2.56E-10
²³⁹ Pu	6.38E+03	4.43E-03	239.05	9.01E-13
²⁴⁰ Pu	2.57E+03	1.79E-03	240.05	3.34E-12
²⁴² Pu	5.65E+02	3.92E-04	242.06	5.80E-14
²³⁷ Np	7.60E+02	5.28E-04	237.05	1.03E-14
²³³ U	1.32E-02	9.18E-09	233.04	1.38E-13
²³⁴ U	2.66E+02	1.85E-04	234.04	8.90E-14
²³⁶ U	4.72E+03	3.28E-03	236.05	9.20E-16
²³⁸ U	9.33E+05	6.48E-01	238.05	4.87E-18
²²⁹ Th	2.90E-06	2.01E-12	229.03	2.78E-12
²³⁰ Th	3.34E-02	2.32E-08	230.03	2.75E-13
²²⁶ Ra	7.34E-06	5.1E-12	226.03	1.37E-11
³⁶ Cl	3.52E-01	2.44E-07	35.97	7.30E-14
⁹⁹ Tc	9.16E+02	6.36E-04	98.91	1.04E-13
¹²⁹ I	2.16E+02	1.5E-04	128.9	1.29E-15
¹³⁵ Cs	4.86E+02	3.37E-04	134.91	9.55E-15

¹from Carter et al. (2013, Table C-2)

²(g isotope/g waste) = (g isotope/MTHM)/(g waste/MTHM), where g waste = g all isotopes

³Weast and Astle (1981)

⁴Decay constants from ORIGEN (Croff, 1983)

Table 4-3. 37-PWR 60-GWd/MTU, 100-year OoR SNF inventory of selected radionuclides for the salt reference case.

Isotope	Inventory (g/MTIHM) ¹	Inventory (g/g waste) ²	Atomic weight (g/mol) ³	Approximate Decay Constant (1/s) ⁴
²⁴¹ Am	1.46E+03	1.01E-03	241.06	5.08E-11
²⁴³ Am	2.69E+02	1.87E-04	243.06	2.98E-12
²³⁸ Pu	2.84E+02	1.97E-04	238.05	2.56E-10
²³⁹ Pu	7.40E+03	5.14E-03	239.05	9.01E-13
²⁴⁰ Pu	4.11E+03	2.85E-03	240.05	3.34E-12
²⁴² Pu	8.17E+02	5.67E-04	242.06	5.80E-14
²³⁷ Np	1.40E+03	9.72E-04	237.05	1.03E-14
²³³ U	4.33E-02	3.01E-08	233.04	1.38E-13
²³⁴ U	5.11E+02	3.55E-04	234.04	8.90E-14
²³⁶ U	6.27E+03	4.35E-03	236.05	9.20E-16
²³⁸ U	9.10E+05	6.32E-01	238.05	4.87E-18
²²⁹ Th	1.48E-05	1.03E-11	229.03	2.78E-12
²³⁰ Th	1.04E-01	7.22E-08	230.03	2.75E-13
²²⁶ Ra	3.99E-05	2.77E-11	226.03	1.37E-11
³⁶ Cl	5.01E-01	3.48E-07	35.97	7.30E-14
⁹⁹ Tc	1.28E+03	8.89E-04	98.91	1.04E-13
¹²⁹ I	3.13E+02	2.17E-04	128.9	1.29E-15
¹³⁵ Cs	7.72E+02	5.36E-04	134.91	9.55E-15

¹from Carter et al. (2013, Table C-2)

²(g isotope/g waste) = (g isotope/MTIHM)/(g waste/MTIHM), where g waste = g all isotopes

³Weast and Astle (1981)

⁴Decay constants from ORIGEN (Croff, 1983)

4.1.3 Waste Form

Freeze et al. (2013b, Section 3.4.1.1) provides a description of commercial SNF. Spent uranium oxide (UO₂) fuel is a polycrystalline ceramic material that is stable to high temperatures and has the potential for slow degradation in the disposal environment. Cladding protects the fuel from degradation in the reactor and can continue to protect the fuel from degradation in the repository. Cladding from commercial light-water reactors (i.e., boiling water reactors and pressurized water reactors) is generally made from Zircaloy, a zirconium alloy that is chemically stable and resistant to corrosion. In the reactor, fuel undergoes physical changes due to heating, radiation damage, and the build-up of fission products. Lighter elements (fission products) become concentrated in voids and the outer margins of the UO₂ matrix.

Concentration of fission products in voids of the waste form results in the waste form releasing radionuclides in two fractions: instant-release (upon waste package breach) and slow-release (according to the UO₂ matrix dissolution rate).

4.1.4 Waste Package

Both waste package configurations (24-PWR and 37-PWR) are assumed to consist of a stainless-steel canister that is 4.7 m in length and 1.8 m in diameter (Greene et al., 2013). The 24-PWR waste package contains 24 SNF assemblies (10.44 MTHM), while the 37-PWR contains 37 SNF assemblies (16.10 MTHM). The MTHM per assembly is scaled from the 12-PWR waste package described by Hardin et al. (2013). Due to gridding limitations, the size of the simulated waste packages in the PA model is 1.67 × 1.67 × 5.0 m, giving it a simulated volume of 13.94 m³, as compared to the actual volume of 11.96 m³.

Waste package porosity is set equal to 30%, which is lower than, but still consistent with Sevougian et al. (2016). The thermal properties are based on that of stainless steel (Shelton, 1934).

The breach time for each package is set randomly using a truncated log normal distribution on the base degradation rate such that 50% of waste packages breach in 10,000 years or less. The salt reference case sets the canister material constant to zero meaning that the waste package degradation rate is temperature independent. See Mariner et al. (2016, Section 4.3.2.5) for a description of the waste degradation algorithm in PFLOTRAN.

4.1.5 Crushed Salt Backfill

The salt reference case assumes that disposal rooms and access halls are filled with run-of-mine-crushed salt backfill. As summarized in Sevougian et al. (2012; 2013), crushed salt backfill is expected to have higher porosity and permeability and lower thermal conductivity than intact salt (Rothfuchs et al., 2003). Over time, it will consolidate to a state approaching that of intact salt (Hansen and Leigh, 2011, Section 2.4.1.7), a process expected to be mostly complete within approximately 200 years (Clayton et al., 2012).

Following the example of Sevougian et al. (2013), to assign properties to the consolidated backfill, the model assumes that the backfill will evolve similarly to a crushed-salt shaft seal or panel closure. Porosity and permeability values are taken from Fox (2008), which lists two distributions for the porosity and permeability of crushed salt in the host rock (“the lower portion of the simplified shaft seal”), one distribution for the first 200 years after emplacement and one for 200-10,000 years after emplacement. The permeability is higher during the initial period, prior to consolidation. The reference case uses the values for the 200 to 10,000-year period, since there are no packages breached in the first 200 years and the reconsolidated values represent the long-term behavior. For the deterministic case backfill is assigned a porosity of 0.0265, which is slightly higher than the DRZ (0.0211) and a permeability of 8.61×10^{-21} m². In probabilistic simulations permeability is sampled while porosity is held constant.

4.1.6 Salt Seals

Shafts will be sealed to prevent migration of water and radionuclides. Seal designs usually consist of clay, asphalt, concrete, and crushed salt components (James and Stein, 2002). Concrete, clay, and asphalt components are expected to provide an immediate barrier to fluid flow, while the crushed salt component is expected to provide a permanent barrier to flow after consolidation (DOE, 2009, Section PA-2.1.3). For the model, we simulate an effective ShaftFill material that is based on crushed salt (i.e., backfill). The ‘ShaftFill’ material permeability is thus higher than native halite, but lower than the DRZ. It is given a thermal conductivity that is slightly less (4.8 W/m*K) than halite (4.9 W/m*K) and a mineral density equal to halite (2170 kg/m³).

4.2 Geosphere / Natural Barriers

Specific post-closure basis information related to the geosphere and natural barriers include:

- Characteristics of the natural barriers (e.g., location, geologic setting) (Section 4.2.1)
- Host rock characterization (Section 4.2.2)
- Disturbed rock zone (DRZ) characterization (Section 4.2.3)
- Characterization of additional geologic units (Sections 4.2.4 and 4.2.5)

4.2.1 Natural Barrier Characteristics

Bedded salt formations, often hundreds of meters thick, form in near-shore and shallow-marine environments during cycles of marine transgression and regression. In addition to beds of very low permeability and low porosity halite (the target for waste isolation), they may contain beds rich in other evaporite minerals (e.g., anhydrite, polyhalite), and carbonate and clastic (e.g., shale, sandstone) interbeds (Perry et al., 2014, Section 4.2.1). The present concept for a mined repository in a bedded salt formation places the repository in a stratum of relatively pure halite (> 50%) at least 76 m thick. Depth to top of the formation should be between 305 m and 1067 m below land surface (Sevougian et al., 2012, Section 3.2.3); sufficiently deep to isolate the salt formation from surface processes but shallow enough to make mining a repository technically and economically feasible. Regionally, the topographic slope should be $\leq 1^\circ$, providing little driving force for deep fluid flow.

The reference repository site occurs in a geologically stable sedimentary basin with low probabilities of seismicity and igneous activity. The bedded salt formation has a lateral extent of tens of thousands of square kilometers (Perry et al., 2014; Sevougian et al., 2012), more than enough for the establishment of a controlled area “no more than 5 kilometers in any direction from the outer boundary” of the repository as specified in 40 CFR 191.12 and 10 CFR 60.2 (Sevougian et al., 2012). The probability of human intrusion is reduced by siting the repository a sufficient distance from known geologic resources (other than the salt itself) such as extensive freshwater aquifers, ore deposits, fossil fuels, or high geothermal heat flux (which offers the potential for geothermal development).

Large areas fitting the depth criteria occur in the Michigan and Appalachian Basins, the Permian Basin, and the Paradox Basin, as shown in Figure 4-1 and range in age from Silurian (444 to 419 Ma) to Permian (299 to 252 Ma) (Sevougian et al., 2012, Section 3.2.3.1). Small areas of other basins fit the criteria as well. Measured heat flow in these locations is generally between 35 and 65 mW/m² (Blackwell et al., 2011), though it may be locally higher or lower. At repository depth, the host rock is saturated with brine. The driving force for regional flow at depth is assumed to be on the order of 0.001 m/m, as observed in deep sedimentary basins (e.g. Downey and Dinwiddie, 1988).

The full-scale stratigraphic section consists of beds of halite and anhydrite, a fractured dolomite aquifer, which is assumed to provide a potential pathway for radionuclide release, and a consolidated sedimentary ‘cap’ (Figure 4-2). Properties of each material, including the undisturbed host rock (halite) and the disturbed rock zone (DRZ) created by mining, are described in the following sections.

Figure 4-1. Distribution and depth to top of salt formations in major sedimentary basins of the U.S. Salt formations are labeled by name or by common reference and listed in stratigraphic order where more than one salt formation is present in a basin. [Figure from Perry et al. (2014).]

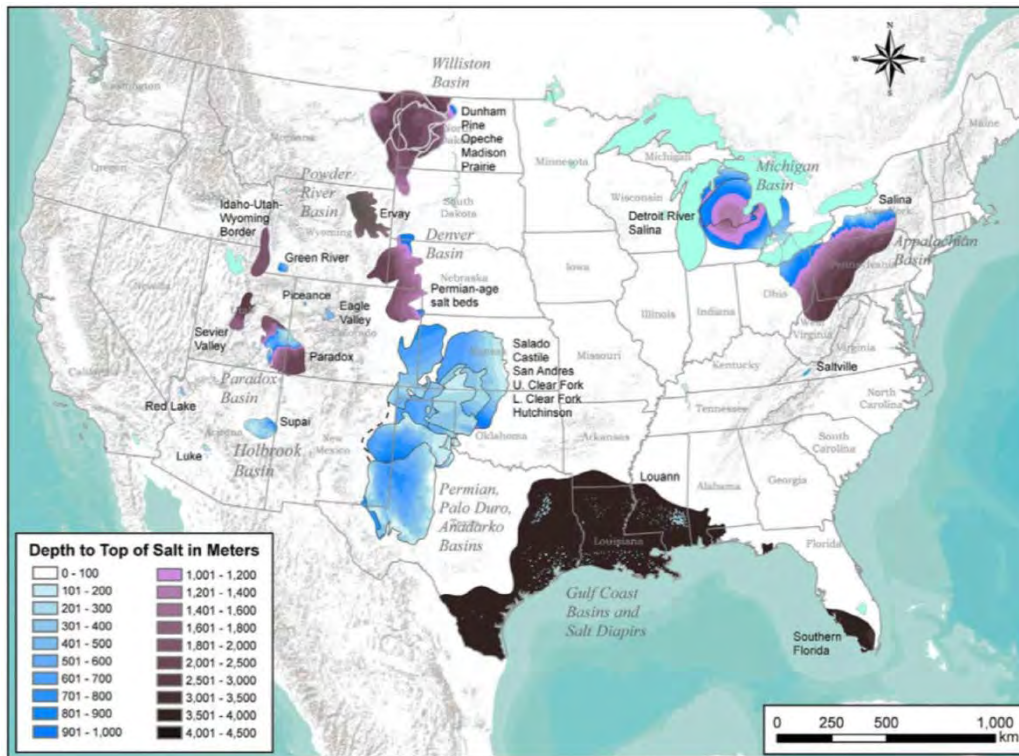
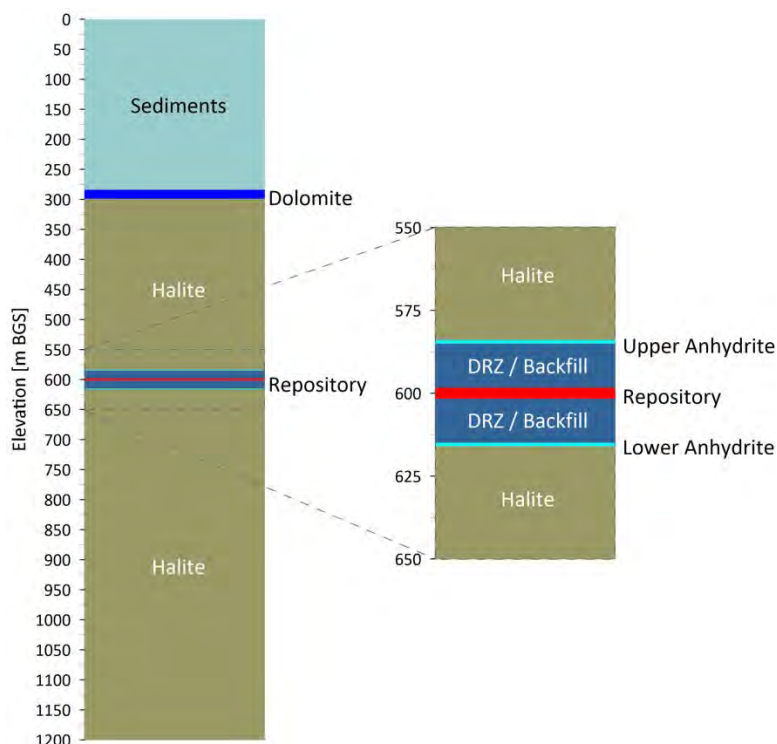


Figure 4-2. Generic stratigraphic column for salt reference case. The repository horizon, including the DRZ and backfill, is centered between two thin beds of anhydrite at $z = 600$ m.



4.2.2 Halite Host Rock

The top of the halite is assumed to be at 299 m below ground surface (BGS) with the bottom truncating at the bottom of the model domain at 1200 BGS, resulting in a total modeled halite thickness of 901 m. Within this thickness, two 1-m thick interbeds of anhydrite sandwich a 30-m thick repository horizon, which includes the DRZ and/or backfill depending on where you are in the repository. Halite is represented using permeability and porosity that are representative of the Permian Basin. Porosity is given the value of 0.0182, which is the mean of a cumulative distribution with a minimum of 0.001, median of 0.01, and maximum of 0.0519 (Fox, 2008; Freeze et al., 2013a; Sevougian et al., 2013; 2014; Mariner et al., 2015). Halite permeability is assigned a value of $3.1623 \times 10^{-23} \text{ m}^2$, which is the mean of the uniform distribution of the \log_{10} values from Fox (2008) (minimum -24, maximum -21).

4.2.2.1 Chemical Environment

Pore fluid chemistry influences the waste package degradation rate, waste form dissolution rate, and solubility and transport (diffusion and sorption) of dissolved radionuclides. Pore fluid chemistry is site-dependent and may vary locally depending on composition and proximity of interbeds and impurities within the halite. Representative brine compositions from several salt formations are given in

(Sevougian et al., 2012, Table 3-2). Solubility is discussed in the following section. The salt reference case assumes no sorption in the halite as per Clayton et al. (2011) and Sevougian et al. (2015). Waste package degradation and waste form dissolution are discussed in Section 4.4.2.5.

Table 4-4. Representative brine compositions for the salt reference case (Sevougian et al., 2012)

Description	Concentration (mg/l)							pH	SG
	Na ⁺	K ⁺	Mg ²⁺	Ca ²⁺	SO ₄ ²⁻	Cl ⁻	C		
1. ONWI Composite Permian Brine (Molecke, 1983)	123000	39	134	1560	3197	191380	30	7.05	NR
2. WIPP Generic Brine A (Molecke, 1983)	42000	30000	35000	600	35000	190000	700	6.5	NR
3. WIPP Generic Brine B (Molecke, 1983)	115000	15	10	900	3500	175000	700	6.5	NR
4 ^a . WIPP GWB Salado (DOE, 2009, App. SOTERM)	81150	18260	24790	560	17000	207750	NR	NR	1.2
5 ^a . WIPP ERDA-6 Castile (DOE, 2009, App. SOTERM)	111960	3790	460	480	16330	170170	980	6.17	1.22
6. MCC Brine (Molecke, 1983)	35400	25300	29600	NR	NR	164000	NR	6.5	NR
7. German Quinare Brine Q (Molecke, 1983)	6500	29000	85000	NR	13000	270000	NR	NR	NR
8. Michigan Basin Devonian Brine (Wilson and Long, 1993)	12400-103000	440-19300	3540-14600	7390-107000	0-1130	120000-251000	NR	3.5-6.2	1.136-1.295
9. Paradox Formation Brine-Moab Region (DOE, 2007)	9800-25966	23400-41957	21000-47789	34000-65800	80-1800	29800-259106	NR	4.8-6.0	NR
10 ^b . Paradox Basin Mississippian Formation (Garrett, 2004; Mayhew and Heylmun, 1966)	132000-168000	NR	324-9000	288-14400	2160-8800	183600-264000	NR	4.6-6.7	NR
11 ^b . Paradox Basin Paradox Formation (Garrett, 2004; Mayhew and Heylmun, 1966)	26640-119880	25680-63000	5160-39480	6036-51240	306-5268	145080-260640	NR	4.9-6.2	NR

a. Converted from ppm assuming an average brine density of 1.2 g/cc.

4.2.2.2 Solubility

Element solubility limits are assumed for a concentrated, reducing brine environment (Clayton et al., 2011; Wang and Lee, 2010) and are applied to the entire model domain. The original authors (Wang and Lee, 2010) describe solubility limits in terms of triangular distributions (Table 4-5). The current iteration of the reference case uses the mode of each of these distributions as the solubility.

If no fractionation of isotopes occurs between the liquid and solid phases, the solubility limit of a given isotope (e.g., ²³⁸Pu, ²³⁹Pu, ²⁴⁰Pu, or ²⁴²Pu) in the transport domain of a cell can be calculated by multiplying the element solubility limit by the isotope's element mole fraction in the transport domain (e.g., ²³⁸Pu/Pu_{Total}) (Mariner et al., 2016, Section 3.2.4).

Table 4-5. Element solubility calculated at T = 25°C in concentrated brine (Wang and Lee, 2010 as cited in Clayton et al., 2011).

Element	Distribution Type	Dissolved Concentration (mol kg ⁻¹)		
		Min	Mode	Max
Am	Triangular	1.85×10^{-7}	5.85×10^{-7}	1.85×10^{-6}
Np	Triangular	4.79×10^{-10}	1.51×10^{-9}	4.79×10^{-9}
Pu	Triangular	1.40×10^{-6}	4.62×10^{-6}	1.53×10^{-5}
Sn	Triangular	9.87×10^{-9}	2.66×10^{-8}	7.15×10^{-8}
Tc	Log-triangular	4.56×10^{-10}	1.33×10^{-8}	3.91×10^{-7}
Th	Triangular	2.00×10^{-3}	4.00×10^{-3}	7.97×10^{-3}
U	Triangular	4.89×10^{-8}	1.12×10^{-7}	2.57×10^{-7}
Cs, Cl, I	N/A	Unlimited ^a		

^a Assumed by Clayton et al. (2011).

4.2.3 Disturbed Rock Zone (DRZ)

The DRZ is defined as the portion of the host rock adjacent to the engineered barrier system that experiences durable (but not necessarily permanent) changes due to the presence of the repository (Freeze et al., 2013b). The DRZ is expected to have elevated permeability and porosity with respect to the properties of the host rock matrix due to the changes in stress induced by mining. For the PA model, the lateral extent of the DRZ within the repository is assumed to be 5 m. Vertically, the DRZ extends to the thin (1-m-thick) anhydrite interbeds above and below the repository (a total thickness of 30 m). The simulations include a 5-m-thick DRZ surrounding each 5-m-wide shaft. Within the halite, DRZ permeability and porosity are based on values in Sevougian et al. (2013). The porosity for the DRZ is set to 0.0211, which is the mean of a cumulative distribution with a minimum of 0.0039, a median of 0.0129, and a maximum of 0.0548. Permeability is allowed to vary in the PA using a log uniform distribution with a minimum of -19.4 and a maximum of -13.5. The maximum value of -13.5 was adjusted down from the -12.5 value used in Mariner et al. (2015) due to convergence issues at the higher values. A mean permeability of $3.548 \times 10^{-17} \text{ m}^2$ (\log_{10} value of -16.45) is used for the single deterministic run. The shaft DRZ is continuous from the repository to the top of the model. Where it crosses overlying units, its permeability is set one order of magnitude higher than that of the adjacent unit.

4.2.4 Anhydrite

Anhydrite beds and interbeds are more permeable than the surrounding halite. Near the repository, they may become fractured due to excavation, and therefore serve as potential pathways for radionuclide transport. The model assumes 1-m-thick anhydrite interbeds located immediately above and below the repository DRZ. Based on parameters representative of those in the Permian Basin, anhydrite porosity is assumed to be 0.011. Log permeability (m^2) is assumed to be -19.05 (permeability = $8.9125 \times 10^{-19} \text{ m}^2$), which is the mean of a Student-t distribution estimated as a uniform distribution with a range of -21.0 to -17.1 (Fox, 2008; Freeze et al., 2013a; Sevougian et al., 2013; 2014; Mariner et al., 2015).

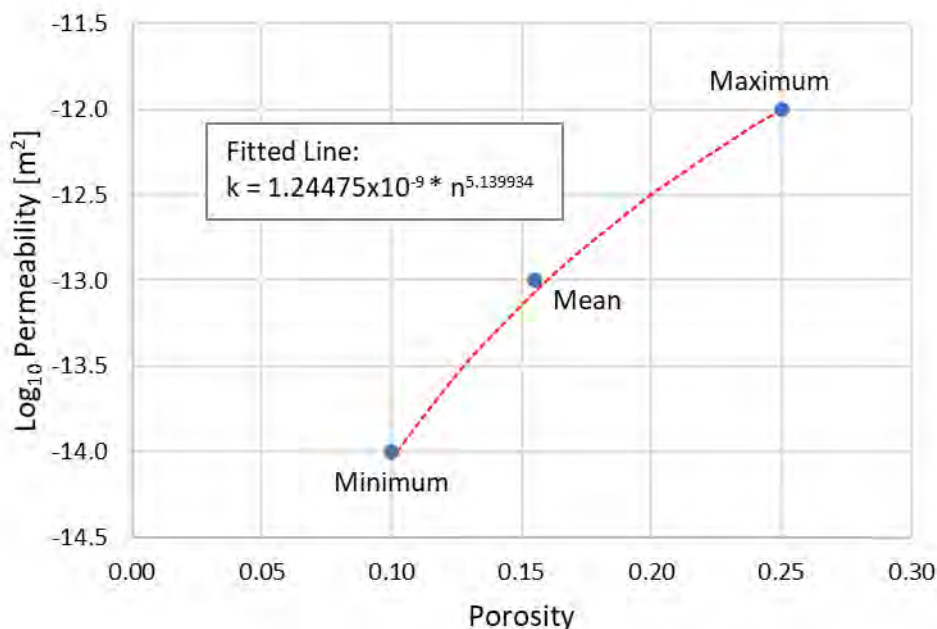
4.2.5 Fractured Dolomite Aquifer

The near-field repository model assumes a 15-m-thick aquifer, embedded directly on the halite. The model assumes that the dolomite sits directly on the halite below a top sediment formation (Figure 4-2). Dolomite permeability was modeled as a function of the porosity by assuming that the permeability distribution used in Mariner et al. (2015) and Sevougian et al. (2016) (uniform from -14 to -12 with a mean of -13 for \log_{10} permeability) is coincident with the porosity distribution from Fox (2008) (cumulative distribution over 0.10 to 0.25 with a mean of 0.175). A power-law function was fit using the 3 pairs of matching values (minimum, maximum, and mean) to give:

$$k = (1.24475 \times 10^{-9})n^{5.139934} \quad (4.1)$$

where k is the permeability [m^2] and n is the porosity. The relationship is plotted in Figure 4-3. In the deterministic simulation, aquifer porosity was set to 0.175 and the permeability of $1.60083 \times 10^{-13} \text{ m}^2$ was calculated using Equation 4.1.

Figure 4-3. Relationship between the Log_{10} permeability distribution of Mariner et al. (2015) and Sevougian et al. (2016) and the porosity distribution of Fox (2008). In the model, permeability (k) is given in m^2 as a function of porosity.



4.2.6 Solubility and Sorption of Radionuclides

As discussed above, solubility controls the amount of radionuclide dissolved into solution. For the salt reference case, the porewater composition is assumed to be in equilibrium with halite, which combined with a lack of oxygen produces a chemically reducing environment that further affects radionuclide concentrations (Wang and Lee, 2010). Solubility limits in the model use the mode of the far-field values from Table 3.1-6 in Clayton et al. (2011), which are based on data and calculations from Wang and Lee (2010). The solubilities used in the salt reference model are listed in

. Solubilities of 1.0×10^4 are effectively infinite in the model. To conserve computational overhead only ^{241}Am , ^{243}Am , ^{129}I , and ^{237}Np are included in the model. We assume that fractionation is minimal due to

the low concentrations of other isotopes and that omitting other isotopes will have a negligible effect on concentrations, especially in the far field. It should be noted that ²⁴³Am is the parent element of ²³⁷Np.

Sorption of radionuclides is modeled using an equilibrium K_d approach, where the K_d distribution coefficient determines the distribution of the radionuclide between water and soil. The values are taken from Table 3.1-7 in Clayton et al. (2011). An assumption has been made that radionuclides do not sorb onto salt, so the only non-zero K_d values are for the dolomite aquifer, the anhydrite and the sediments. The sediments are given the same values as the dolomite.

Table 4-6. K_ds and Solubility for the materials included in the salt reference case model.

Element	K _d [kg H ₂ O/ m ³ bulk]						Solubility [M]
	Halite	Dolomite	Anhydrite	Sediments	Backfill	Waste Package	
Am	0.0	5.10×10 ⁵	1.53×10 ⁵	5.10×10 ⁵	0.0	0.0	5.85×10 ⁻⁷
I	0.0	0.0	0.0	0.0	0.0	0.0	1.00×10 ⁴
Np	0.0	2.44×10 ⁵	1.35×10 ⁴	2.44×10 ⁵	0.0	0.0	1.11×10 ⁻⁵

4.3 Biosphere

The biosphere is usually thought of as the point in the repository far-field where radioactivity may be accessed or released to the biosphere. The model domain is extended 5 km down-gradient from the end of the repository to represent the artificial point where this connection may occur and for a full performance assessment, where the dosage to the biosphere would be calculated. Here, we look at the concentration in the dolomite aquifer at a point 5 km downstream on the centerline of the repository. No dosage calculations are made.

4.4 Post-Closure Performance Assessment Model

4.4.1 Conceptual Model

The conceptual framework for the salt reference case focuses on the components of the engineered barrier and the natural barrier and assumes an undisturbed scenario outside the repository zone. Key characteristics of, and processes occurring in the components of each system, are summarized in Table 4-7 (taken from Mariner et al. (2016) and Sevougian et al. (2016)).

Processes accounted for in the conceptual model include waste package degradation, waste form (UO₂) dissolution, equilibrium-controlled radionuclide sorption and precipitation/dissolution, radioactive decay and ingrowth in all phases (aqueous, adsorbed, precipitate), coupled heat and fluid flow, and radionuclide transport via advection and diffusion. Mechanical dispersion is conservatively neglected in this iteration of the salt reference case. Including it would result in earlier arrival of radionuclides at observation points, but lower peak concentrations (Freeze and Cherry, 1979).

Table 4-7. Conceptual representation of key components in the salt reference PA model.

Region	Component	Key Characteristics	Key Processes
Engineered Barrier	Waste Form	Commercial SNF (UO ₂)	Radionuclide decay, instant release fraction, waste form dissolution
	Waste Package	Stainless steel	Degradation and breach
Natural Barrier	Halite	Low permeability, high heat conductance	Radionuclide advection, diffusion, sorption, decay
	DRZ	Enhanced permeability	Radionuclide advection, diffusion, sorption, decay
	Dolomite Aquifer	High permeability, potable water	Radionuclide advection, diffusion, sorption, decay
Biosphere	Regional Flow	Regional flow in aquifer to model boundary	Radionuclide advection, diffusion, sorption, decay

4.4.2 Numerical Implementation

The salt reference PA model simulations consist of 200 probabilistic simulations conducted using Latin hypercube sampling (LHS) via the Design Analysis Toolkit for Optimization and Terrascale Analysis (DAKOTA) software (Adams et al., 2020). The LHS process samples seven uncertain parameters: the porosity of the dolomite, the permeabilities of the anhydrite, DRZ, backfill, and ShaftFill, and the mean and standard deviation of the waste package degradation rate coefficient. All parameters are uniformly distributed except for the mean of the waste package degradation rate coefficient, which has a triangular distribution. The distributions and their parameters for each sampled variable is listed in Table 4-8.

The unstructured mesh was gridded with Cubit (Blacker et al., 2016). The model simulates flow and transport using PFLOTRAN (Hammond et al. 2014) in “TH” (thermal and hydrological) mode.

Table 4-8. Listing of the uncertain variables and their probabilistic distributions used in the LHS PA simulations.

Variable Name	Variable Description	Distribution	Distribution Parameters		
			Minimum	Maximum	Mean
doloPor	Dolomite Porosity [-]	Uniform	0.10	0.25	0.175
anPerm	Log10 of Anhydrite Permeability [log(m ²)]	Uniform	-21.0	-17.1	-19.05
drzPerm	Log10 of DRZ Permeability [log(m ²)]	Uniform	-19.4	-13.5	-16.45
bfPerm	Log10 of Backfill Permeability [log(m ²)]	Uniform	-22.5	-18.0	-20.25
shftPerm	Log10 of ShaftFill Permeability [log(m ²)]	Uniform	-22.5	-18.0	-20.25
viStdDev	Log10 of Waste Package Degradation Rate Standard Deviation [log(1/yr)]	Uniform	0.30	0.70	0.50
vitMean	Log10 of Waste Package Degradation Rate Mean [log(1/yr)]	Triangular	Minimum	Maximum	Mode
			-4.7	-3.4	-3.6

4.4.2.1 Model Domain and Discretization

Figure 4-4 shows the repository layout as discussed above. The half-symmetry model domain (Figure 4-5) is 2250 m in width (Y ; south-north), 1200 m in height (Z ; elevation), and 7155 m in length (X ; west-east). The X domain is long enough to place an observation point 5000 m down gradient from the eastern edge of the repository (regional flow is west to east). The default grid size for most of the domain is 15 m in each direction, which is refined to 5 m per side in the repository area, and 5/3 m per side in the drifts. The grid consists of 9,156,747 elements and 9,313,850 nodes.

Figure 4-4. Repository layout at 600 m elevation showing the drifts numbered left to right, longhall, shorthalls, access halls, and shafts. Drifts 1 to 31 contain 24-PWR's while drifts 32-51 contain 37-PWR's. The model assumes a mirrored image along the closed southern boundary.

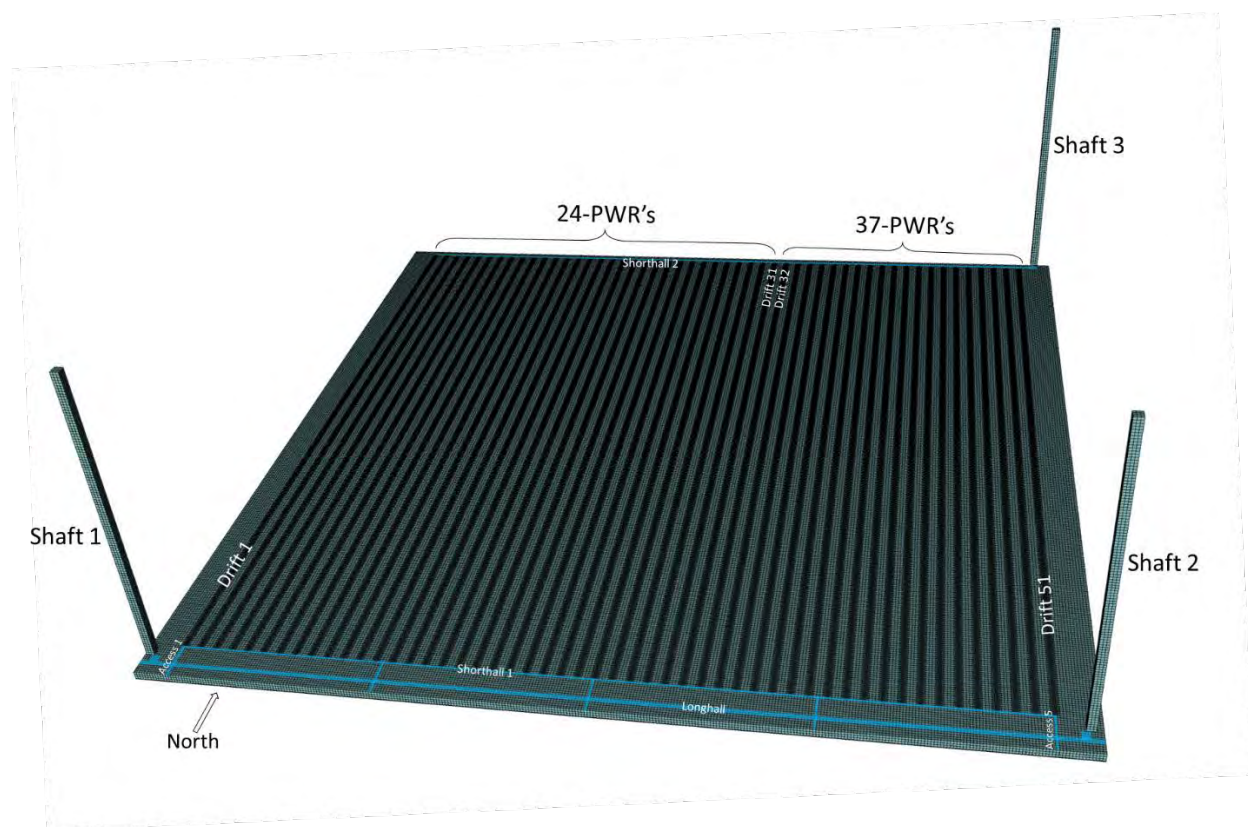
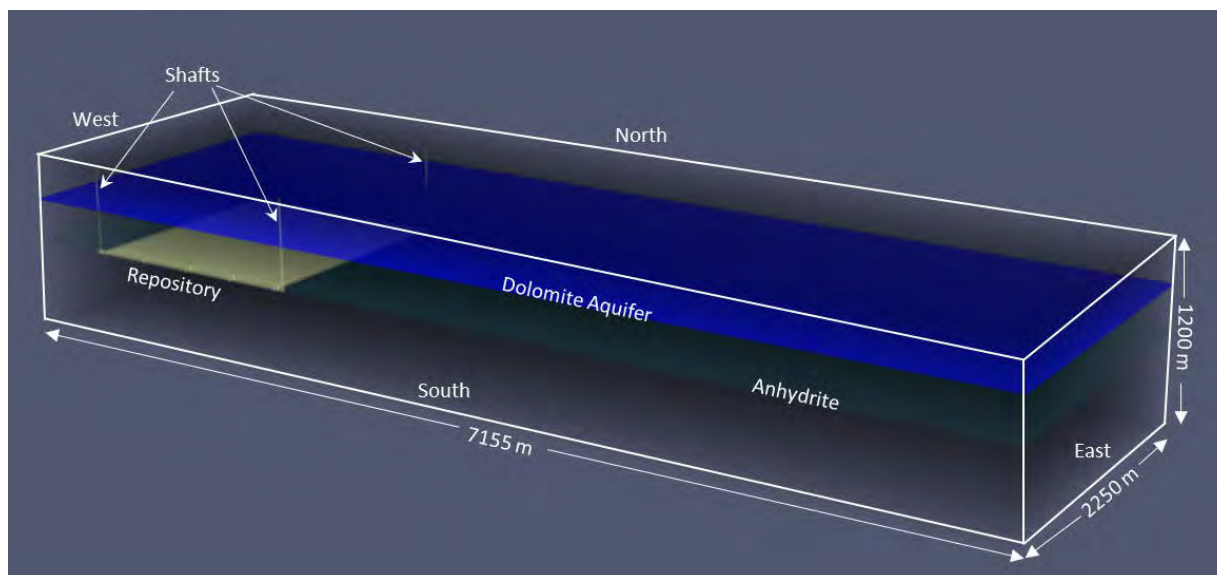


Figure 4-5. Salt Reference PA model grid showing the repository and shafts in relation to the dolomite aquifer and anhydrite layers.



4.4.2.2 Initial Conditions

Initial conditions specified are pressure, temperature, and radionuclide concentrations. The initial temperature of the system assumes a surface temperature of 20°C and a temperature gradient of 0.009°C/m, which results in a bottom temperature of 30.8°C. The initial pressure is set by the constant pressure boundary conditions on the west and east boundaries that are used to set up the regional flow. Initial concentrations of ^{241}Am , ^{243}Am , ^{129}I , and ^{237}Np are set to 10^{-20} mol/L across the entire domain.

4.4.2.3 Boundary Conditions

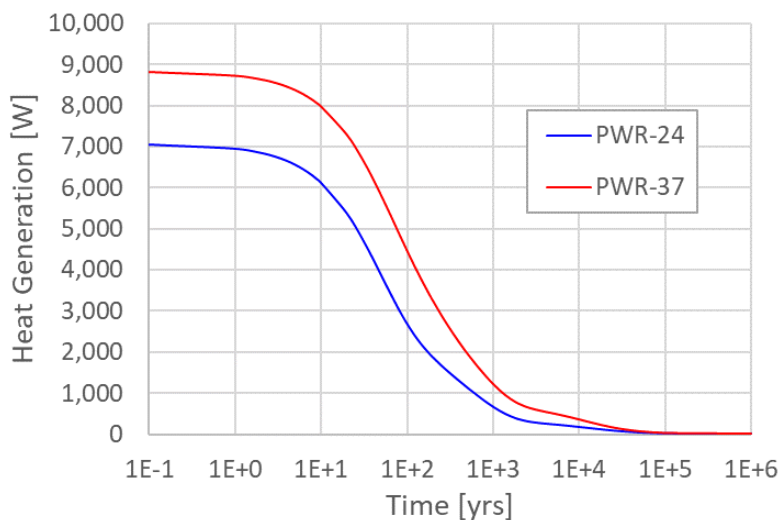
Boundary conditions must be set for the six faces of the model domain. The model sets zero flux of fluid and solute at the top, north, and south boundaries. At the west and east boundaries, initial pressure and temperature gradients are held constant, with a pressure gradient of -0.00125 m/m between the west and east faces (9-meter head drop). Solute and fluid flux for the bottom boundary are also set to zero. The bottom boundary heat flux is set to 28.85 mW/m² to maintain a 0.009°C/m temperature, which is representative of the temperature gradient in the Permian Basin (Blackwell, 2011b). This was determined by adjusting the bottom heat flux in a 1-dimensional column model run to steady-state until the proper gradient was reached. Radionuclide concentrations are held such that any fluid entering the model domain contains 10^{-20} mol/L of each radionuclide, while fluid exiting the model domain carries ambient concentrations. Diffusive flux across outflow boundaries is disallowed by specifying a zero-concentration gradient.

4.4.2.4 Waste Package Heat Sources

Each waste package is modeled as a transient heat source. The energy (watts per waste package) entering the model domain is updated periodically according to values in a lookup table that is generated from the inventory in Carter et al. (2013, Table C-1). To keep the initial heat-load consistent between the 24-PWR packages and the 37-PWR packages, the inventory in the 24-PWR canisters is assumed to be 50 years OoR with a burn-up of 40 GWd/MTHM while that in the 37-PWR canisters is assumed to be 100 years

OoR with a burn-up of 60 GWd/MTHM. This results in initial heat generation of 7058 W for the 24-PWR packages and 8810 W for the 37-PWR packages. Between times specified in the lookup table, the energy input is linearly interpolated. A plot of the heat generation decay for each canister type is shown in Figure 4-6.

Figure 4-6. Plot of heat generation over time for the PWR-24 and PWR-37 canisters.



4.4.2.5 Waste Package Breach and Radionuclide Source Term

The waste package degradation model implemented in PFLOTRAN (Mariner et al., 2016, Section 4.3.2.5) calculates normalized remaining canister thickness at each time step as a function of a base canister degradation rate, a canister material constant, and temperature. Waste package breach occurs when this thickness reaches zero. The PA simulations assign a canister degradation rate for each waste package by sampling on a truncated triangular distribution with a mode of $10^{-3.6}/\text{yr}$, a lower bound of $10^{-4.7}/\text{yr}$, and an upper bound of $10^{-3.4}/\text{yr}$, all of which are the same as in Sevougian et al., 2016. The standard deviation is also sampled but as a uniform distribution with a maximum of 0.7 and a minimum of 0.3 (log units).

PFLOTRAN calculates the decayed radionuclide inventory in each waste package region at each time step. From the time of waste package breach, the waste form releases radionuclides in two fractions: instant-release and slow-release. The instant-release fraction is due to the accumulation of fission products in void spaces of the waste form and occurs at the time of waste package breach. The salt reference case assumes a non-zero instant-release fraction for ^{129}I of 0.10 (Johnson et al., 2005) and zero for ^{241}Am , ^{243}Am , and ^{237}Np . The slow-release fraction is due to fuel matrix (UO_2) dissolution, which is modeled using a fractional dissolution rate of $10^{-7}/\text{yr}$ starting from the time of waste package breach. This rate is the mode of a log triangular distribution appropriate for fuel 3,000 – 10,000 years OoR and strongly reducing conditions – for a complete discussion refer to Sassani et al. (2016, Section 3.2.1).

4.4.2.6 Material Properties

Material properties for the constant parameters are listed in Table 4-9. Material properties and distributions for the sampled variables in the salt reference PA model are listed above in Table 4-8.

Table 4-9. Material properties for constant parameters.

Model Region	Permeability (m ²)	Porosity ϕ	Tortuosity	Effective Diffusion Coefficient ¹ (m ² /s)	Saturated Thermal Conductivity (W/m/K)	Heat Capacity (J/kg/K)	Grain Density (kg/m ³)
Halite	3.1623× 10 ^{-23a}	0.0182 ^a	0.01	4.19 × 10 ⁻¹³	4.9 ^b	916 ^b	2170 ^c
Dolomite	f(porosity)	sampled	0.15 ^d	6.04 × 10 ^{-12h}	4.8 ^e	870 ^c	2820 ^a
Anhydrite	sampled	0.011	0.22	5.57 × 10 ⁻¹¹	4.9	916	2960 ^d
Sediment	1.0 × 10 ^{-15d}	0.20 ^d	0.58	2.67 × 10 ⁻¹⁰	1.5	927	2700
DRZ	sampled	0.0211 ^a	0.23	1.12 × 10 ⁻¹¹	4.9	916	2170
Backfill	sampled	0.02645 ^f	0.02 ^g	1.22 × 10 ⁻¹²	4.8	916	2170
ShaftFill	sampled	0.02645 ^f	0.02	1.22 × 10 ⁻¹²	4.8	916	2170
Waste Package	1.0 × 10 ⁻¹⁶	0.30 ^d	1.0	6.90 × 10 ⁻¹⁰	16.7	466	5000

¹ Effective diffusion coefficient = $D_w \phi \tau s$, where the free water diffusion coefficient (D_w) = 2.3 × 10⁻⁹ m²/s (Cook and Herczeg, 2000) and saturation (s) = 1

^aFox, 2008

^bUrquhart and Bauer, 2014, Halite at 75°C

^c Waples and Waples, 2004, Table 1, page 101

^dMariner et al., 2015

^eRobertson USGS, 1988

^fCamphouse et al., 2012 (run of mine panel closure)

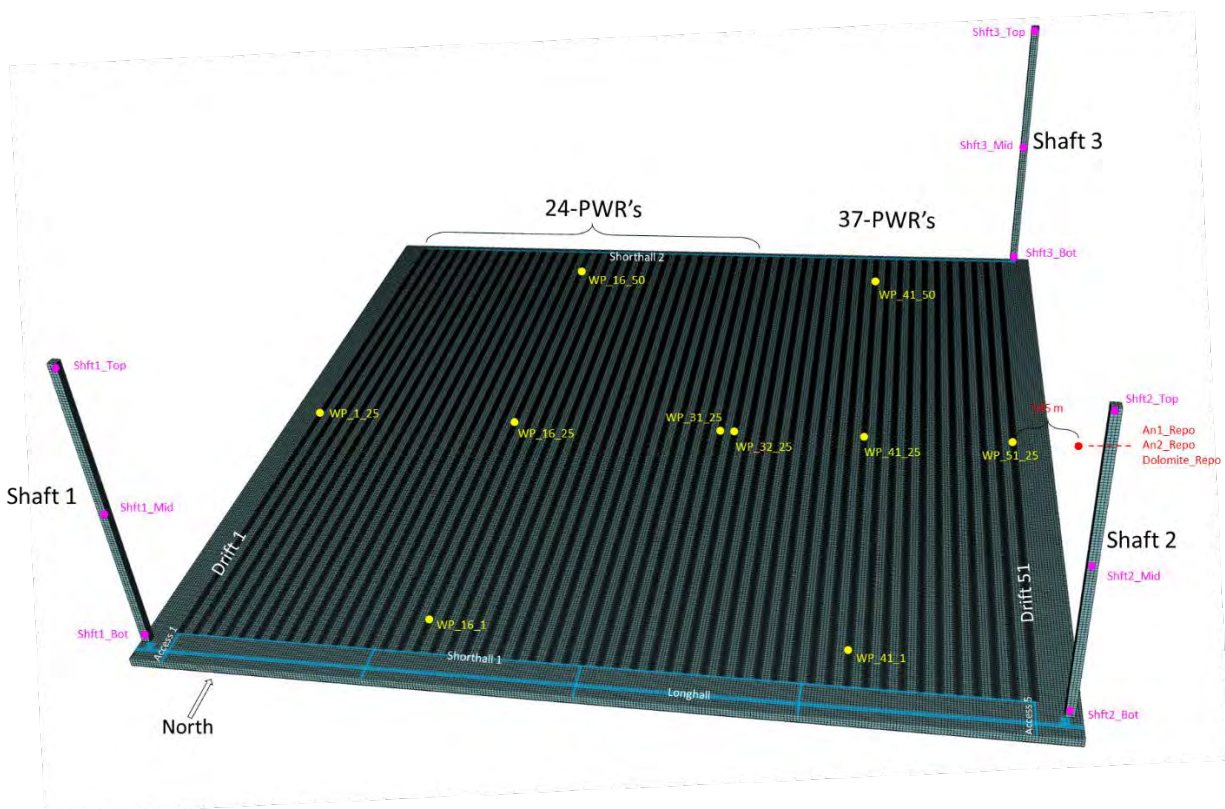
^gSlightly higher than intact salt

^hBased on the distribution mean porosity of 0.175

4.5 Deterministic PA Simulation

Initially a single deterministic simulation is run with representative values for all sampled quantities. To examine the results, temperature, ¹²⁹I and ²³⁷Np concentrations, and waste package breach times are considered. Figure 4-7 shows the observation points monitored for the simulation in relation to the repository layout. Not shown in the figure are 3 additional observation points placed in the two anhydrite layers and the dolomite aquifer at the down gradient end of the model, 5000 m from the repository.

Figure 4-7. Repository view of the observation points in the model. For the waste packages, observation points were placed along the center-line in waste package #25 in drifts 1, 16, 31, 32, 41, and 51. In addition, waste package observation points were placed at the ends of drifts 16 and 41, which are in the center of the block of 24-PWRs and block of 37-PWRs, respectively. Observation points were also placed at the bottom, mid-elevation, and top of each shaft. For the anhydrite layers and the dolomite aquifer (An1_Repo, An2_Repo, and Dolomite_Repo), observation points were placed 185 m down gradient of drift 51 at the appropriate elevation for each layer (they appear as the same point in the figure). The same was done for each layer at the east end of the model, 5000 m down gradient of the repository (not shown).



4.5.1 Temperature

Figure 4-8 shows the average temperature across the 200 simulations for the waste package observation points. There is a clear difference between the heat generated by the 37-PWR packages and that of the 24-PWR packages, although both cool down to nearly the same value after 100,000 years. The waste packages heat up and cool relatively quickly, with average peak temperatures reached by the 24-PWR waste packages and 37-PWR packages between 5 and 20 years. The waste packages on the 'edges' of the repository (WP_1_25, WP_16_1, WP_16_50, WP_41_1, WP_41_50, and WP_51_25) peak the earliest; 5 years for the 24-PWRs peaking at 119.59°C and 9 years for the 37-PWRs at 144.96°C. The waste packages on the interior of the repository peak at 20 years for both the 24-PWRs and 37-PWRs at 123.41°C and 152.34°C, respectively.

Across the 200 simulations, the variability of the peak temperature is relatively small. For the 24-PWRs the peak temperature varies the most towards the interior of the repository with a minimum of 122.175°C and a maximum of 123.441°C for WP_16_25. For the 37-PWRs the range is larger with a minimum of 151.375°C and a maximum of 154.652°C at WP_41_25. The hottest 24-PWRs are in drift 31, which is adjacent to the 37-PWRs.

Figure 4-9 shows a close up of the repository temperatures at 20 years and at 300 years. The diffusion of heat through the system over time is clearly evident. Also evident is the temperature difference between

the 24-PWRs and the 37-PWRs as is the higher temperatures on the interior of the repository as compared to the edge of the repository.

Figure 4-10 shows the temperatures at points in the backfill and in the DRZ immediately down gradient of each waste package observation point. Like the waste packages themselves, the hottest temperatures occur towards the center of the repository with the hottest in the center of the 37-PWRs. One interesting note is the time delay between the waste packages, the backfill, and the DRZ. Due to the heat diffusion time, peak temperatures in the backfill occur approximately 10-20 years after the peak temperatures in the waste packages. For the DRZ, the peak is delayed another 200-300 years.

For the anhydrite layers and the dolomite aquifers, temperatures rise approximately 27°C for observation points 185 m laterally downgradient of drift 51 (observation points An1_Repo, An2_Repo, and Dolomite_Repo – note that the thermal gradient creates an initial temperature in the dolomite aquifer of 25.54°C, and 27.25°C and 27.43°C in the upper (An1) and lower (An2) anhydrite layers, respectively). There is a slight difference in the maximum peak temperature between the upper anhydrite and lower anhydrite layers with the upper layer (An1) reaching 54.60°C after 20,000 years and the lower layer reaching 54.55°C at the same time (Figure 4-11). The dolomite observation point, which is 293 m above An1 peaks at 54.28°C after 20,000 years. For the far-field observation points 5 km down gradient (An1_End, An2_End, and Dolomite_End), there is a very slight increase in temperature of 0.03°C in both the anhydrite layers and 0.07°C increase in the dolomite, all after 100,000 years. After about 1000 years, the anhydrite layers experience a cooling of 0.0035°C in the upper layer and 0.0054°C in the lower level. This is a numerical artefact associated with the east boundary condition.

Figure 4-8. Average waste package temperature across the 200 PA simulations versus time for the waste package observation points shown in Figure 4-7 and Figure 4-9.

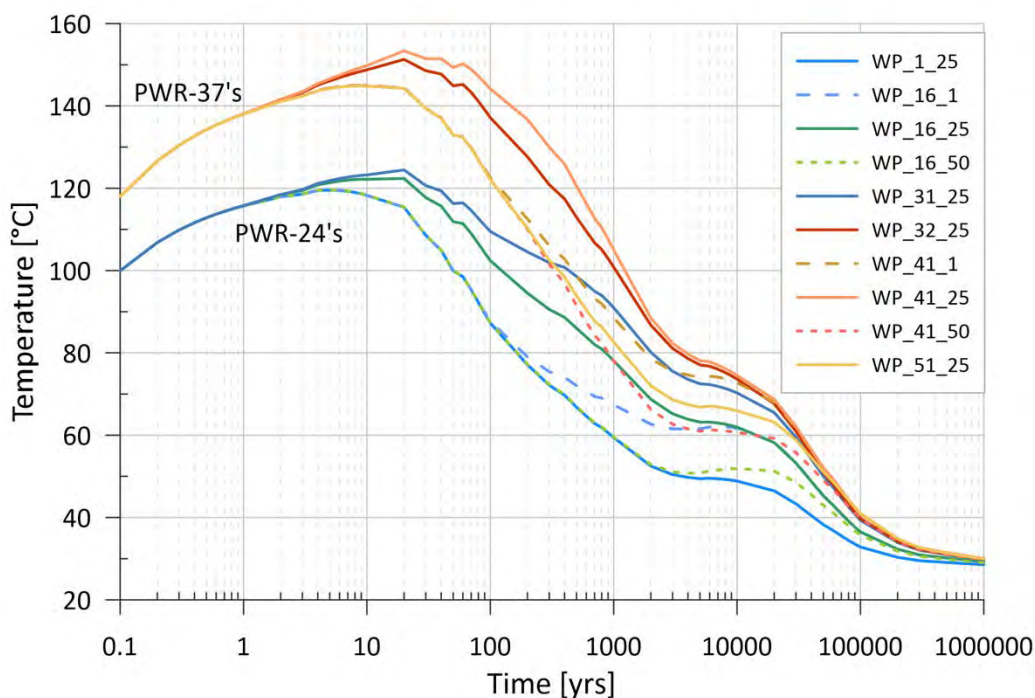


Figure 4-9. Plan view of temperatures in the repository after 20 years (left) and 300 years (right) for the deterministic run. The position of the waste packages corresponding to those in Figure 4-8 are indicated on the 20-year plot.

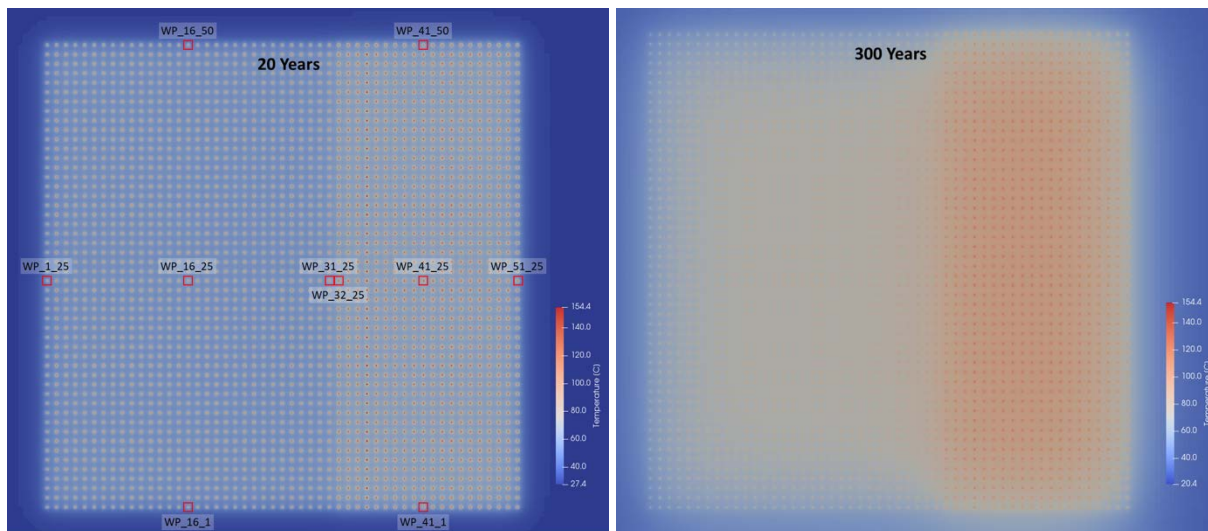


Figure 4-10. Average temperature across the 200 PA simulations versus time in the backfill (left) and the DRZ (right) immediately downgradient from the waste package observation points. [See Figure 4-7 for the observation point locations.]

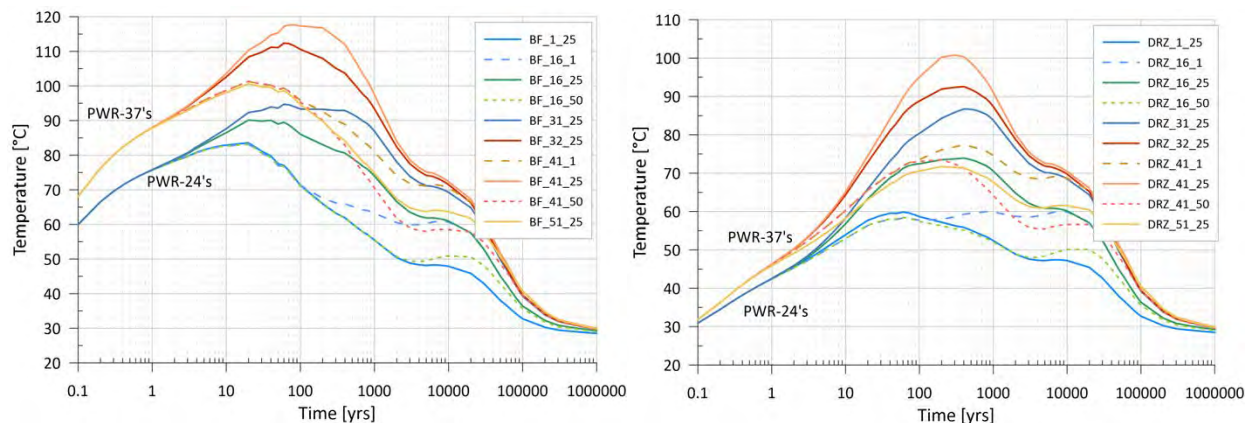
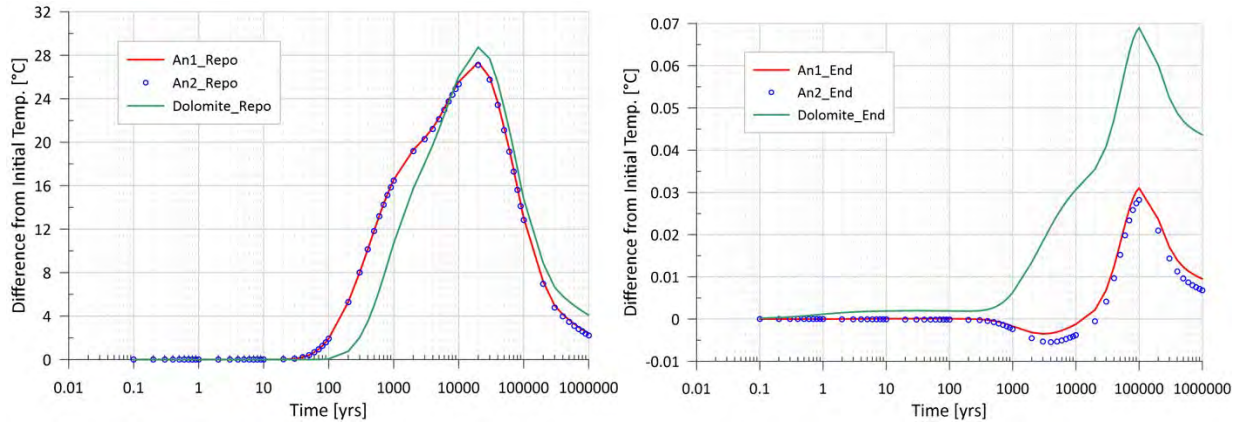


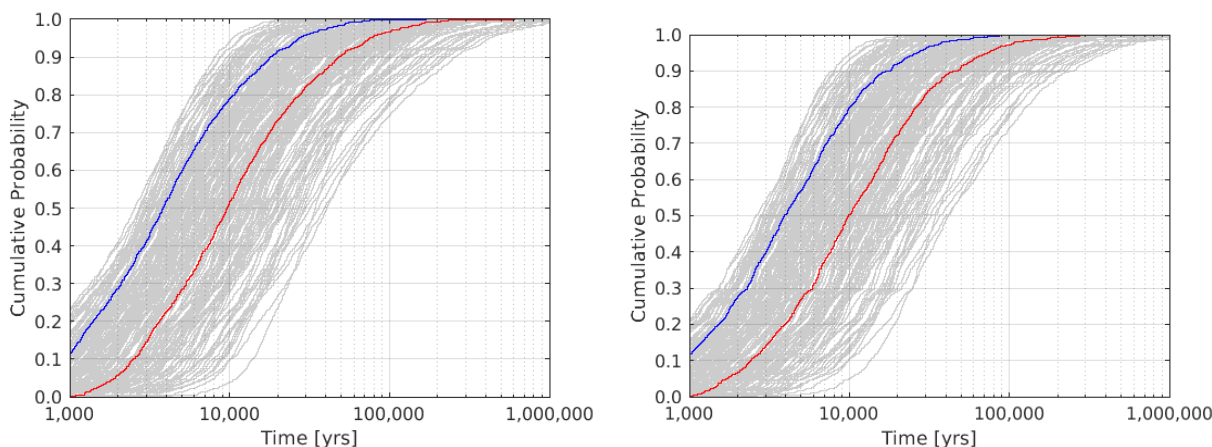
Figure 4-11. Average temperature across the 200 PA simulations versus time in the upper (An1) and lower (An2) anhydrite layers and the dolomite aquifer for points 185 m (left) and 5 km (right) down gradient of the repository.



4.5.2 Waste Package Breach

As introduced above, the salt reference case uses a randomly generated waste-package degradation rate with a truncated \log_{10} normal distribution on the degradation rate such that 50% of waste packages breach in 10,000 years or less. Figure 4-12 shows a cumulative distribution plot of the time to breach for the 24-PWR waste packages and the 37-PWR waste packages for each of the 200 simulations along with the 200-simulation average (red line) and the deterministic run (blue line) that uses the mode of the mean waste package degradation rate and the mean parameter values for the other variables. Recall that the mean waste package degradation rate is represented by a triangular distribution so that the mode is the most probable value, the other variables use a uniform distribution. The difference between the red and blue lines is due to the skewed nature of the triangular distribution given to the mean waste package degradation rate, which has a mode of -3.6 and a mean of -3.9. The average time to breach for the 24-PWRs across all 200 simulations is 21,068 years while for the 37-PWRs, the average time to breach is 20,756 years, which are statistically identical, as they should be because the WPs are assumed to be made of the same material, the thickness of the outer barriers are the same, and the temperature relationship to degradation rate was removed (Section 4.4.2.5). Taken together, the average breach time for the repository is 20,920 yrs.

Figure 4-12. Cumulative distribution plots of breach time for the 24-PWRs (left) and 37-PWRs (right) 200 PA simulations. The red line is the average of the 200 simulations and the blue line is the results of the single deterministic run using the average parameter values.



4.5.3 Radionuclide Transport

To investigate radionuclide transport, ^{237}Np and ^{129}I are considered since they are relatively persistent over the 1,000,000-year simulation period. ^{129}I is modeled with unlimited solubility, no sorption, and a half-life of 17 million years while ^{237}Np is modeled as low solubility, sorbing solute with a half-life of just over 2 million years and K_d values of 1.35×10^4 and 2.44×10^5 kg $\text{H}_2\text{O}/\text{m}^3$ bulk in the anhydrite and dolomite aquifer, respectively (See Table 4-6).

Figure 4-13 shows the iso-volume of ^{237}Np at a limit of 1.0×10^{-12} M after 1,000,000 years. The figure shows that the main transport mechanism to the dolomite aquifer is via the DRZ connection with the shafts, with Shaft 3 showing a clear pathway of higher concentration ($>1.0 \times 10^{-9}$ M) solute. Figure 4-14 shows the iso-volume of ^{129}I at a limit of 1.0×10^{-10} M after 1,000,000 years. The higher solubility, lack of sorption, higher instant-release fraction, and longer half-life result in higher concentration of ^{129}I throughout the system as compared to ^{237}Np .

Figure 4-15 plots the concentrations of ^{237}Np and ^{129}I at the bottom, mid-point, and top of each of the shafts. Not surprisingly, the concentration is highest in the bottom of each shaft and then declines towards the top, where concentrations are at background levels. Vertical velocities are fastest in the DRZ around the shafts at approximately 0.0025 m/yr resulting in a cell Peclet number of about 0.17, which indicates a diffusion dominated system. The cell Peclet number is the ratio of the cell velocity and the diffusion coefficient multiplied by the cell dimension in the direction of flow (5 m in the z-direction for vertical flow up the shafts). Numbers less than one are generally considered as diffusion dominant systems. Once solute reaches the dolomite aquifer (immediately above the mid-point elevation of the shafts) the solute is carried down gradient with the regional flow and no longer continues up the shaft, resulting in background levels of radiation in the top of the shafts. The regional pressure gradient creates an east to west velocity of about 0.08 m/yr resulting in a cell Peclet number of 16.5 (cell dimension of 15 m in the x-direction), which indicates an advection dominated system. This can also be seen in Figure 4-13 and Figure 4-14.

Figure 4-16 shows a plan view of the concentration of ^{237}Np in the dolomite aquifer at 10,000, 100,000, and 1,000,000 years. At 10,000 years, the aquifer has experienced inflow from the shafts and the down-gradient transport is clear. The 100,000-year case shows a large ‘hot spot’ around shaft 3, which begins to consolidate by 1,000,000 years.

Figure 4-17 shows the concentration of ^{129}I in the dolomite aquifer at 10,000, 100,000, and 1,000,000 years. At 10,000 years, the plume down-gradient from shaft 3 is narrow and of high concentration ($\sim 3.0 \times 10^{-6} \text{ M}$ – the figure truncates concentrations at 10^{-8} M for clarity). After 100,000 years, the plume is diffusing so where the maximum concentration down-gradient of shaft 3 is about 1 order magnitude less. By 1,000,000 years, diffusion has reduced the maximum concentration another 4 orders of magnitude (to 7.5×10^{-11}) where the plume has spread throughout the aquifer.

The same dynamics of higher concentrations and higher rates of diffusion for ^{129}I as compared to ^{237}Np can be seen in Figure 4-18 and Figure 4-19 which show the radionuclide concentrations in the upper anhydrite layer (the lower anhydrite layer is not shown but is almost identical to the upper). The transport mechanism is diffusion through the backfill and DRZ. As in the dolomite aquifer, concentrations of ^{129}I are approximately 5 orders of magnitude higher than ^{237}Np , mainly due to the solubility limit of ^{237}Np and the 0.10 instant release fraction for ^{129}I . Low concentration spots in the interior of the repository at 10,000 years correspond to waste packages that have not yet been breached.

Figure 4-20 and Figure 4-21 show the ^{237}Np and ^{129}I concentration values at 10,000, 100,000, and 1,000,000 years on a vertical slice that passes through shafts 2 and 3. This slice is slightly angled since shafts 2 and 3 are one grid cell offset from each other in the x-direction. It should also be noted that the slice does not intersect the repository but rather passes just east of the repository, which is why high concentration drift and waste package areas cannot be seen. In both the 10,000-year plots, there appears to be transport through the anhydrite layers to the shafts. In the later time plots, diffusion into the surrounding DRZ zone can be seen as can some transport to the sediment layer. The highest concentrations in the dolomite aquifer occur in the shaft and DRZ material that passes through the aquifer. This implies that water pumped from a hypothetical nearby well would have a much lower concentration due to converging flows from all directions to the well that dilute the radionuclide concentrations slowly entering the aquifer from the shaft/DRZ material via diffusion-limited mass transfer.

Figure 4-13. ^{237}Np concentration iso-volume at a limit of 1.0×10^{-12} M after 1,000,000 years for the deterministic simulation. The pathway up the shafts is clearly evident as is the transport along the dolomite aquifer from Shaft 3. Note the scale difference from Figure 4-14. The "gold band" is the elevation of the dolomite aquifer.

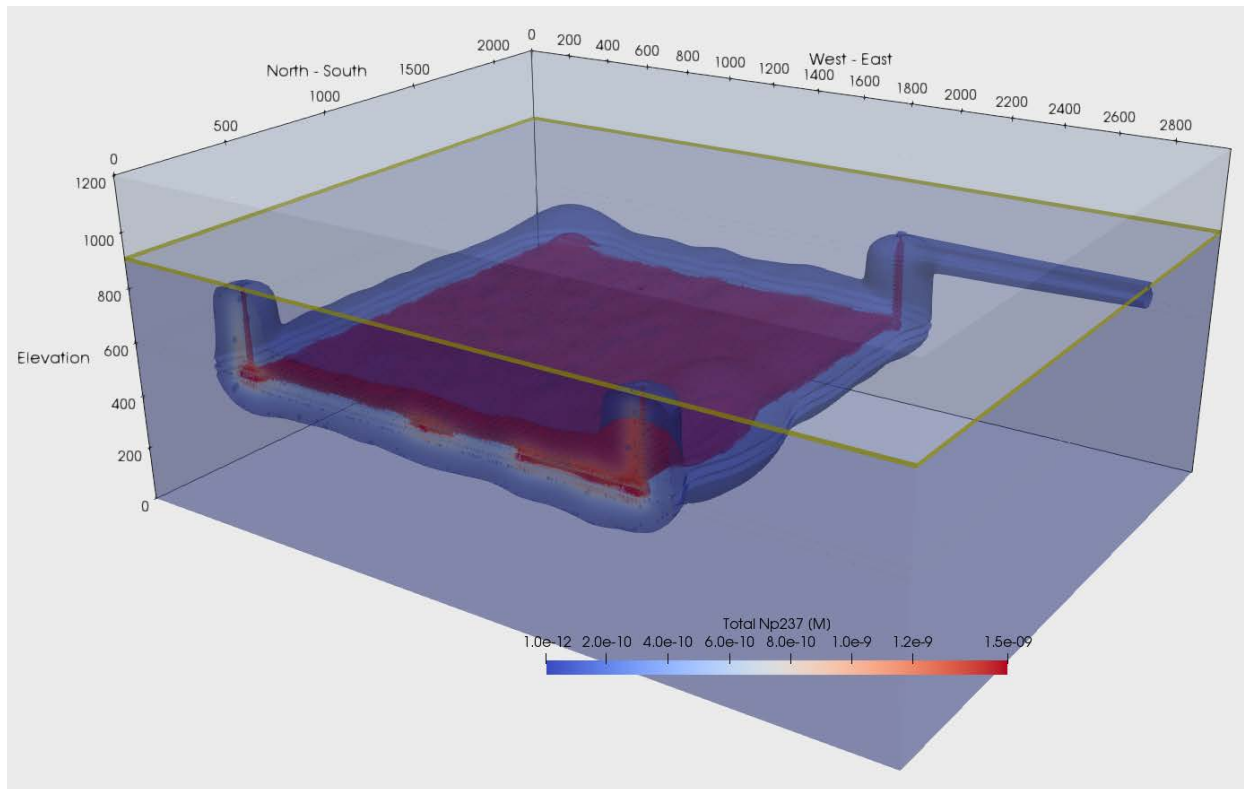


Figure 4-14. ^{129}I concentration iso-volume at a limit of 1.0×10^{-10} M after 1,000,000 years for the deterministic simulation. The pathway up the shafts is clearly evident, as is the transport along the dolomite aquifer from Shafts 2 and 3 although the column of high concentration solute has diffused out as compared to ^{237}Np . Note the scale difference from Figure 4-13. The "gold band" is the elevation of the dolomite aquifer.

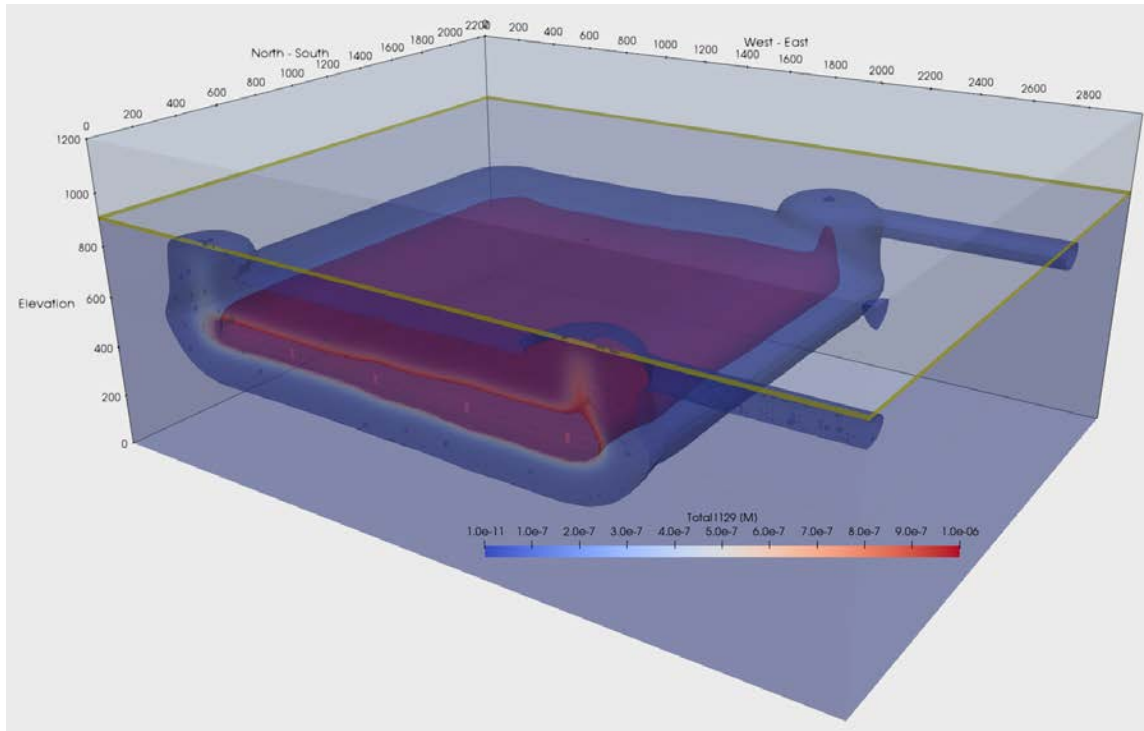


Figure 4-15. Concentration of ^{237}Np (left) and ^{129}I (right) at the bottom, mid-point, and top of each shaft for the deterministic simulation.

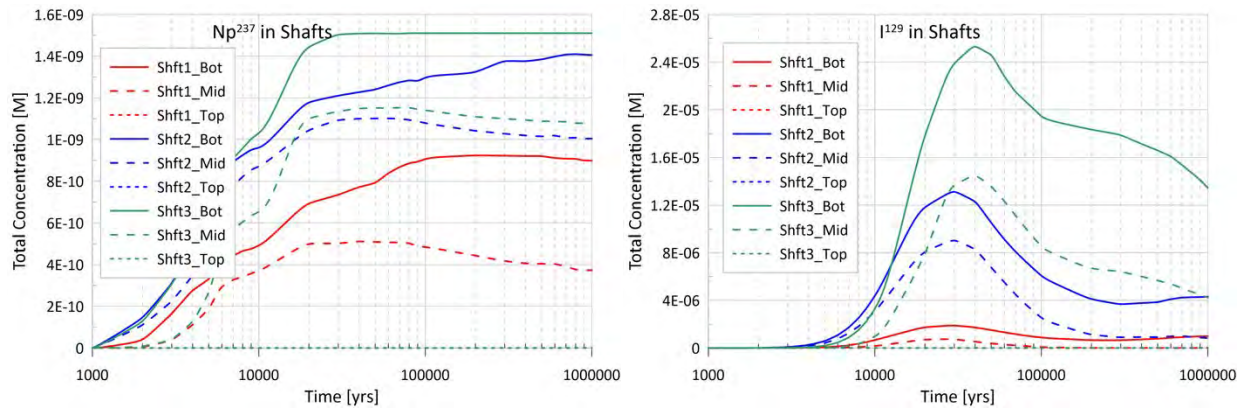


Figure 4-16. ^{237}Np concentrations in a horizontal slice through the center of the dolomite aquifer after 10,000, 100,000, and 1,000,000 years for the deterministic simulation. Units are \log_{10} molar concentration values.

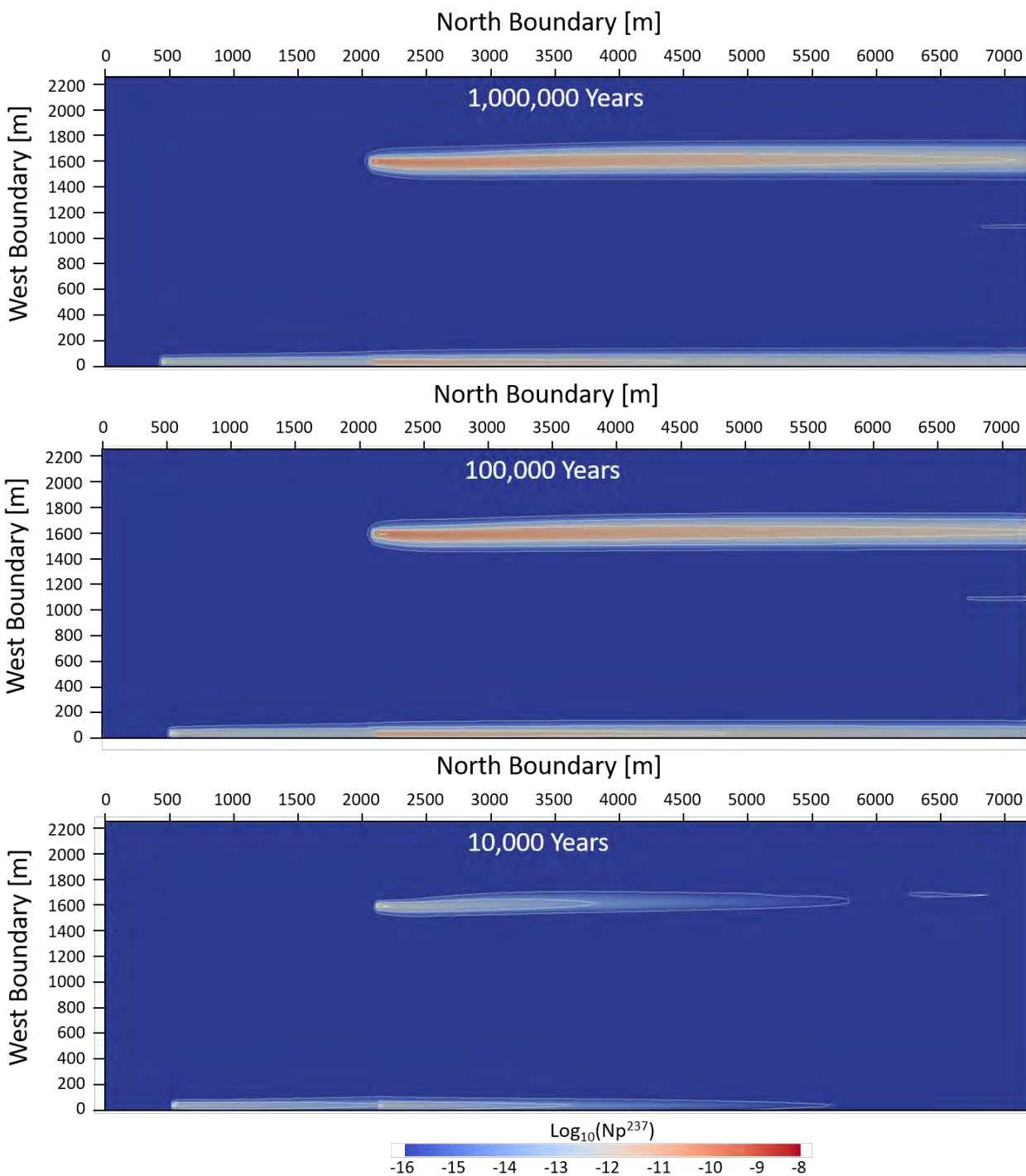


Figure 4-17. ^{129}I concentrations in a horizontal slice through the center of the dolomite aquifer after 10,000, 100,000, and 1,000,000 years for the deterministic simulation. Units are \log_{10} molar concentration values.

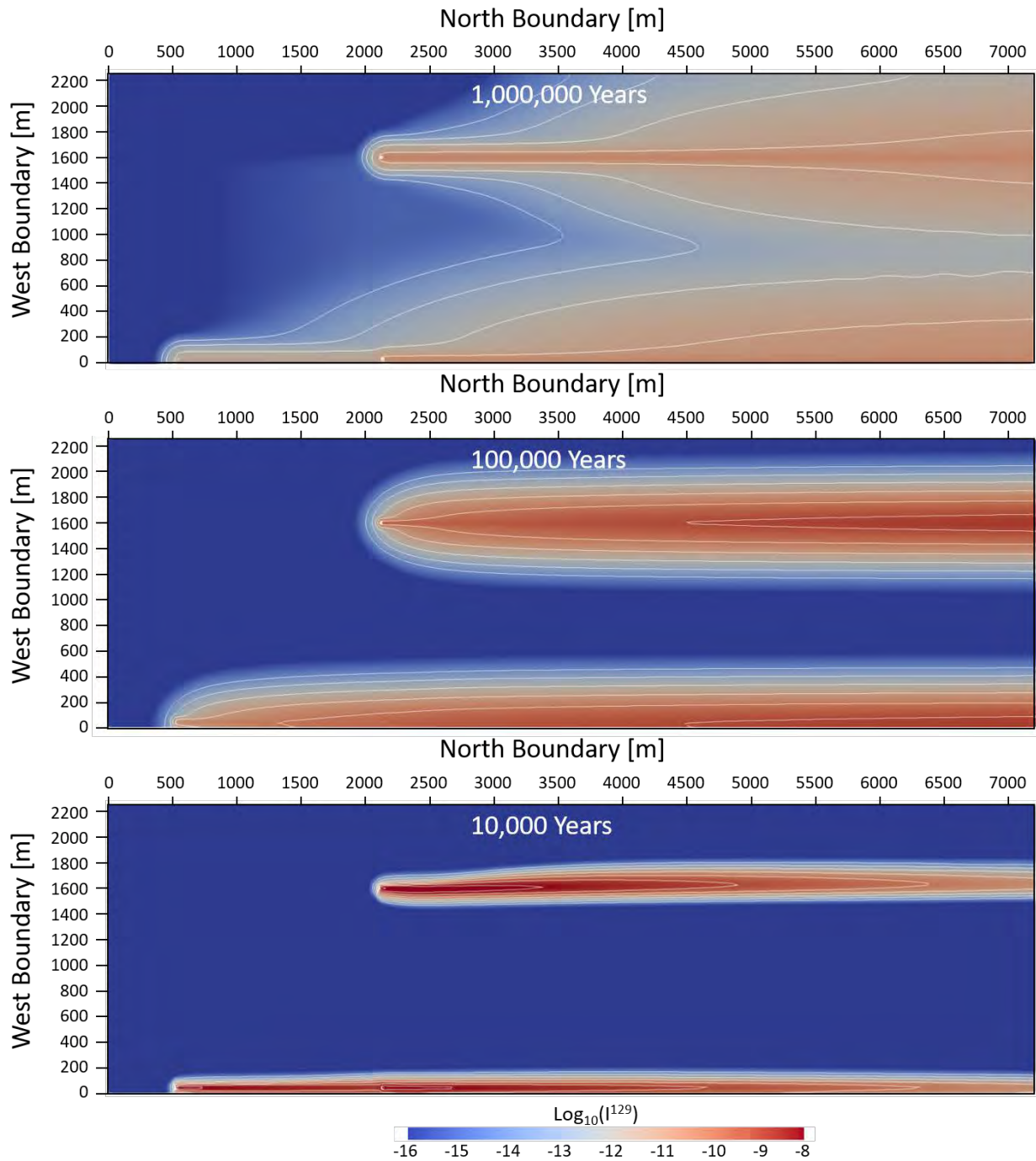


Figure 4-18. ^{237}Np concentrations in a horizontal slice through the center of the upper anhydrite layer after 10,000, 100,000, and 1,000,000 years for the deterministic simulation. Units are \log_{10} molar concentration values. Maximum concentrations are slightly higher than the plotted limit.

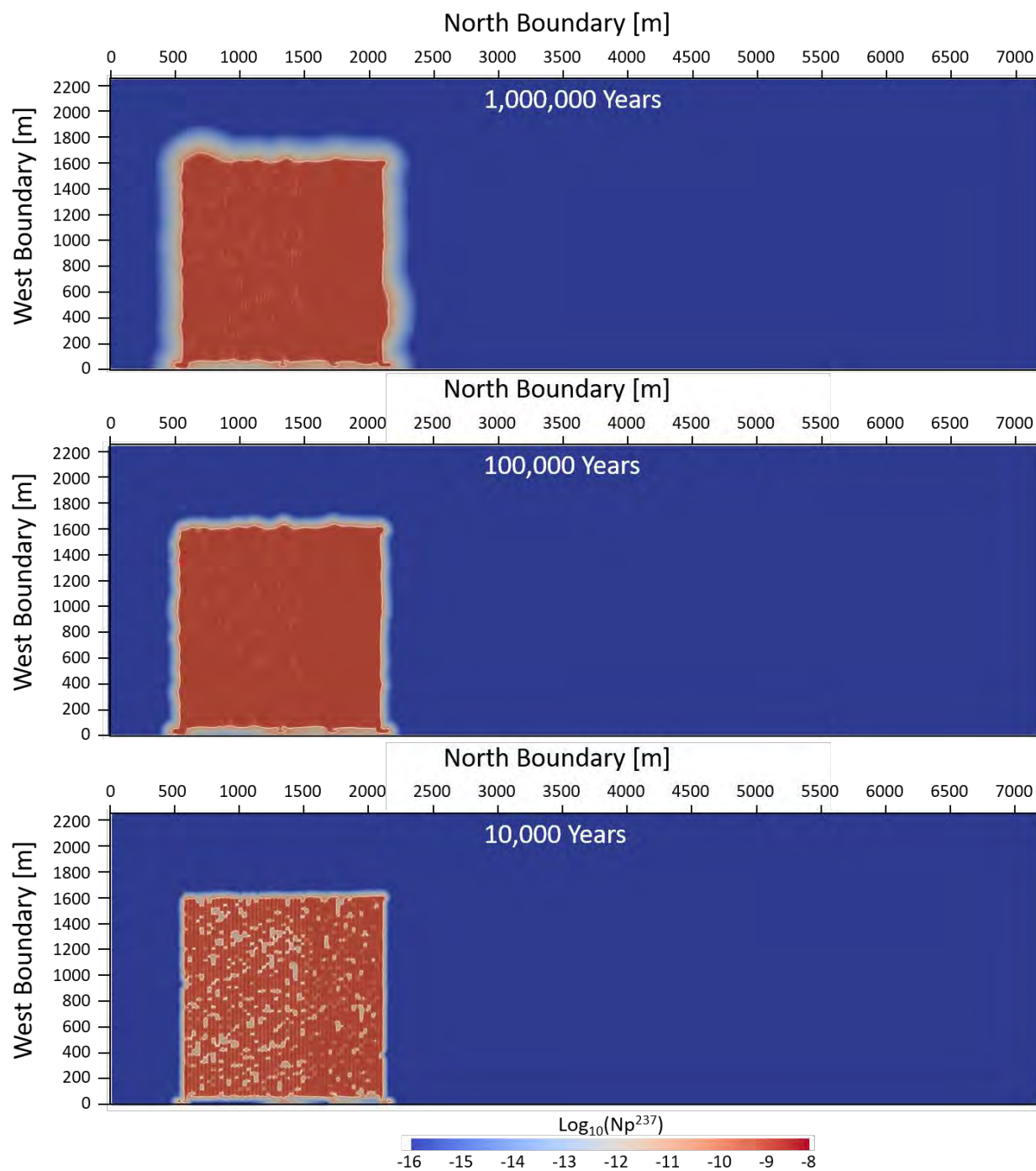


Figure 4-19. ^{129}I concentrations in a horizontal slice through the center of the upper anhydrite layer after 10,000, 100,000, and 1,000,000 years for the deterministic simulation. Units are \log_{10} molar concentration values.

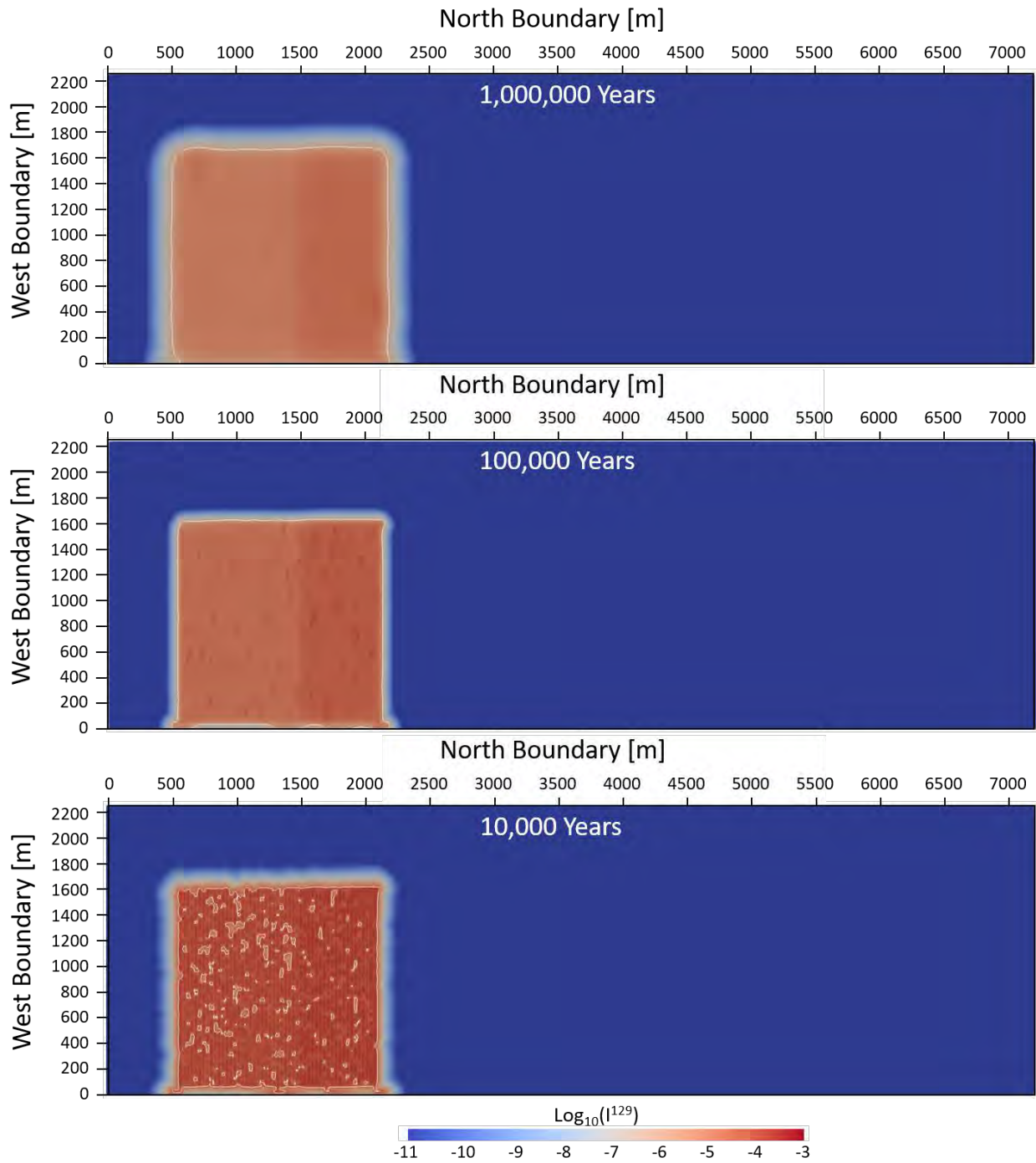


Figure 4-20. ^{237}Np concentrations on a vertical slice through shafts 2 (left) and 3 (right) at 10,000, 100,000, and 1,000,000 years for the deterministic simulation.

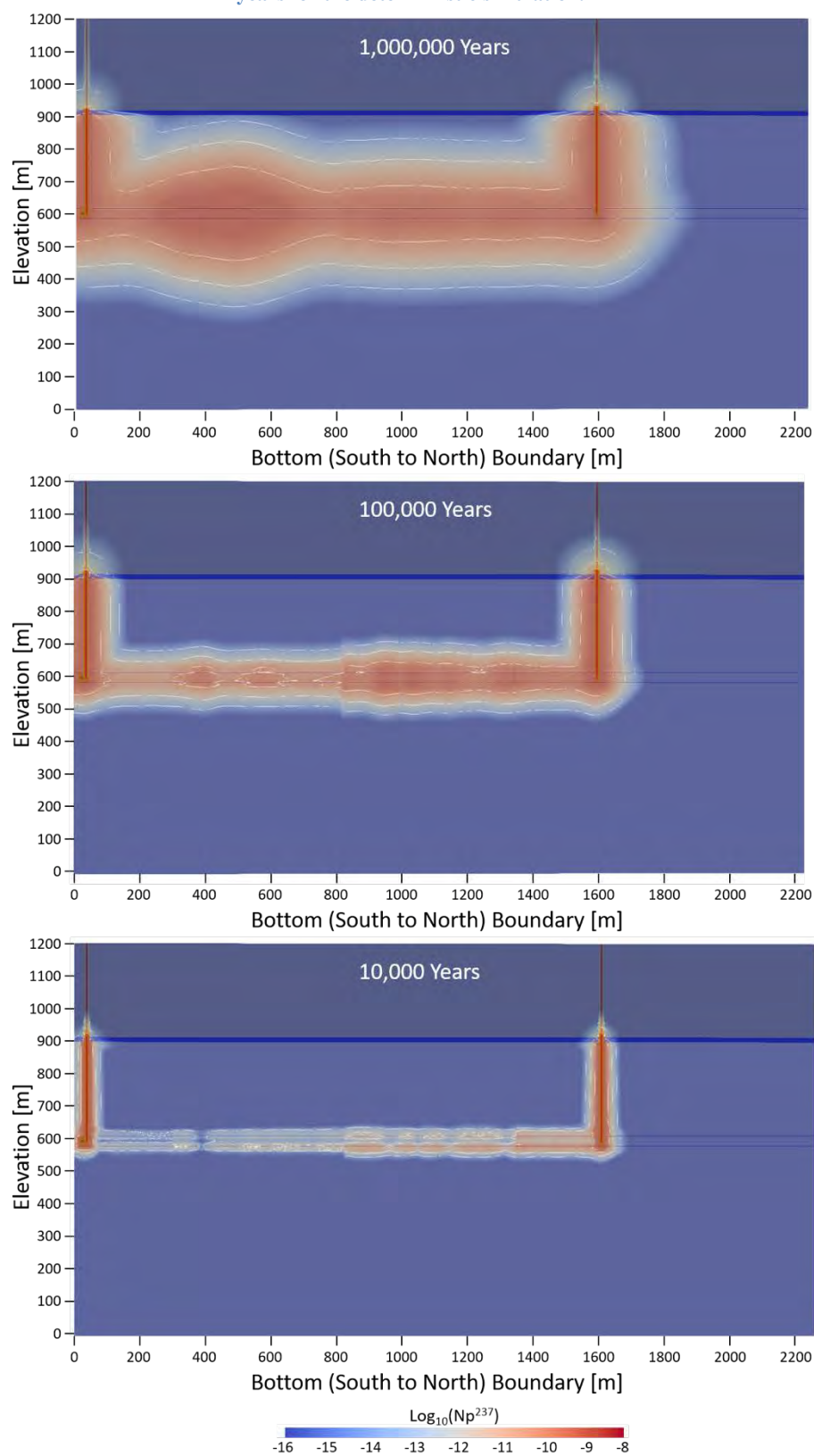
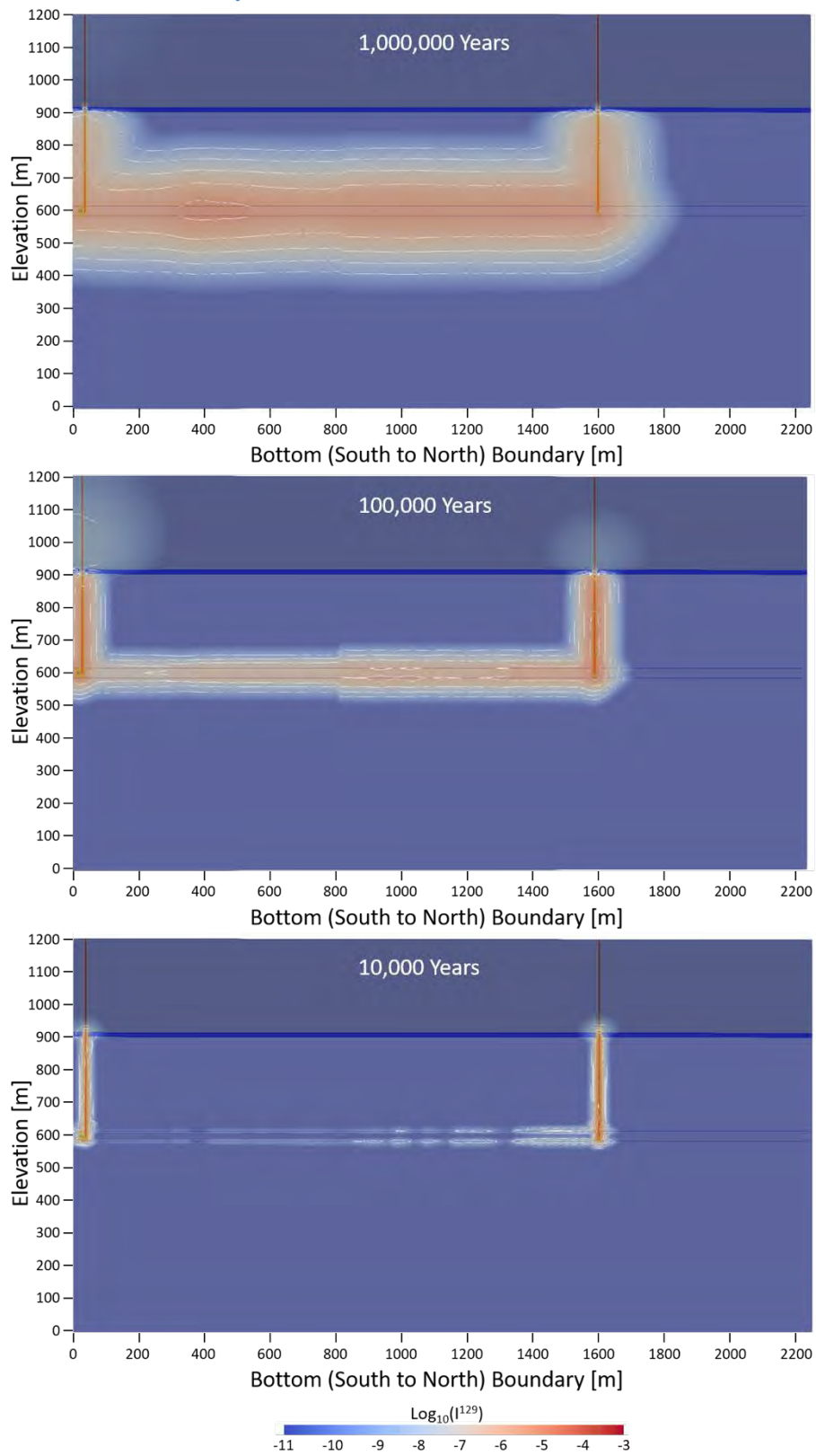


Figure 4-21. ^{129}I concentrations on a vertical slice through shafts 2 (left) and 3 (right) at 10,000, 100,000, and 1,000,000 years for the deterministic simulation.



4.6 Probabilistic Assessment

As discussed above, 200 probabilistic simulations are conducted using Latin hypercube sampling (LHS) via the Design Analysis Toolkit for Optimization and Terrascale Analysis (DAKOTA) software (dakota.sandia.gov). The LHS process samples seven uncertain parameters using the distributions and parameterizations listed in Table 4-8.

The PA analysis is presented by focusing on several key observation points that highlight the correlations between variable values and results and potential interactions between the input variables. The observation points are the dolomite aquifer immediately east of the repository (Dolomite_Repo), the dolomite aquifer at the end of the model domain (Dolomite_End), the top anhydrite layer immediately east of the repository (An1_Repo), the mid-point of shaft 3 (Shft3_Mid), and two points in the DRZ in the center of the block of 24-PWRs (DRZ_16_25) and of the 37-PWRs (DRZ_41_25). See Figure 4-7 for location of all monitoring points.

The output metrics are the ^{129}I and ^{237}Np molar concentrations over time at each observation point, which enables the examination of: 1) variability, 2) sensitivities and correlations, and 3) variable interactions, all with respect to each of the sampled variables. The distributions for the sampled variables are listed in Table 4-8.

4.6.1 Anhydrite East of the Repository

Figure 4-22 shows plots of the ^{129}I molar concentrations over time at the upper anhydrite repository observation point (An1_Repo) colorized by the peak concentration, anhydrite permeability, DRZ permeability, dolomite porosity, backfill permeability, and mean waste package degradation rate at that point over the simulation period. This type of plot is known as a “horsetail” plot. These types of plots are useful for visualizing repository performance over time and the timing of plume migration. The parameters used to color the realizations were normalized by the maximum value over all realizations using

$$C_{P_i} = \frac{C_{max_i}}{C_{max_{all}}} \quad (4.1)$$

where C_{P_i} is the normalized peak concentration for run “i”, C_{max_i} is the maximum (peak) concentration for run “i”, and $C_{max_{all}}$ is the maximum (peak) concentration across all runs.

Peak ^{129}I concentrations show a positive correlation with the anhydrite permeability (upper right) and a negative correlation with the DRZ permeability (middle left), although the correlation with the DRZ permeability is not as strong. Counterintuitively, there is also a negative correlation with the mean waste package decay parameter (vitMean in the lower right). It is unclear why this is the case and requires further study. Further simulations with runtimes greater than 1 million years would be needed to determine this for certain. These trends also show up in the scatter plots of the peak ^{129}I concentrations versus the sampled variable values (Figure 4-23).

Figure 4-24 and Figure 4-25 are the horsetail and scatter plots, respectively for ^{237}Np concentrations. The same dynamic can be seen with the ^{237}Np however the correlations are not as strong. This is due to the large K_d values of ^{237}Np in the anhydrite (1.35×10^4) that slows down the migration of the plume, especially dispersive migration where concentrations are low.

Figure 4-22. Plots of ^{129}I molar concentrations at the An1_Repo observation point colored by peak concentration (upper left), anhydrite permeability (upper right), DRZ permeability (middle left), dolomite porosity (middle right), backfill permeability (lower left), and mean degradation rate (lower right).

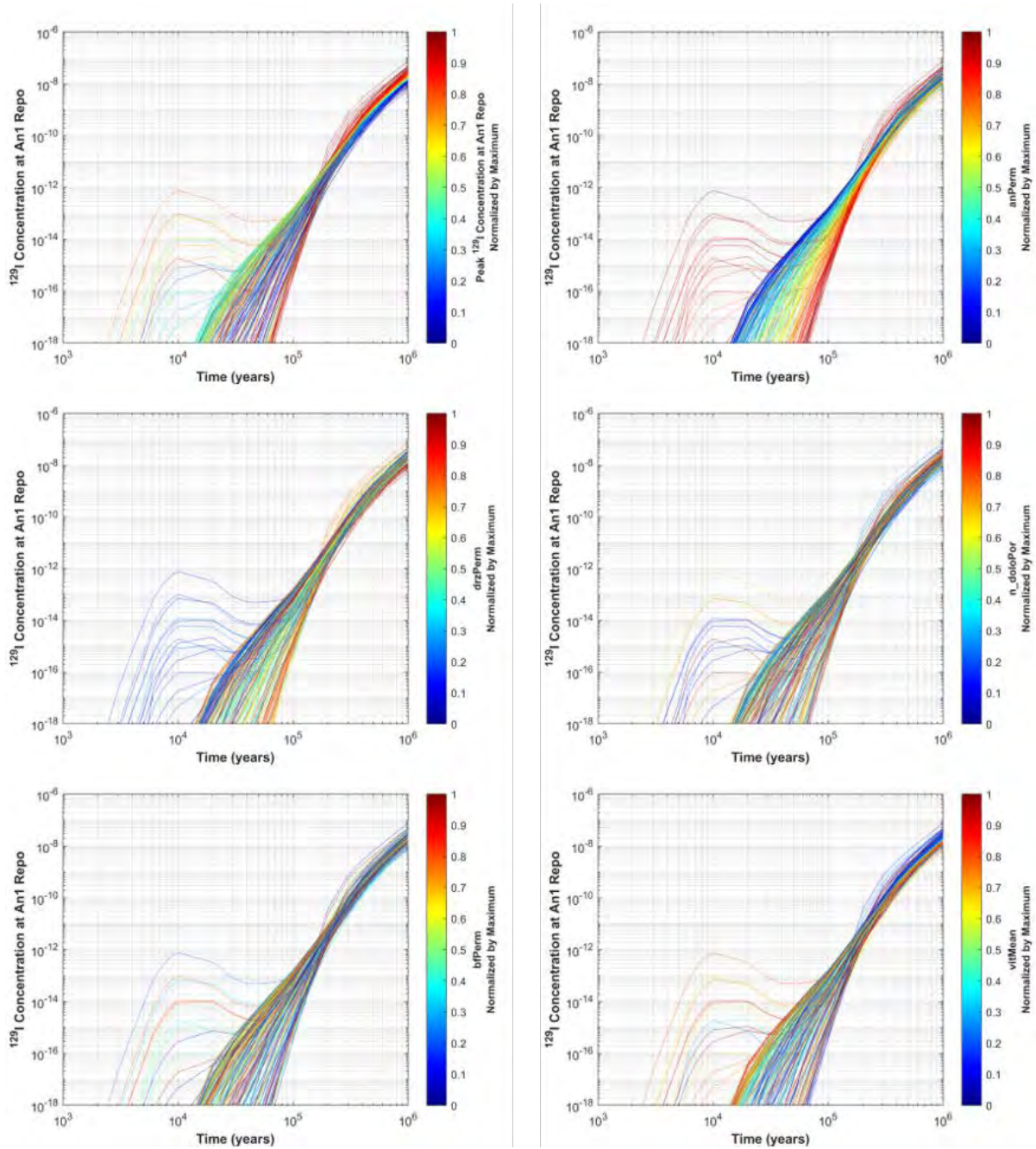


Figure 4-23. Scatter plot of the maximum (peak) ^{129}I molar concentration at the An1_Repo observation point versus values of the sampled variables.

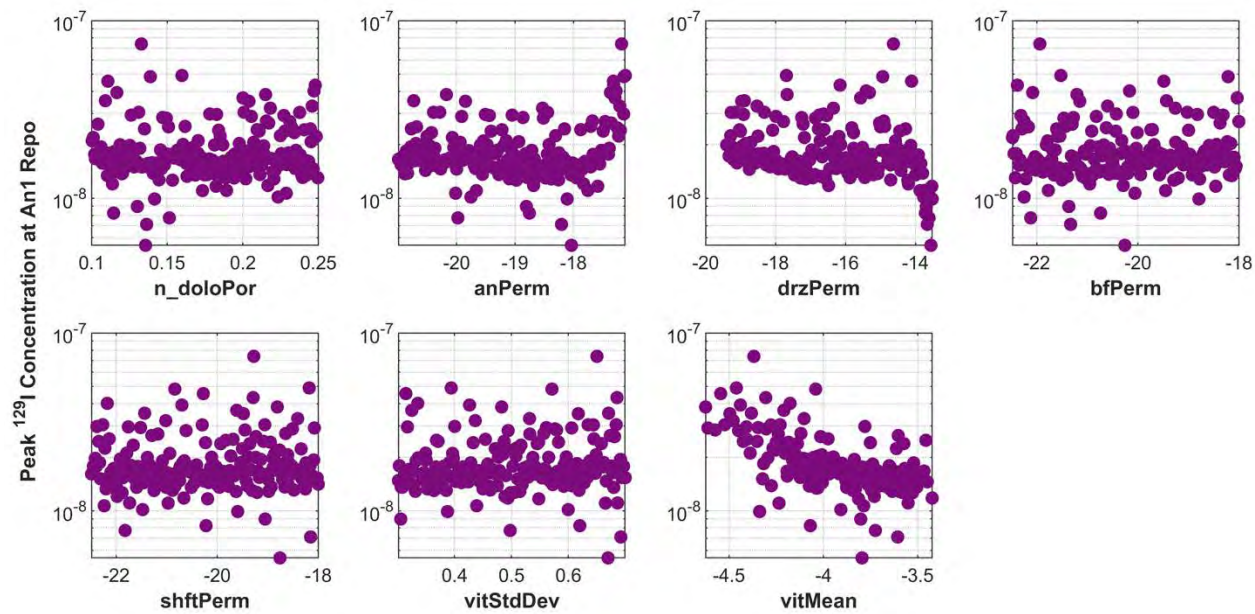


Figure 4-24. Plots of ^{237}Np molar concentrations at the An1_Repo observation point colored by peak concentration (upper left), anhydrite permeability (upper right), DRZ permeability (middle left), dolomite porosity (middle right), backfill permeability (lower left), and mean degradation rate (lower right).

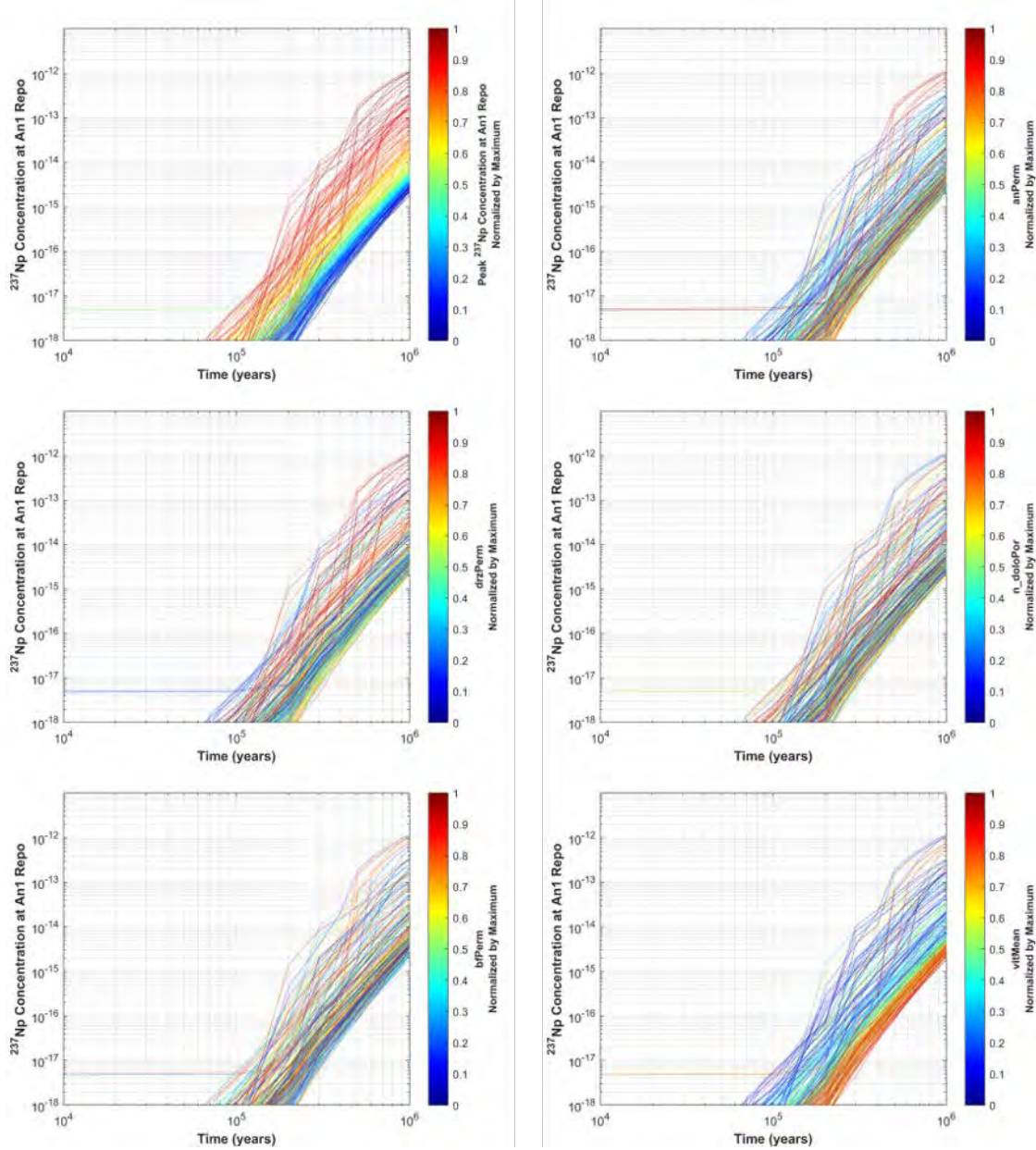
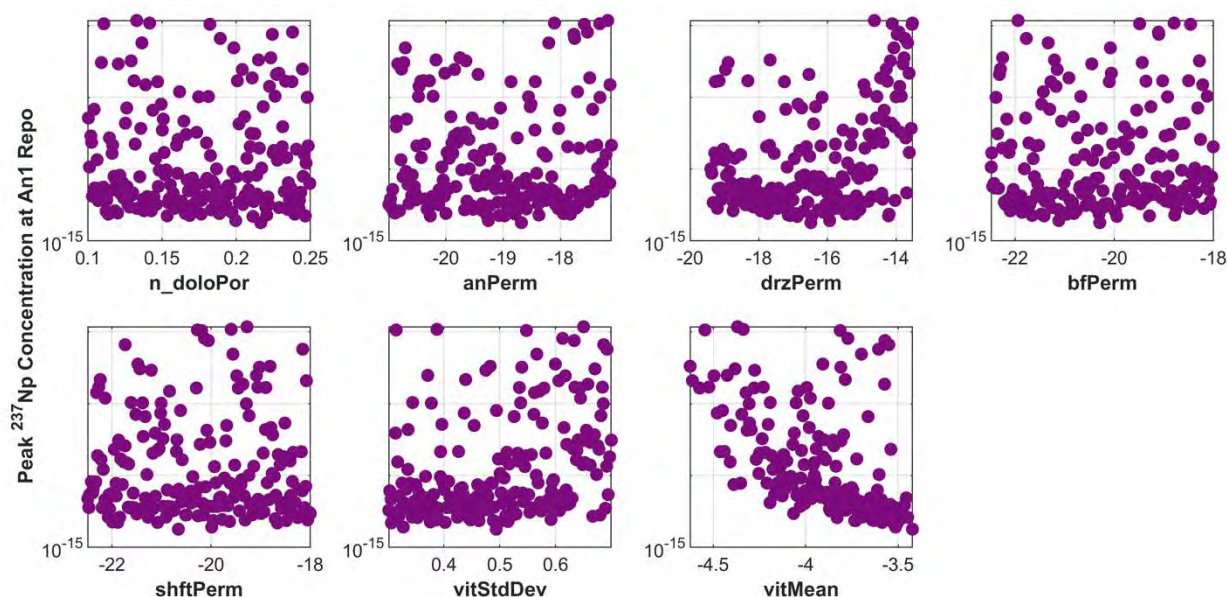


Figure 4-25. Scatter plot of the maximum (peak) ^{237}Np molar concentration at the An1_Repo observation point versus values of the sampled variables.



4.6.2 Dolomite East of the Repository

The dolomite aquifer near the repository shows similar behavior to the anhydrite but the mechanisms and processes are different. Figure 4-26 shows plots of the ^{129}I molar concentrations over time at the dolomite repository observation point (Dolomite_Repo) colorized by peak concentration, anhydrite permeability, DRZ permeability, dolomite porosity, ShaftFill permeability, and mean degradation rate. There is a peak in about 10% of the simulations at 20,000 years (upper left) that can be seen to be correlated with lower values of dolomite porosity (and by function, dolomite permeability – middle right). When the porosity/permeability is low, the advective velocity is slow, allowing dispersion of the plume versus channelizing and advecting down-gradient. This is illustrated in Figure 4-28 which compares the ^{129}I concentration in the dolomite from Run #71, which has the highest concentration at the Dolomite_Repo observation point and a cell Peclet number of 0.4 (diffusion dominated), to Run #92, which has the lowest concentration and a cell Peclet number of 80.6 (advection dominated). The concentrations in the shafts at the aquifer elevation are similar between the two simulations ($\sim 1 \times 10^{-6}$) as are the concentrations in the cells immediately down gradient from the shafts in the dolomite ($\sim 4 \times 10^{-8}$). The porosity/permeability in the dolomite aquifer for Run #71 is $0.1012 / 9.56 \times 10^{-15} \text{ m}^2$ and for Run #92 it is $0.2346 / 7.23 \times 10^{-13} \text{ m}^2$. There is also a weaker relationship with the mean waste package decay parameter (lower right).

Similar to the dynamics at the An1_Repo observation point, ^{237}Np transport mimics that of ^{129}I at the Dolomite_Repo observation point, although the effect is diminished due to the high K_d value of ^{237}Np in the dolomite aquifer (2.44×10^5). The horsetail and scatter plots for ^{237}Np at Dolomite_Repo are shown in Figure 4-29 and Figure 4-30, respectively. The diminished correlation with the dolomite porosity/permeability is evident in Figure 4-30 (upper left plot).

Figure 4-26. Plots of ^{129}I molar concentrations at the Dolomite Repo observation point colored by peak concentration (upper left), anhydrite permeability (upper right), DRZ permeability (middle left), dolomite porosity (middle right), ShaftFill permeability (lower left), and mean degradation rate (lower right).

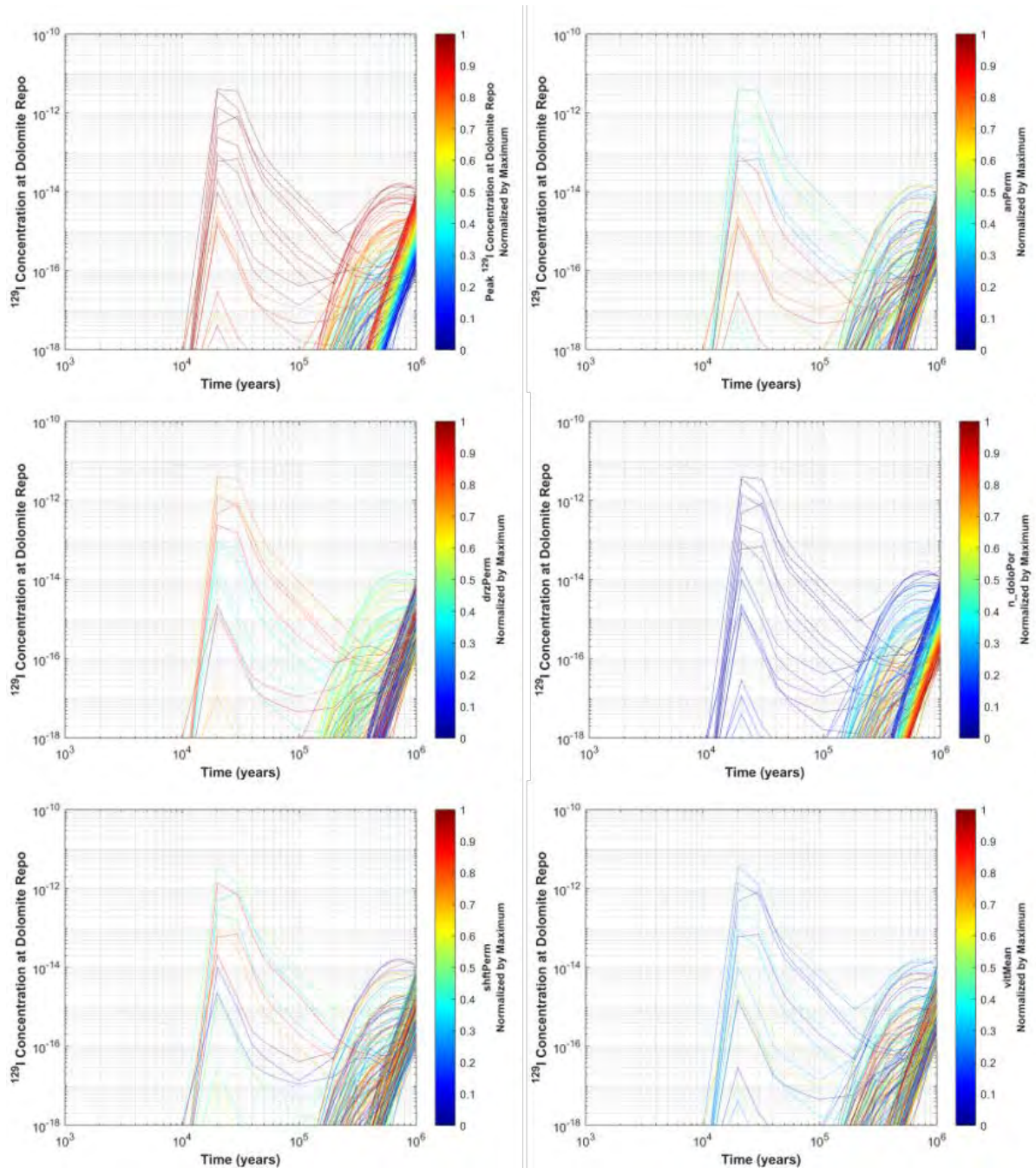


Figure 4-27. Scatter plot of the maximum (peak) ^{129}I molar concentration at the Dolomite_Repo observation point versus values of the sampled variables.

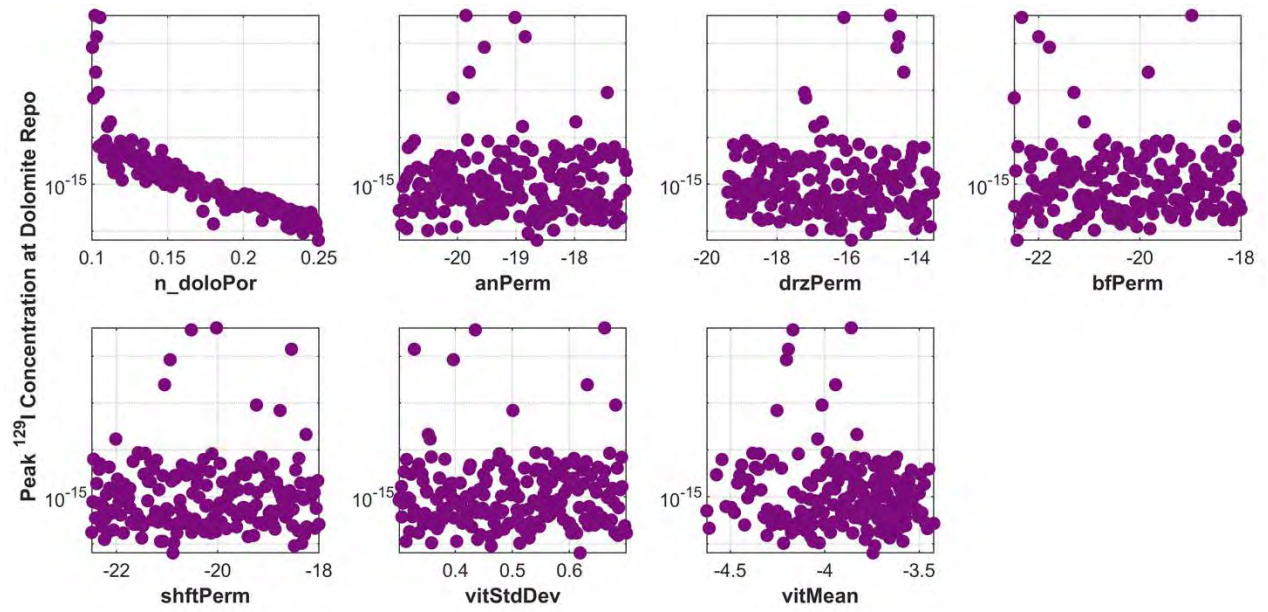


Figure 4-28. Planview comparison of Run #71 and Run #92, which have the highest and lowest ^{129}I concentration at the Dolomite_Repo observation point (marked by red dot) respectively after 1,000,000 years. The blue dot indicates the location of the Dolomite_End observation point. The actual maximums are slightly higher than the plotted maximum.

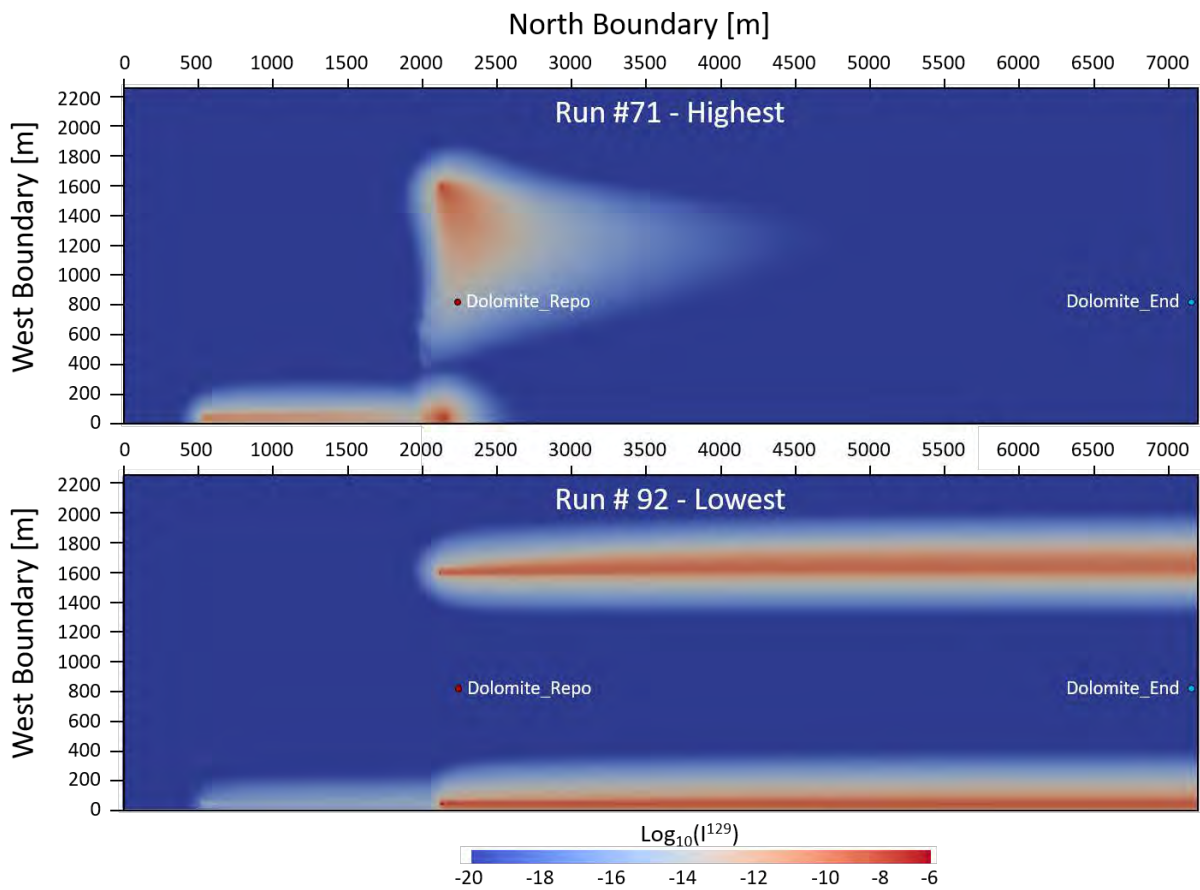


Figure 4-29. Plots of ^{237}Np molar concentrations at the Dolomite_Repo observation point colorized by peak concentration (upper left), anhydrite permeability (upper right), DRZ permeability (middle left), dolomite porosity (middle right), ShaftFill permeability (lower left), and mean degradation rate (lower right).

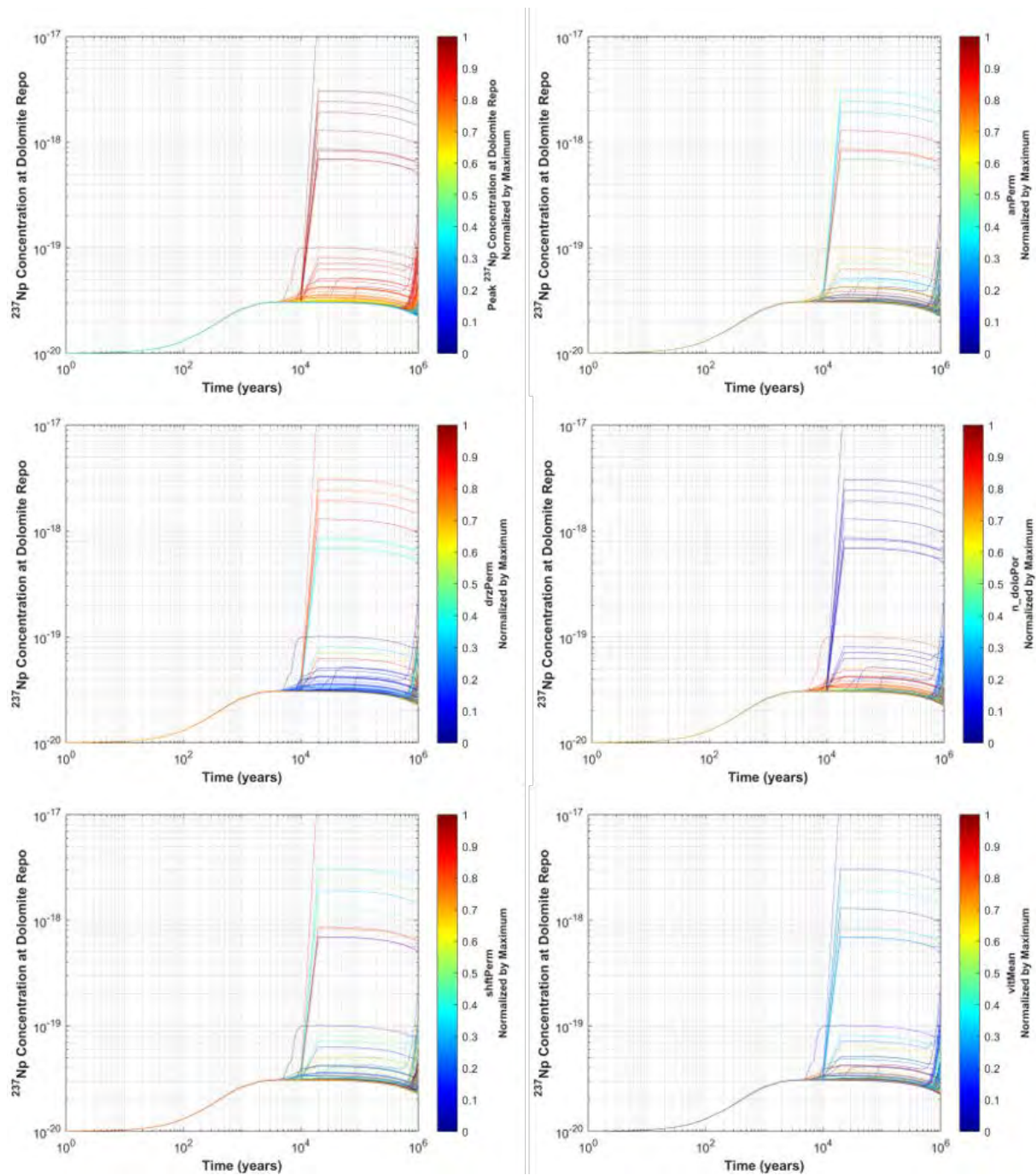
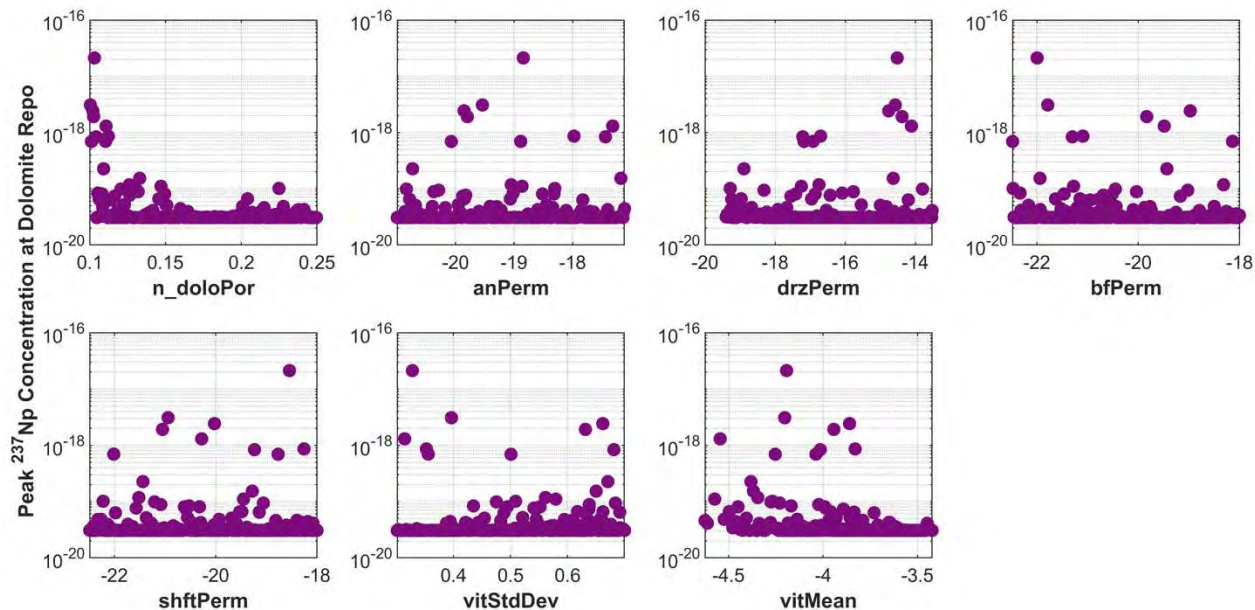


Figure 4-30. Scatter plot of the maximum ^{237}Np molar concentration at the Dolomite_Repo observation point versus values of the sampled variables.



4.6.3 Dolomite End

The Dolomite_End observation point is located in the dolomite aquifer downgradient from the center line of the simulated drifts at the eastern boundary of the model domain (Figure 4-28). The horsetail plots for ^{129}I (Figure 4-31) show a negative correlation with the dolomite porosity/permeability and a positive correlation with the DRZ permeability. These relationships also show up in the scatter plots (Figure 4-32). The reason for the negative correlation with porosity/permeability is the same as that for the Dolomite_Repo observation point where lower advective flow reduces channelization and allows for dispersive transport to the observation point. If the observation points were directly down-gradient of the shafts, the trend would be the opposite. There also seems to be a weak positive correlation with the timing of the plume to DRZ permeability where higher values of permeability result in an earlier arrival time (Figure 4-31, middle left plot).

For ^{237}Np , there is a strong correlation between the peak concentration and the dolomite porosity/permeability in the horsetail plots, which indicates a correlation with the timing of the plume (Figure 4-33), but no real correlation in the maximum concentration shown in the scatter plots (Figure 4-34). The DRZ permeability correlation with the timing of the plume is negative (Figure 4-33, middle left plot) where higher values of permeability result in a later arrival of the plume.

Figure 4-31. Plots of ^{129}I molar concentrations at the Dolomite_End observation point colored by peak concentration (upper left), anhydrite permeability (upper right), DRZ permeability (middle left), dolomite porosity (middle right), ShaftFill permeability (lower left), and mean degradation rate (lower right).

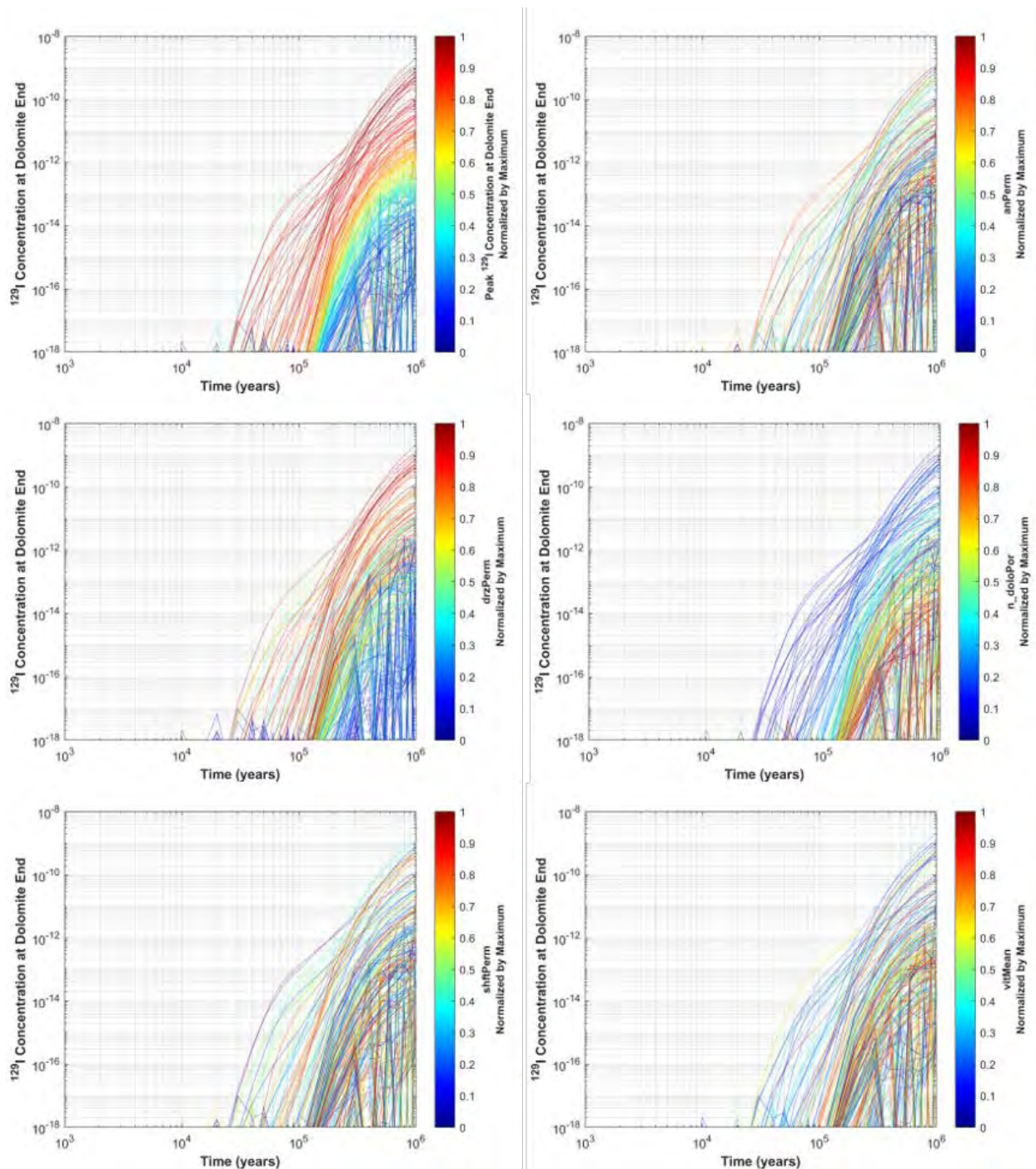


Figure 4-32. Scatter plot of the maximum ^{129}I molar concentration at the Dolomite_End observation point versus values of the sampled variables.

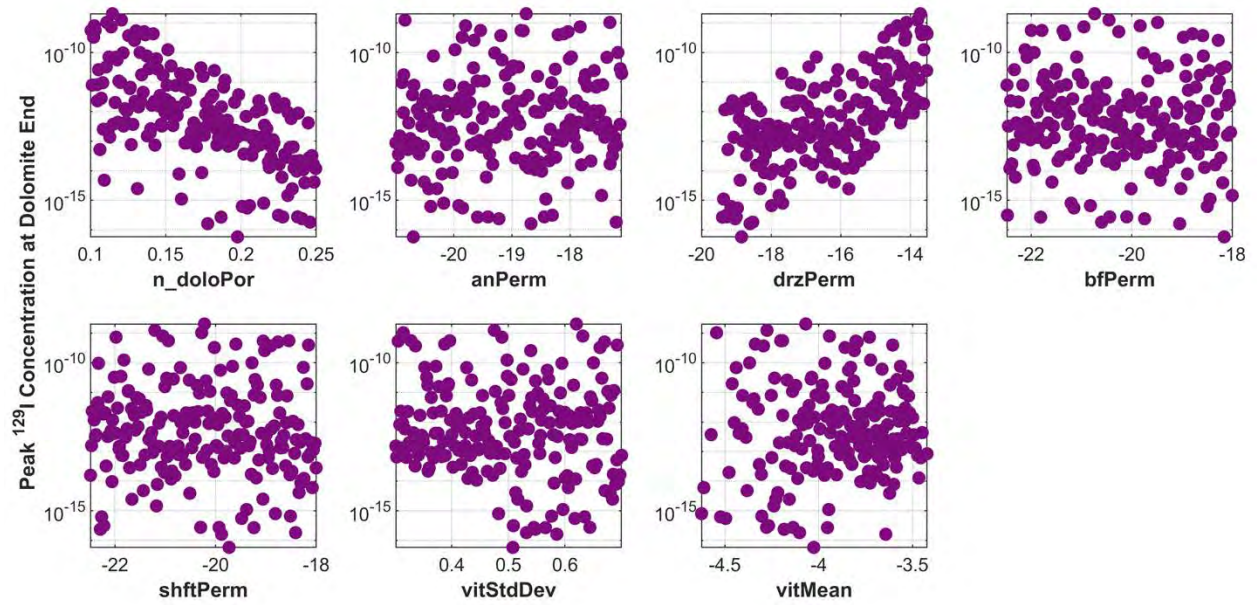


Figure 4-33. Plots of ^{237}Np molar concentrations at the Dolomite_End observation point colored by peak concentration (upper left), anhydrite permeability (upper right), DRZ permeability (middle left), dolomite porosity (middle right), ShaftFill permeability (lower left), and mean degradation rate (lower right).

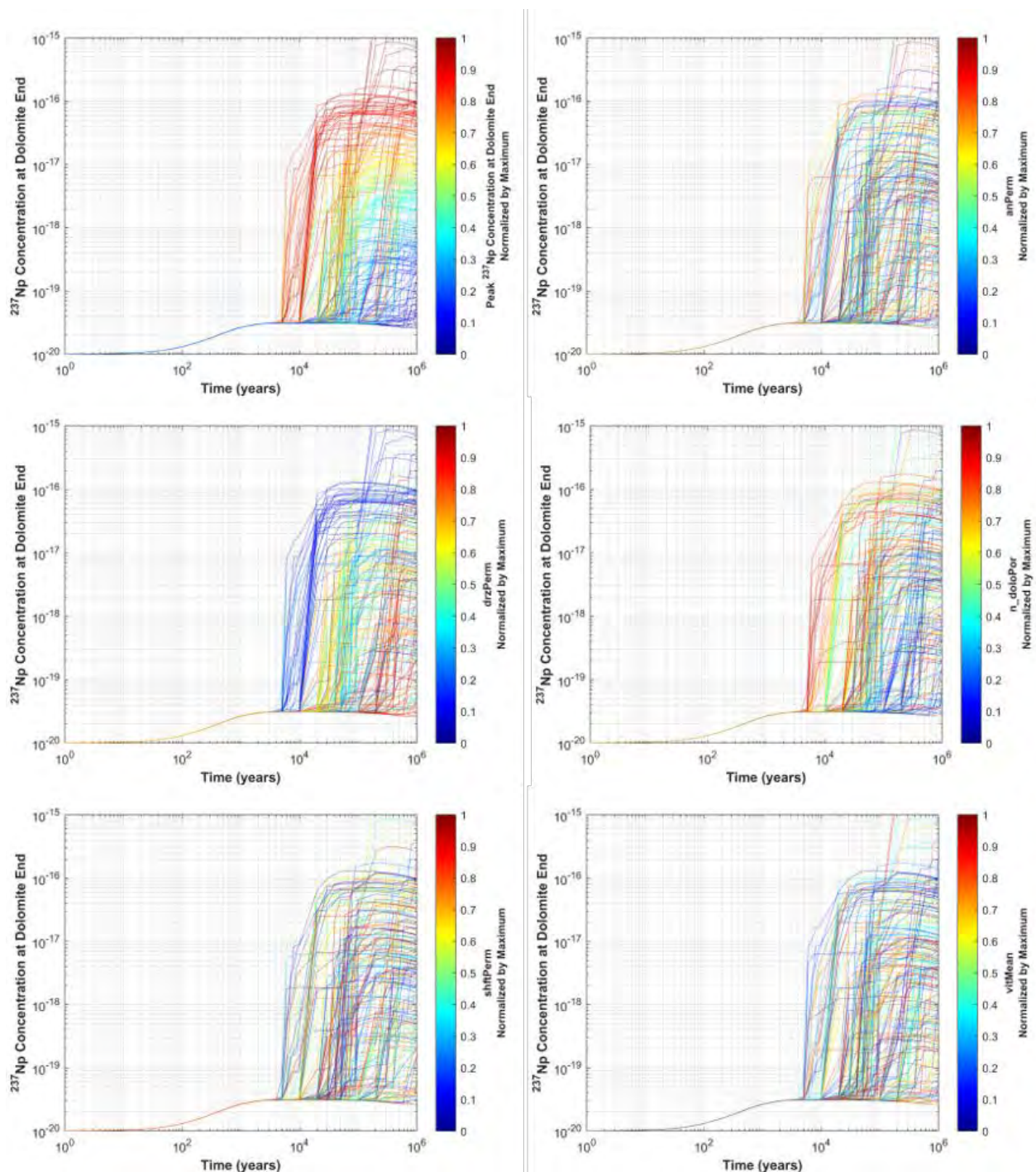
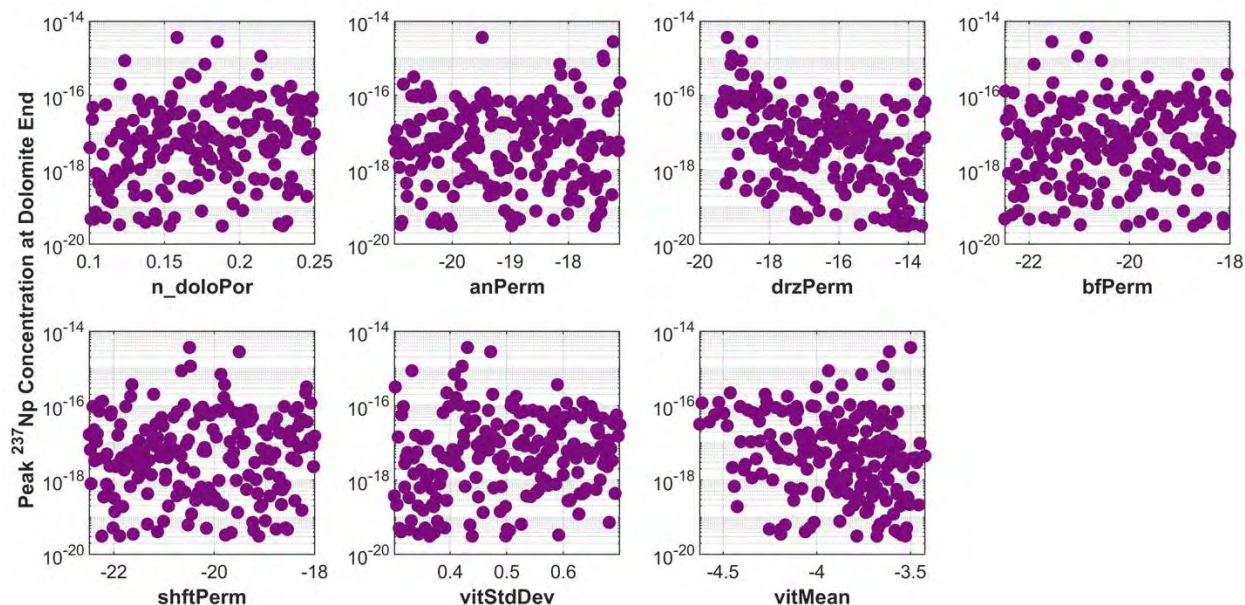


Figure 4-34. Scatter plot of the maximum (peak) ^{237}Np molar concentration at the Dolomite_End observation point versus values of the sampled variables.



4.6.4 DRZ_16_25 & DRZ_41_25

The DRZ_16_25 and DRZ_41_25 observation points are located on the downgradient side (to the east) from the 25th waste packages in drifts 16 and 41, respectively, placing the points in the center of each waste type block (Figure 4-7). Figure 4-35 and Figure 4-37 show the horsetail plots and Figure 4-36 and Figure 4-38 show the scatter plots of ^{129}I concentrations for the two observation points. In both cases, there is a negative correlation between the waste package degradation rate (vitMean) and the timing and magnitude of peak concentrations with higher values of vitMean resulting in earlier arrivals and slightly lower peak concentrations. It is unclear why this is the case and requires further study. The correlation with vitMean is more pronounced with the 37-PWRs (DRZ_41_25) than with the 24-PWRs (DRZ_16_25).

For ^{237}Np (Figure 4-39 and Figure 4-40), there is also a relationship between the waste package degradation rate, vitMean, and the arrival time of the plume to the observation point. However, the scatter plots (not shown) show no sensitivity of the peak concentration to any of the variables since the peak tops out at 1.51×10^{-9} M for all simulations based on the solubility limit of ^{237}Np .

Figure 4-35. Plots of ^{129}I molar concentrations at the DRZ_16_25 observation point colorized by peak concentration (upper left), anhydrite permeability (upper right), DRZ permeability (middle left), backfill permeability (middle right), ShaftFill permeability (lower left) and mean degradation rate (lower right).

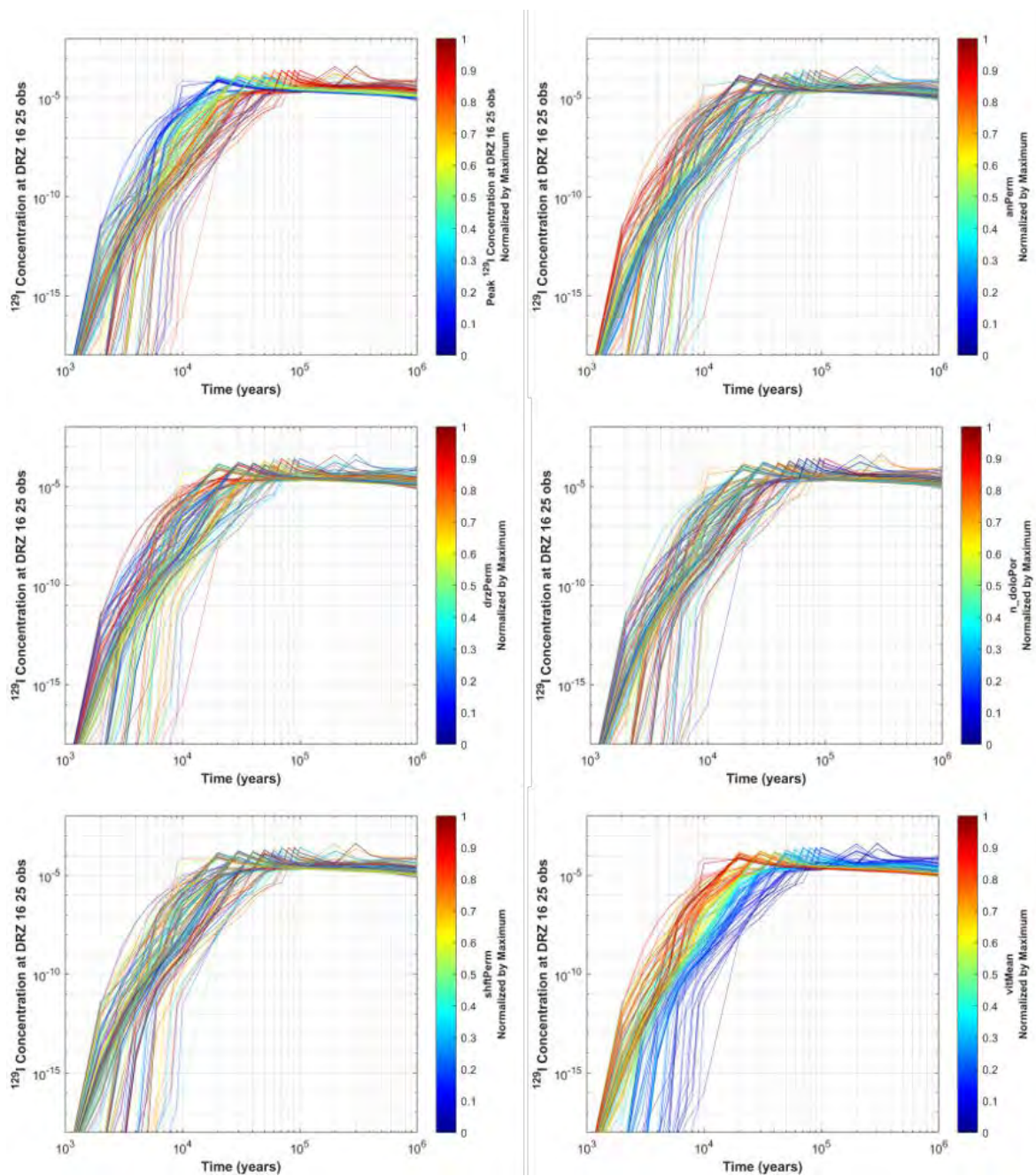


Figure 4-36. Scatter plot of the maximum ^{129}I molar concentration at the DRZ_16_25 observation point versus values of the sampled variables.

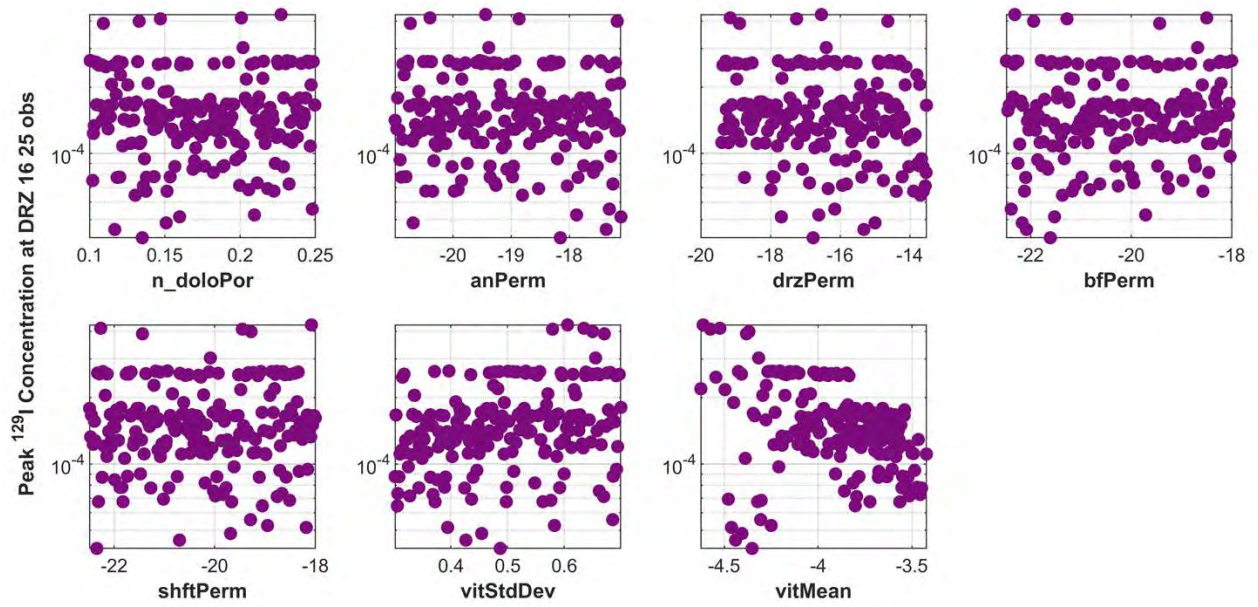


Figure 4-37. Plots of ^{129}I molar concentrations at the DRZ_41_25 observation point colorized by peak concentration (upper left), anhydrite permeability (upper right), DRZ permeability (middle left), backfill permeability (middle right), ShaftFill permeability (lower left) and mean degradation rate (lower right).

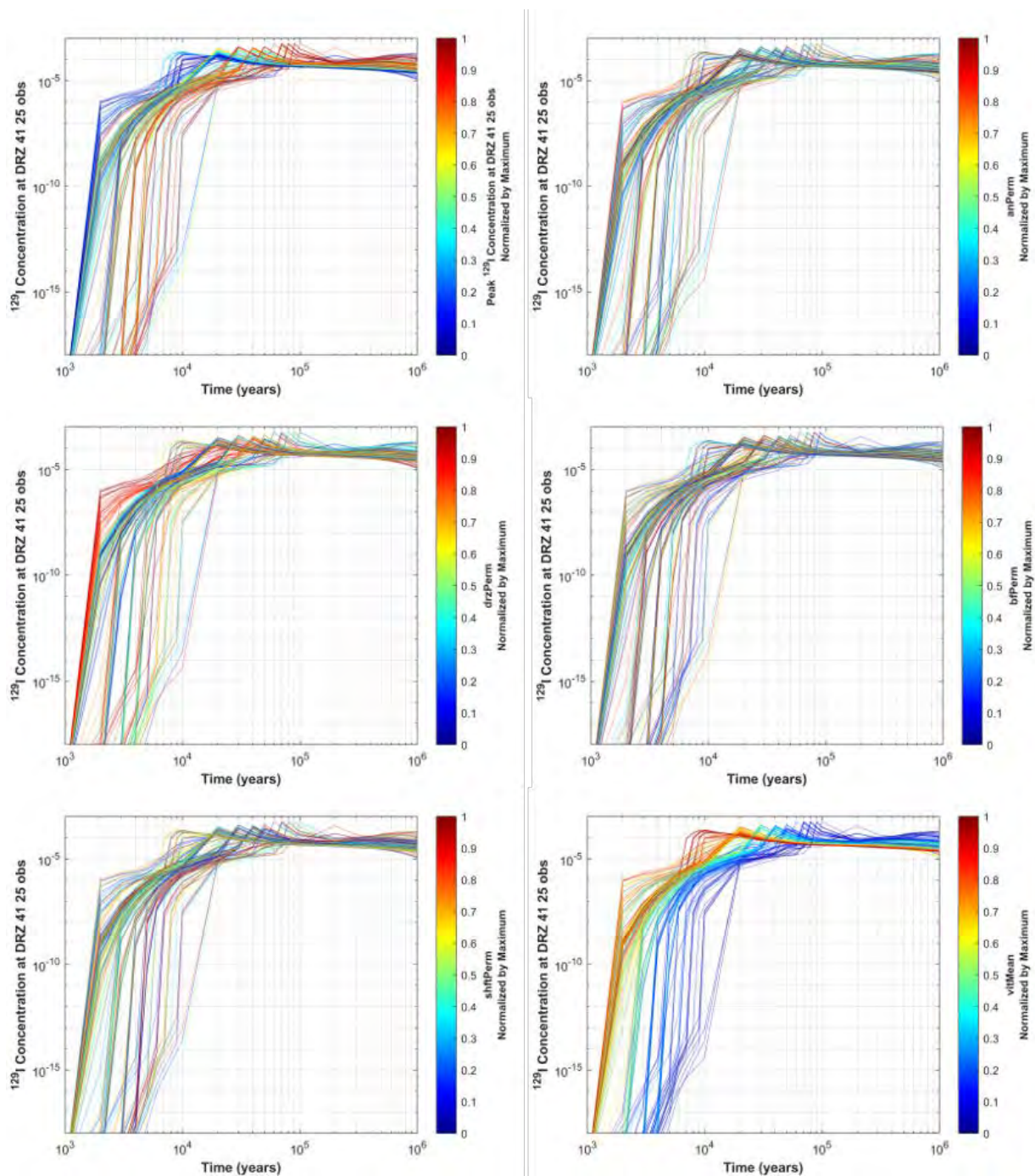


Figure 4-38. Scatter plot of the maximum (peak) ^{129}I molar concentration at the DRZ_41_25 observation point versus values of the sampled variables.

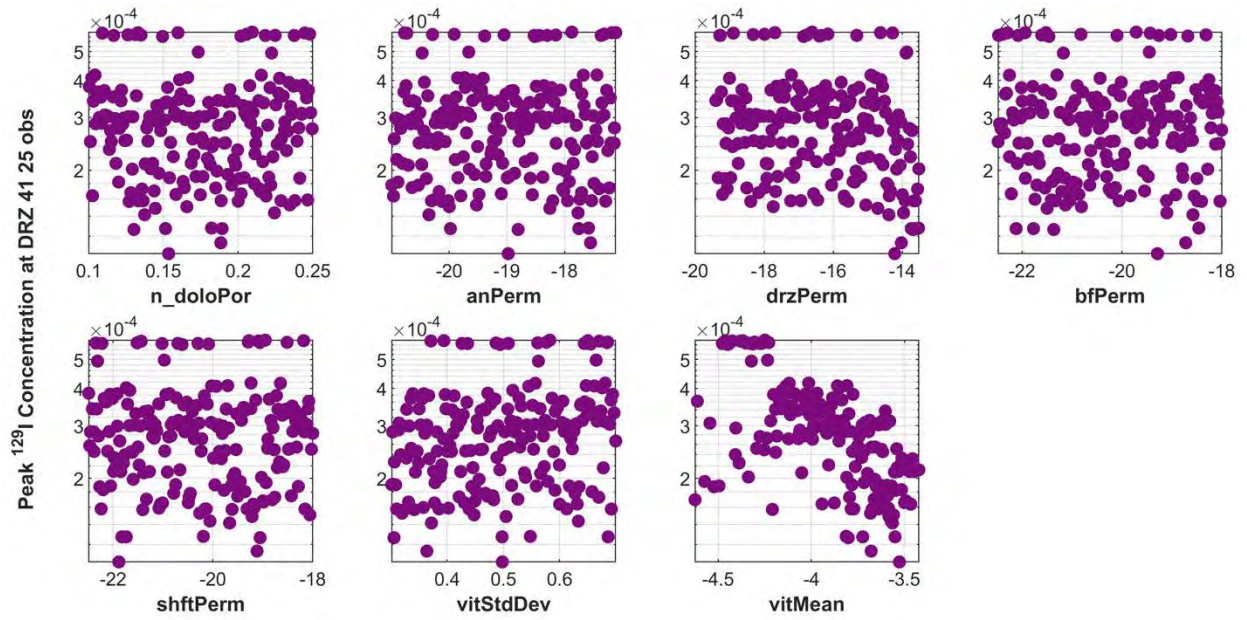


Figure 4-39. Plots of ^{237}Np molar concentrations at the DRZ_16_25 observation point colored by peak concentration (upper left), anhydrite permeability (upper right), DRZ permeability (middle left), backfill permeability (middle right), ShaftFill permeability (lower left) and mean degradation rate (lower right).

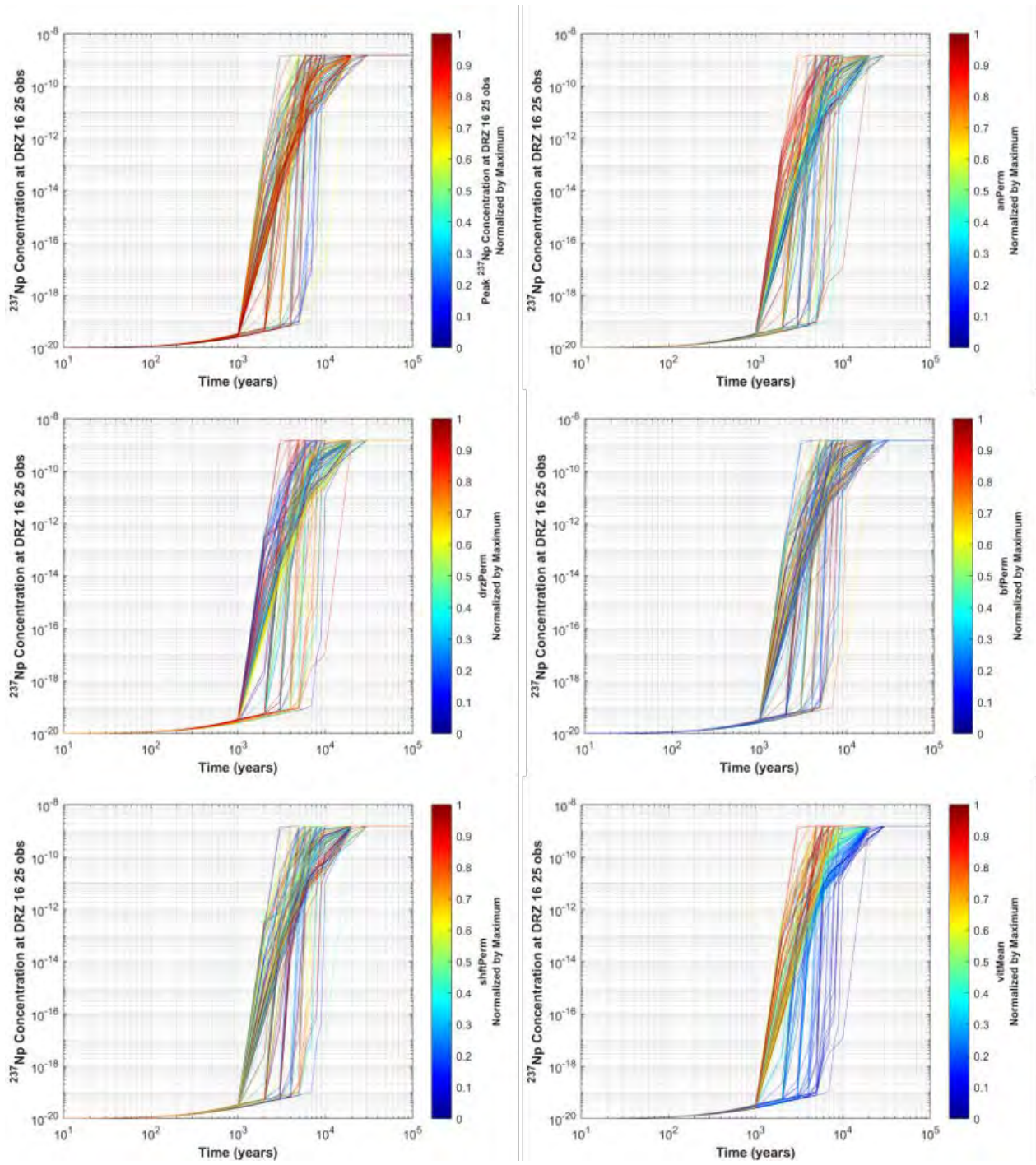
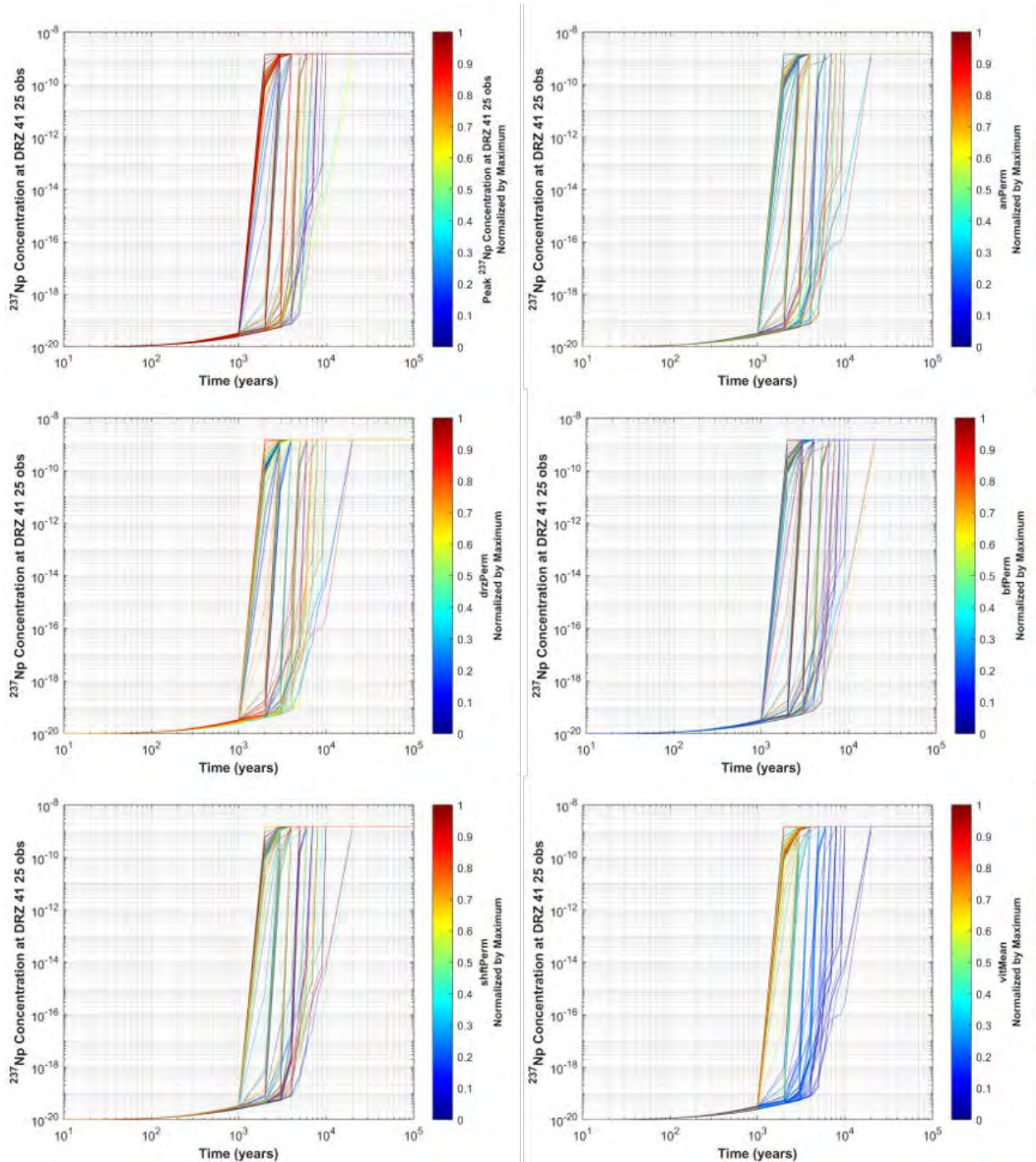


Figure 4-40. Plots of ^{237}Np molar concentrations at the DRZ_41_25 observation point colored by peak concentration (upper left), anhydrite permeability (upper right), DRZ permeability (middle left), backfill permeability (middle right), ShaftFill permeability (lower left) and mean degradation rate (lower right).



4.6.5 Shaft3 Mid

Shaft 3 is located in the northeast portion of the repository and extends from the top of the lower anhydrite layer (An2) to the surface. Figure 4-41 and Figure 4-43 are the horsetail plots for the ^{129}I and ^{237}Np concentrations respectively, while Figure 4-42 and Figure 4-44 are the scatter plots for the peak concentrations. The peak concentration in the shaft shows a strong correlation with the DRZ permeability while there is no correlation of the peak with the shaft permeability. There are two reasons for this. First is the sampled ranges of the respective permeabilities -19.4 to -13.5 for the DRZ and -22.5 to -18.0 for the ShaftFill (all values are \log_{10} of permeability in m^2). The second reason is the relative cross-sectional area for each material type. The shaft itself is $5 \times 5 \text{ m}$, with the DRZ extending outward from all sides an additional 5 m. This results in a cross-sectional area of 25 m^2 for the shaft, and 200 m^2 for the DRZ. Flow perpendicular to the cross-section is analogous to flow along heterogeneous parallel layers. This means the effective permeability across the entire cross-section is 89% the DRZ permeability and 11% the shaft permeability ($200 \text{ m}^2 \div 225 \text{ m}^2$ for the DRZ, $25 \text{ m}^2 \div 225 \text{ m}^2$ for the shaft). The scatter plot also shows a higher sensitivity to the DRZ permeability in the region where the two permeabilities overlap (-19.4 to -18). Dynamics for ^{237}Np (Figure 4-43 and Figure 4-44) are similar to that of ^{129}I for concentration values below 1.51×10^{-9} as explained above.

Figure 4-41. Plots of ^{129}I molar concentrations at the Shaft3_Mid observation point colored by peak concentration (upper left), anhydrite permeability (upper right), DRZ permeability (middle left), dolomite porosity (middle right), ShaftFill permeability (lower left) and mean degradation rate (lower right).

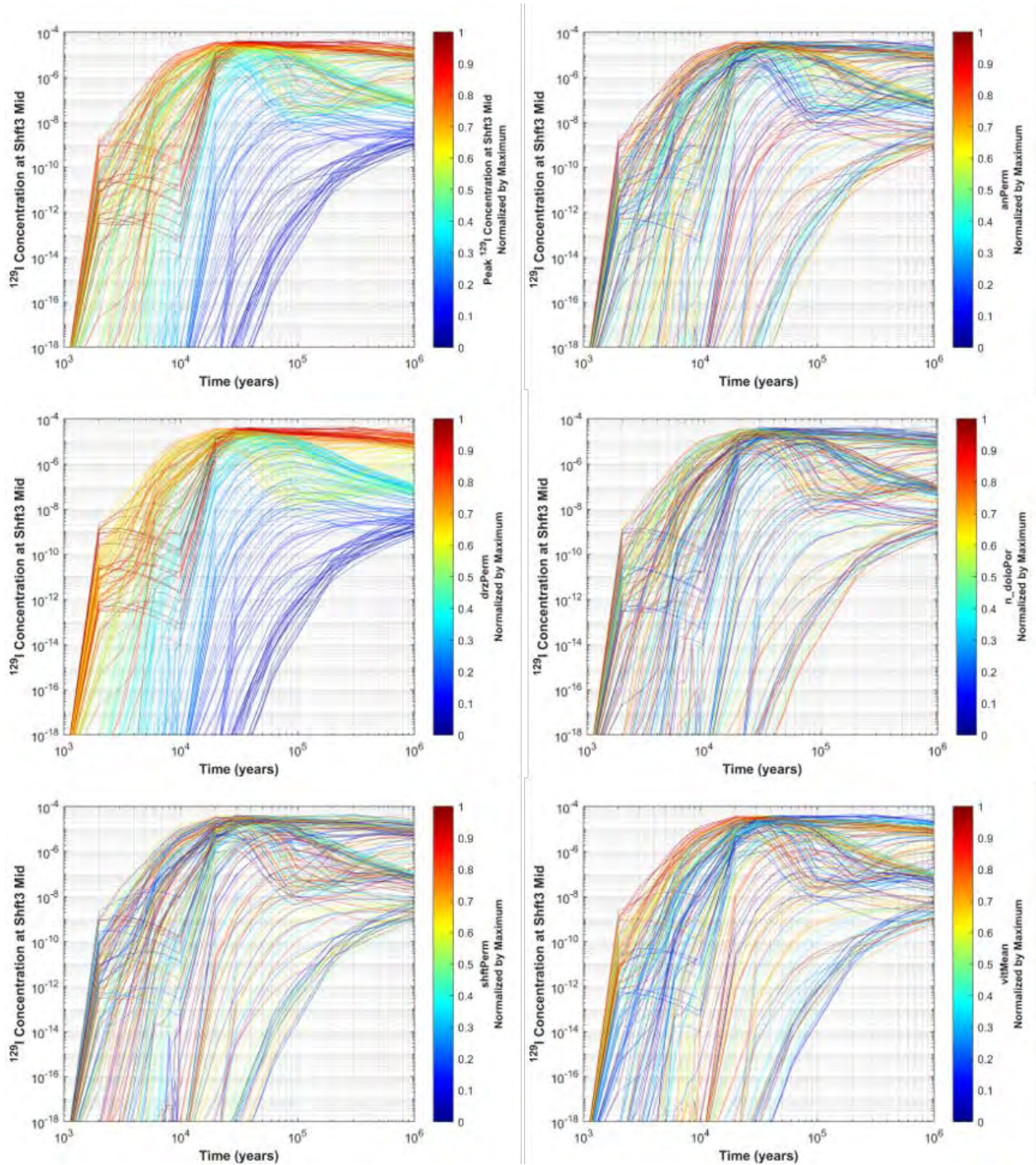


Figure 4-42. Scatter plot of the maximum (peak) ^{129}I molar concentration at the Shaft3_Mid observation point versus values of the sampled variables.

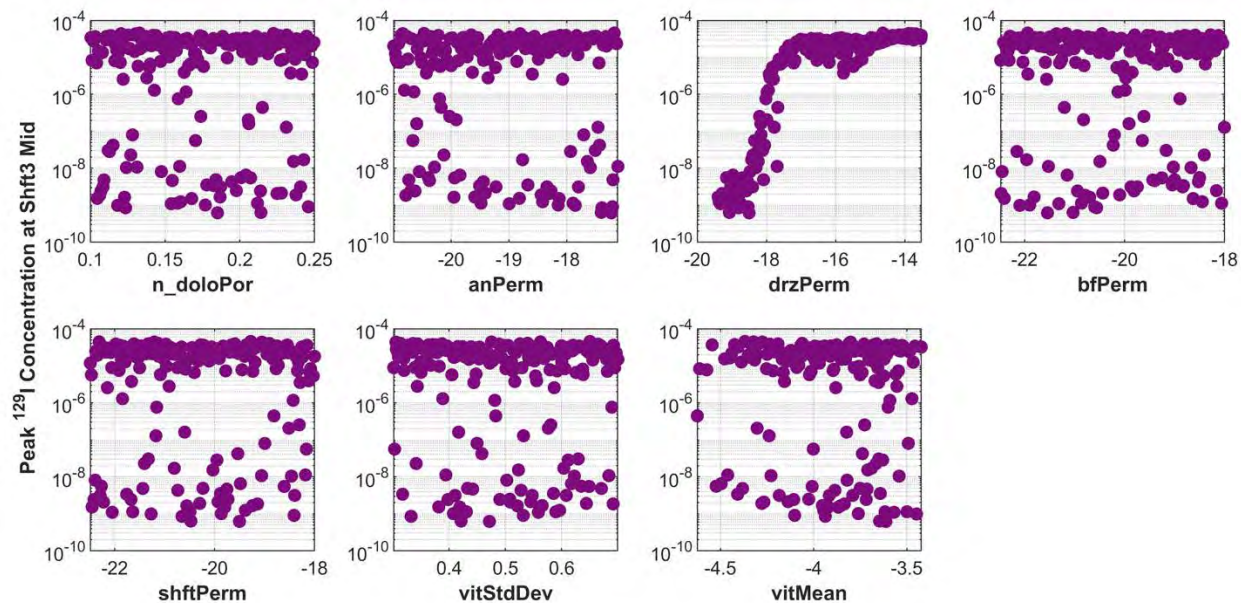


Figure 4-43. Plots of ^{237}Np molar concentrations at the Shaft3_Mid observation point colored by peak concentration (upper left), anhydrite permeability (upper right), DRZ permeability (middle left), dolomite porosity (middle right), ShaftFill permeability (lower left) and mean degradation rate (lower right).

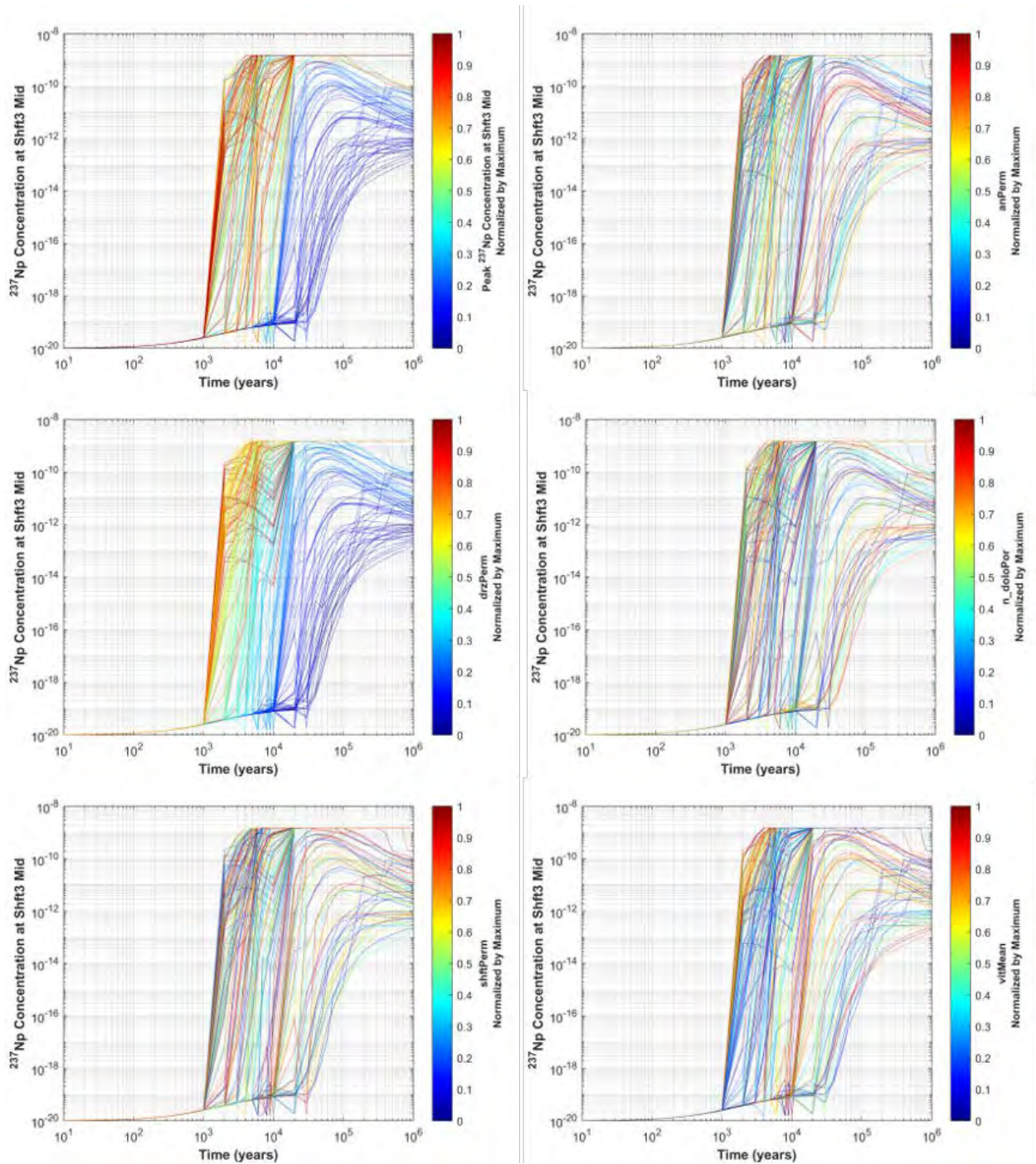
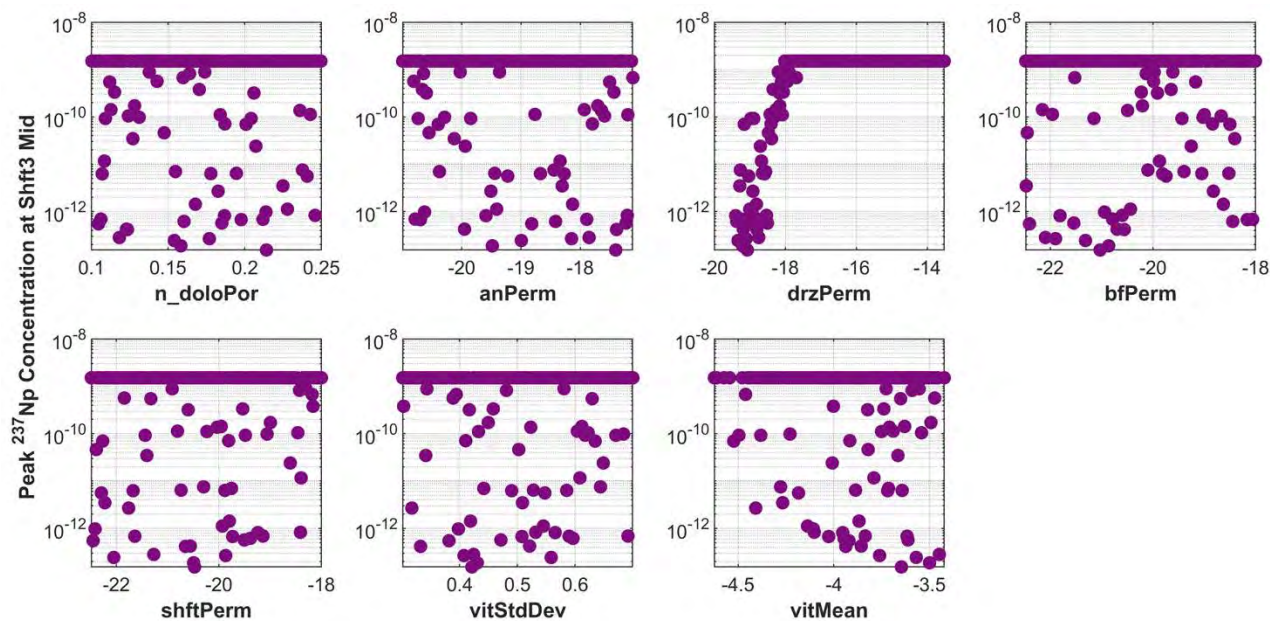


Figure 4-44. Scatter plot of the maximum (peak) ^{237}Np molar concentration at the Shaft3_Mid observation point versus values of the sampled variables.



4.6.6 Sensitivity

To further examine the sensitivity of peak concentrations to parameter values, we conducted a variance-based decomposition global sensitivity analysis. This section provides a brief summary of the models and methods used for global sensitivity analysis.

The measures of sensitivity obtained from variance-based decomposition are called Sobol indices, or sensitivity indices. The main effect sensitivity index for a parameter describes the proportion of the variance in the quantity of interest that can be explained by the variance in that parameter alone. The total effect sensitivity index for a parameter describes the proportion of the variance in the quantity of interest that can be explained by the variance in that parameter alone as well as through its interaction with other parameters.

The sensitivity indices can be interpreted using a few key concepts: 1) the higher the main or total index for a parameter, the more important uncertainty in that parameter is for explaining uncertainty in the quantity of interest, 2) when the main and total effect indices are equal, this means there are no interaction effects, and 3) when the total effect index is larger than the main effect, there are interaction effects and further analysis may be necessary to identify those interactions.

Sobol indices require many more simulations to calculate than can typically be performed with complex simulation codes, such as PFLOTRAN. However, these indices can be estimated using surrogate models. Enough simulations must be performed to fit a representative surrogate model, and the surrogate model can then be evaluated hundreds of thousands of times to estimate the sensitivity indices.

For this analysis, we used several surrogate models: a gaussian process model (GP), a polynomial chaos expansion model of order 2 (PCE2), and a polynomial function model of order 2 (Quad). We supplemented these results with partial correlation coefficients, which also provide a measure of sensitivity with direction. Multiple surrogates were used because they have different strengths and weaknesses. If all of the different surrogates agree that a specific parameter is important, this is likely the

case. If the models disagree on the importance of a parameter, that relationship may need further investigation.

The simplest of the surrogate models we used is the polynomial function. Because the order of the polynomial was limited to two (meaning only two-way interactions were included), this is a quadratic regression. The Gaussian process model for a set of variables is a stochastic process for which any finite subset has a joint multivariate Gaussian distribution. Polynomial chaos expansion is a stochastic expansion in an orthogonal polynomial basis.

Partial correlation coefficients were also calculated to supplement the sensitivity indices. These coefficients are somewhat limited in that they only describe linear relationships; however, they can be useful because (unlike sensitivity indices) the partial correlation coefficient gives the direction of the linear relationship. The partial correlation coefficient for a parameter is essentially the linear correlation between that parameter and the quantity of interest, except that it has been corrected to account for the effects of the other parameters. The partial correlation coefficient can be used to detect nonlinear monotonic effects by calculating the coefficient on the rank-transformed inputs and quantity of interest.

Figure 4-45 shows the sensitivity indices and correlation results the \log_{10} of peak concentration for ^{129}I at the An1_Repo, Dolomite_Repo, and Dolomite_End observation points for each of the uncertain variables. At An1_Repo, most of the variability is due to changes in the mean waste package degradation rate (vitMean), the anhydrite permeability (anPerm), and to a lesser extent, the DRZ permeability (drzPerm). The vitMean and drzPerm variables are negatively correlated while the anPerm parameter is positively correlated, which is consistent with our interpretation of the scatter plots Figure 4-23.

The Dolomite_Repo observation point shows a strong negative correlation to the dolomite porosity/permeability, which again controls the amount of channeling of the plume and the resultant dispersion. The Dolomite_Repo concentrations may be slightly sensitive to the backfill, DRZ, and anhydrite permeabilities. However, these sensitivities are dominated by interaction effects, not main effects. This is why the corresponding partial correlation coefficients are relatively small. At the Dolomite_End observation point, the concentration is clearly sensitive to the DRZ permeability, which as noted above controls the solute transport up the shafts, and the dolomite porosity/permeability, which controls the amount of dispersion/channelization. These relationships were also evident in the scatter plot analysis, Figure 4-32.

For ^{237}Np (Figure 4-46) the relationships are similar except that sensitivity and correlation to the permeability of the host rock type for each observation point (anhydrite for An1_Repo and dolomite for Dolomite_Repo and Dolomite_End) is diminished due to the high sorption coefficient of ^{237}Np .

The two observation points in the DRZ (DRZ_16_25 and DRZ_41_25) show similar sensitivities and correlations to the dolomite aquifer but as mentioned above, the relationships are stronger for the DRZ_41_25 point located in the 37-PWR waste packages (Figure 4-47). The sensitivity of the concentration to DRZ permeability is clearly evident for the Shaft3_Mid observation point (Figure 4-47). For ^{237}Np , there is no sensitivity for the DRZ observation points due to the concentration reaching the solubility limits of ^{237}Np at those points; there is no variance in the peak concentrations so variance-based decomposition cannot be used. For Shaft3_Mid, the correlation and sensitivity of ^{237}Np transport is similar to that of ^{129}I transport (Figure 4-48).

The results from the global sensitivity analysis and partial correlation calculations are generally consistent with the behavior seen in the horsetail plots and scatter plots. However, the variance-based decomposition results suggest higher interaction effects between input parameters than can be seen in plots.

Figure 4-45. Sensitivity (left column) and correlation coefficients for the An1_Repo, Dolomite_Repo, and Dolomite_End observation points for Log₁₀ of peak ¹²⁹I concentration.

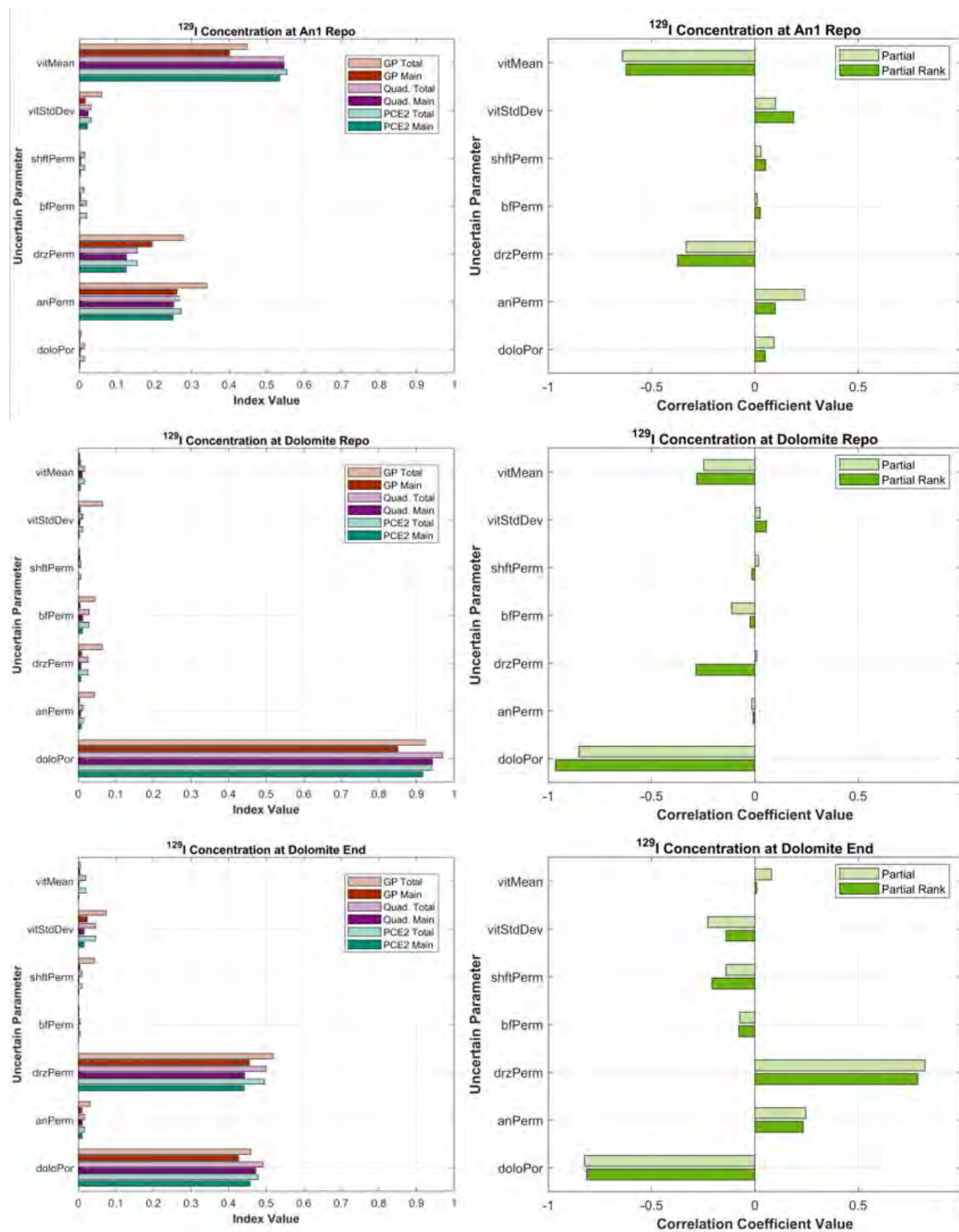


Figure 4-46. Sensitivity (left column) and correlation coefficients for the An1_Repo, Dolomite_Repo, and Dolomite_End observation points for Log₁₀ of peak ²³⁷Np concentration

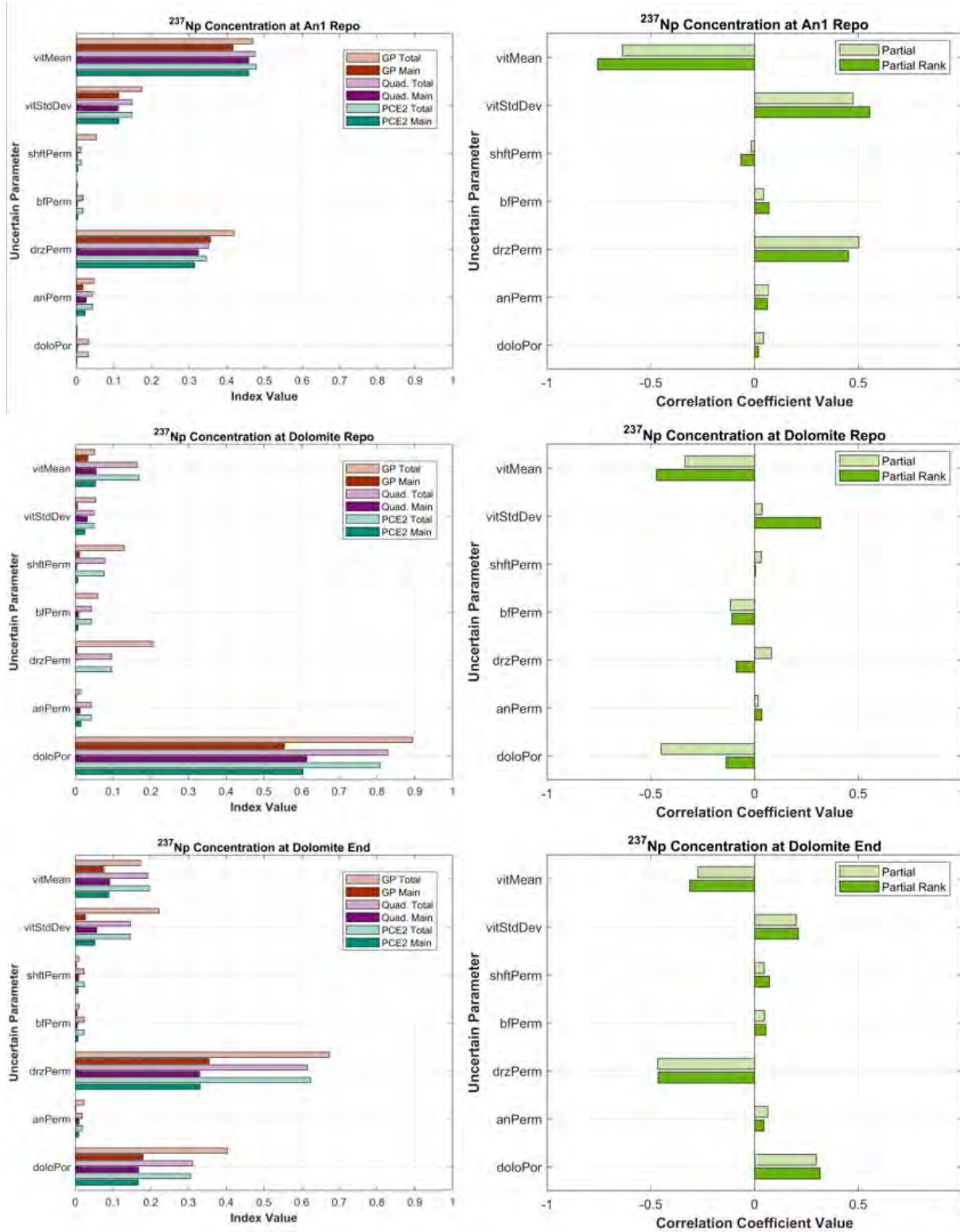
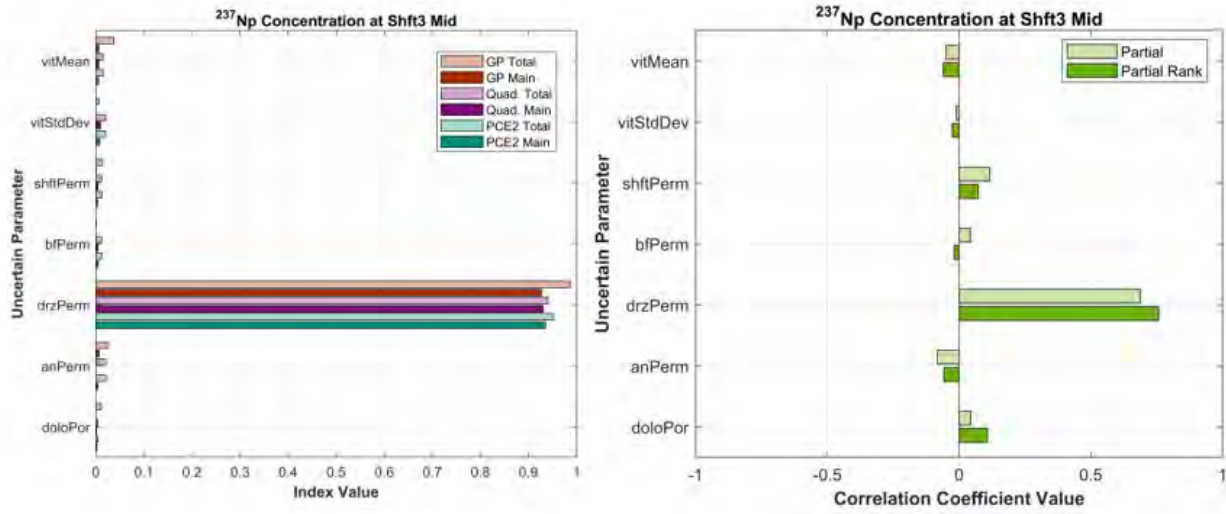


Figure 4-48. Sensitivity (left column) and correlation coefficients for the Shaft3_Mid observation points for Log₁₀ of peak ²³⁷Np concentration



5. DECOVALEX CRYSTALLINE AND SALT REFERENCE CASES

5.1 Introduction

DECOVALEX (DEveloping COupled models and their VALidation against Experiments; <https://decovalex.org>) is an international collaboration initiated in 1992 for the purpose of improving understanding of the coupled thermal, hydrologic and mechanical (THM) processes affecting repository evolution. In recent years chemical processes have also been considered. DECOVALEX activities run in 4-year phases. This FY, a new phase – DECOVALEX 2023 – was initiated. SNL is leading Task F, a comparison of the models and methods used in deep geologic repository performance assessment (PA), on behalf of the US DOE's SFWST Campaign.

Teams participating in Task F will compare post-closure performance assessment approaches to physics simulation, uncertainty propagation, and sensitivity analysis on two generic reference case repositories: one in a fractured crystalline host rock and one in a salt formation. Nine teams from 6 countries are participating in the crystalline reference case comparison and 3 teams (from 3 countries) are participating in the salt reference case comparison.

The primary objectives of Task F are to build confidence in the models, methods, and software used for post-closure PA, and/or to bring to the fore additional research and development needed to improve PA methodologies. Although a direct comparison cannot be made between simulations of a crystalline repository and simulations of a salt repository, it is expected that lessons learned regarding, for instance, methods of coupling process models, propagating uncertainty, or conducting sensitivity analysis will be transferable between concepts.

For each reference case, a common set of conceptual models and parameters describing features, events, and processes (FEPs) that impact performance will be given, and teams will be responsible for determining how best to implement and couple the models. The comparison will be conducted in stages, beginning with a comparison of key outputs of individual process models, followed by a comparison of a single deterministic simulation of the full reference case, and moving on to uncertainty propagation and uncertainty and sensitivity analysis. The Task Specification (Stein et al., 2020b) provides background information, a summary of the proposed reference cases, and a staged plan for the analysis.

The generic crystalline and salt repository reference cases will be developed in detail over the first year of the project. The following sections present concepts to be considered.

5.2 Crystalline Reference Case

A preliminary description of the DECOVALEX crystalline reference case and the choices to be made regarding features and processes to be simulated is available in Stein et al. (2020b). To facilitate decision making, participating teams answered a questionnaire (Appendix B DECOVALEX Crystalline questionnaire). The following overview draws on Stein et al. (2020b) omitting options where the results of the questionnaire favored one option over another.

5.2.1 Geologic Setting and Repository Design

The DECOVALEX generic crystalline reference case assumes a mined repository located at 500 m depth in sparsely fractured crystalline rock. It uses the KBS-3V emplacement concept developed for the Swedish and Finnish repository programs (Pettersson and Lönnerberg, 2008). Copper canisters each containing a nominal inventory of 4 pressurized water reactor (PWR) assemblies are emplaced within rings of compacted bentonite in vertical deposition holes beneath the floor of a deposition tunnel.

Compacted bentonite blocks fill the deposition hole below and above the waste canister, and tunnels are backfilled.

The repository system isolates radionuclides from the biosphere primarily through containment, and secondarily through retardation. The depth of burial together with the hydraulic, chemical, and mechanical environment at depth protects the canisters from failure due to corrosion or mechanical loading. The canister itself is designed to withstand mechanical loading and resist corrosion under geochemical conditions at depth. The bentonite buffer additionally protects the canister by slowing transport of corrodents, absorbing shear motion, and preventing direct contact of the canister with the host rock. In the case of canister failure and depending on failure mechanism, the low permeability and high adsorption capacity of the bentonite retards radionuclide transport. Adsorption and matrix diffusion along fracture flow paths also retard radionuclide transport.

5.2.2 Waste Form and Inventory

The waste inventory is 4350 metric tons uranium (MTU) in the form of PWR SNF. Assuming each PWR assembly contains 0.435 MTU, 2500 4-PWR canisters are required to dispose of the inventory. The waste inventory is deliberately small in order to reduce the computational burden of simulations, and may be made smaller if deemed appropriate by the group.

Fuel rods are comprised of UO₂ pellets in Zircaloy cladding tubes. No performance credit is taken for the cladding. Upon inundation of a breached canister, radionuclides are released from the UO₂ fuel in two fractions. A fraction of the fission products (accumulated in void spaces within the fuel rods) is released instantly. All other radionuclides are released by rate-controlled congruent dissolution of the UO₂ waste form.

Initial radionuclide inventories and heat of decay as a function of time are calculated assuming an initial enrichment of 4.73 wt% U-235, 60 GWd/MTU burnup, and 50 years' time out of the reactor (Carter et al., 2013). UO₂ dissolution is modeled assuming a fractional rate appropriate for the geochemical environment (Werme et al., 2004, Section 3.7).

5.2.3 Waste Canister

The waste canister is comprised of a 5-cm thick copper shell and a cast iron insert. The mechanical strength of the insert resists isostatic loading (due to glaciation) and shear stress (due to movement on intersecting fractures). In the reducing environment of the repository, the copper shell is expected to corrode very slowly via reaction with sulfide. The rate of corrosion depends on the rate at which sulfide can be supplied to the surface of the canister, which in turn depends on the fluid flow rate in fractures intersecting the deposition hole (SKB, 2010a).

Characteristics of the waste canister are taken from SKB (2010b, Sections 3.1 and 3.2). Depending on the interests of the group, waste canister failure mechanisms that may be considered include shear failure due to activation of a sufficiently large intersecting fracture, corrosion, and/or pinhole failure (initial defect).

5.2.4 Buffer (in Deposition Holes)

Each canister is surrounded by blocks of compacted bentonite. Gaps between bentonite blocks and the wall of the deposition hole are filled with bentonite pellets. Saturated bentonite swells to fill gaps and provides a low permeability barrier to fluid flow and advective transport. Bentonite erosion may occur in deposition holes intersected by fractures large enough to support high fluid flow rates at two times: 1) during the saturation process before the bentonite has swelled enough to create a low permeability barrier;

or 2) if dilute water infiltrates changing the electrostatic charge balance at mineral surfaces. Deposition hole rejection criteria based on fracture size and/or inflow rates at the time of excavation can be used to minimize the potential for bentonite erosion (SKB, 2011, Section 5.2).

The importance of radionuclide transport processes in the buffer to repository performance depends on the waste canister failure mechanism. In the case of pinhole failure or shear failure, diffusion and adsorption in the buffer play a role in retarding radionuclide transport. Because canister failure by corrosion is assumed to require bentonite erosion and advective conditions in the buffer, diffusion and adsorption in the buffer may be neglected in this case (SKB, 2010a).

Thermal, hydraulic, mechanical, and chemical characteristics of the bentonite buffer may be derived from SKB (2010c Section 4 and related references). Alternatively, a participating team may provide a dataset for bentonite properties.

5.2.5 Backfill (in Tunnels)

Deposition tunnels are backfilled with compacted bentonite blocks and bentonite pellets. For simplicity, the reference case will assume that main tunnels, ramps, and shafts are backfilled with the same. Although the processes that can occur in the backfill are similar to those that occur in the buffer, they are of less interest in the reference case because the backfill exerts less influence on canister integrity and radionuclide transport. For this reason, the reference case will not consider processes such as erosion or settling that may affect the performance of the backfill.

Thermal, hydraulic, mechanical, and chemical characteristics of the bentonite backfill may be derived from SKB (2010d Section 4 and related references). Alternatively, a participating team may provide a dataset for bentonite properties.

5.2.6 Fractured Host Rock

The crystalline host rock is characterized by occurrence of large-scale, highly-fractured brittle deformation zones and intervening masses of competent rock containing sparse networks of connected fractures. Following the example of SKB (e.g., Joyce et al., 2010), the former are named Hydraulic Conductor Domains (HCD) and the latter are named Hydraulic Rock Mass Domains (HRD).

Hydraulic Conductor Domains (HCD) are defined as local to regional-scale deformation zones with widths of meters and lengths greater than a kilometer that contain a high density of transmissive fractures. HCDs are observable on surface outcrops, as surface lineaments, and as highly fractured intervals in boreholes. Their locations, dimensions, and orientation are constrained by these observations, so that they are included as deterministic features in hydrogeological models and in flow and transport simulations.

Hydraulic Rock Mass Domains (HRD) outside the HCDs contain fractures and minor deformation zones with lengths ranging from less than 1 m up to 1 km that are not deterministically mapped. A subset of these features (generalized as discrete fractures) forms a connected network of open and partially open fractures through which groundwater can flow. Within each HRD and/or depth interval within an HRD, fractures can be grouped into fracture sets on the basis of orientation, and characterized by fracture density and probability distributions for size, orientation, and location. Stochastic realizations of discrete fracture networks (DFNs) for use in the hydrogeological model are generated from these distributions.

The reference case will employ a representative set of deterministic deformation zones whose spacing and orientations are derived from observations of HCDs at Forsmark (e.g., Follin et al., 2008, Section 3.2.2) and Brittle Fracture Zones (BFZ) at Olkiluoto (e.g., Hartley et al., 2018, Section 3.1.5). Fracture density and probability distributions describing size, orientation, and location of fractures in the HRD will be

borrowed from either the western central hydraulic unit (CHUW) at Olkiluoto (Hartley et al., 2016, Table 4-2) or FFM01/06 at Forsmark (Joyce et al., 2014, Table 2).

5.2.7 Evolutionary Scenarios

One or more scenarios for simulation will be constructed around the choice of canister failure mechanism. Time permitting, the effects of glacial loading on boundary conditions and stress state may be considered. Any scenario choice will involve simulation of the processes affecting flow and transport in fractures, and will require teams to make choices regarding, for instance, fracture size range, transmissivity functions, use of a discrete fracture network, equivalent continuous porous medium or other fracture representation, and treatment of matrix diffusion. Possible scenarios include:

Canister failure by corrosion: In this scenario, fracture flow rates at one or more deposition holes are large enough to cause erosion of bentonite, creating an advective pathway to the copper canister. Resulting transport rate of sulfide to the canister is sufficient to cause the copper to corrode through. This scenario provides an opportunity to investigate the coupling between fracture flow rates, bentonite erosion, solute transport, and corrosion.

Shear failure due to seismic event: In this scenario, a seismic event occurs that is large enough to cause shear failure of one or more canisters. Bentonite buffer remains essentially intact, so that the dominant transport mechanism between canister and fractured host rock is diffusion. This scenario provides an opportunity to investigate the coupling between stress, slip on fractures, and canister shear failure (for geomechanics enthusiasts) and/or to investigate alternate models for radionuclide retardation in the bentonite including adsorption isotherms, ion exchange, and/or surface complexation (for geochemistry enthusiasts).

Pinhole failure: In this scenario, random failure occurs due to a manufacturing defect. No coupled processes are required to fail a canister. Radionuclide transport in the buffer is diffusion dominated.

Glacial loading: In this scenario, glacial loading causes pore pressures and the stress field to change. The changes in normal and shear stress on each fracture (and deterministic HCD) cause changes in transmissivity. This scenario provides an opportunity to explore the effect of boundary conditions on flow and transport in the fracture network as well as an opportunity to investigate coupling between changes in stress field and canister failure mechanisms.

5.2.8 Benchmark problems

Benchmark cases provide a means to understand differences in model implementation that affect how a problem can be defined and how values are calculated. Simple test cases or process models allow performance measures to be compared and facilitate understanding of the complete repository system model. Steady-state flow and transient advection and dispersion benchmark cases were developed in 2020.

The benchmark cases for flow and transport problems use analytical solutions adapted from Kolditz et al. (2015). Pressure solutions for steady-state, single phase flow in one, two, and three dimensions are used for comparison. The model domain for 1D steady flow is a 100 m beam and uses constant pressure (Dirichlet) boundary conditions (Kolditz et al., 2015 Section 2.2.1). The 2D steady flow is a 1 x 1 m domain and uses Dirichlet boundary conditions on the faces of the domain orthogonal to the x and y axes (Kolditz et al., 2015 Section 2.2.3). In the 3D steady flow problem a 1x1x1m domain is used where all six faces use Dirichlet boundary conditions (Kolditz et al., 2015 Section 2.2.5). Analytical solutions for the 2D and 3D steady-state problems are plotted in Figure 5-1. The 1D analytical solution is not shown. PFLOTRAN simulations are verified to converge to essentially zero error for all benchmark problems.

Transient transport (advection and dispersion) in 1D are used for comparison to analyze three tracers (conservative, decaying, and adsorbing). At the inflow face, concentrations are held at 1 mol/L from 0 to 15000 seconds and zero afterwards (Kolditz et al., 2015 Section 2.5.2). The concentration of the analytical solutions at 20,000 s are plotted in Figure 5-2. PFLOTRAN simulations are verified to converge to within 9-11% relative error for all three tracers over the first 5m of the domain. Error using this metric is dominated by parts of the curves with small values. Future and ongoing test cases include adding tests for fracture networks, radionuclide source terms, and buffer and canister processes.

Figure 5-1. Left: Analytical pressure solution for 2D steady state flow. Right: Analytical pressure solution for 3D steady state flow at $z = 0.45$ m

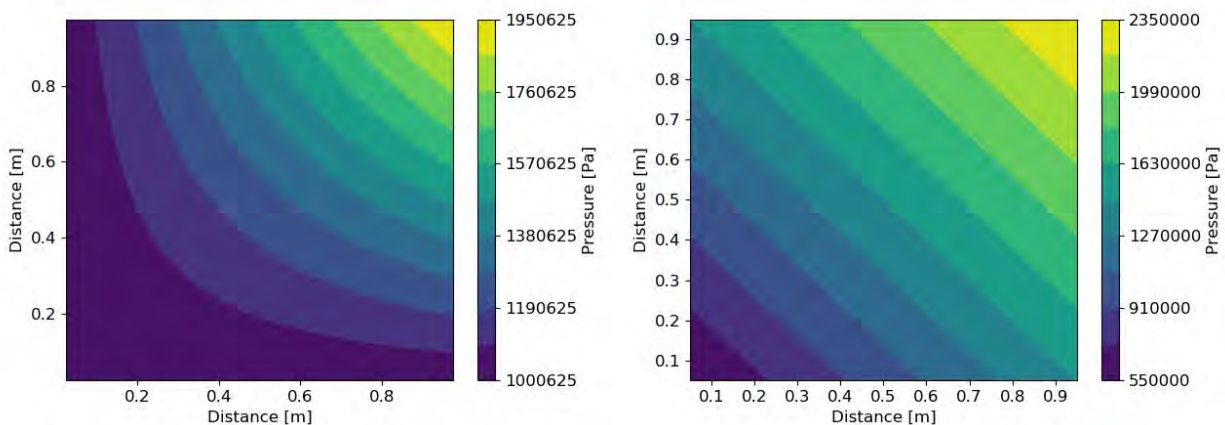
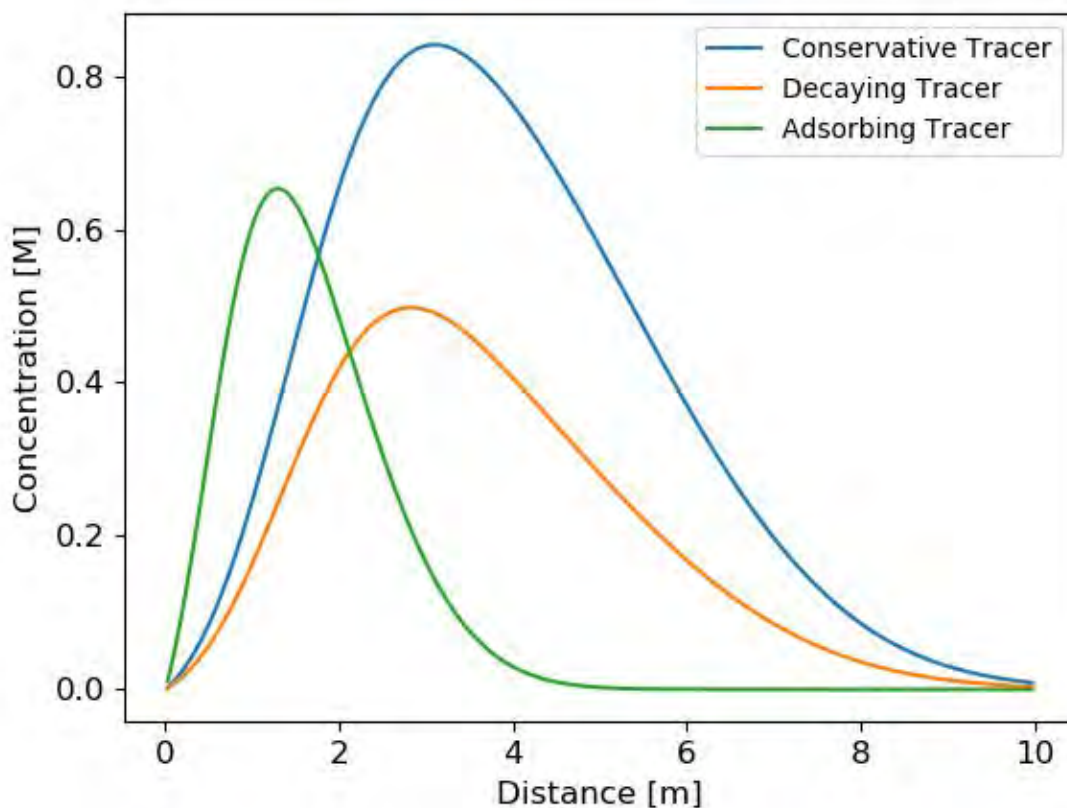


Figure 5-2. Analytical solution at 20,000 sec for 1D transient transport for a conservative, decaying, and adsorbing tracer.



5.3 DECOVALEX Salt Reference Case

Development of the DECOVALEX-2023 reference case for a SNF repository in a salt formation was initiated during the Salt Scenarios Meeting in August 2020. To develop the reference case and model comparison, interested teams will agree upon characterization of the natural and engineered barriers, key FEPs, conceptual models and parameterization, and choose individual process models for benchmarking and comparison (e.g., salt creep, crushed salt reconsolidation, thermal conduction).

Here we present an overview of previously published reference cases in the United States (Sevougian et al. 2016), Germany (Bollingerfehr et al. 2017, Bolingerfehr et al. 2018), and the Netherlands (Prij et al. 1989, Prij et al. 1993), which will be used to provide the basis for the DECOVALEX-2023 salt reference case.

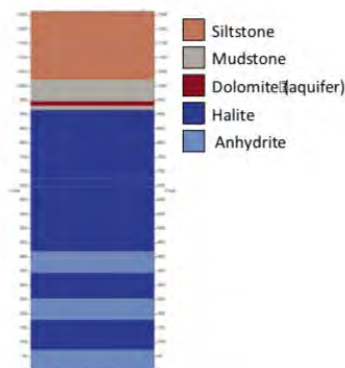
5.3.1 Generic Geologic Setting

5.3.1.1 United States

The generic salt reference case for deep geologic disposal of defense-related HLW and SNF is hosted in bedded geologic salt, similar to the case considered in Section 4 of this report. The mined repository is

located at 661 m depth within a bedded salt, with the depth to the top of the halite at 345 m depth and a total thickness of 497 m of pure halite. Within this thickness are two 1 m thick interbeds of anhydrite that sandwich a 30 m thick repository region. Figure 5-3 illustrates the generic stratigraphy utilized in Sevougian et al. (2016). There are a number of bedded salt formations in the United States with depth and thickness amenable to repository siting (i.e. Michigan, Appalachian, Permian, and Paradox Basins) as discussed in Sevougian et al. (2016).

Figure 5-3. Generic stratigraphic column used for U.S. salt reference case (from Sevougian et al., 2016). The potential storage formation is between the very two thin anhydrite layers in the center of the figure.

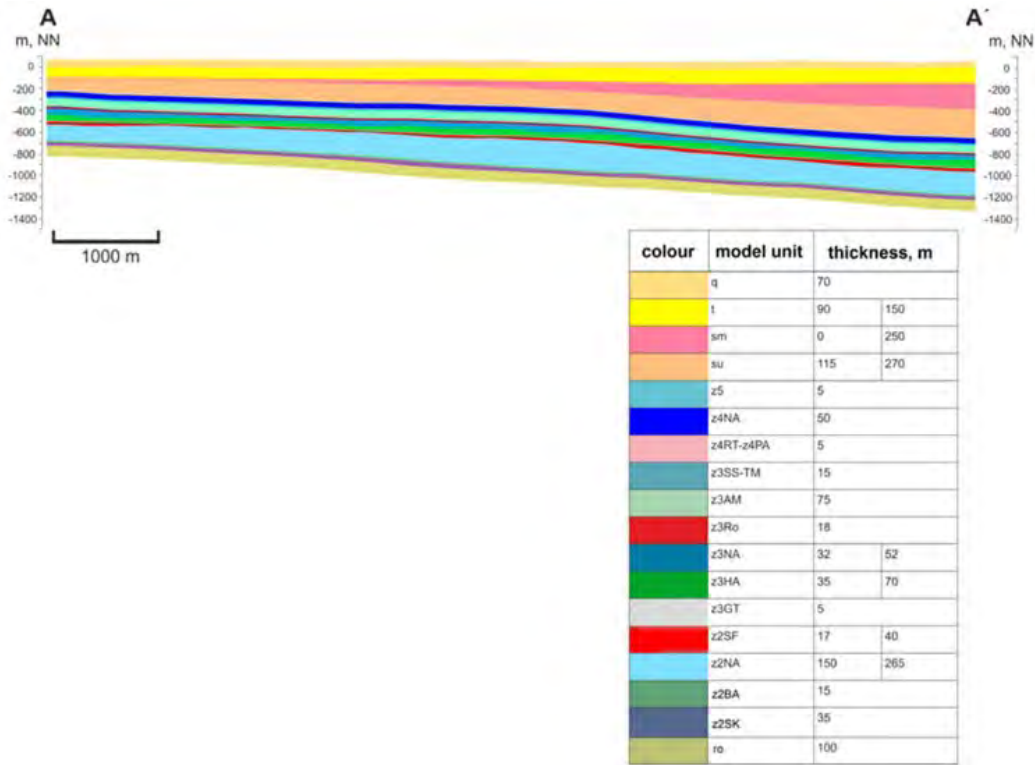


5.3.1.2 Germany

KOSINA

Bollingerfehr et al. (2018) investigates two different geological situations for disposal: flat-bedded salt-rock-salt successions and salt pillows. Flat-bedded rock salt successions are composed of a sequence of evaporitic deposits of at least several tens of meters. Salt pillows are considered a special type of bedded evaporitic sequences by the KOSINA project, where dome-like structures (brachyanticlines) develop as a result of migration of salt into a geologic structure (i.e., anticline). For the flat-bedded salt case, the total thickness of the salt formation is 150 m – 265 m with a 5° – 7° dip, with the depth to the top of salt from 610 m to 1050 m below ground level (Figure 5-4). Similarly, the salt pillow scenario considers a salt pillow within a salt formation dipping 5° – 7°, with a thickness ranging from 150 m to 600 m where the thickest portion of the salt is considered the pillow. Depth to the top of formation ranges from 460 m to 1045 m below ground level (Figure 5-5).

Figure 5-4. Geologic reference profile for the "flat-bedded" salt formation scenario (from Bollingfehr et al., 2018). The potential storage formation is the light blue z2NA formation.



KOMTESSA

The German KOMTESSA project evaluates a safety case that takes place within the Gorleben salt dome. The Gorleben salt dome is described as having a horizontal outline of ~15 km x 4 km wide. The base of the salt dome lies at a depth of 3200 m to 3500 m, with the top of the salt only 250 m below ground level (Bollingfehr et al., 2017). Figure 5-6 shows a simplified cross-section of the Gorleben salt dome used for the KOMTESSA salt reference case.

Figure 5-5. Geologic reference profile for the "salt pillow" scenario (from Bollingfehr et al., 2018). The potential storage formation is the light blue z2NA formation.

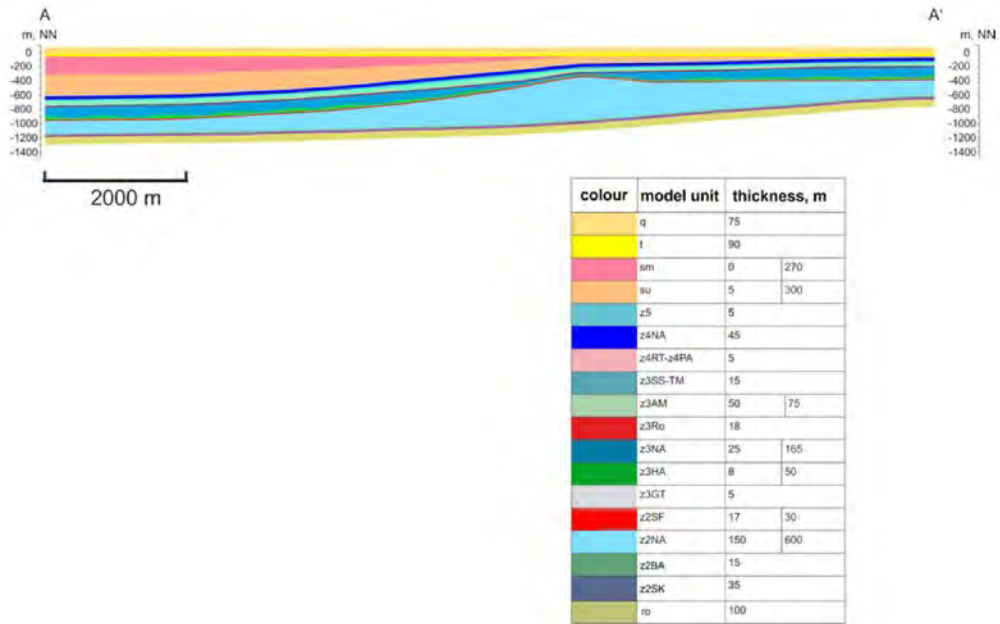
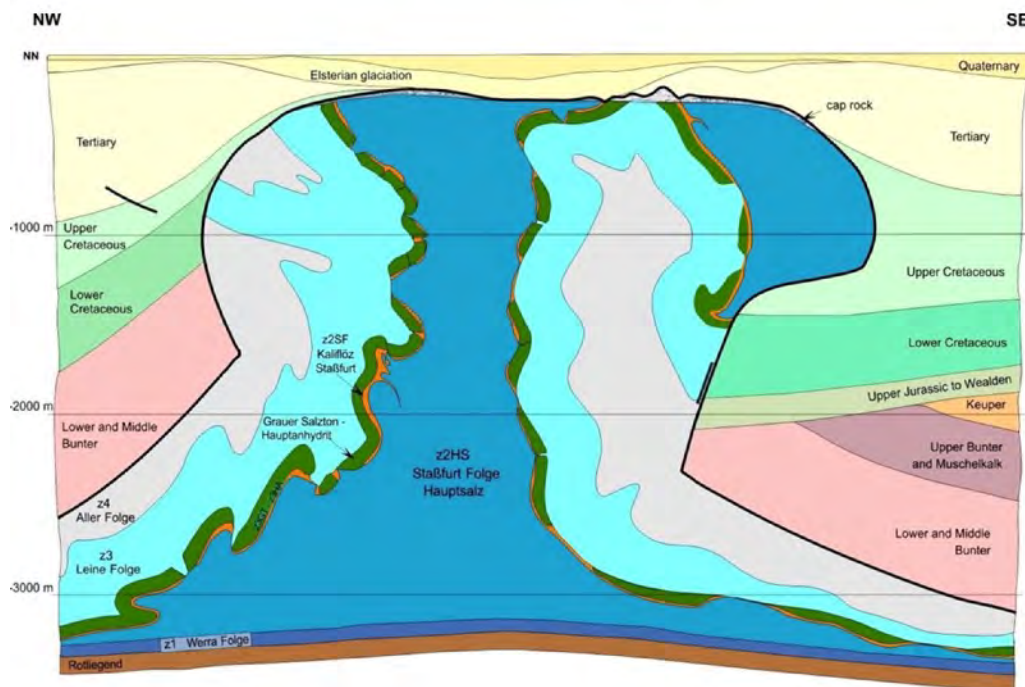


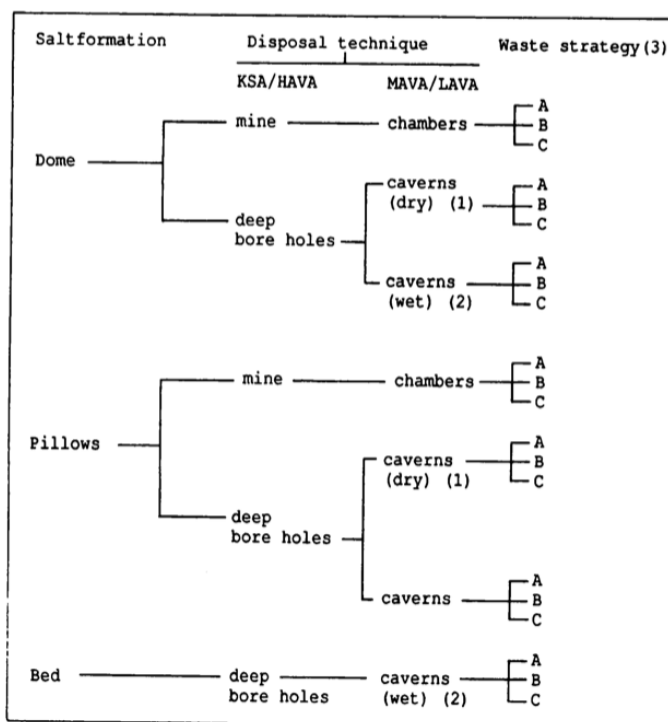
Figure 5-6. Simplified NW-SE geological cross-section of the Gorleben salt dome (from Bollingfehr et al., 2017). The potential storage formation is the light blue z2HS formation in the center of the dome.



VEOS

The geologic inventory performed for OPLA illustrates there are many salt deposits that can be considered for disposal sites for nuclear waste disposal (OPLA, 1989). However, the main focus of VEOS are salt domes, salt pillows, and bedded salt. Table 5-1 shows how each type of salt formation has its own unique combination of disposal technique and waste strategy analyzed within the VEOS project.

Table 5-1. Disposal concepts considered by Prij et al. (1989).



PROSA

PROSA (PROBabilistic Safty Assessment of geologically disposed radioactive waste) in the Netherlands has been defined based on the results of VEOS. PROSA takes a probabilistic approach and a variety of salt formations are considered salt domes, pillows, and salt beds (Prij et al., 1993). For each scenario the parameters that describe the salt are based on the best estimated values of global parameters in Table 6.3 of Prij et al. (1993).

5.3.2 Waste Inventory, Waste Form, Waste Package, and Emplacement Concept

The waste inventory, waste form, waste package, and emplacement concept for each country is unique. For example, Sevougian et al. (2016) has a waste inventory of 70,000 MTHM while the KOMTESSA (Bollingfehr et al., 2017) project accounts for 10,550 MTHM. Additionally, the type of salt formation also impacts the emplacement concept. As a result of these significant differences there are differences in waste form and waste package as well. In order to succinctly cover each of these topics, table 5-2 summarizes the major differences and similarities for each country.

Table 5-2. The waste inventories, waste form, maximum allowable temperatures within the repository, waste package type, and emplacement concept proposed by previously published safety cases for each country.

Country	United States	Germany		Netherlands	
Project	Sevougian et al. (2016)	KOSINA Bollingerfehr et al. (2018)	KOMTESSA Bollingerfehr et al. (2017)	VEOS et al. (1989)	Prij PROSA (PRObabilistic Safety Assessment) Prij et al. (1993)
Waste Inventory	70,000 MTHM Capacity	10,445 MTHM	10,550 tonnes heavy metal	Low and Intermediate Level Waste (LILW)	KCB + KCD (500 Mwe total) 50 years interim storage
	PWR UNF assemblies		35,563 spent fuel elements	Technically Enhanced Naturally Occuring Radioactive Material ((TE)NORM)	KCB + KCD (30 years energy production at 3000 MWe) interim storage for 50 years
	0.435 MTHM		7973 canisters - CSD-V, -B, -C	HLW – 628 Canisters heat generating (478 CSD-V, 150 ECN)	- All fuel elements are assumed to be reprocessed
	50-year OoR		See Table 4.2 Spent Fuel Table (Bollingerfehr et al., 2017)	HLW – 800 canisters non-heat generating	
	Assume 60 GWd/MTHM				
Waste Form & Temp. Constraints	PWR UNF	POLLUX casks = up to 10 PWR	Assume 500 yr durability (heat-gen)		HLW – horizontal boreholes no overpack
	burnup 60 GWd	BSK (mostly CASTOR) = 3 PWR			HLW – vertical boreholes w light overpack
	initial enrichment 4.73% ²³⁵ U	Max T = 200C		Max T = 167C	HLW – vertical boreholes w heavy overpack
	Each PWR 0.435 MTHM (1.44 x 10 ⁶ g/MTHM)				Super containers (e.g. POLLUX) – 10 m spacing
	See Table 4-4 (SAND_2015) UNF degradation rates				MAX T = 100C
Waste Package	Stainless Steel	POLLUX	PWR – 6,920 thm	HLW – Konrad type II container – 1.6 x 1.6 x 1.6m ~20,000 kg	KSA (W11-1)
	12 PWR UNF	CASTOR	POLLUX-10, CASTOR V/19, BSK	Possibility of super containers (POLLUX containers – 24,000 kg)	HAVA-200 (W14-1)
	5 m x 1.29 m				HAVA-1430 (W12-3)
					HAVA-220 (W13-8)
					HAVA-2200 (W13-5)
					MAVA-1200 (W42-10)
					LAVA-665 (W42-7)
Emplacement Concept	On floor placement	Flat-bedded salt - POLLUX casks in horizontal drifts - BSK-H casks in lined horizontal drifts	Variant 1: POLLUX and CASTOR casks in horizontal drifts	See Table 2.1 (Prij et al., 1989)	Borehole Flank Drift Chamber Flank Drift
		Salt Pillow - BSK-V in lined vertical boreholes - Transport and storage casks in short horizontal boreholes	Variant 2: various retrievable canisters in deep vertical boreholes		Borehole Disposal Drift
					Chamber Disposal Drift
					Borehole Medium level waste
					Borehole HLW
					Chamber

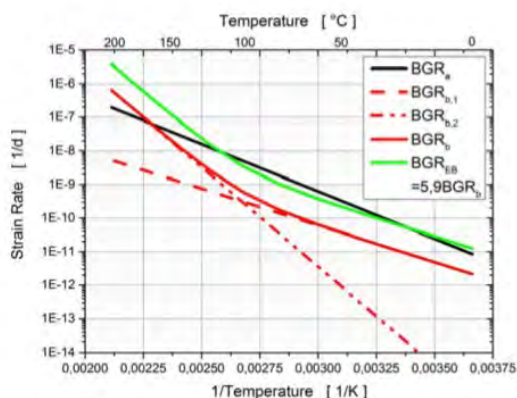
5.3.3 Backfill

The United States, Germany, and the Netherlands all assume that disposal rooms and access halls are filled with run-of-mine crushed salt backfill. While all scenarios use similar initial hydraulic parameters for the crushed salt (i.e., porosity = 30 – 35% with permeability higher and thermal conductivity lower than intact salt), each scenario approaches how the backfill will consolidate over time differently. Sevougian et al. (2016) utilizes a permeability and porosity distribution for the first 200 years from Fox (2008). After 200 years backfill is assigned a porosity of 0.113 and permeability of 10^{-18} m^2 for the deterministic run. For probabilistic simulations, Sevougian et al. (2016) sample on porosity using a uniform uncertainty distribution over a range of 0.01-0.20.

Prij et al. (1989) estimates backfill consolidation by implementing a model that is based on a constant convergence rate. In contrast, Prij et al. (1993) utilizes an improved convergence model for consolidation of backfill and room closure which is explained in detail in section 5.2.3 of the final PROSA report.

Bollingfehr et al. (2017) implements constitutive laws into their models that factor in how salt behavior changes as a function of the temperature and compaction process (Figure 5-7.). Bollingfehr et al. (2018) utilizes a steady-state creep rate based on a sinh-relation described in detail in Section 5.3 (Eq. 5.1 – 5.11) of the KOSINA report.

Figure 5-7. Structural factor and Arrhenius term as part of the BGR constitutive laws (from Bollingfehr et al., 2018).



5.3.4 Process-Events

Each country reports the significant processes and events that are accounted for within their respective reference cases. Due to the amount of detail required to adequately cover each process and event of the reference cases, Table 5-3 is used to illustrate a generalized summary for each country. The processes and events are broken up into three broad categories; natural phenomena, phenomena induced by waste, and human induced events.

Table 5-3. Generalized summary of process and events for each country. This is a simplified summary that lumps many processes and events into categories, for more detail see published reference cases.

Generalized Summary			
	United States (Sevougian et al., 2016)	Germany (Bollingfehr et al., 2017 & 2018)	Netherlands (Prij et al., 1989 & 1993)
Natural Phenomena			
Climate Fluctuations	X	X	X
Glacial	X	X	X
Denudation and Erosion	X	X	X
Magmatic Activity	X	X	X
Orogenic		X	X
Static Fault			X
Solution, subrosion	X	X	X
Sedimentation			X
Flooding			X
Undiscovered geology	X	X	X
Meteorites			X
Earthquakes	X	X	X
Phenomena Induced by Waste			
Thermal Effects	X	X	X
Chemical Effects	X	X	X
Mechanical Effects	X	X	X
Hydrological Effects	X	X	X
Biological	X	X	X
Nuclear Criticality	X		
Human Induced			
Poor design/planning/Early Failure	X		X
Intentional Intrusion	X	X	X
Unintentional Intrusion	X	X	X

This page intentionally left blank

6. PRELIMINARY INVESTIGATION INTO ALTERNATIVE MESHES

6.1 Motivation for alternate meshing

One overarching GDSA Framework goal is to have open-source codes for generating repository simulations from building a simulation model through to analysis of results. One piece that has been missing is meshing software. PA-scale simulation meshes are currently generated using Sandia in-house software CUBIT, which is not open-source. There is also uncertainty as to the usability of flexed hexagonal meshes as we move to simulations on more complex and realistic representations of the subsurface based on geological framework models (GFMs) (See Sevougian et al., 2019b section 5.1.1.3). The flexing of hexagonal meshes increases numerical error and if many small grid cells are introduced to capture geological surfaces this will slow down simulations. Also, even ideal hexagonal meshes have all the faces aligned with the coordinate axes, which can introduce grid orientation effects, even in surprisingly simple simulations. Two alternative types of meshes have been explored: polyhedral and Voronoi.

6.1.1 Polyhedral meshes

One alternative to hexagonal meshes is polyhedral meshes. Polyhedral meshes are unstructured and so it is easier to mesh complex shapes without ending up with badly-scaled or large numbers of grid cells in the mesh. Each grid cell, or element, is a polyhedron with an arbitrary number of sides, so grid orientation effects are expected to be lower than hexagonal meshes.

In Section 6.2 a commercial polyhedral meshing software, ANSYS-Fluent (Fluent, 2019) is used to test the ease of use and accuracy of PFLOTRAN simulations on polyhedral meshes. The longer-term goal is to use open-source meshing software and this exploratory study is intended to be a proof (or disproof) of concept.

6.1.2 Voronoi meshes

Voronoi meshes have two major advantages over using hexagonal meshes. The first advantage is that the unstructured mesh can easily be mapped to many types of complex surfaces, like polyhedral meshes. The second advantage is that in Voronoi-type meshes the flux between two adjacent cell centers is always perpendicular to the boundary between the two cells. This reduces numerical error in flow and transport calculations. Non-flexed hexagonal meshes also have this quality, but when a hexagonal mesh is flexed to conform to complex surfaces the fluxes become misaligned and numerical error increases.

VoroCrust is an SNL in-house meshing software that is being explored as an alternative meshing tool. It is still in the early stages of development. GDSA is supporting a collaboration for the development of VoroCrust meshing capability specifically tailored to creating meshes for PFLOTRAN simulations on realistic geological domains (see Mariner et al., 2020). In Section 6.3 PFLOTRAN simulations on Voronoi meshes are explored.

6.2 ANSYS-Fluent simulations

This subsection details the workflow for running PFLOTRAN simulations on domains meshed using the software ANSYS-Fluent. Section 6.2.1 discusses the geometry and process of meshing two domains for simulation. Section 6.2.2 shows the results of PFLOTRAN simulations on each domain.

6.2.1 Setting up models

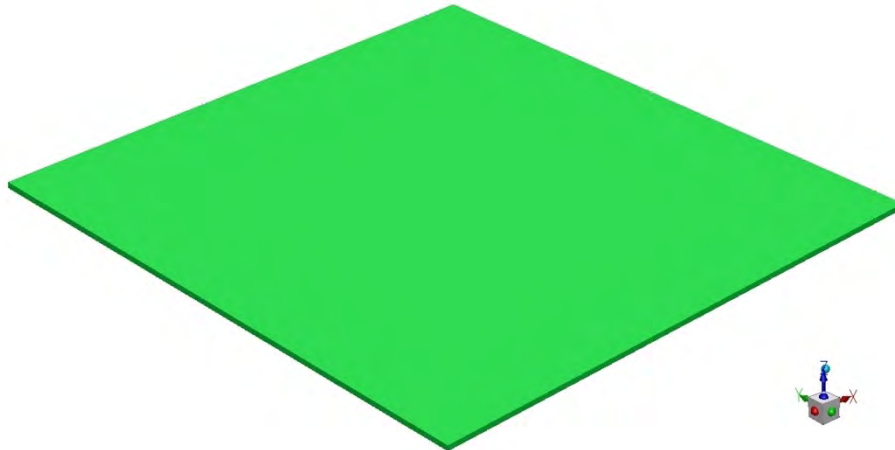
The first domain is a simple rectangular box model that is used for two benchmark simulations. A coarse hexagonal (Ansys1), a fine hexagonal (Ansys2) and one polyhedral (Ansys3) mesh are generated for this domain. The second is representative of a $\frac{1}{4}$ waste package modelling domain and a single hexagonal mesh is generated.

6.2.1.1 Geometry

2D Rectangular Domain

The 2D rectangular model is a 100x100x1m box. The geometry was generated in CUBIT and exported in a SAT file format for use in ANSYS. Figure 6-1 shows the geometry after the SAT file is imported into ANSYS as an external geometry.

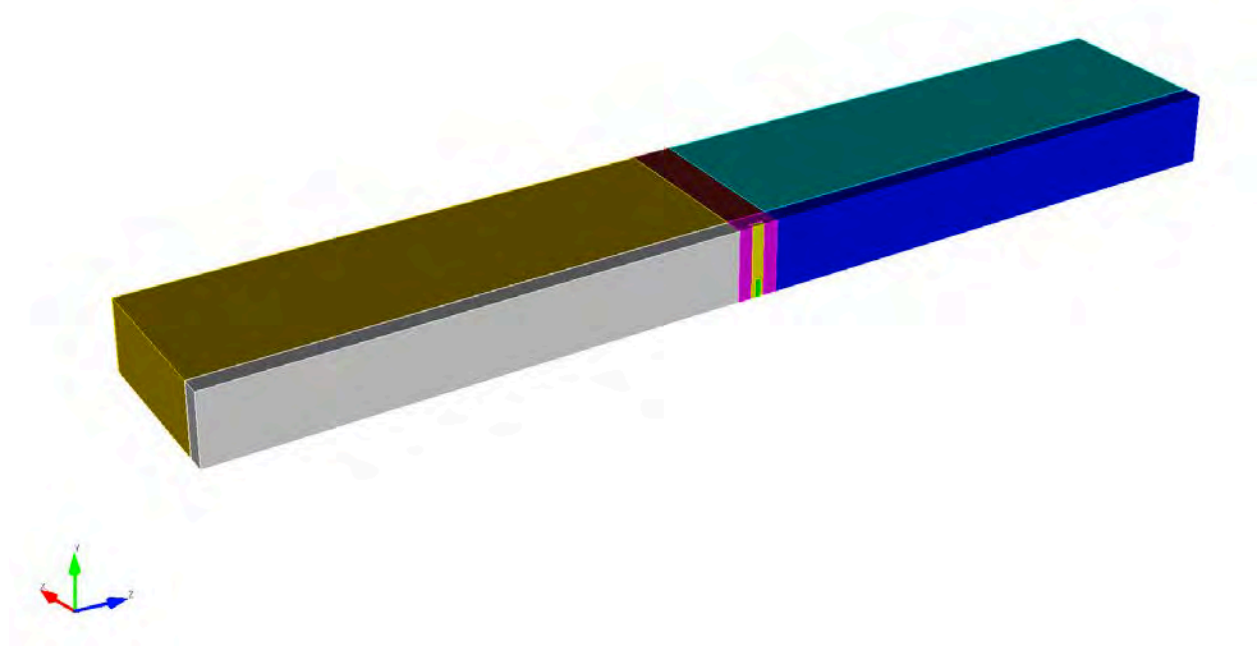
Figure 6-1. Isometric view of 2D rectangular model with 100x100 x1m domain in ANSYS Fluent.



One Quarter Waste Package Model

The geometry for the $\frac{1}{4}$ waste package model is generated in CUBIT and is identical to the geometry in Sevougian et al. (2019b) Section 4.2.3. It is one quarter of a full waste package and with closed lateral (reflection) boundaries this domain can be used to model a waste package that is in the center of an infinite array. Figure 6-2 shows an isometric view of the one quarter waste package model. All features in the model have been converted from cylindrical shape to equivalent-volume boxes for ease in meshing. In Figure 6-2 the waste package is colored in green, buffer in yellow, disturbed rock zone (DRZ) in pink and shale host rock in the remaining colored bodies.

Figure 6-2. Isometric view of the nearfield one quarter waste package model in a 25x10x150m domain in CUBIT.



6.2.1.2 ANSYS Fluent Meshing

ANSYS Fluent (Fluent, 2019) is used to generate the meshes on the two model domains. Three meshes are made for the 2D rectangular 100x100x1m model domain and one for the $\frac{1}{4}$ waste package model.

For both model domains, files containing the geometric surfaces for meshing are generated in CUBIT (Blacker et al., 2016) and imported into ANSYS-Fluent (Fluent, 2019). All ANSYS meshes are exported in MSH (.msh) ASCII file format and then converted into the PFLOTTRAN UGE (.uge) file format using Python scripts (Van Rossum and Drake, 2009). As part of the file conversion process, .ex files suitable for use as PFLOTTRAN boundary conditions are created for any boundaries that are aligned with the coordinate axes. Two separate mesh converters are required, one for hexagonal meshes and one for polyhedral meshes.

2D Rectangular Domain

Ansyl1, shown in on the left of Figure 6-3, has a surface mesh of 10,000 hexahedral cells with one element across the thin face. Ansys2, shown on the right of Figure 6-3, has a surface mesh of 160K and 4 elements across the thin face for a total of 640,000 hexahedral cells. Ansys3, shown in Figure 6-4, consists of 23,083 polyhedral cells generated on the 2D rectangular model domain. The properties of these meshes are shown in Tale 6-1.

Table 6-1. Properties for the ANSYS Fluent mesh of the 100x100x1m domain. Monitoring points and results for simulations of the 2D domain benchmark against Richards equation analytical solution are also shown. All simulation times are for parallel simulations using 8 nodes on a Linux Workstation with two cores of 8 nodes each.

Mesh name	Number of cells	Monitoring points (x, y, z)	Maximum error	Simulation time (min)
Ansys1	10,000 (hexahedral)	a (24.5, 24.5, 0.5), b (49.5, 49.5, 0.5), c (49.5, 74.5, 0.5), d (74.5, 74.5, 0.5)	0.05%	0.09
Ansys2	640,000 (hexahedral)	a (24.875, 24.875, 0.375), b (49.875, 49.875, 0.375), c (49.875, 74.875, 0.375), d (74.875, 74.875, 0.375)	0.04%	10.5
Ansys3	23,083 (polyhedral)	a (24.33, 24.428, 0.388), b (49.713, 49.891, 0.35), c (49.876, 74.964, 0.345), d (74.686, 74.317, 0.346)	49.71%	0.78

Figure 6-3. Top view of meshes generated on the 2D rectangular model with 100x100x1m domain in ANSYS Fluent. Left: Ansys1 mesh with 10,000 hexahedral elements. Right: Ansys2 mesh with 640,000 hexahedral elements.

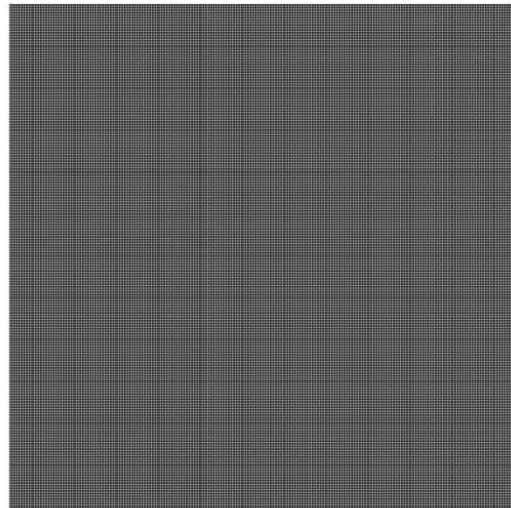
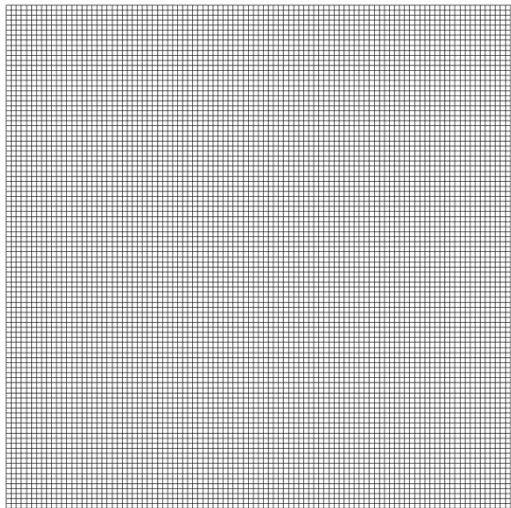


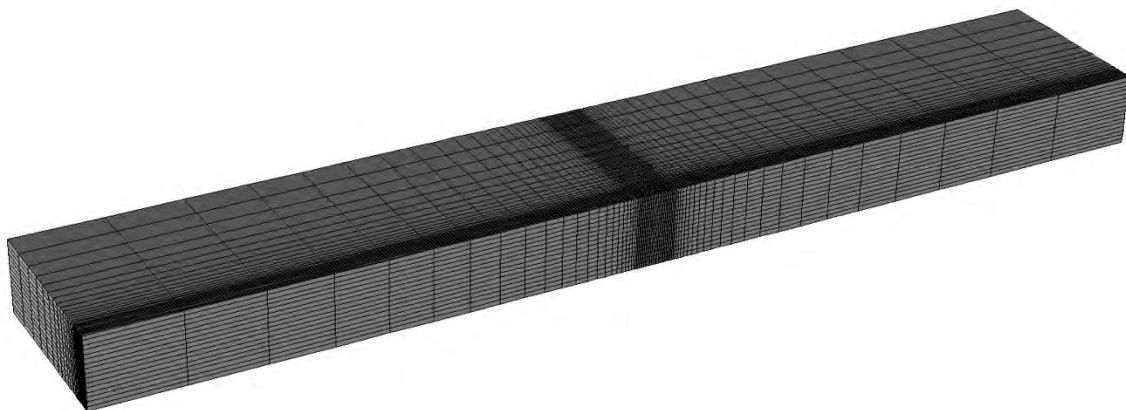
Figure 6-4. Isometric perspective projection of Ansys3 (23,083 polyhedral elements) generated on the 2D rectangular model with 100x100x1m domain in ANSYS Fluent.



One quarter waste package model

The mesh for the one quarter waste package model is shown in Figure 6-5. This mesh is a submap mesh of 37,440 cells on a nearfield modelling domain that is 25x10x150m. This mesh was generated in ANSYS Fluent, exported as an ANSYS Fluent .msh file and converted to a .uge mesh file for PFLOTRAN. Only one hexahedral mesh was generated for this problem.

Figure 6-5. Isometric view of submap mesh scheme (37,440 cells) of the one quarter waste package model with a 25 x 10 x 150m domain generated on ANSYS Fluent.



6.2.2 PFLOTRAN Simulations

This section presents three sets of simulation results. The first simulations test tracer propagation in the 2D rectangular model domain. The second is a benchmark simulation against a 2D Richards equation analytical solution on the same domain. The third is a nearfield shale one quarter waste package model simulation.

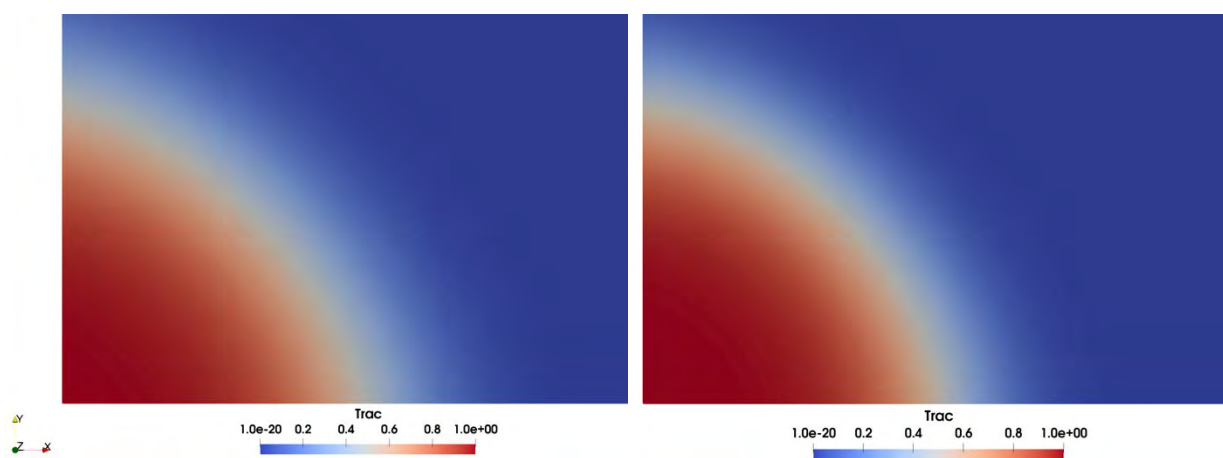
Tracer Propagation on 2D Rectangular Domain

The 2D rectangular model domain is set up to have injection at the corner where $x=0$ and $y=0$. The boundary is held constant at the initial conditions on the large x - and y -axis. All other boundaries are closed to study approximately radial tracer propagation in this simulation. Visualization software ParaView (Ayachit, 2015) is used to visualize the resulting simulations on the generated meshes. ParaView is an open-source, multi-platform data analysis and visualization application developed by SNL (<https://www.paraview.org/>). The left side of Figure 6-6 shows a ParaView visualization of the pressure and tracer propagation on the Ansys1 mesh of this model domain.

The Ansys1 mesh has 10,000 hex cells, and is the coarse model in this study, but this same simulation was run on coarser Fluent meshes of 4, 16, 100, and 400 hex cells (not shown). The coarse meshes resulted in a flat tracer front propagating outward, whereas in the more refined Ansys1 propagation is radial from the injection point on the lower left corner. The right side of Figure 6-6 shows the same tracer simulation on the finer Ansys2 mesh. The tracer propagation for the Ansys1 and Ansys2 meshes are very similar when compared with one another.

A simulation on Ansys3 also run but the results did not appear correct, likely due to errors in the conversion of the mesh to PFLOTRAN .uge format.

Figure 6-6. Left: ParaView visualization of left corner view of Ansys1 (10K hex mesh) generated on the 2D rectangular model with 100x100x1m domain showing tracer concentration. Right: ParaView visualization of top view of Ansys2 (640K hex mesh) generated on the 2D rectangular model with 100x100x 1m domain showing tracer concentration.



Richards Mode on 2D Rectangular Domain

The domain in this example is again the 100x100x1m slab with meshes Ansys1-Ansys3. The simulation is of a model with an analytical solution for two-dimensional transient single-phase flow that is taken from Kolditz et al. (2015, Section 2.2.10). Except for the mesh, the PFLOTRAN simulation is identical

to the example in the PFLOTRAN Quality Assurance (QA) test harness available at www.qa.pflotran.org (Frederick, 2018).

In this work the simulation meshes are externally generated and are of sufficiently high discretization that it is expected that all simulated solutions will be well within a 2% error tolerance of the analytical solution. The error metric chosen for this simulation is the maximum percent error at any timestep for any of the monitoring points. A stringent timestep control is used to ensure that the simulations all take exactly 1000 timesteps of size 1×10^{-4} days, so that the error comparison on each mesh has the same output times and is not skewed towards early- or late-time error.

The left side of Figure 6-7 shows the initial pressure field in for the simulation and the right shows pressure at the end of 0.1 days. An unusual color scale has been shown to emphasize that the initial condition is symmetric in all coordinate directions, but the evolution of the pressure field is only symmetric about the axes $x=50\text{m}$ and $y=50\text{m}$. Due to the left/right and top/bottom symmetry of the analytical solution, several points in the mesh correspond to the same solution. They are labeled a-d on Figure 6-7. Monitoring points b and c have the same initial condition, but due to the different boundary conditions they do not have the same pressure evolution during the simulation.

Figure 6-8 shows the pressure evolution as a function of time in days for the four unique monitoring points in the domain for Ansys1. The analytical solution and PFLOTRAN simulation of the pressure time series are indistinguishable. As listed on Table 6-1, Ansys1 resulted in a maximum error of 0.05%; surprisingly, there was only a 0.01% error improvement for Ansys2. This may indicate that the simulated error is approaching the accuracy of the internal approximations of PFLOTRAN. The main difference between the two is in the computational time required for the simulations to complete, (see Table 6-1 above). The computational time needed to run a simulation on Ansys1 is 0.09 minutes, and 10.5 minutes for Ansys2. This suggests Ansys1 might be preferred over Ansys2 due to the much shorter computation time and small error improvement.

Ansys3, the polyhedral mesh, has a large simulated error of nearly 50% and did not converge to the analytical solution. This benchmark test confirms that the mesh conversion for polyhedral meshes is incorrect. This does not have any implications for the accuracy of the hexagonal mesh conversion. ANSYS-Fluent has different output formats for the hexahedral and polyhedral meshes and there was a separate mesh conversion script, as discussed above.

Figure 6-7. Pressure on the plane $z=0.5$ for the Richards Equation test problem on a $100 \times 100 \times 1\text{m}$ domain with $380 \times 380 \times 3$ structured mesh. Left: Initial pressure condition. Right: Pressure at $t=0.1$ days.

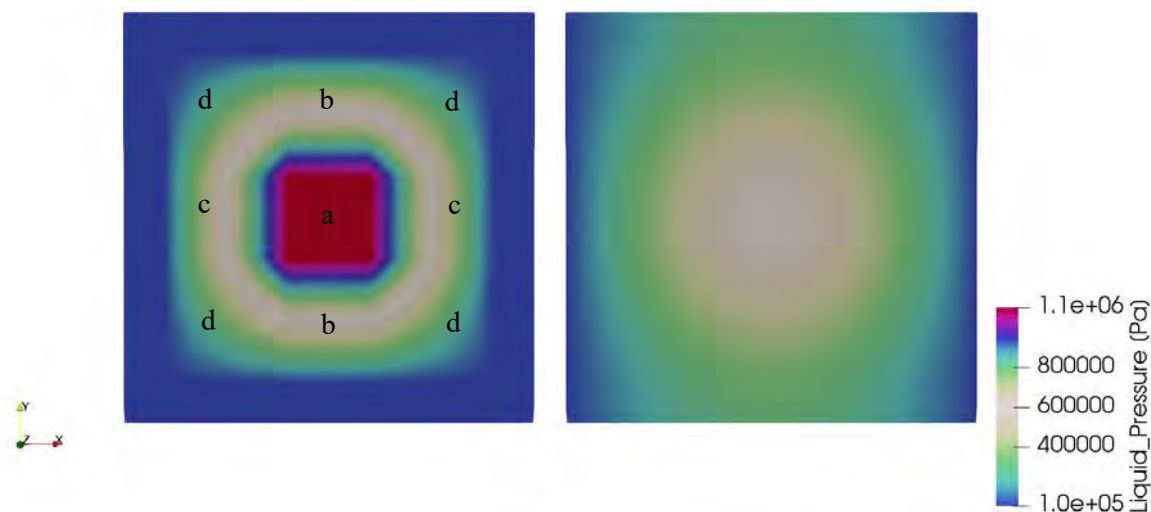
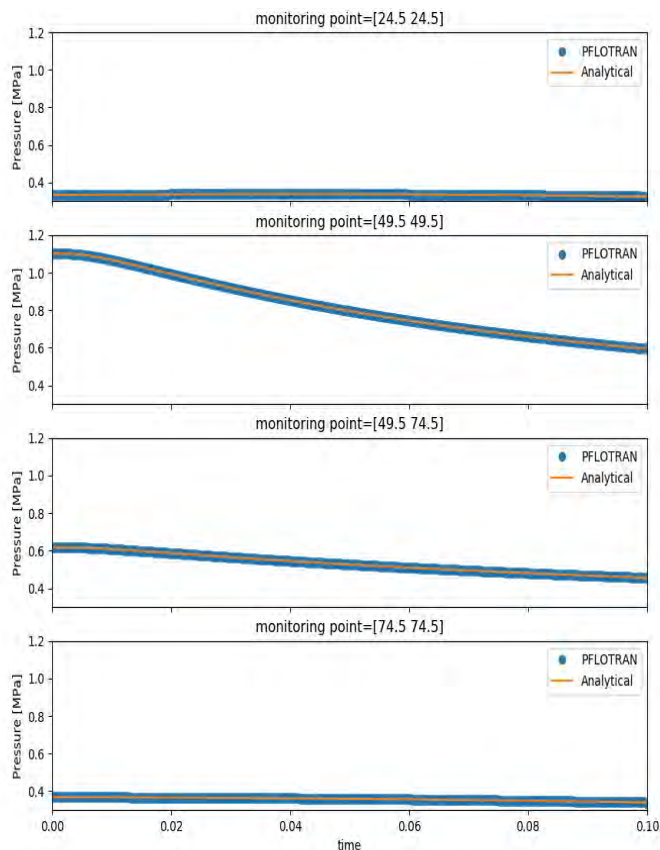


Figure 6-8. Pressure as a function of time in days at four monitoring points for the Richards Equation test problem on mesh Ansys1. Top: Monitoring point a (24.5, 24.5, 0.5). Second: Monitoring point b (49.5, 49.5, 0.5). Third: Monitoring point c (49.5, 74.5, 0.5) Bottom: Monitoring point d (74.5, 74.5, 0.5).



One Quarter Waste Package Model

The simulation performed on Ansys4, the one quarter waste package problem is on a truly 3D domain. The simulation properties are identical to those given in Sevougian et al. (2019b) Section 5.2.2, with the geometry taken from Section 4.2.3 of the same work. The waste package is assumed to be a 24-PWR 100 years OoR. The simulation domain is ¼ waste package with reflective boundaries, so the heat source is simulated with ¼ the energy output of a representative waste package. A tracer is simulated in the waste package which is injected at a very slow constant rate, as to not disturb the thermally-driven flow field. Simulation time is one million years and it takes 12.49 minutes to run using 16 nodes of a Linux workstation. Simulation details and monitoring points are shown in Table 6-2.

Visualization of 3D results is a challenge for the unstructured ANSYS-Fluent meshes, so the simulated outcomes are shown as dots that are colored according to each property. Figure 6-9 shows three snapshots in time in the columns (100y,1000y,10000y). On each of these columns from the top down, the total tracer concentration, liquid pressure and temperature are presented. The results are as expected, with high temperature at the waste package and high pressure across the model at 100 years, cooling and lower pressures at 1000 years, and a return to near initial conditions by 10,000 years. The results suggest the tracer is diffusing into the formation from the waste package at a very slow rate throughout the simulation, which is also what is expected (see also Figure 6-10). Figure 6-10 shows Total Tracer as a function of time in years for the full million-year simulation at four monitoring points for the nearfield one quarter waste package problem. Monitoring point wp is in the waste package. Monitoring point buffer

is in the buffer adjacent to the waste package. Monitoring point drz is in the DRZ near the waste package. Monitoring point shale is in the shale near the disturbed rock zone., Figure 6-11 and Figure 6-12 show the evolution of the total tracer concentration, liquid pressure, and temperature as a function of time for four unique monitoring points in the domain.

The total tracer evolution for the million-year simulations is plotted as a function of time in Figure 6-10. As expected, the plot shows that the highest tracer concentration throughout the simulation is found in the WP, the source of the tracer, and increases slowly but continuously with time throughout the simulation. At early time tracer spreads more rapidly, likely driven by the expansion of water as the waste package heats up.

The liquid pressure evolution as a function of time for the first 50 years of the simulation is shown in Figure 6-11. Pressure spikes in the waste package in the first few years of the simulation and quickly decreases to near the pressure of the rest of the monitoring points. The buffer pressure has a small, but observable peak in the first five years. The DRZ and shale pressure gradually increase throughout the 50 years shown.

The temperature evolution as a function of time for the first 10,000 years of the simulation is shown in Figure 6-12. Very early on the temperature spikes at 218 °C for the WP. The surrounding bodies (buffer, DRZ, shale) also see a rapid increase in temperature but the peak is not as high. By about 70,000 years, all four monitoring points reach a steady temperature near the initial value.

Table 6-2. Simulation summary for ANSYS Fluent generated mesh on nearfield one quarter waste package model. The simulation time is for a parallel simulation using 16 nodes on a Linux Workstation with two cores of 8 nodes each.

Mesh name	Number of cells	Monitoring points (x, y, z)	Simulation time (min)
Anslys4	37,440	wp (0.093, 1.562, 74.907), buffer (0.274, 5.312, 74.909), drz (1.438, 5.312, 73.726), shale (5.708, 5.312, 75.083)	12.49

Figure 6-9. Simulation results for the nearfield one quarter waste package model showing the Total tracer (M), Liquid Pressure (Pa) and Temperature (C) on three columns, each representing a different time. Column 1 represents time at 100 years, column 2 at 1,000 years and column 3 at 10,000 years.

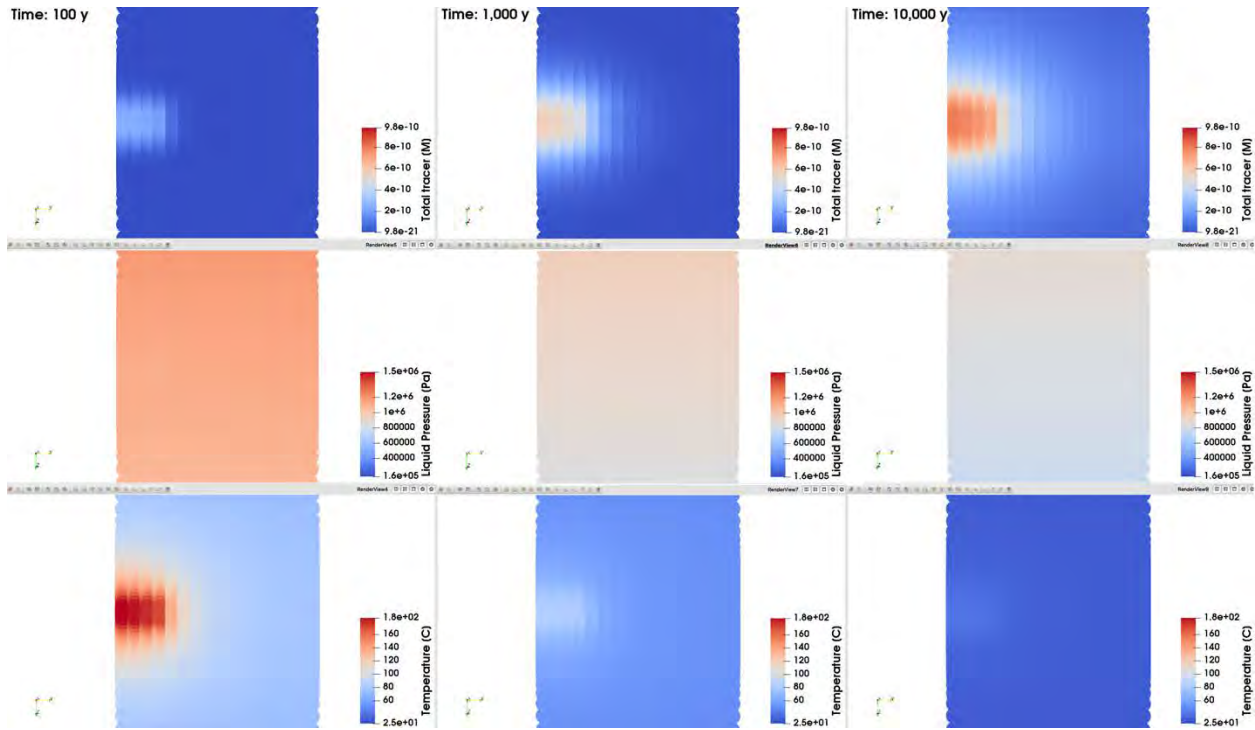


Figure 6-10. Total Tracer as a function of time in years for the full million-year simulation at four monitoring points for the nearfield one quarter waste package problem. Monitoring point wp is in the waste package. Monitoring point buffer is in the buffer adjacent to the waste package. Monitoring point drz is in the DRZ near the waste package. Monitoring point

shale is in the shale near the disturbed rock zone.

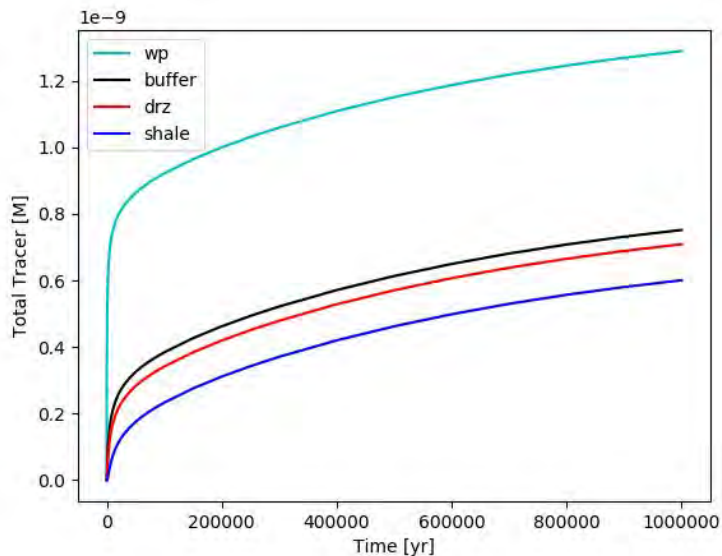


Figure 6-11. Liquid pressure as a function of time in years for the first 50 years of the simulation at four monitoring points for the nearfield one quarter waste package problem. Monitoring point wp is in the waste package. Monitoring point buffer is in the buffer adjacent to the waste package. Monitoring point drz is in the DRZ near the waste package. Monitoring point shale is in the shale near the disturbed rock zone.

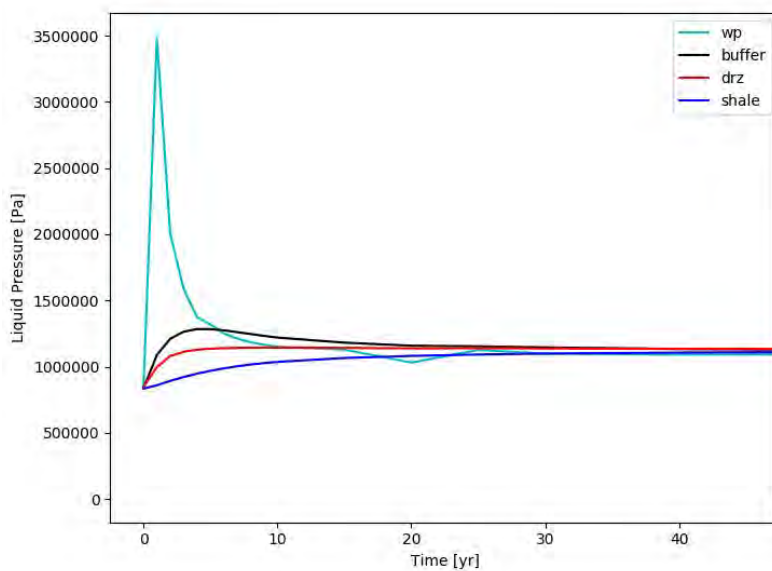
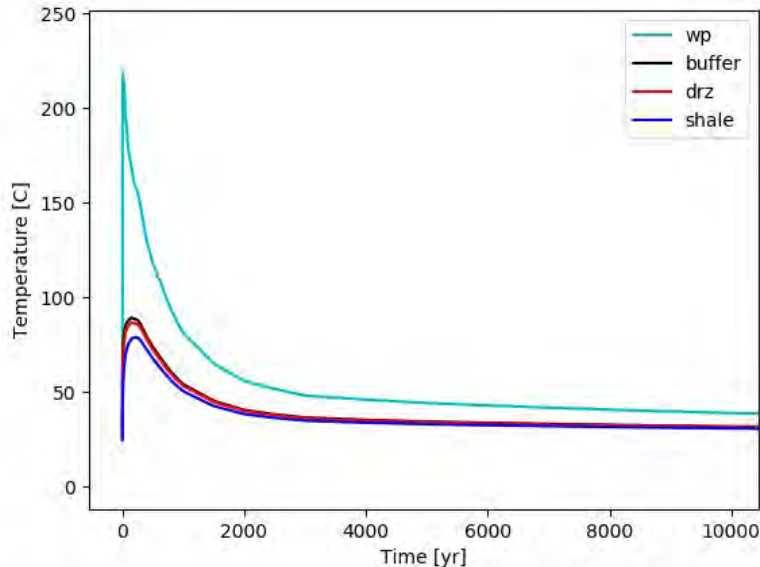


Figure 6-12. Temperature as a function of time in years for the first 10,000 years of the simulation at four monitoring points for the nearfield one quarter waste package problem. Monitoring point wp is in the waste package. Monitoring point buffer is in the buffer adjacent to the waste package. Monitoring point drz is in the DRZ near the waste package. Monitoring point shale is in the shale near the disturbed rock zone.



6.3 VoroCrust Simulations

In this section the results of PFLOTTRAN simulations on VoroCrust-generated Voronoi meshes are presented. Several intermediate processing steps are required to translate VoroCrust output into files that can be used by PFLOTTRAN and the workflow is outlined. Three analytical benchmark simulations are presented, followed by simulations on two realistic geological domains.

6.3.1 VoroCrust development overview

In the past year there has been substantial development of VoroCrust to improve its capability to generate Voronoi meshes for use in simulation. This work is detailed in Mariner et al. (2020) and briefly summarized here.

Development has included parallelization of parts of the code to speed up meshing, accepting user input to request monitoring points in the mesh, and accepting input with duplicate vertices. VoroCrust can accept nonmanifold surfaces and will automatically detect and assign region numbers to all enclosed volumes in the model. To improve ease of use there is now a webpage (<https://vorocrust.sandia.gov/>), gitlab code repository, dedicated help person for Sandia users and our LANL collaborators, and it can be installed on Mac and LINUX systems.

6.3.2 Workflow to make meshes suitable for PFLOTTRAN simulation

VoroCrust accepts Wavefront Object (.obj) files as input surfaces for meshing. All input surfaces must be watertight, though duplicate vertices are accepted. However, generating the .obj files is not a trivial task.

It is possible to create surfaces of virtually any geometric shape in CUBIT, but the stereolithography (.stl) files often were not watertight after conversion into .obj files. LaGrit (Los Alamos Grid Toolbox, 2017) is an open source code available at <http://lagrit.lanl.gov> that was developed at Los Alamos National Laboratory to create meshes for geological applications. LaGrit is able to read in surfaces created by geological mapping software and can also be used to create surfaces of geometric objects. In the VoroCrust workflow LaGrit is used to output surface .stl files. These files are converted to .obj files using

the visualization software ParaView (Ayachit, 2015). The .obj files are then read into VoroCrust, and Voronoi meshes are created in a fully automated process.

VoroCrust can read in a file of desired monitoring points in the domain. They are used as initial seeds. Sometimes as part of the meshing process the points are eliminated, so it can take several iterations of randomly generating a mesh to retain the monitoring points. The workflow for converting VoroCrust output into PFLOTRAN UNSTRUCTURED_EXPLICIT meshes is discussed in Appendix C VoroCrust output conversion.

6.3.3 Analytical benchmark models

Two analytical benchmark models are created for VoroCrust meshes. The first model tests simulations of pressure propagation in single-phase flow in the same thin 2D slab simulation used in Section 6.2 and shown in Figure 6-7. The second model tests simulation of radial heat conduction in a two-material cylinder.

6.3.3.1 VoroCrust Meshes

Example 1 Richards Mode

Five meshes were randomly generated of a 100x100x1m box domain to test the quality and consistency of VoroCrust mesh generation. The five meshes had between 431,656 and 432,941 grid cells as shown in Tale 6-3, which demonstrates good consistency in the grid size and hence resolution for this problem. VoroCrust was initialized with nine monitoring points for each mesh, representing the four unique points in the solution (a, b, c, and d) and five redundant monitoring points for the analytical solution shown in Figure 6-7. Only mesh Voro3 retained all four unique monitoring points in the final mesh, as shown in Table 6-3. Assigning monitoring points on a random mesh is discussed in more detail in Mariner et al. (2020).

A simulation on a structured 380x380x3 cell mesh with 433,200 nearly cubic cells was also run for comparison. Due to the mesh resolution, in the structured mesh the cell center of the monitoring cell was not exactly the same, as shown in Table 6-3. Error was calculated at the monitoring points shown, rather than the exact desired monitoring points. The initial condition and result of this simulation are shown in Figure 6-7.

Table 6-3. Properties for the VoroCrust and PFLOTRAN meshes of the 100x100x1m domain. Monitoring points and results for simulations of the 2D domain benchmark against Richards equation analytical solution are also shown. All simulation times are for parallel simulations using 12 nodes on a Linux Workstation with two cores of 12 nodes each.

Mesh name	Number of cells	Monitoring points	Maximum error	Simulation time (min)
Structured	433,200	a (50.132, 50.132, 0.5), b (50.132, 75.132, 0.5), c (75.132, 50.132, 0.5), d (75.132, 75.132, 0.5)	0.045%	8.49
Voro2	432,941	b (50, 25, 0.5),	0.025%	20.8

		d (25, 25, 0.5)		
Voro3	432,486	a (50, 50, 0.5), b (50, 25, 0.5), c (75, 50, 0.5), d (25, 25, 0.5)	0.043%	19.6
Voro4	432,102	a (50, 50, 0.5), b (50, 75, 0.5), d (75, 75, 0.5)	0.040%	22.2
Voro5	432,259	b (50, 25, 0.5), c (75, 50, 0.5), d (75, 75, 0.5)	0.043%	21.6
Voro6	431,656	a (50, 50, 0.5), d (75, 75, 0.5)	0.041%	21.3

Example 2 Heat Diffusion

This is the most complex of the benchmark problems, both computationally and in terms of the simulation domain. The simulation is of a radial two-domain heating problem based on the heat diffusion from a well problem presented in Dake (1978). There is an inner domain from $r=0$ to $r=50\text{m}$ with effective thermal diffusivity κ_1 and an outer domain from $r=50\text{m}$ to $r \rightarrow \infty$ with effective thermal diffusivity κ_2 . Where $\kappa = k_e / c_e \rho_e$ when k_e is the effective saturated thermal conductivity, c_e is the effective saturated specific heat and ρ_e is the effective density. The heat source is at $r=0$ and extends the full z -length of the domain. The composite problem can be constructed as two heat diffusion problems as outlined in Carslaw and Jaeger, (1959). It can be solved in Laplace transform space (e.g. Carslaw and Jaeger, 1959; Farlow, 1993; Greenberg, 1998) to give solution:

$$\begin{aligned}\bar{T}_1 &= c_1 I_0 \left(r \sqrt{s/\kappa_1} \right) + \frac{H}{s} K_0 \left(r \sqrt{s/\kappa_1} \right) \\ \bar{T}_2 &= c_4 K_0 \left(r \sqrt{s/\kappa_2} \right)\end{aligned}$$

where

$$\begin{aligned}c_1 &= \frac{\frac{H}{s} \left[\sqrt{\frac{\kappa_1}{\kappa_2}} \frac{K_1 \left(r_c \sqrt{s/\kappa_1} \right)}{K_1 \left(r_c \sqrt{s/\kappa_2} \right)} - \frac{K_0 \left(r_c \sqrt{s/\kappa_1} \right)}{K_0 \left(r_c \sqrt{s/\kappa_2} \right)} \right]}{\left[\frac{I_0 \left(r_c \sqrt{s/\kappa_1} \right)}{K_0 \left(r_c \sqrt{s/\kappa_2} \right)} + \sqrt{\frac{\kappa_1}{\kappa_2}} \frac{I_1 \left(r_c \sqrt{s/\kappa_1} \right)}{K_1 \left(r_c \sqrt{s/\kappa_2} \right)} \right]} \\ c_4 &= \sqrt{\kappa_1/\kappa_2} \left[\frac{\frac{H}{s} K_1 \left(r_c \sqrt{s/\kappa_1} \right)}{K_1 \left(r_c \sqrt{s/\kappa_2} \right)} - \frac{c_1 I_1 \left(r_c \sqrt{s/\kappa_1} \right)}{K_1 \left(r_c \sqrt{s/\kappa_2} \right)} \right],\end{aligned}$$

I_0 and K_0 are the Modified Bessel Functions of the first and second kind and order zero, $H = \frac{E}{2\pi h\kappa_1\tau_1}$ is a positive constant. The Laplace transform is inverted numerically using the Stehfest algorithm (Stehfest, 1970).

The simulation is calculated on a $\frac{1}{4}$ radial mesh for computational efficiency and ease of gridding. The domain is shown in Figure 6-13. For the simulation the outer radius is $r=100\text{m}$, which is sufficiently far away to not impact the simulated solution at short times.

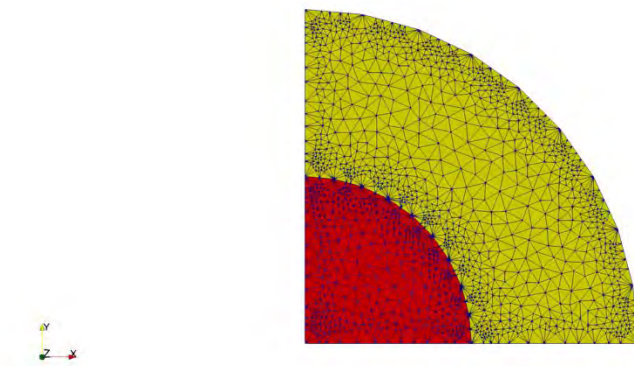
As in the previous example, the simulated solution for the two-domain heating problem using the VoroCrust mesh is compared to results using a PFLOTRAN-generated structured mesh and the analytical solution. The PFLOTRAN generated mesh is a 1D radial mesh, compared to the $\frac{1}{4}$ cylinder used for the VoroCrust simulation (see Figure 6-13). The VoroCrust mesh contained 13,857 cells, while the PFLOTRAN internally-generated mesh was 500×1 cells.

To compare the results between the two different meshes and the analytical solution, observation points were set at two different radii. The observation points were set at $r = 25$ and $r = 62.5$, these values were chosen to ensure results were obtained from both material layers in the domain. In the VoroCrust mesh, three points were selected along the arc for each radius to see if boundary effects on the x and y axis were causing changes in temperature values across the $\frac{1}{4}$ domain (since it was not a full circle). Table 6-4 summarizes the mesh properties and locations of the observation points.

Table 6-4. Properties of the VoroCrust and PFLOTRAN meshes for the two-domain radial simulation. Monitoring points and results for simulations benchmarked against the two-domain heating analytical solution are also shown.

Mesh name	Number of cells	Monitoring points	Maximum Relative Error	Simulation time (sec)
PFLOTRAN 1D radial	500	(25, 0.5) (62.5, 0.5)	0.0421% 0.0158%	16.17
VoroCrust ¼ cylinder	13,857	r=25 (4.341, 24.62, 5) (8.551, 23.4, 5) (24.62, 4.341, 5)	0.0244% 0.0251% 0.0296%	1.4669x10 ³
		r=62.5 (40.175, 47.8775, 5) (47.8775, 40.175, 5) (61.55, 10.8525, 5)	0.0722% 0.0832% 0.0225%	

Figure 6-13. Example surface mesh for the two-domain heating benchmark problem. Material 1 is red and exists from r=(0,50) and Material 2 is yellow and exists from (50,100).



6.3.3.2 PFLOTRAN Simulations

Example 1 Richards Mode

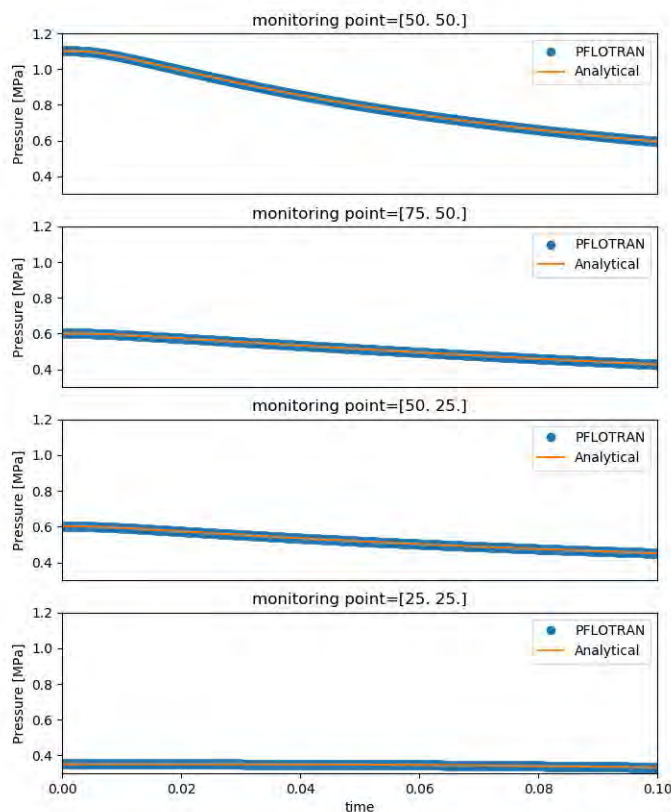
This is the same benchmark problem as presented in the Section 6.2.1.3 on ANSYS Fluent simulations. The solution on a structured mesh is shown in Figure 6-7. Though this simulation is a benchmark against the 2D analytical solution for transient single-phase flow from Kolditz et al. (2015), all VoroCrust meshes are three-dimensional and have vertical discretization of at least two grid cells everywhere in the domain. The monitoring points retained on each mesh are shown in Table 6-3.

Figure 6-14 shows the pressure evolution as a function of time for the four unique monitoring points in the domain for mesh Voro3. The analytical solution and PFLOTRAN simulation of the pressure are indistinguishable.

The simulation timestep constraint and error metric for these simulations are the same as in the section ANSYS Fluent simulations of the same problem in Section 6.2.3.1. The error in Table 6-3 is the maximum percent error at any timestep for any of the monitoring points that appear in the final mesh. This could introduce some inconsistency between the errors, as only mesh Voro3 has all four unique monitoring points. As shown in Table 6-3 the simulations are very accurate and have a similar level of accuracy with all meshes having between 0.025% and 0.043% error.

The VoroCrust mesh simulation errors are lower than the error in the benchmark structured mesh simulation of similar resolution, which had 0.045% error, though the difference is likely too small to be significant. This indicates that the simulations of this simple problem on VoroCrust meshes are at least as accurate as the same simulation on a structured mesh with nearly cubic grid cells. Simulation time is between 19.6 and 22.2 minutes for all the VoroCrust meshes (see Table 6-3). Consistency of simulation time across the mesh realizations is another indication of consistent mesh quality. The simulation times on the structured mesh is significantly shorter at 8.49 minutes, even though all simulations are forced to take the same number of time steps. Simulation of a simple rectangular domain such as this one is expected to be faster on the hexagonal mesh than an unstructured mesh. For the hexagonal mesh the matrix in the linear solver is a banded matrix that is strongly diagonally-dominant, which results in a relatively easy matrix problem in the PFLOTRAN solver. Conversely, the matrix for the completely unstructured VoroCrust meshes has no pre-defined form and results in a numerically more difficult matrix problem.

Figure 6-14. Pressure as a function of time in days at the four monitoring points for the Richards Equation test problem on mesh Vor03. Top: Monitoring point a (50,50,0.5). Second: Monitoring point c (75,50,0.5). Third: Monitoring point b (50,25,0.5) Bottom: Monitoring point d (25,25,0.5).



Example 2 Heat Diffusion

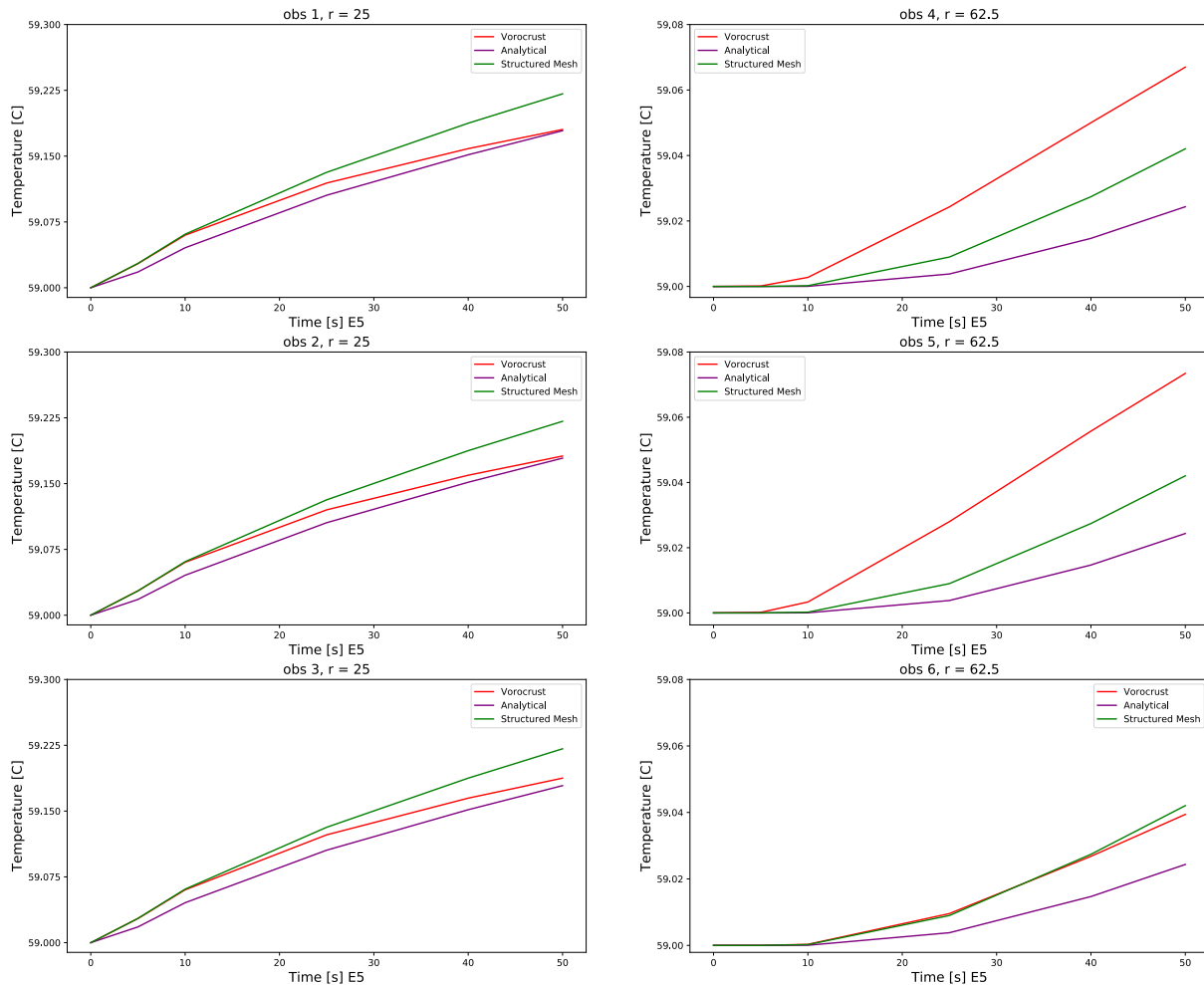
As discussed above, the simulated solution for the two-domain heating problem using the Vor0Crust mesh is compared to the analytical solution and the results using a PFL0TRAN-generated structured mesh of similar resolution. To account for the fact that the Vor0Crust mesh is a ¼ circle, the Vor0Crust mesh simulation heat source was set with ¼ the energy generation rate (2500 J/s) of the 1D simulation and the analytical solution. As would be expected with the larger mesh, the computation time for the Vor0Crust simulation was 1.47×10^3 seconds (24.5 min), compared to the 1D-radial PFL0TRAN mesh simulation that finished in only 16.17 seconds, as shown in Table 6-4.

Table 6-4 also shows the maximum relative error at each monitoring point compared to the analytical solution found at the same radius. The results showed that all the simulated results still fell well within reasonable error bounds. Errors are so low that it is unclear if there were boundary effects due to the ¼ domain.

Figure 6-15 displays plots of both of the simulated results compared to the analytical solutions. As can be seen, the observation points provided similar temperature values across the radial arcs for both monitoring points. The Vor0Crust mesh simulation was closer to the analytical solution at a radius of 25 for all observation point locations, while the 1D-radial PFL0TRAN mesh provided better results at the radius of 62.5 for two of the three radial points used in the Vor0Crust mesh.

Figure 6-15. PFLOTRAN 1D-radial structured and VoroCrust mesh temperature results compared to analytical solution at radii of 25 and 62.5 (Note: Structured mesh results are the same for each set of figures for their respective radii since only one simulation was ran for each).

Vorocrust vs Analytical, r=25 and r=62.5



6.3.4 Large-scale simulations

In this section two examples of PFLOTRAN simulations on VoroCrust meshes of large domains are presented. Both are geologically realistic. The first example is a simplification of the Rock Springs Uplift in Wyoming, while the second is a sector model from the shale GFM created in Sevougian et al 2019b) Section 5.1.

6.3.4.1 Wyoming Uplift tracer example

The Rock Springs Uplift, Wyoming example contains 8 curved surfaces with 7 materials between them. The surfaces in LaGrit were generated for studies in CO₂ storage (Deng et al., 2012). The surfaces generated for FEHM simulations in that work were demonstrated in Sevougian et al. (2019b) to be usable

for creating Vorocrust meshes. The model is stretched to 6x vertical exaggeration for ease of meshing and visualization. The Vorocrust surface mesh and material IDs of the Wyoming uplift model are shown in Figure 6-16. This realization of the mesh has 204,965 grid cells. Visualization of results on Vorocrust meshes remains a challenge. The best visualization method for this example is to have circles at each of the cell centers and color them according to simulation result quantity.

Contrasting permeability and porosity are assigned to each layer, as shown in Table 6-5. Left to right flow with an ideal tracer is simulated. This simulation uses RICHARDS flow mode in PFLOTRAN. The pressure gradient is enforced by a permeability-weighted injection with rate $5 \times 10^5 \text{ kg/s}$ all along the small x boundary (left) and constant initial pressure at the large x (right) boundary. The tracer source is the entire small x boundary so that it is transported into the domain with the injected water.

Figure 6-17 shows the pressure and tracer profiles for the Wyoming uplift simulation. Layers 6 and 7 at the top and bottom have been assigned very low permeability, so there is little pressure change or tracer invasion in those layers. Layers 1, 3 and 5 are the most permeable zones, so they have the greatest tracer invasion. The simulation took 20.0 hours on 12 cores of a Linux workstation. Gravity is omitted from the simulation to avoid very long computation time on this complex modelling domain.

Table 6-5. Permeability and porosity of each layer in the Wyoming uplift tracer example.

Layer Number	Permeability [m^2]	Porosity
1	1×10^{-12}	0.1
2	1×10^{-13}	0.15
3	1×10^{-12}	0.2
4	1×10^{-14}	0.15
5	1×10^{-12}	0.3
6	1×10^{-18}	0.01
7	1×10^{-18}	0.01

Figure 6-16. Left: VoroCrust surface mesh of the Wyoming uplift. Right: Material IDs of the Wyoming uplift in the simulation model.

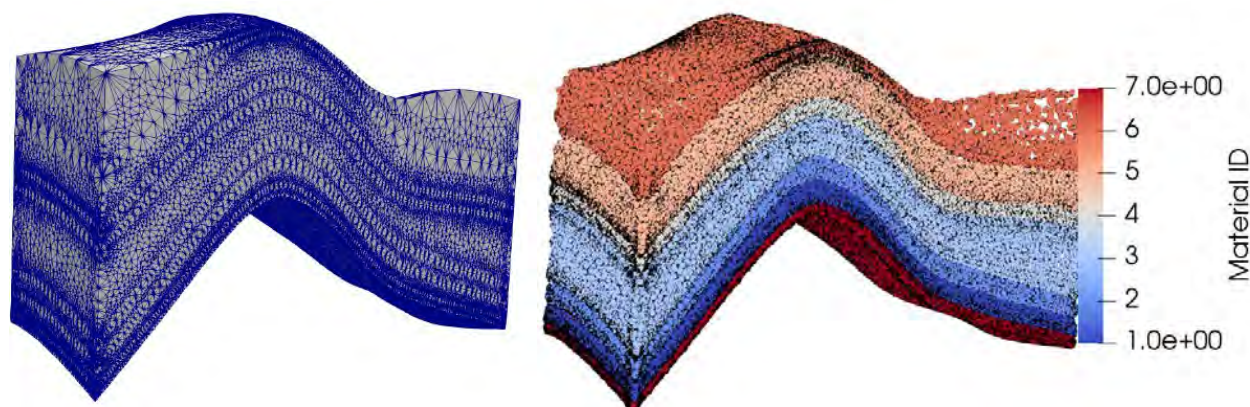
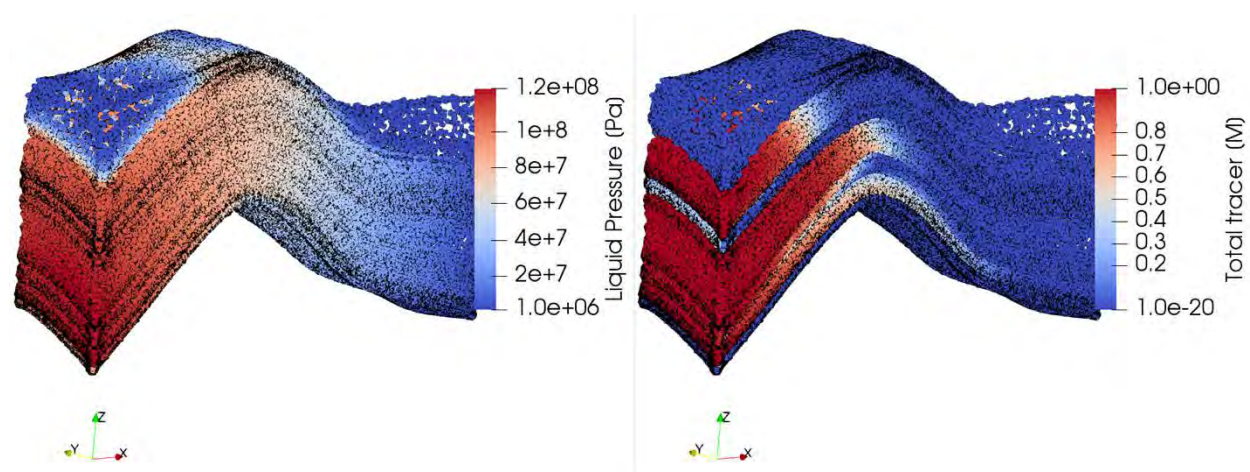


Figure 6-17. Left: Pressure during tracer injection into the Wyoming uplift. Right: Tracer concentration.



6.3.4.2 Unfractured shale GFM

The shale GFM model from Section 5.1 of Sevougian et al. (2019b) is used in this example. A 2.0x1.75km sector of the southwestern corner was clipped out of the full 69x83km (east/west x north/south) GFM model, reproduced in Figure 6-18. This is around $\frac{1}{4}$ of the size of the representative shale repository model PA model used in Sevougian et al. (2019a). Meshing a sector model reduces domain size and also improves the aspect ratio of the individual rock volumes in the model for VoroCrust meshing. The Fox Hills Sandstone at the top of the model is omitted because it does not span the full extent of the model and pinches out in multiple locations. Pinch outs are difficult to mesh because the intersection of two layers is often not watertight and VoroCrust cannot currently handle non-watertight surface intersections.

Even in the sector model some of the formations in the GFM model are very thin, which was challenging to mesh in VoroCrust and would have resulted in a large number of elements. A simplified model that omits some of the lower surfaces was meshed for simulation purposes. The omitted surfaces are the bases of the Undifferentiated Jurassic-Triassic shale, Opeche Shale, and Minnelusa Formation (See Figure 6-18).

The resulting simulation model lumps the volume of the Minnekahta Limestone into the Undifferentiated Jurassic-Triassic shales, and treats the Opeche Shale, Minnelusa Formation, and Madison Group as a single unit. This simplification should not greatly impact simulation results as the volume and properties of the Pierre Shale, Cretaceous Shale (K-shale), and the two most likely transport pathways, the Niobrara and Inyan Kara Group, are all preserved.

As part of the meshing work flow the GFM surfaces were put into a box with flat top and bottom surfaces. This simplifies the workflow to convert the surfaces created by Sevougian et al. (2019b) into the wavefront object (.obj) files that VoroCrust needs, however it adds additional cells to the model that must be assigned near-zero flow properties in the simulation. The workflow is discussed in more detail in Subsection 6.3.2 and Appendix C VoroCrust output conversion.

The simplified stratigraphy and VoroCrust mesh with 101,319 cells are shown in Figure 6-19. Detail of the simulation mesh around the Niobrara Formation is shown in Figure 6-20. The Niobrara is the thinnest layer in the simulation model, so in and around this layer the mesh is very fine and then it coarsens upwards into the Pierre Shale and downwards into the K-Shales.

The simulation is RICHARDS mode tracer flow of a highly simplified conceptual model of release from a repository. The mesh does not contain an explicitly-gridded repository, as this is beyond the capabilities of the current VoroCrust meshing workflow. Instead the tracer source is assigned to a box that is 200x200x40m. The large box is required for the source because the mesh has naturally coarsened in the center of the K-shale. In this realization of the mesh there are only three grid cell centers in the source region. The box is located in the K-Shale and the center is approximately 500m below the top of the Pierre Shale. Because the Fox Hills Sandstone was omitted from the simulation model, the Pierre Shale is too shallow in the modelling domain for disposal. The tracer source is in the middle of the domain in the east/west (x) dimension and is 200m south of the center of the repository in the y-direction.

Three tracers are simulated: an ideal tracer, an adsorbing tracer with adsorption coefficient similar to what is expected for Uranium in a shale, and a decaying tracer with decay coefficient equivalent to the half-life of ²³⁹Pu. No other chemical properties are assigned to the tracers and they are not otherwise representative of nuclear waste. Each tracer has a constant dimensionless initial condition $T_j=1.0$ at time $t=0$ in the repository, with no ongoing source of tracer during the one million year simulation.

Background flow is simulated by implementing a permeability-averaged injection condition of 3.835×10^4 kg/s to the entire southern (small y) boundary. The northern boundary is held constant at the initial pressure, and all other boundaries are closed. There is no gravity in this simulation due to long simulation times. The permeability and porosities for the simulation are the average values reported in Table 5-1. Disposal concepts considered by Prij et al. (1989).of Sevougian et al. (2019b). The lumped Minnekahta Limestone and Jurassic-Triassic shales are assigned the Jurassic-Triassic shale properties and the lumped Opeche Shale, Minnelusa Formation, and Madison Group are assigned Minnelusa properties. The non-physical top and bottom regions of the mesh are assigned near-zero permeability and porosity. Figure 6-21 and Figure 6-22 show the simulation results for the three tracers.

Figure 6-21 shows the tracer concentrations after 100,000 years. The concentrations are shown as both dots (top) and Delaunay interpolated values (bottom) because of the challenges in visualization. The ideal tracer (left) and decaying tracer (center) are diffusing through the K-shale and then flowing northward in the increasing y-direction through the overlying Niobrara shale/limestone and underlying Inyan Kara sandstone aquifer. The adsorbing tracer has hardly moved from the source. It is nearly impossible to see the adsorbing on the top subfigures, and it looks very uneven on the Delaunay projection. This is an artefact caused by the having only three cell centers within the repository/source region on the mesh.

Outside the repository, dimensionless concentration of the adsorbing tracer is never larger than 1×10^{-7} [-] at any simulated time.

Tracer concentrations at four monitoring points in the simulation domain are shown Figure 6-22. The top left subfigure shows that the ideal and decaying tracer flow and diffuse out of the source region, while the adsorbing tracer concentration remains near 1.0 for the full million-year simulation. The other three subfigures show low concentrations of the two mobile tracers exiting the domain at all three downstream monitoring points. For the ideal tracer flow in the over- and underlying-formations reaches a peak in the first half of the simulation and then gradually declines, but in the K-shale the outlet concentration is highest at very late time. For the decaying tracer concentrations downstream peak and then decline in the first 200,000 years and then drops off as the tracer decays away. By the end of 1,000,000 years the decaying tracer has virtually disappeared from the simulation.

Though the simulated scenario is greatly simplified from and smaller than PA calculations, these trends are consistent with what we would expect for radionuclide disposal in a layered shale formation such as the Pierre Shale. These results indicate that the VoroCrust meshes are capturing the formation shapes correctly and that PFLOTRAN is able to simulate on the unstructured meshes accurately and in a reasonable timeframe, as simulations took just under 3 hours using 12 processors on a Linux workstation.

Figure 6-18. GFM model of the Pierre Shale from the northeast at 10x vertical resolution (taken from Sevougian et al., April 2019).

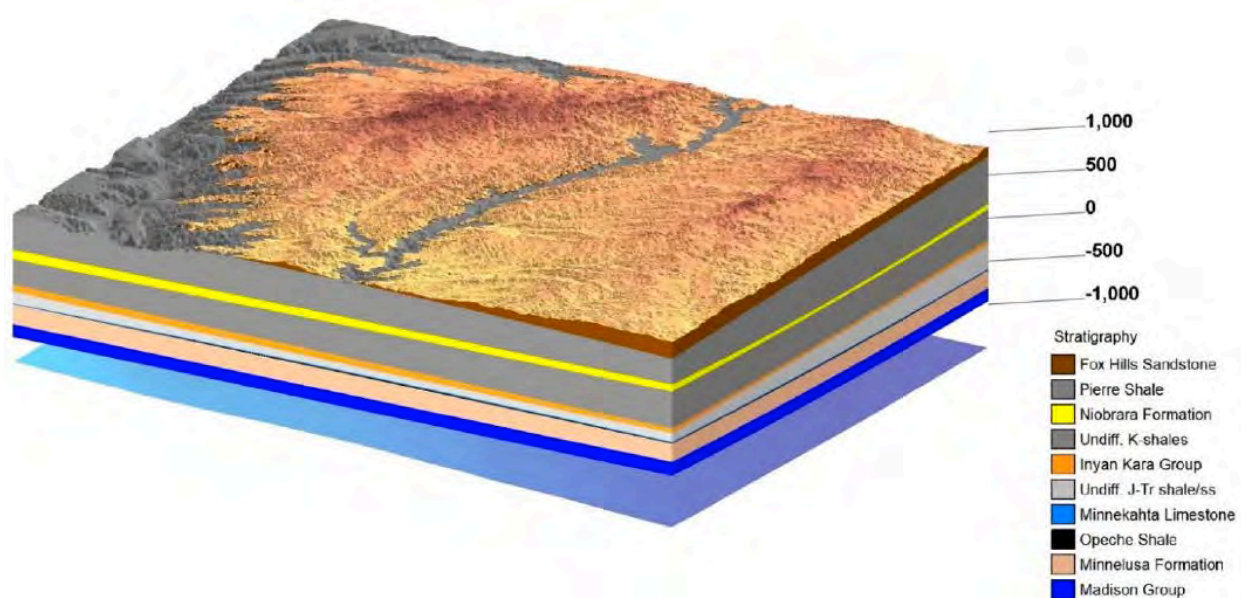


Figure 6-19. 2.0x1.75 km sector of the shale GFM model simplified to 6 representative rock volumes. Colors are the same as in Figure 6-18 above. Left: Formation volumes. Right: Surface mesh generated in VoroCrust.

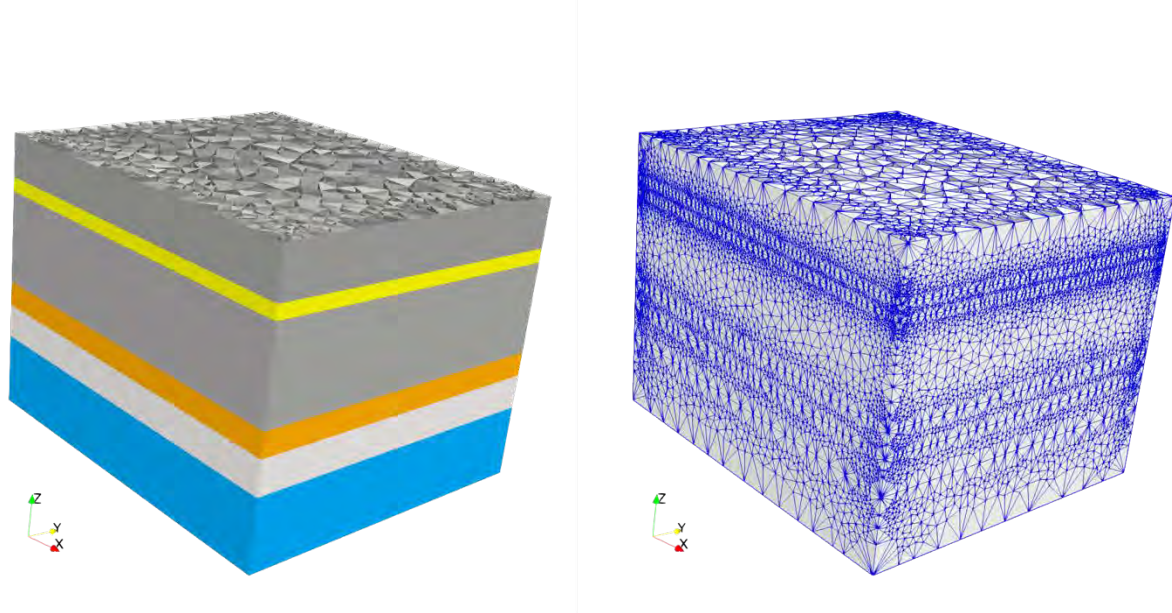


Figure 6-20. Close up of the VoroCrust mesh around the Niobrara Formation, the thinnest layer in the simulation model.

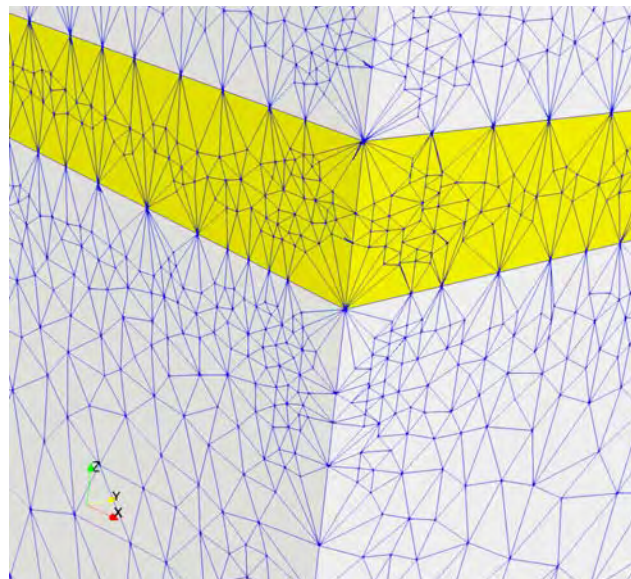


Figure 6-21. Tracer concentrations 100,000 years after release. Left: ideal tracer. Middle: decaying tracer. Right: adsorbing tracer. North is in the direction of increasing y to the right.

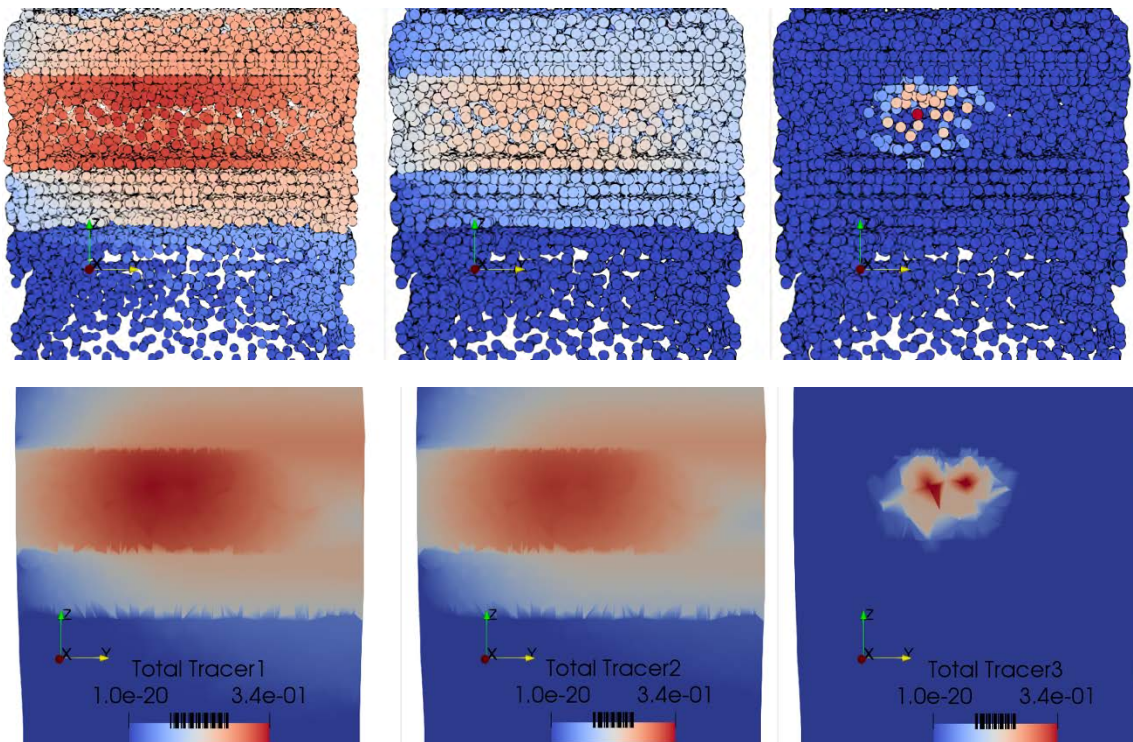
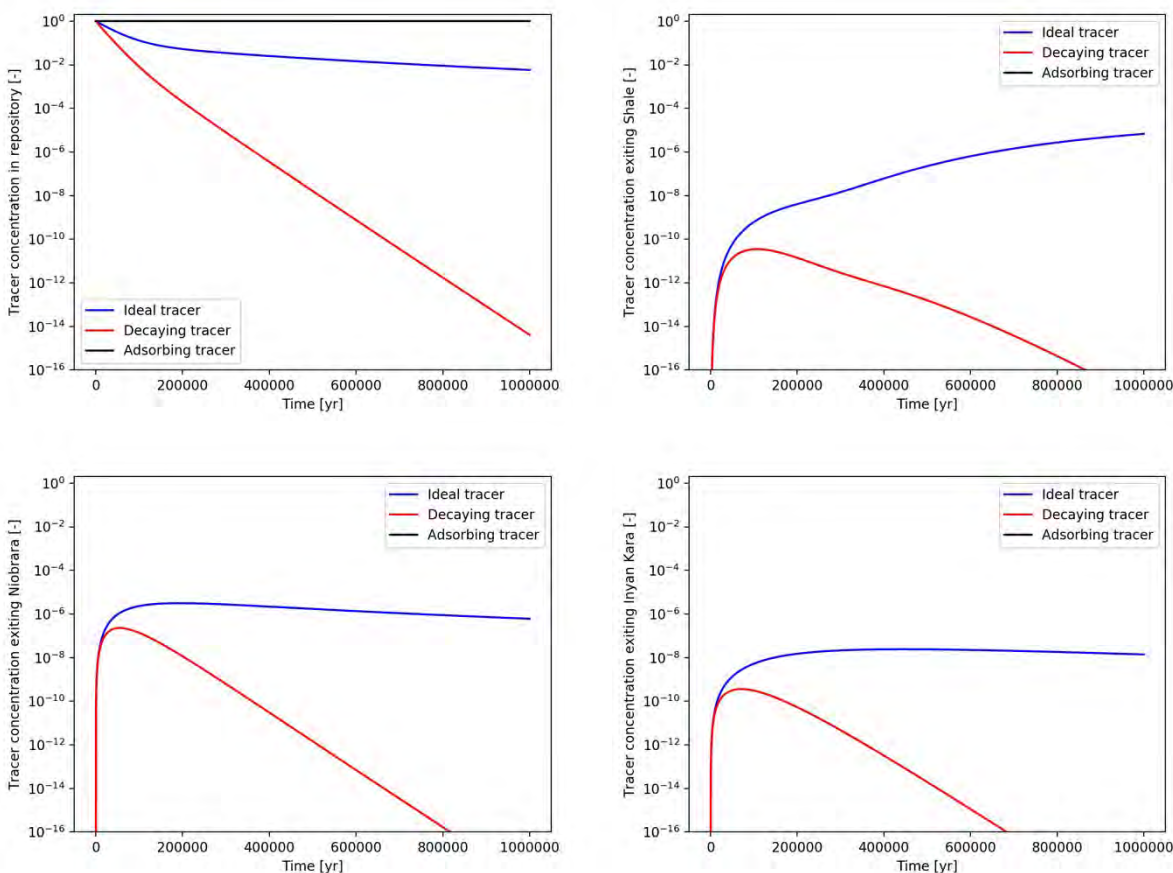


Figure 6-22. Tracer concentrations as a function of time at four monitoring points in the shale GFM sector model. Top Left: In the K-shale at the tracer source. Top Right: In the K-shale at the model boundary immediately downstream of the tracer source. Bottom Left: In the Niobrara aquifer at the model boundary immediately downstream of the tracer source. Bottom Right: In the Inyan Kara aquifer at the model boundary immediately downstream of the tracer source. Notice that the x-scale is logarithmic and adsorbing tracer concentration is so low ($\sim 1 \times 10^{-20}$) it has been cut off all of the subplots except for the one in the repository.



6.3.5 Vorocrust simulation results and future work

The two analytical benchmark problems demonstrate that PFLOTRAN simulations on Vorocrust meshes have a high level of accuracy and reproducibility. Though the two benchmarks have simple physics, they are 1D and 2D domains, which makes them challenging to mesh using the inherently 3D simulation meshes that Vorocrust creates. The analytical benchmarks converged less than 0.1% error. All benchmark simulations were as accurate on Vorocrust meshes as the similar-sized structured PFLOTRAN meshes used for comparison.

The two geological-scale tracer examples showed the capability of Vorocrust to generate meshes from geological models and the ability of PFLOTRAN to simulate on them. The PFLOTRAN simulations showed tracer flow that is consistent with the expected results and were achieved in acceptable computation times, considering the scale and complexity of the problems.

The simulation results also indicate areas where future work is needed. Generating Vorocrust meshes for volumes with high aspect ratios can be time-consuming, and may fail entirely, as happened in the case of

the full shale GFM. Further parallelization of VoroCrust would speed up the mesh generation process. Anisotropic meshing would reduce number of grid cells in narrow regions and allow for narrower regions to be meshed. Work on visualization of 3D results is ongoing, but was not available in time for this report.

For future PFLOTRAN PA simulations it is necessary to be able to explicitly introduce a repository into the simulation mesh. The small number of large grid cells in the shale simulation undoubtedly caused numerical diffusion in the tracer concentrations near the source. The PFLOTRAN simulations presented do not include gravity because of long computation times and/or convergence failure when gravity is included on these unstructured explicit meshes. The exact cause is unclear, but requires further investigation.

6.4 Comparison of ANSYS-Fluent and VoroCrust meshes

Sections 6.2 and 6.3 both discuss exploration of new meshing software and with new types of grids. PFLOTRAN benchmark and more complex demonstration problems were run on meshes created from both ANSYS_Fluent and Vorocrust software. The Richards mode analytical benchmark had a similar level of accuracy on both types of meshes.

The ANSYS-Fluent meshes proved to be unexpectedly difficult to convert into the PFLOTRAN UNSTRUCTURED_EXPLICIT format for simulations. Ultimately it was only possible to convert hexagonal Fluent meshes correctly.

Given the difficulty in converting the ANSYS-Fluent meshes, and that only VoroCrust is open-source, it is clear that only the VoroCrust meshes are worth continued study. Furthermore, VoroCrust can and will be further tailored to GDSA needs in future years as part of our ongoing collaboration with the developers.

This page intentionally left blank

7. REFERENCES

Adams, B. M., W. J. Bohnhoff, K. R. Dalbey, M. S. Ebeida, J. P. Eddy, M. S. Eldred, R. W. Hooper, P. D. Hough, K. T. Hu, J. D. Jakeman, M. Khalil, K. A. Maupin, J. A. Monschke, E. M. Ridgway, A. A. Rushdi, D. T. Seidl, J. A. Stephens, L. P. Swiler, and J. G. Winokur. 2020. *Dakota, A Multilevel Parallel Object-Oriented Framework for Design Optimization, Parameter Estimation, Uncertainty Quantification, and Sensitivity Analysis: Version 6.12 User's Manual*. SAND2020-5001. Sandia National Laboratories, Albuquerque, NM.

ANDRA, 2005. *Dossier 2005 argile – architecture and management of a geological disposal system*. December 2005. Andra.fr/international/download/Andra-international-en/document/editions/268va.pdf.

Ayachit, U., 2015, *The ParaView Guide: A Parallel Visualization Application*, Kitware, ISBN 978-1930934306

Banerjee, K., Robb, K.R., Radulescu, G., Miller, P.L., Scaglione J.M., Cuta, J.M., and Liljenfeldt, H., 2016. *UNF-ST&DARDS: A Unique Tool for Automated Characterization of Spent Nuclear Fuel and Related Systems*, PATRAM 2016, Japan Society of Mechanical Engineers and Atomic Energy Society of Japan, Kobe, Japan.

Belcher, W.R., Sweetkind, D.S., Elliott, P.E., 2002. *Probability distributions of hydraulic conductivity for the hydrogeologic units of the Death Valley Regional Ground-Water Flow System, Nevada and California*. U.S. Geological Survey Water-Resources Investigations Report 02-4212, 24 p.

Bernier, F., Li, X. L., Bastiaens, W., Ortiz, L., Van Geet M., Wouters, L., Frieg, B., Blümling, P., Desrues, J., Viaggiani, G. Coll, C., Chanchole, S., De Greef, V., Hamza, R., Malinsky, L., Vervoort, A., Vanbrabant, Y., Debecker, B., Verstraelen, J., Govaerts, A., Wevers, M., Labiouse, V., Escoffier, S., Mathier, J. F., Gastaldo, L., Bühler, 2007. *Fractures and self-healing within the excavation disturbed zone in clays (SELFRAC)*, SELFRAC Project Final Report, European Commission.

Blacker, T., Owen, S. J., Staten, M. L., Quador, R. W., Hanks, B., Clark, B., Meyers, R. J., Ernst, C., Merkley, K., Morris, R., McBride, C., Stimpson, C., Plooster, M., and Showman, S., 2016. *CUBIT Geometry and Mesh Generation Toolkit 15.2 User Documentation*, SAND2016-1649R, Sandia National Laboratories, Albuquerque, New Mexico.

Blackwell, D. D., Richards, M. C., Frone, Z. S., Batir, J. F., Williams, M. A., Ruzo, A. A., and Dingwall, R. K., 2011. “*SMU Geothermal Laboratory Heat Flow Map of the Conterminous United States, 2011*,” Supported by Google.org. Available at <http://www.smu.edu/geothermal> Retrieved October 25, 2016.

Bock, H., Dehandschutter, B., Martin, C.D., Mazurek, M., de Haller, A., Skoczylas, F., Davy, C. 2010. *Self-sealing of fractures in argillaceous formations in context with the geological disposal of radioactive waste*. OECD/NEA report 6184, OECD Nuclear Energy Agency, Paris, France, 312 p.

Bollingerfehr, W., Bertrams, N., Buhmann, D., Eickemeier, R., Fahland, S., Filbert, W., Hammer, J., Kindlein, J., Knauth, M., and Wenting, L., 2018. *Concept developments for a generic repository for heat-generating waste in bedded salt formations in Germany*. Synthesis Report (No. BGE TEC 2018-13). BGE TECHNOLOGY GmbH.

Bollingerfehr, W., Buhmann, D. and Doerr, S., 2017. *Evaluation of methods and tools to develop safety concepts and to demonstrate safety for an HLW repository in salt*. Final Report (No. TEC-03-2017-AB). DBE Technology GmbH.

Bourg, I. C., 2015. *Sealing Shales versus Brittle Shales: A Sharp Threshold in the Material Properties and Energy Technology Uses of Fine-Grained Sedimentary Rocks*. *Environmental Science & Technology Letters*, 2(10), 255-259.

Bredehoeft, J. D., Neuzil, C. E., and Milly, P.C.D., 1983. *Regional Flow in the Dakota Aquifer: A Study of the Role of Confining Layers*. Water-Supply Paper 2237. United States Geological Survey, Alexandria, Virginia. 50 p.

Buhmann, D.; Mönig, J., Wolf, J., Keller, S.; Mrugalla, S.; Weber, J.R.; Krone, J. Lommerzheim, A., 2010. *Behandlung von Unge- wisshheiten im Langzeitsicherheitsnachweis für ein HAW-Endlager im Salzgestein. ISIBEL Projekt*. Gemeinsamer Bericht von DBE TECHNOLOGY GmbH, BGR und GRS, Peine.

Bustin R.M., Bustin, A.M.M., Cui, X., Ross, D.J.K., and Pathi, V.S.M. 2008, "Impact of shale properties on pore structure and storage characteristics," *In SPE shale gas production conference*. Fort Worth, Texas, USA. Nov. 16-18, 2008, SPE 119892-MS.

Camphouse, C., D. C. Kicker, T. Kirchner, J. Long, B. Malama, and T. R. Zeitler 2012. *Summary Report and Run Control for the 2012 WIPP Panel Closure System Performance Assessment*. Sandia National Laboratories, Waste Isolation Pilot Plant, Carlsbad, NM.

Caporuscio, F. A., Sauer, K. B., and Rock, M. J. 2019. LA-UR-19-24222. Los Alamos National Laboratory, Los Alamos, NM.

Carlsaw, H. S. and Jaeger, J. C., 1959, *Conduction of heat in solids*. Oxford University Press, Oxford, UK, 2nd edition.

Carter, J., Luptak, A. J., Gastelum, J., Stockman, C. T., and Miller, A., 2013. *Fuel Cycle Potential Waste Inventory for Disposition*. FCR&D-USED-2010-000031 Rev 6. Savannah River National Laboratory, Aiken, SC.

Carter, J.T., Rodwell, P.O, Robinson, B., and Kehrman, B., 2012. *Defense Waste Salt Repository Study*, FCRD-UFD-2012-000113, May 5, 2012.

Cartwright, K. 1970. *Groundwater discharge in the Illinois Basin as suggested by temperature anomalies*. *Water Resources Research* 6, no. 3: 912–918.

Casey, G.D., 1996. *Hydrogeologic framework of the midwestern basins and arches region in parts of Indiana, Ohio, Michigan, and Illinois (Regional aquifer-system analysis-midwestern basins and arches)*. U.S. Geological Survey professional paper 1423-B). 54 p.

Chen, D., Pan, Z.J., and Ye, Z.H., 2015, *Dependence of gas shale fracture permeability on effective stress and reservoir pressure: model match and insights*, *Fuel*, 139:383-392.

Circular 528, 49 p.

Clarity, J. B., Banerjee, K., Liljenfeldt, H. K., Marshall, W. J., 2017. *As-Loaded Criticality Margin Assessment of Dual-Purpose Canisters Using UNF-ST&DARDS*, Nuclear Technology 199 no. 3: 245-275.

Clayton, D., Freeze, G., Hadgu, T., Hardin, E. L., Lee, J., Prouty, J., Rogers, R., Nutt, W.M., Birkholzer, J., Liu, H.H., Zheng, L., and Chu, S., 2011. *Generic Disposal System Modeling – Fiscal Year 2011 Progress Report*. FCRD-USED-2011-000184, SAND2011-5828P. U.S. Department of Energy, Office of Nuclear Energy, Used Fuel Disposition Campaign, Washington, DC.

Clayton, D.J., Arguello Jr, J.G., Hardin, E.L., Hansen, F.D., and Bean, J.E., 2012. “*Thermal-Mechanical Modeling of a Generic High-Level Waste Salt Repository.*” In: *SALTVII, 7th Conference on the Mechanical Behavior of Salt*, Paris, France. April 16-19, 2012. (www.saltmech7.com), SAND2012-2741C.

CO₂ Sequestration and Application to Illinois Basin, Reporting Period: October 1, 2009 - September 30, 2012. DOE Award Number: DE-FC26-FE0001161. New Mexico Tech, Department of Earth and Environmental Sciences, Socorro NM. 34 p.

Commissie Opberging te Land (OPLA), 1989. *Onderzoek naar geologische opberging van radioactief afval in Nederland*. Eindrapport Fase 1. Ministerie van Economische Zaken. Den Haag.

Cook, P. and Herczeg, A.L., 2000. *Environmental Tracers in Subsurface Hydrology*, Kluwer Academic Publishers, Norwell, MA.

Dake, L. P., 1983, *Fundamentals of reservoir engineering*. Elsevier.

Deng, H., Stauffer, P.H., Dai, Z., Jaio, Z., Surdam, R.C., 2012, *Simulation of Industrial-Scale CO₂ Storage: Multi-Scale Heterogeneity and its Impacts on Storage Capacity, Injectivity and Leakage*, Int. J. Greenhouse Gas Control, Volume 10, September 2012, Pages 397–418.

DOE (U.S. Department of Energy), 2012. *Used Fuel Disposition Campaign Disposal Research and Development Roadmap*. FCR&D-USED-2011-000065, REV 1, U.S. DOE Office of Nuclear Energy, Used Fuel Disposition, Washington, D.C., September 2012.

DOE, 2009. *Waste Isolation Pilot Plant Compliance Recertification Application*. DOE 2009-24-34. March 2009.

Downey, J. S. and Dinwiddie, G.A., 1988. *The Regional Aquifer System Underlying the Northern Great Plains in Parts of Montana, North Dakota, South Dakota, and Wyoming - Summary*. Professional Paper 1402-A. United States Geological Survey, Washington, DC.

Droste, J. B., and Vitaliano, C. J., 1976. *Geologic report of the Maquoketa Shale, New Albany Shale, and Borden Group rocks in the Illinois Basin as potential solid waste repository sites*. Oak Ridge National Laboratory, Oak Ridge, Tennessee. Y/OWI/SUB--7062/1. 56 p.

- Eaton, T. T., Hart, D. J., Bradbury K. R., and Wang, H. F., 2000. *Hydraulic Conductivity and Specific Storage of the Maquoketa Shale*. WGNHS Open-File Report 2000-01. University of Wisconsin, Water Resources Institute, Madison, WI. 38 p.
- Farlow, S. J., 1993, *Partial Differential Equations of Scientists and Engineers*. Dover Publications, Inc, New York, USA, 1st edition.
- Fluent User's Guide, Nov. 2019, Fluent Inc., Part II: Meshing Mode.
- Fox B., 2008. *Parameter Summary Report for CRA-2009, Revision 0*, WIPP:1.2.5:PA:QA-L:547488, Sandia National Laboratories, Carlsbad, New Mexico.
- Frederick, J.M., 2018. PFLOTRAN QA Test Suite. Retrieved July 28, 2020 from qa.pflotran.org.
- Freeze, G., Voegelé, M., Vaughn, P., Prouty, J., Nutt, W.M., Hardin, E. and Sevougian, S.D., 2013b. *Generic Deep Geologic Disposal Safety Case*. FCRD-UFD-2012-000146 Rev. 1, SAND2013-0974P, August 2013, Sandia National Laboratories, Albuquerque, New Mexico.
- Freeze, G., Gardner, P., Vaughn, P., Sevougian, S.D., Mariner, P., Mousseau, V. and Hammond, G., 2013. *Enhancements to Generic Disposal System Modeling Capabilities*. FCRD-UFD-2014-000062. SAND2013-10532P. Sandia National Laboratories, Albuquerque, New Mexico.
- Gale, J. F. W., Laubach, S. E., Olson, J. E., Eichhubl, P., and Fall, A., 2014. *Natural fractures in shale: a review and new observations*. AAPG Bulletin 98 (11), 2165-2216.
- Gonzales, S., and Johnson, K.S., 1985. *Shale and other argillaceous strata in the United States*. Oak Ridge National Laboratory report 84-64794, 594 p.
- Greenberg, M. D. 1998, *Advanced Engineering Mathematics*. Prentice Hall, Upper-Saddle River, New Jersey, USA, 2nd edition.
- Greene, S.R., Medford, J.S. and Macy, S.A., 2013. *Storage and Transport Cask Data for Used Commercial Nuclear Fuel – 2013* U.S. Edition. ATI-TR-13047. Knoxville, Tennessee: Advanced Technology Insights, LLC; Oak Ridge, Tennessee: EnergX.
- Gupta, N., and Bair, E.S., 1997. *Variable-density flow in the midcontinent basins and arches region of the United States*. Water Resources Research, 33. 1785-1802.
- Hammond, G.E., Lichtner, P.C. and Mills, R.T., 2014. *Evaluating the performance of parallel subsurface simulators: An illustrative example with PFLOTRAN*. Water Resources Research, 50(1), 208-228. doi: 10.1002/2012wr013483
- Hansen, F.D. and Leigh, C.D., 2011. *Salt Disposal of Heat-Generating Nuclear Waste*, SAND2011-0161, Sandia National Laboratories, Albuquerque, New Mexico.
- Hardin, E., Clayton, D., Howard, R., Scaglione, J.M., Pierce, E., Banerjee, K., Voegelé, M.D., Greenberg, H., Wen, J., Buscheck, T.A., Carter, J.T., Severynse, T., and Nutt, W.M., 2013. *Preliminary Report on Dual-Purpose Canister Disposal Alternatives (FY13)*, August 2013, FCRD-UFD-2013-000171 Rev. 0.
- Hartley, L., Baxter, S., and Williams, T., 2016. *Geomechanical Coupled Flow in Fractures during Temperate and Glacial Conditions*. Working Report 2016-08. Posiva Oy, Eurajoki, Finland.

- James, S. and Stein, J., 2002. *Analysis Plan for the Development of a Simplified Shaft Seal Model for the WIPP Performance Assessment*, AP-094 Rev. 0, December 11, 2002, Sandia National Laboratories, Carlsbad, New Mexico.
- Jove Colon, C. F., Weck, P., Zheng, L., Rutqvist, J., Steefel, C. I., Kim, K., Nakagawa, S., Houseworth, J., Birkholzer, J., Caporuscio, F. A., Cheshire, M., Rearick, M. S., McCarney, M. K., Zavarin, M., Benedicto, A. B., Kersting, M. S., Jerden, J. L., Frey, K. E., Copple, J. M., and Ebert, W. L., 2014. *Evaluation of Used Fuel Disposition in Clay-Bearing Rock*. FCRD-UFD-2014-000056 / SAND2014-18303R. Sandia National Laboratories, Albuquerque, NM.
- Joyce, S., Hartley, L., Applegate, D., Hoek, J., and Jackson, P., 2014. *Multi-scale groundwater flow modeling during temperate climate conditions for the safety assessment of the proposed high-level nuclear waste repository site at Forsmark, Sweden*. Hydrogeology Journal, 22(6), 1233-1249. doi: 10.1007/s10040-014-1165-6
- Kolata, D.R. and Graese, A.M., 1983. *Lithostratigraphy and depositional environments of the Maquoketa Group (Ordovician) in northern Illinois: Illinois State Geological Survey*
- Kolditz, O., Shao, H., Wang, W., and Bauer, S., 2015. *Thermo-Hydro-Mechanical-Chemical Processes in Fractured Porous Media: Modelling and Benchmarking Closed-Form Solutions* (O. Kolditz, H. Shao, W. Wang, & S. Bauer Eds.). Switzerland: Springer International Publishing.
- Kwon, O., Kronenberg, A.K., and Gangi, A.F., 2001. *Permeability of Wilcox shale and its effective pressure law*, Journal of Geophysical Research, 106(B9): 19339-19353.
- Lake, L. W., Bryant, S. L., and Araque-Martinez, A. N., 2002, *Geochemistry and fluid flow*. Vol. 7. Gulf Professional Publishing.
- Lineback, J. A., 1970, *Stratigraphy of the New Albany Shale in Indiana: Indiana Geological Survey*, Bulletin 44, 73 p.
- Liu, H.-H., Rutqvist, J., and Berryman, J.G., 2009. *On the relationship between stress and elastic strain for porous and fractured rock*, International Journal of Rock Mechanics and Mining Science, 46:289-296.
- Lloyd, O.B., and Lyke, W.L., 1995. *Ground Water Atlas of the United States: Illinois, Indiana, Kentucky, Ohio, Tennessee*. United States Geological Survey HA 730-K. https://pubs.usgs.gov/ha/ha730/ch_k/
- Lomenick, T. F., Gonzales, S., Johnson, K. S., and Byerly, D. W., 1983. *Regional Geological Assessment of the Devonian-Mississippian Shale Sequence of the Appalachian, Illinois, and Michigan Basins Relative to Potential Storage/Disposal of Radioactive Wastes*, ORNL-5703, Oak Ridge National Laboratory, Oak Ridge, TN. 160 p.
- Los Alamos Grid Toolbox, 2017, LaGriT V3.3, Los Alamos National Laboratory, < <http://lagrit.lanl.gov> >.
- Mariner, P.E., Nole, M.A., Basurto, E., Berg, T.M., Chang, K.W., Debusschere, B.J., Eckert, A.C., Ebeida, M.S., Gross, M., Hammond, G.E., Harvey, J., Jordan, S.H., Kuhlman, K.L., LaForce, T.C., Leone, R.C., McLendon III, W.C., Mills, M.M., Park, H.D., Perry, F.V., Salazar III, A., Seidl, D.T., Sevougian, S.D., Stein, E.R., Swiler, L.P., 2020. *Advances in GDSA Framework Development and Process Model Integration* SAND2020-xxxx. Sandia National Laboratories, Albuquerque, NM

Mariner, P. E., Connolly, L. A., Cunningham, L. J., Debusschere, B. J., Dobson, D. C., Frederick, J. M., Hammond, G. E., Jordan, S. H., LaForce, T. C., Nole, M. A., Park, H. D., Perry, F. V., Rogers, R. D., Seidl, D. T., Sevougian, S. D., Stein, E. R., Swift, P. N., Swiler, L. P., Vo, J., and Wallace, M. G., 2019. *Progress in Deep Geologic Safety Assessment in the U.S. since 2010*, M2SF-19SN010304041, U.S. Department of Energy, Spent Fuel and Waste Science and Technology Campaign, Office of Spent Fuel and Waste Disposition, Washington, DC, September 16, 2019

Mariner, P. E., Stein, E. R., Frederick, J. M., Sevougian, S. D., and Hammond, G. E., 2017. *Advances in Geologic Disposal System Modeling and Shale Reference Cases*. SFWD-SFWST-2017-000044 / SAND2017-10304R. Sandia National Laboratories, Albuquerque, NM.

Mariner, P. E., Gardner, W. P., Hammond, G. E., Sevougian, S. D., and Stein, E. R., 2015. *Application of Generic Disposal System Models*. FCRD-UFD-2015-000126 / SAND2015-10037R. Sandia National Laboratories, Albuquerque, NM

Mariner, P. E., Gardner, W. P., Hammond, G. E., Sevougian, S. D. and Stein, E. R., 2015. *Application of Generic Disposal System Models*. SAND2015-10037R; FCRD-UFD-2015-000126. Sandia National Laboratories, Albuquerque, New Mexico.

Mariner, P. E., Stein, E. R., Frederick, J. M., Sevougian, S. D., Hammond, G. E., and Fascitelli, D. G., 2016. *Advances in Geologic Disposal System Modeling and Application to Crystalline Rock*, FCRD-UFD-2016-000440, SAND2016-96107R. Sandia National Laboratories, Albuquerque, NM, September 22, 2016.

Mariner, P. E., Stein, E. R., Sevougian, S. D., Cunningham, L. J., Frederick, J. M., Hammond, G. E., Lowry, T. S., Jordan, S., and Basurto, E., 2018. *Advances in Geologic Disposal Safety Assessment and an Unsaturated Alluvium Reference Case*, SFWD-SFWST-2018-000509, SAND2018-11858R, 130 p.
Mastalerz, M., Schimmelmann, A., Drobnik, A., and Chen, Y., 2013. *Porosity of Devonian and Mississippian New Albany Shale across a maturation gradient: Insights from organic petrology, gas adsorption, and mercury intrusion*. AAPG Bulletin. 97. 1621-1643.

Melvin, R. L., de Lima, V., and Stone, B. D., 1992. *The Stratigraphy and Hydraulic Properties of Tills in Southern New England*. U.S. Geological Survey Open-File Report 91-481. 57 p,

Neuzil, C. E., 2019. *Permeability of clay and shales*, Annual Review of Earth and Planetary Sciences.

Noger, M. C., and Drahovzal, J. A., 2005. *Lithostratigraphy of Precambrian and Paleozoic Rocks along Structural Cross Section KY-1, Crittenden County to Lincoln County, Kentucky*. Kentucky Geological Survey, Report of Investigations 13, Series XII, 36 p.

Nuttal, B. C., 2013. *Middle and Late Devonian New Albany Shale in the Kentucky Geological Survey Marvin Blan No. 1 Well, Hancock County, Kentucky*. Kentucky Geological Survey, Report of Investigations 17, Series XII, 72 p.

Panno S. V., Askari, Z., Kelly, W. R., Parris, T.M., Hackley, K. C., 2017. *Recharge and Groundwater Flow Within an Intracratonic Basin, Midwestern United States*. Ground Water 56. 32-45.

Perry, F. V., Kelley, R.E., Dobson, P.F. and Houseworth, J.E., 2014. *Regional Geology: A GIS Database for Alternative Host Rocks and Potential Siting Guidelines*. LA-UR-14-20368, FCRD-UFD-2014-000068. Los Alamos National Laboratory, Los Alamos, New Mexico.

Person, M., 2012. *Final Technical Report: Analytical-Numerical Sharp-Interface Model of CO₂ Sequestration and Application to Illinois Basin*. New Mexico Tech: Department of Earth and Environmental Sciences, Socorro, NM.

Pettersson, S., and Lönnerberg, B., 2008,. *Final Repository for Spent Nuclear Fuel in Granite - The KBS-3V Concept in Sweden and Finland*. Paper presented at the International Conference Underground Disposal Unit Design & Emplacement Processes for a Deep Geological Repository, Prague, Czechia. June 16-18, 2008.

Price, L. L., Alsaed, A. A., Brady, P. V., Gross, M. B., Hardon, E. L., Nole, M., Prouty, J. L., Banerjee, K., and Davidson, G.G., 2019, *Postclosure Criticality Consequence Analysis - Scoping Phase*, SAND2019-XXXX , 65 p.

Prij, J., Blok, B. M., Laheij, G. M. H., van Rheenen, W., Slagter, W., Uffink, G. J. M., Uijt de Haag, P., Wildenborg, A. F. B., and Zanstra, D. A., 1993. *PRObabilistic Safety Assessment*. Final Report (OPLA-1A)

Prij, J., van Dalen, A., Englund-Borowiec, G., Glasbergen, P., de Haas, J. B. M., Jong, C. T. J., de Jong, E. J., Köster, H. W., Nijhoff-Pan, I., Roodbergen, H. A., Slagter, W., van Weers, A. W., and Znastra, D. A., 1989. *Safety Evaluation of Disposal Concepts in Rock Salt*. Final Report (IL 369; OPLA 89-08)

Richards, J. A., Budai, J. M., Walter, L. M., and Abriola, L. M., 1994. *Fracture analysis of the Upper Devonian Antrim Shale, Michigan Basin (abs.)*: American Association of Petroleum Geologists Bulletin, v. 78, no. 8. 1333.

Robertson, E. C., 1988. *Thermal Properties of Rocks*. U.S. Geological Survey Open-File Report 88-441, Reston, VA.

Rothfuchs, T., Wieckzorek, K., Bazargan, B., and Olivella, S., 2003. *Results of the BAMBUS II Project – Experimental and Modelling Results concerning Salt Backfill Compaction and EDZ Evolution in a Spent Fuel Repository in Rock Salt Formations*. Eurosafe Forum. Paris, France. November 25-26, 2003.
www.eurosafe-forum.org

Rutqvist, J., Ijiri, Y., & Yamamoto, H., 2011. *Implementation of the Barcelona Basic Model into TOUGH-FLAC for simulations of the geomechanical behavior of unsaturated soils*. Computers & Geosciences, 37(6), 751-762.

Ryder, R. T., 1996. *Fracture patterns and their origin in the Upper Devonian Antrim Shale gas reservoir of the Michigan basin: A review*. United States Geologic Survey, Open-File Report 96-23. 33 p.

Sassani, D., Birkholzer, J., Camphouse, R., Freeze, G., Stein, E. R., 2020. *SFWST Disposal Research R&D 5-Year Plan - Draft Report*. SAND 2020-XXXXXX. Sandia National Laboratories, Albuquerque, New Mexico.

Sevougian, S. D., Stein, E. R., Gross, M. B., Hammond, G. E., Frederick, J. M., and Mariner, P. E., 2016. *Status of Progress Made Toward Safety Analysis and Technical Site Evaluations for DOE Managed HLW and SNF*. SAND2016-11232R. Sandia National Laboratories, Albuquerque, NM.

Sevougian, S. D., Stein, E. R., LaForce, T., Perry, F. V., Lowry, T. S., Cunningham, L. J., Nole, M., Haukwa, C. B., Chang, K. W. and Mariner, P. E., 2019a. *GDSA Repository Systems Analysis Progress Report*. SAND2019-5189R. Sandia National Laboratories, Albuquerque, New Mexico, April 30, 2019.

Sevougian, S. D., Stein, E. R., LaForce, T., Perry, F. V., Nole, M., Haukwa, C. B., and Chang, K. W., 2019b. *GDSA Repository Systems Analysis FY19 Update*. SAND2019-11942R. Sandia National Laboratories, Albuquerque, New Mexico, Sept 27, 2019.

Sevougian, S. D., Mariner, P. E., Connolly, L. A., MacKinnon, R. J., Roger, R. D., Dobson, D. C., and Prouty, J. L., 2019c. *DOE SFWST Campaign R&D Roadmap Update*. M2SF-19SN010304042 SAND2019-5179R. Sandia National Laboratories, Albuquerque, NM.

Sevougian, S. D., Freeze, G. A., Gardner, W. P., Hammond, G. E. and Mariner, P. E., 2014. *Performance Assessment Modeling and Sensitivity Analyses of Generic Disposal System Concepts*. FCRD-UFD-2014-000320, SAND2014-17658. Sandia National Laboratories, Albuquerque, New Mexico, September 12, 2014.

Sevougian, S. D., Freeze, G. A., Gross, M. B., Lee, J., Leigh, C. D., Mariner, P. E., MacKinnon, R. J. and Vaughn, P., 2012. *TSPA Model Development and Sensitivity Analysis of Processes Affecting Performance of a Salt Repository for Disposal of Heat-Generating Nuclear Waste*. FCRD-UFD-2012-000320 Rev. 0, U.S. Department of Energy, Office of Used Nuclear Fuel Disposition, Washington, DC.

Sevougian, S. D., Freeze, G. A., Vaughn, P., Mariner, P. E., and Gardner, W.P., 2013. *Update to the Salt R&D Reference Case*. FCRD-UFD-2013-000368, SAND2013-8255P. Sandia National Laboratories, Albuquerque, New Mexico.

Sevougian, S. D., Stein, E. R., Gross, M. B., Hammond, G. E., Frederick, J. M. and Mariner, P. E., 2016. *Status of Progress Made Toward Safety Analysis and Technical Site Evaluations for DOE Managed HLW and SNF*, SAND2016-11232 R; FCRD-UFD-2016-000082, Rev. 1. Sandia National Laboratories, Albuquerque, New Mexico.

Shi, J.-Q., and Durucan, S., 2016. *Near-exponential relationship between effective stress and permeability of porous rocks revealed in Gangi's phenomenological models and application to gas shales*, International Journal of Coal Geology, 154-155: 111-122.

Shoesmith, D. W., 2007. *Used Fuel and Uranium Dioxide Dissolution Studies – A Review*, NWMO TR-2007-03, Nuclear Waste Management Organization, 22 St. Clair Avenue East, 6th Floor, Toronto, Ontario M4T 2S3, Canada.

Shurr, G. W., 1977. *The Pierre Shale, Northern Great Plains, a Potential Isolation Medium for Radioactive Waste*, United States Department of the Interior Geological Survey, Open File Report 77-776

Siegel, D. L., 1989. *Geochemistry of the Cambrian-Ordovician aquifer system in the northern Midwest*, United States: U.S. Geological Survey Professional Paper 1405-D, D1-D76.

SKB (Svensk Kärnbränslehantering AB) 2010a. *Corrosion calculations report for the safety assessment SR-Site*. SKB TR-10-66. Svensk Kärnbränslehantering AB, Stockholm, Sweden.

SKB (Svensk Kärnbränslehantering AB) 2010b. *Design, production and initial state of the canister*. SKB TR-10-14. Svensk Kärnbränslehantering AB, Stockholm, Sweden.

SKB (Svensk Kärnbränslehantering AB) 2010c. *Design, production and initial state of the buffer*. SKB TR-10-15. Svensk Kärnbränslehantering AB, Stockholm, Sweden.

SKB (Svensk Kärnbränslehantering AB) 2010d. *Design, production and initial state of the backfill and plug in deposition tunnels*. SKB TR-10-16. Svensk Kärnbränslehantering AB, Stockholm, Sweden.

SKB (Svensk Kärnbränslehantering AB) 2011. *Long-term safety for the final repository for spent nuclear fuel at Forsmark, Main report of the SR-Site project, Volume 1*. SKB TR-11-01. Svensk Kärnbränslehantering AB, Stockholm, Sweden.

SKB 2010. *Design, production and initial state of the canister*. SKB TR-10-14. Svensk Kärnbränslehantering AB, Stockholm, Sweden.

Stehfest, J., 1970, *Algorithm 368: Numerical inversion of Laplace transforms*. Communications of the ACM, 13:47-49.

Stein, E. R., C. Bryan, D. C. Dobson, E. L. Hardin, C. J. Colón, C. M. Lopez, E. N. Matteo, S. Mohanty, M. Pendleton, F. V. Perry, J. L. Prouty, D. C. Sassani, J. Rutqvist, L. Zheng, K. B. Sauer, R. Howard, A. Adeniyi, K. Banerjee, R. Joseph 2020a. *Disposal Concepts for a High-Temperature Repository in Shale*. SAND2020-xxxx. Sandia National Laboratories, Albuquerque, NM.

Stein, E. R., Leone, R. C., and Nguyen, S., 2020b. *DECOVALEX-2023 Task F Specification Revision 1*. SAND2020-8494 O. Sandia National Laboratories, Albuquerque, NM.

Stephens, M. B., 2010. *Forsmark site investigation: Bedrock geology – overview and excursion guide*. SKB (Sweden) R-10-04. 47 p.

Strobel, M. L., 1993. *Hydraulic properties of three types of glacial deposits in Ohio*: U.S. Geological Survey Water-Resources Investigations Report 92-4135, 41 p.

Urquhart, A. and Bauer, S., 2014. *Experimental determination of single-crystal halite thermal conductivity, diffusivity and specific heat from 75°C to 300°C*. Sandia National Laboratories, Albuquerque, NM, SAND2014-16353J.

Van Rossum, G., Drake, F. L., 2009, *Python 3 Reference Manual*. Scotts Valley, CA: CreateSpace.

Vaughn, P., Sevougian, S. D., Hardin, E. L., Mariner, P. E., and Gross, M. B., 2013. *Reference Case for Generic Disposal of HLW and SNF in Salt*, in *Proceedings of the 2013 International High-Level Radioactive Waste Management Conference*, Albuquerque, NM, April 28 – May 2, 2013, American Nuclear Society, La Grange Park, Illinois. (www.ans.org).

Wang, Y. and Lee, J. H., 2010. *Generic Disposal System Environment Modeling - Fiscal Year 2010 Progress Report*. SAND2010-8202P. Sandia National Laboratories, Albuquerque, NM.

Waples, D. W., and Waples, J. S., 2004. *A Review and Evaluation of Specific Heat Capacities of Rocks, Minerals, and Subsurface Fluids. Part 1: Minerals and Nonporous Rocks*. Natural Resources Research, v13(2), pp 97-122

Werme, L. O., Johnson, L. H., Oversby, V. M., King, F., Spahiu, K., Grambow, B., and Shoesmith, D.

W., 2004. *Spent fuel performance under repository conditions: A model for use in SR-Can*. SKB TR-04-19. Svensk Kärnbränslehantering AB, Stockholm, Sweden.

Young, H. L., 1992. *Hydrogeology of the Cambrian-Ordovician aquifer system in the northern Midwest, United States Regional aquifer-system analysis-northern Midwest*. U.S. Geological Survey professional paper 1405-B. 108 p.

Zhang, C-L., and Rothfuchs, T., 2008. *Damage and sealing of clay rocks detected by measurements of gas permeability*. Physics and Chemistry of the Earth, 33, S363–S373.

Zhang, R., Ning Z., Yang F., Zhao H., and Wang, Q., 2016. *A laboratory study of the porosity-permeability relationships of shale and sandstone under effective stress*, Int. J. Rock Mech. Min. Sci., 81: 19-27.

Zheng, J., Zheng, L., Liu, H.-H., and Ju, Y. 2016, *Relationships between permeability, porosity and effective stress for low-permeability sedimentary rock*, Int. J. Rock Mech. Min. Sci., 78: 304-318.

This page intentionally left blank

Appendix A Argillite Concepts Meeting Agenda

2020 Argillite Concepts Meeting

DRAFT AGENDA v2

February 25-26, 2020
 (Sandia Bldg. 823, Rm 2279)

Instructions:

- Please prepare slides presenting at least two options for your particular repository feature/component.
- Discuss the effect of various processes occurring in that feature on radionuclide mobilization and transport (including, if relevant, waste package integrity).
- Describe the key advantages/disadvantages of each option related to both (1) performance (ISC; importance to safety case) and (2) R&D needs (SAL; state of the art level).
- Presentations can be short. Leave ample time for discussion.

DAY 1, TUESDAY, 2/25/2020	
8:30 a.m.	Introduction and Objectives, Stein/Sevougian <ul style="list-style-type: none"> • Develop a shared concept for a high-temperature argillite repository across SFWST to inform modeling and experiments • Group will choose an option for each feature/component with a “prejudice” for improving our capabilities
8:45 a.m.	FEPs Context, Price
9:00 a.m.	NATURAL SYSTEM Host Rock, Perry <ul style="list-style-type: none"> • Sealing vs. (somewhat) brittle shale: options in the U.S. • Characteristics of materials (porosity, permeability, fractures, mineralogy, sorption, mechanical strength) Groundwater Chemistry, Jové Colón <ul style="list-style-type: none"> • Options for representative groundwater chemistry • Major element chemistry; pH; redox chemistry; mineral equilibria, etc. Discussion/preliminary selection of options, All
10:15 a.m.	<i>Break</i>
10:30 a.m.	WP LOADING; REPOSITORY LAYOUT & CONSTRUCTION Inventory, Howard (w/ Hardin) <ul style="list-style-type: none"> • Option(s) for representative WP loading • Option(s) for bounding WP loading (considering future projections) • Burn-up; time OoR; heat of decay; radionuclide inventory • Heterogeneity and variability in WP loading Repository Layout and Constructability, Hardin (w/ Howard) <ul style="list-style-type: none"> • Construction options considering sealing v. (somewhat) brittle shale • Construction method; excavation sequence; ground support • Drift diameter; WP and drift spacing; possible sacrificial zone • Other materials (e.g., seals, backfill); access (shaft v. ramp) Discussion/preliminary selection of options, All

2020 Argillite Concepts Meeting

12:00 p.m.	Lunch
1:30 p.m.	<p>WASTE PACKAGE Waste Package Materials and Design, Howard/Hardin</p> <ul style="list-style-type: none"> • Options for overpack: materials, thickness, welding/sealing, etc. • Canister & internals • Mechanical strength and mechanical failure considerations <p>Innovative Overpack Materials, Wang</p> <ul style="list-style-type: none"> • Cu, Pb, etc. and applicability to shale repository <p>Discussion, All</p>
3:00 p.m.	Break
3:15	<p>WASTE PACKAGE, continued Overpack Corrosion Rates and Reactions, Caporuscio/Jove Colon</p> <ul style="list-style-type: none"> • Corrosion of stainless steel and copper materials • Associated changes in buffer and buffer amendments (quartz, graphite, ...). • Interactions between WP material, groundwater chemistry, buffer, ground support materials, etc. <p>Corrosion Mechanisms, Bryan</p> <ul style="list-style-type: none"> • Corrosion mechanisms and their influence on design of WP, buffer, and ground support materials • Dependence on groundwater chemistry? <p>Discussion/preliminary selection of options, All</p>
5:00 p.m.	Adjourn for the day

DAY 2, WEDNESDAY, 2/26/2019	
8:30 a.m.	<p>In-Package Chemistry: Waste form, cladding, neutron absorbers, Sassani (w/Sauer)</p> <ul style="list-style-type: none"> • Options for UO₂ degradation model (dissolution mechanisms/rates) • Options for cladding: materials; failure mechanisms; degradation rates • Neutron Absorbers: Boral degradation (Sauer) • In-package chemistry considerations/interactions/coupling <p>Discussion/preliminary selection of options, All</p>
10:00 a.m.	Break
10:15 a.m.	<p>Buffer Design and Materials, Zheng/Wang</p> <ul style="list-style-type: none"> • Two (or more) options: Buffer material and amendments • Buffer construction (bricks, pellets, layered? Etc. • Material properties, evolution of properties affecting RN transport <p>Discussion/preliminary selection of options, All</p>
11:45 a.m.	Lunch

2020 Argillite Concepts Meeting

1:00 p.m.	Ground Support Design and Materials (e.g. Cement), <i>Matteo</i> <ul style="list-style-type: none">▪ Two (or more) options: Ground support materials▪ Construction▪ Material properties, evolution of properties affecting RN transport Discussion/preliminary selection of options, <i>All</i>	
2:00 p.m.	Disturbed Rock Zone, <i>Rutqvist</i> <ul style="list-style-type: none">▪ Extent▪ Properties, evolution of properties affecting RN transport▪ Consider sealing v. (somewhat) brittle Discussion/preliminary selection of options, <i>All</i>	
2:45 p.m.	<i>Break</i>	
3:00 p.m.	Group Discussion and Draft of Argillite Concept (Outline), <i>Stein/Price as facilitators</i>	
5:00 p.m.	<i>Adjourn</i>	

Appendix B DECOVALEX Crystalline Questionnaire

CRYSTALLINE REFERENCE CASE QUESTIONNAIRE DECOVALEX23, TASK F

T	Thermal
H	Hydrological
M	Mechanical
C	Chemical
DFN	Discrete Fracture Network
ECPM	Equivalent Continuous Porous Medium
U/SA	Uncertainty and Sensitivity Analysis
PWR	Pressurized Water Reactor

SAND2020-6613 O

Emily Stein (ergiamb@sandia.gov)

June 25, 2020

Sandia National Laboratories is a multimission laboratory managed and operated by National Technology and Engineering Solutions of Sandia, LLC, a wholly owned subsidiary of Honeywell International Inc., for the U.S. Department of Energy's National Nuclear Security Administration under contract DE-NA0003525.

TEAM

Institution(s)

Team members

Technical expertise and/or particular interests within the reference case and performance assessment

Modeling approach

Likely approach to simulating flow in fractured rock (DFN; ECPM; channel; other?)

Likely approach to simulating transport in fractured rock (advection/dispersion equation; particle tracking?)

Software*

Creation of DFN, ECPM, or other hydrogeologic representation of fractured rock

THMC processes

Uncertainty and sensitivity analysis (U/SA)

Computing resources

**dfnWorks* (DFN and ECPM generation), *PFLOTRAN* (THC simulator), and *Dakota* (U/SA) are available to anyone who would like to use them.

FEATURES

Geologic setting

Complexity of model domain (check one).

- Our meshing software can handle an island with simple shoreline and topography.
- Input format for irregular surfaces or volumes is _____.
- Our meshing software is better suited to a rectilinear (box-shaped) model domain.

Emplacement concept

[Question raised at kick-off meeting: Is it desirable to simplify the model domain by choosing an emplacement concept that uses in-drift axial emplacement?]

Preferred choice is (check one):

- KBS-3V (4-PWR canister in vertical deposition hole)
- KBS-3H (4-PWR canister in horizontal boreholes)
- In-drift axial emplacement of 4-PWR canisters
- In-drift axial emplacement of larger (12-PWR) canisters
- Other (please describe): _____

Inventory

How much waste (check one):

- Proposed inventory sounds good: 4350 MTU (2500 4-PWR canisters)
- <4350 MTU (please suggest): _____
- >4350 MTU (please be aware of simulation size): _____

Waste characteristics (check all that apply)

- Pressurized water reactor (PWR) spent nuclear fuel assemblies with radionuclide inventory and heat of decay calculated assuming initial enrichment of 4.73 wt% U-235, 60 GWd/MTU burnup, 50 years out of reactor (OoR) (Carter et al. 2013) – to be provided by U.S. team.
- Instead of this (please describe): _____
- In addition to this (please describe): _____

Repository layout

This sounds good to me (check all that apply):

- 500 m deep
- 100 C temperature limit in the buffer
- Allow higher buffer temperatures to accommodate 12-PWR waste packages
- Canister and drift spacing to be determined depending on emplacement concept, thermal limit, and prescribed offset from deterministic deformation zones. (KBS-3V results in minimum 40 m tunnel spacing; 6 m deposition hole spacing; SKB TR-11-01, Section 5.2.2)
- Offset from deformation zone and deposition hole rejection criteria to be discussed.
- Other considerations (please list): _____

Engineered Barrier System

Canister (check one)

- Cast iron insert with 5-cm copper shell (specifications from SKB TR-10-14, Section 3.1 and 3.2).
- Stainless steel insert with carbon steel shell (specifications from Surao)

Buffer (check one)

- Compacted bentonite blocks with pellets to fill gaps (specifications from SKB TR-10-15, Section 4)
- Other well-characterized bentonite (please suggest): _____ [Coordinate with reference pore water chemistry for surface complexation modeling.]

Natural Barrier System

[We will attempt to make these features reasonably self-consistent, but for now offer any suggestion you like.]

Hydraulic Conductor Domains (large deterministic features) (check one)

- Representative set derived from observations at Forsmark or Olkiluoto
- Appropriate dataset provided by a participating team (please suggest): _____

Hydraulic Rock Mass Domains (stochastic distributions of smaller features) (check one)

- Western Central Hydraulic Unit (CHUW) at Olkiluoto, (Hartley et al. 2016, Table 4-2). Calibrated with relationship describing fracture transmissivity as a function of stress. Requires more options in software that generates DFN.

- FFM01/FFM06 +/- FFM02 at Forsmark (Joyce et al. 2014, Table 2). Not calibrated with fracture transmissivity as a function of stress. Requires fewer options in software that generates DFN.
- Appropriate DFN parameterization provided by a participating team (please suggest): _____
- Optional, ambitious, and perhaps out of scope: If sufficiently large raw data set is available (pumping, injection, other flow log, and/or tracer test), interested teams could calibrate unique stochastic permeability models to it. Appropriate dataset provided by a participating team (please suggest): _____

Overburden (check one)

- Stylized regolith and alluvial/glacial deposits derived from Forsmark or Olkiluoto surficial deposits.
- Overburden description provided by a participating team (please suggest): _____

Excavation Damage Zone properties (permeability, porosity, etc.) (check one)

- Borrow from Forsmark (SKB TR-10-50, Section 6.3.4) or Olkiluoto
- Appropriate dataset provided by participating team (please suggest): _____

Crystalline rock matrix properties (porosity, tortuosity, effective diffusion coefficient, K_d) (check one)

- Borrow from Forsmark (SKB TR-10-50, Section 2.5) or Olkiluoto
- Appropriate dataset provided by a participating team (please suggest): _____

EVENTS

Rank from 1 to 4, with 1 being most relevant to you, and 4 being least relevant to you:

- Pinhole failure (assuming current/temperate climate conditions)
 - In this scenario, random failure occurs due to manufacturing defect.
 - No coupled processes required to fail the canister. (Good initial comparison of transport in the PA model domain?)
 - Near field radionuclide transport is diffusion dominated. (Adsorption models are more relevant.)

- Canister failure by corrosion (assuming current/temperate climate conditions).
 - In this scenario, infiltration of dilute meteoric water causes buffer erosion and advective conditions in a deposition hole, increasing the flux of sulfide to the surface of the copper canister.
 - Coupled (T)HMC processes affecting corrosion are fracture flow, buffer erosion, and reactive transport.
 - Near field radionuclide transport is advection dominated.
 - *[Replace with alternate corrosion model if alternate canister material is preferred by majority.]*

- Shear failure of canister due to ground motion (seismic event).
 - At time of ground motion event, fail canisters meeting the failure criteria.
 - Near field radionuclide transport is diffusion dominated. (Adsorption models are more relevant.)
 - Possibility of recalculating DFN transmissivity as a function of stress/strain.
 - Possibility of invoking a seismic hazard curve, and completing a probabilistic risk assessment (risk=probability*consequence).

- Canister failure by any of the above mechanisms assuming cyclical glacial loading
 - Glacial loading alters hydrologic boundary conditions and stress state
 - Depending on ambition, coupled THM processes include isostatic loading, crustal flexure, development of fluid overpressures, permafrost formation, fracture compression and dilation, etc.

PROCESSES**Natural Barrier System**

[Check all that apply]

(T)HC coupling affecting radionuclide transport in the fractured host rock

[This is where we're starting!]

- Transient and/or steady-state single-phase flow
- Advection, dispersion in fractures
- Fracture-matrix diffusion
- Radionuclide decay and ingrowth
- Adsorption
- Precipitation and dissolution of phases controlling radionuclide solubility (can be screened out in far field)
- Other (please describe): _____

THM coupling in the near field fractured host rock

- Thermal overpressure -> apertures of existing fractures -> fracture transmissivity (SKB screens this out because effect is small with 4-PWRs)
- Other (please describe): _____

(T)HM coupling in the far field fractured host rock

- Glacial loading -> hydrologic boundary conditions -> flow paths
- Glacial loading -> apertures of existing fractures -> fracture transmissivity
- Seismic event -> apertures of existing fractures -> fracture transmissivity
- Other (please describe): _____

Engineered Barrier System

[check all that apply]

(T)HMC coupling affecting canister corrosion

- After saturation, buffer erosion rate depends on flow rate (infiltration of dilute meteoric H₂O destabilizes buffer and causes chemical erosion)
- Advective (and diffusive) transport of HS⁻ to copper canister in eroded bentonite
- Diffusive (and advective) transport of HS⁻ to copper canister in intact bentonite
- Advective and diffusive transport of corrosion products
- Corrosion at canister surface

(T)HC coupling affecting radionuclide transport in the buffer

[More mechanistic models will require more complete definition of reference pore water chemistry and buffer properties.]

- Advection/diffusion/dispersion
- Radionuclide decay and ingrowth
- Adsorption, possibilities include
 - Isotherm(s)
 - Surface complexation
 - Ion exchange
- Radionuclide solubility, possibilities include
 - Precipitation and dissolution of mineral phases
 - Solubility limits
- Other (please describe): _____

(T)HC coupling affecting degradation of UO₂ waste form

- I'll use the simple (non-mechanistic) rate-controlled model (Werme et al. 2004, Section 3.7).
- I'm interested in simulating coupled electrochemical processes (Sassani et al. 2013). (Probably beyond the scope of Task F, but tossing it out there anyway.)
- Other (please describe): _____

Appendix C VoroCrust Output Conversion

All the mesh information PFLOTRAN needs to run a simulation is included in the VoroCrust mesh.vcg file as shown in Figure A3-1. The first column of each row under CELLS is the cell ID, the second-fourth columns are the (x,y,z) coordinates of the node, which is analogous to the cell center. The fifth column is the ID of the region that this node is inside.

Under the CONNECTIONS heading the first two columns are the ID of the cells that are connected. The third to fifth column are the (x,y,z) coordinates where line connecting the two cells intersects the plane of the face connecting them. This point may not be on the face between the cells, but the line is always perpendicular to the face on a Voronoi mesh. The sixth column is the area of the face connecting the two cells. Columns seven to nine are the outward normal of the face connecting the two cells. Boundary nodes are included in this section and are flagged as connections to themselves, for example connection 1 1 in the last line of Figure A3-1.

The python script is used to split the mesh information into three types of files that PFLOTRAN needs for simulations and is freely available upon request. The cells and internal connections are put into an out_mesh.vcg file that can be imported into PFLOTRAN as a mesh using the UNSTRUCTURED_EXPLICIT option. The material IDs are put into a matID.h5 file that can be read into the PFLOTRAN STRATA block to define different properties for each region in the domain. For rectangular domains six boundary files that can be read into the REGION block and used to implement boundary conditions are created: bdry_smX.ex, bdry_lgX.ex, bdry_smY.ex, bdry_lgY.ex, bdry_smZ.ex, and bdry_lgZ.ex. For non-rectangular domains the script will make boundary region files for the sides that are aligned with coordinate axis planes and an additional file called bdry_unclaim.ex that contains all other boundary cells. This file could be used as a boundary region as well.

```

CELLS 432182
1 18.33621081318728 65.29916651100994 0.7814267048805539 0.02361552565071427 1
2 18.30461284038969 65.03372419799233 0.7611174348192239 0.02886008348460395 1
3 18.07338415362041 64.98139916284454 0.7886211238343368 0.02927525940117367 1
4 18.31226226526461 65.33024991488516 0.7868876284703697 0.02787447084973901 1
5 17.99200424897747 65.29714767505311 0.8066914236058266 0.03183422152169257 1
6 75.60310276879191 78.92670603829416 0.1989870735802718 0.03367981013391631 1
7 75.7124936727314 78.82952535313274 0.1727541077993841 0.01916344163862832 1
8 75.29313529110505 78.91423122488362 0.1436947627793348 0.02553730334610672 1
9 75.60054659605333 78.55582513846872 0.2116221933857704 0.03277880150296188 1
10 75.40657019149576 78.50358533650969 0.1734457588922159 0.01293329187858919 1

CONNECTIONS 2643800
1 4 18.32423653922594 65.31470821294755 0.7841571666754619 0.2150244837464929 -0.6044968071489668 0.784591135068414 0.1378417967046379
1 120005 18.34213956076958 65.21632498316771 0.5122966298588231 0.04020196879486414 0.02104976914860921 -0.2941253633739099 -0.9555350217752123
1 326601 18.46262883679147 65.16677509786183 0.7653955292963111 0.00512568406626668 0.6879694894680153 -0.7204767984557213 -0.0872419878734562
1 94816 18.43971905838797 65.19429137015605 0.5159472786860475 1.328908924982231e-06 0.34090808974743818 -0.3454027219814553 -0.8743474925617175
1 120008 18.30382765989096 65.33343106598457 0.4760816357900851 0.003342140647912448 -0.1048122871058189 0.1109016883158612 -0.9882890265506032
1 92341 18.45986041873226 65.35647209409107 0.5043900633007596 0.01536609849341372 0.3983142524620933 0.1858014145475397 -0.0982335946944409
1 319650 18.47489670176667 65.27547315993996 0.7775572718740151 0.1368798173533216 0.9853458378708114 -0.1683382866213166 -0.02749183602577069
1 216317 18.51623722513159 65.41386373530943 0.7896702202747552 0.006247901386146042 0.8427467888179435 0.536925201256734 0.03858987163052172
1 1 18.33621081318728 65.29916651100994 1 0.04001433435719833 0 0 1
    
```

Figure A3-1. Example VoroCrust mesh.vcg output file